Forces and Pressures on Core-Loc Armour Units in Rubble Mound Breakwaters Measured via Instrumented "Smart-Units"

by:

Derek Eden

Thesis submitted to the Faculty of Graduate and Post Doctoral Studies
in partial fulfillment of the requirements for the
Master of Applied Science degree in Civil Engineering

University of Ottawa, Canada

Department of Civil Engineering

April 2019

Preface

This thesis submission, to the Faculty of Graduate and Post Doctoral Studies, is in partial fulfillment of the requirements for the Master of Applied Science (M.A.Sc.) degree in Civil Engineering. The duration of this graduate program was funded by NSERC CGS-M, OGS Graduate, and UOttawa Admission Scholarships.

The research project undertaken in the current study is a portion of an ongoing joint initiative between University of Ottawa, National Research Council Canada (NRC-OCRE), W.F. Baird & Associates, and Imperial College London. This research initiative is composed of multiple experimental and numerical phases taking place at the University of Ottawa Hydraulics Laboratory, NRC-OCRE, and Imperial College London. A brief summary of the different project phases is outlined below. Data from all experimental phases outlined below were used for numerical validation by Imperial College London.

Phase 0: Controlled drop tests at the University of Ottawa Hydraulics Laboratory. This set of experiments was undertaken in order to observe the development of forces and force coefficients on Core-Loc armour units at varying sizes, densities, and orientations in different steady and unsteady flow conditions.

Phase 1: Horizontal Single Unit (HSU) tests at NRC-OCRE. This set of testing consisted of a single Core-Loc unit fixed on a horizontal slope, fully submerged and subjected to wave action. This phase of experimental testing was meant to supplement Phase 0, and provide additional information regarding force development and force coefficients during unsteady and oscillatory flow conditions at different scales and orientations.

Phase 2: Slope Single Unit (SSU) tests at NRC-OCRE. This set of testing consisted of a single Core-Loc unit fixed on a breakwater slope and subjected to wave action. This set of testing was geared towards understanding the hydrodynamic response of Core-Loc armour units under varying sea state parameters, and at different locations along the breakwater slope. This phase included the development and testing of an instrumented Core-Loc unit and also contained a numerical modeling aspect in OpenFOAM to replicate the NRC-OCRE experiments. This phase is the focus of the current study.

Phase 3: Slope Multi Unit (SMU) tests at NRC-OCRE. This set of testing consisted of full armour layers fixed on a breakwater slope, subjected to wave action. The focus of this phase of testing was understanding the hydrodynamic response of armour layers, and units within armour layers. This testing utilizes the instrumented armour unit developed in Phase 2, and explored the effects of location, orientation and slope permeability. This phase will also include a numerical portion.

Phase 4: Free Multi Unit (FMU) tests at NRC-OCRE. This set of testing is currently being planned and scheduled for completion. This phase focuses on the development of a fully wireless instrumented unit, and testing similar to Phase 3 but with fully dynamic armour layers.

Abstract

Today, more than forty percent of the world's population lives within 100 kilometers of a coastal area, and population densities are only increasing. In recent years, extreme conditions have resulted in several failures of coastal protection structures around the world. During these failure events, the incurred cost of damages and loss of life has been nearly immeasurable.

Rubble mound breakwaters have been used for millennia, and are critical even today for the protection of coastal areas. In the last several decades, the popularity of using concrete armour units in place of natural rock has risen greatly. However, the quantitative interaction between wave hydrodynamics and the armour layer is still not clearly understood. Due to highly complex, turbulent flow patterns that occur in the armour layer, direct assessment of forces acting on individual units has not been practical. This has prevented the coastal engineering field from applying a force-balance design approach that is commonplace in other civil engineering disciplines. Instead, a wealth of experimental testing and past case studies have resulted in a wide array of empirical formulae and design techniques. These approaches are often very idealized and do not account for all parameters that have been shown to affect armour unit stability.

The current study aims to quantify the forces and pressures acting on units within an armour layer, using an experimental approach. This was achieved by developing an instrumented Core-Loc armour unit. This armour unit was outfitted with 6 pressure sensors, and the ability to be mounted on a force transducer. This unit was then put through a performance analysis and calibration procedure, before being extensively tested in a breakwater setting. Wide ranges of wave conditions were utilized, with the unit at three different locations along the breakwater slope. This was done to isolate both the effect of various sea state parameters, and the effect of unit location along a breakwater slope versus generated forces and pressures. In addition to the experimental study, an accompanying numerical study was performed in OpenFOAM. This had the intent of both developing general modeling rules of thumb for rubble mound breakwaters, and for replicating the experimental results.

The results showed that using relatively low-tech, low-cost, and widely available instrumentation was capable of performing in a coastal engineering setting. The performance of the unit showed great promise for "smart-units" to usher in a new paradigm of experimental testing for rubble mound breakwaters. From the results of the performance analysis and calibration procedure, it was evident that the unit could record forces and pressures to a high degree of accuracy. From the breakwater testing program, notable relationships between unit location, surf similarity, and wave steepness emerged. It appeared that the largest hydrodynamic interaction with units occurs slightly below the SWL. As well, both decreased surf similarity, and increased wave steepness resulted in higher hydrodynamic interaction for all locations. General rules of thumb for modeling armour units, as well as wave conditions in a breakwater setting were developed for the numerical study in OpenFOAM. Additionally, the calibrated numerical model was capable of reproducing the experimental results with reasonable accuracy.

Acknowledgements

First, I would like to thank my academic supervisor, Dr. Ioan Nistor. He is the professor who sparked my interest in the coastal engineering field during my undergraduate studies, and encouraged me to pursue my academic goals. Throughout my undergraduate and graduate studies, he has been a friend and mentor who has provided me with countless opportunities to become involved and further my academic career. His dedication to his students is remarkable and admirable; I could have not asked for a better supervisor for my graduate studies. I am very grateful to have been mentored with his hard work ethic, attention to detail, and technical expertise that has improved both my research and knowledge of the field as a whole.

I would also like to thank Dr. Andrew Cornett from the Ocean, Coastal and River Engineering Research Centre at the National Research Council of Canada (NRC-OCRE). His input, guidance, and oversight during the experimental portion of this work were instrumental in the process, outcome and quality of the testing program. A special thank you also goes out to the rest of the team at NRC-OCRE for their technical training and assistance throughout the experimental program.

Of course, none of this could have been completed without the help of my friends and research colleagues: Steven Douglas and Adrian Simpalean. It was an honour and great experience working with this team over the past two years. I truly enjoyed the time we spent developing and implementing all aspects of the research program. They were there for me during the highs and the lows, challenged me to be my best, and made this an all around more enriching experience that I will remember for years to come.

I would also like to express my deepest thanks and gratitude to our collaborating research team at Imperial College London, for their unwavering interest and involvement in this project, and for the hospitality during my research stay in London, UK. A special thank you goes out to Lluis Via-Estrem, Dr. John Paul Latham, and Dr. Jason Zheng for making this an amazing experience that I will never forget.

Lastly, I would like to thank my friends and family, for their unending support that has gotten me to where I am today. Without them, I would not have had the influences and opportunities in my life that has allowed me to chase my dreams to become an engineer.

To all those who have been involved in my life and my development to this point, I thank you sincerely.

Table of Contents

List of Figures

List of Tables

List of Symbols

Symbol	Description	Units
a	Van der Meer Empirical Parameter	-
A	Area	m^2
ADC_{output}	Raw ADC Output	-
ADC_{zero}	ADC Zero Value	-
b	Van der Meer Empirical Parameter	-
c	Calibration Coefficient	mV/Pa
C	Characteristic Height	m
C_α	Compression Coefficient	-
d	Water Depth	m
D_n	Nominal Armour Unit Diameter	m
F	Total Force	N
F_B	Buoyant Force	N
F_H	Hydrodynamic Force	N
F_s	Fluid Mass Flux	kg/s
g	Gravitational Acceleration	m/s^2
H	Wave Height	m
H_D	Diffracted Wave Height	m
H_I	Incident Wave Height	m
$H_{1/3}$	Statistical Significant Wave Height	m
H_{m0}	Spectral Significant Wave Height	m
H_R	Reflected Wave Height	m
k	Turbulent Kinetic Energy	m^2/s^2
K_D	Hudson's Equation Empirical Parameter	-
K_R	Reflection Coefficient	-
k_Δ	Armour Layer Coefficient	-
L	Wavelength	m
L_0	Deep-water Wave Length	m
L_x	Length in X-Direction	m
L_y	Length in Y-Direction	m
N	Number of Waves	-
n	Number of Layers	-
N_a	Packing Density	$1/m^2$
N_{od}	Number of Displaced Units per D_n Along	-
N_{omov}	Number of Moving Units	-
N_s	Stability Number	-
n_v	Armour Layer Porosity	-
N_x	Number of Units in X-Direction	-
N_y	Number of Units in Y-Direction	-
P	Notional Breakwater Permeability	-
p	Pressure	Pa

R_D	Run-down Height	m
R_U	Run-up Height	m
$R_{U2\%}$	Run-up Height with 2% Probability of	m
S	Spectral Density	m^2/Hz
s_{om}	Deep-water Wave Steepness using T_m	-
T	Wave Period	s
t	Time	s
T_m	Mean Wave Period	s
T_p	Spectral Peak Wave Period	s
$\mathbf{U}$	Velocity Vector	m/s
U_c	Compression Velocity Vector	m/s
U_{AVG}	Average Velocity	m/s
V_a	Volume of Armour Unit	m^3
V_{air}	Volume of Air	m^3
V_{total}	Total Volume	m^3
V_{max}	Maximum Output Voltage	V
V_{output}	Output Voltage	V
W	Armour Unit Weight	N
W'	Submerged Armour Unit Weight	N
W_{core}	Core Material Weight	N
$W_{underlayer}$	Underlayer Material Weight	N
α	Phase Fraction	-
Δ	Relative Submerged Armour Unit Density	-
ε	Turbulent Energy Dissapation	m^2/s^3
θ	Breakwater Slope Angle	Degrees
μ	Dynamic Viscosity	Ns/m^2
μ_{eff}	Effective Dynamic Viscosity	Ns/m^2
μ_s	Coefficient of Static Friction	-
μ_t	Turbulent Eddy Viscosity	Ns/m^2
ξ_0	Deep-water Iribarren Number	-
ρ_a	Armour Unit Density	kg/m^3
ρ_w	Density of Water	kg/m^3
σ	Surface Tension Coefficient	N/m
$\boldsymbol{\tau}$	Stress Tensor	Pa
Υ_b	Berm Influence Factor	-
Υ_f	Roughness Influence Factor	-
Υ_a	Specific Weight of Armour Unit	N/m^3
Υ_w	Specific Weight of Water	N/m^3
Υ_β	Oblique Influence Factor	-
ω	Wave Frequency	Hz

1.0 Introduction

1.1 Background

Today, more than forty percent of the world's population lives within one 100 kilometers of a coastal area. With the anticipated climate-related changes to coastal environments, and increasing population densities along the world's shorelines, the safe design of coastal protection structures has never been more important. In recent years, extreme conditions have given rise to several failures of coastal protection structures around the world. The consequences of such failures have shown the importance of a proper design for these types of structures.

Breakwaters have been used throughout history to protect coasts and to create harbours; the simplest form being rubble mound breakwaters. A typical cross section of a rubble mound breakwater is depicted in Figure 1. In its' simplest form, it is essentially a porous mound of stone rubble, as the name implies. The outer-layer that is subjected to wave action is known as the armour layer; this layer is constructed using the largest stones. The weight, and stabilizing interlocking forces of each stone maintains the integrity of the structure during wave action. Simultaneously, the hydrodynamic interaction with the complex pores between the armour stones produces highly turbulent flow patterns that dissipate incident wave energy.

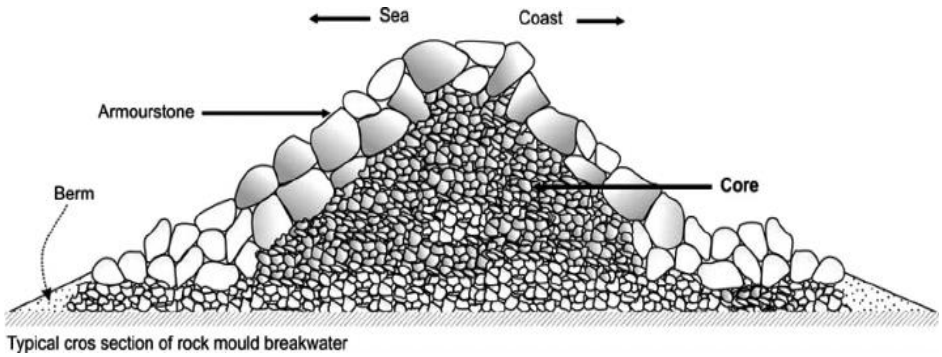

Figure 1: Idealized Cross-Section of a Rubble Mound Breakwater from Karsten (2007)

In the last several decades, the popularity of breakwaters with armour layers constructed of concrete armour units (CAUs) has risen greatly. These units are essentially unreinforced concrete that is moulded into various shapes. These shapes achieve different stability effects, and attempt to mimic or improve upon the behaviour of natural rock in a rubble mound breakwater.

CAUs become preferable to natural rock when considering project specific constraints. These include: location, availability of rock, rock quality, shipping logistics, required size, and other factors. When constructing deep-water breakwaters (≈ 40 m or deeper), the required rock size begins to become unfeasible to quarry. CAUs are easily handled and

placed on a breakwater slope via crane. They also have the advantage of the ability to be manufactured anywhere; the construction of concrete armour units is simple and quality parameters are easily repeatable on a massive scale.

The Core-Loc armour unit was developed and patented by the U.S. Army Corps of Engineers Coastal and Hydraulics Laboratory in the 1990s. With projects around the world, this has proven to be a highly dissipating and cost-effective armour unit shape. This specific unit is the focus of the current study. The Core-Loc unit, and a typical breakwater constructed from this type of unit is shown in Figure 2.

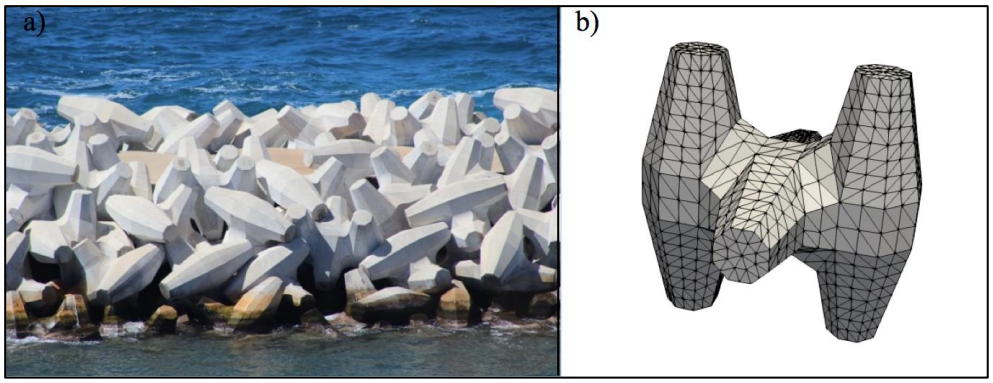

Figure 2: a) Typical Core-Loc Breakwater from CLI (2018), b) Core-Loc Armour Unit

Breakwaters have been used extensively throughout history, and are critical to protecting today's shorelines. However, the complex interaction between the armour layer and wave hydrodynamics is not clearly understood. Consequently, the typical force-balance design approach applied in most civil engineering structures is not applied in current design methods. Failure of a single armour unit occurs when the "dislodging" forces generated during wave action exceed the forces that hold it in place. It would then be reasonable to assume, that an accurate approach to designing the armour layer would be based on the balance of these forces. However, the extremely complex flow due to waves, associated run-up, and run-down, through a porous armour layer causes a range of secondary effects. These effects include the motion of units, unit-to-unit interactions, porous under-layer interaction, and a host of other effects not easily quantified. This has caused direct assessment of the forces on individual units to be difficult and impractical for design purposes.

This has led researchers to develop empirical design methods and equations based on a wealth of scaled experimental testing, and analysis of past breakwater failures. It is these empirical design methods that are commonplace in the industry today. The current design process lacks the quantification of unit forces, concrete stresses, and hydrodynamic pressures. As well, non-linear effects such as unit movement, unit collisions, concrete fatigue, debris impacts and other design related factors are not considered.

The current study focuses on furthering the understanding of the interaction of armour units during wave action. This is done by quantifying induced forces and pressures on individual units, which can be used for a force-balance design approach.

1.2 Research Motivation

The principle motivation of the current study is to further understand the hydrodynamic interaction of armour units in an armour layer during wave action, and to develop methods for advancing the force balance design approach of rubble mound breakwaters. This study will add to the advancement of the design methods currently used in the breakwater field, and could lead to improved design guidelines for the safeguarding of human life and protection of coastal areas.

Additionally, there are hopes that this study will provide insight and ideas for future similar works that will introduce a new type of rubble mound breakwater research technique, i.e. instrumented "Smart-Units".

1.3 Research Objectives

The current study is composed of three main sections, all of which are focused on determining forces and pressures acting on individual armour units, advancing current design techniques and numerical modeling techniques. The main objectives of each section of the current study are proposed as follows:

1. Development of Instrumented Core-Loc "Smart-Unit"

    - To develop and construct a 3D printed Core-Loc armour unit, capable of measuring pressure and force, with the ability to transmit data wirelessly
    - Develop a python based interface to control the Core-Loc armour unit
    - Conduct a comprehensive performance analysis and calibration procedure
    - Develop a proof-of-concept for future versions of instrumented units with more advanced capabilities

2. NRC-OCRE Experimental Flume Testing Program

    - Test instrumented Core-Loc unit in wave flume in breakwater setting
    - Observe and analyze performance of instrumented unit during wave action
    - Compare the effects of various sea state parameters, and breakwater properties on the generated hydrodynamic forces and pressures during testing

3. OpenFOAM Numerical Model

    - Develop a numerical model of NRC-OCRE experimental tests in OpenFOAM
    - Develop rules of thumb for modeling rubble mound breakwaters with armour units
    - Perform mesh sensitivity analysis
    - Analyze the effects of different wall functions and turbulence models
    - Validate results of calibrated model with experimental results

1.4 Research Scope

The primary objective of the study is focused on the determination of forces and pressures acting on individual armour units in a rubble mound breakwater. This is achieved by using an instrumented unit designed to measure these quantities.

During the development of the instrumented Core-Loc armour unit, a complex circuit of microcontrollers, amplifiers, analog-digital-converters, and pressure sensors was constructed that was capable of fitting within a semi-hollow, 3D printed, 0.12m Core-Loc amour unit. Core-Loc units were 3D printed at the University of Ottawa MakerSpace, and fitted with the circuit. These units were designed in a way such that they can be mounted on any force transducer via an embedded coupling nut in the unit. After a python module capable of interfacing with the unit was developed, the completed unit then underwent a comprehensive performance testing and calibration procedure, where the unit's measurement and operational specifications were determined.

The instrumented unit was then subjected to wave conditions on a breakwater slope in the Steel Wave Flume (SWF) at NRC-OCRE. Various wave conditions were initially run to assess the performance of the instrumented unit. The instrumented unit then underwent a comprehensive experimental testing program. During this program, the effects of different wave climate, sea state parameters, and location along the breakwater slope was analyzed with respect to induced hydrodynamic forces and pressures.

A numerical model was then developed in OpenFOAM open-source CFD software to replicate the experimental test program. General rules for modelling these types of structures, and armour units were developed. A comprehensive mesh sensitivity analysis was performed to achieve mesh independence with respect to wave conditions, wave propagation, force and pressure results. Different wall functions and turbulence models and their effects on the results were also studied. The final calibrated model was then validated against select data from the NRC-OCRE experimental study.

1.5 Research Novelty

The novelty of this study lies in the data that will be produced from the instrumented unit. Time histories of both generated forces and pressure distributions on an armour units' face during wave action has never been recorded. The results produced as part of the NRC-OCRE experimental study has never been attempted in this way, and provides a novel set of data for understanding the hydrodynamic response of armour units in an unprecedented manner.

Another novelty of the current study is the idea of the fully instrumented armour unit. As well, the concept that his study has proven: this low cost relatively low-tech solution is capable of being reproduced on a massive scale and is capable of ushering a new paradigm of rubble mound breakwater design. The present study has proven the novelty of the "smart-unit" concept, and that future versions of these units with more advanced capabilities are absolutely possible and promising.

With the ability to collect data on individual units within an armour layer, researchers can develop force-balance design methods using comprehensive data sets while accounting for linear and non-linear effects. Researchers could collect near real-time data on full armour layers, including: unit location, unit attitude, unit movements, unit-to-unit interactions, hydrodynamic forces on units, hydrodynamic pressures on unit, pore pressures, peak accelerations, concrete strain; the list goes on. This type of data would be instrumental in the advancement of numerical models capable of accurately simulating rubble mound breakwaters. This is the motivation behind the collaboration with the current study and Imperial College London (ICL). The team at ICL has developed a novel coastal modelling tool, Latham (2013), capable of simulating the above-mentioned parameters, and will use experimental data produced from the joint-collaborative project for validation.

As part of this research project, a novel numerical model in OpenFOAM was developed, and a novel image-processing tool was developed. This image-processing tool is capable of tracking the free-surface elevation of the experimental wave conditions at the breakwater slope.

1.6 Publications

Listed below are all publications collaborated on by the current author, as part of the current study, and ongoing initiative between University of Ottawa, NRC-OCRE, W.F. Baird & Associates, and Imperial College London.

Journal Articles

- *Submission in progress* - Eden D., Douglas S., Simpalean A., Nistor I.,Cornett A., Via-Estrem L., Latham J.P., "Measurement of Forces and Pressures on Core-Loc Units via Instrumented Smart-Units", *Journal TBD*

Conference Papers

- *Submission in progress* – Eden D., Douglas S., Simpalean A., Nistor I.,Cornett A., Via-Estrem L., Latham J.P., "Forces and Pressures on Armour Layers Measured via Instrumented Core-Loc Units", Coastal Structures 2019, Hannover DE, ASCE COPRI Institute, September 30 – October 2 2019 (Author)

- Douglas S., Eden D., Simpalean A., Nistor I., Cornett A., Via-Estrem L., Latham J.P., "Hydrodynamic Analysis of Core-Loc Armour Units via Controlled Drop Tests", Coastlab18, Santander Cantabria, May 22-26 2018 (Co-Author)

- Douglas S., Eden D., Simpalean A., "Groundwork for an Experimental Project on the Stability of Concrete Breakwater Armour Units", Eastern Canada Water Resources Engineering Graduate Student Conference 2017, Montreal, QC, May 25-26 2017. (Co-Author)

1.7 Thesis Outline

Chapter 1 is an introduction to the study. This chapter provides background information on the study, outlines the motivation, objectives, scope, and novelty of the research. Publications related to the current study are also listed in this section.

Chapter 2 presents a comprehensive literature review of rubble mound breakwaters constructed from CAUs. Different types of armour units are introduced, as well as their stability mechanisms and classifications. Core-Loc specific information is briefly discussed, as well as the manufacturing and placement of concrete armour units. An in-depth overview of armour unit design considerations, and current design methods is presented. This details the various empirical methods and equations currently utilized in the industry. Similar research that inspired the current study is then discussed. Lastly, a brief section on the numerical model, OpenFOAM, completes the literature review.

Chapter 3 outlines the scope, the construction, and the results from the development of the Core-Loc armour unit. An in-depth look of the procedure required to construct the 3D printed instrumented Core-Loc armour unit is shown. As well, the interface, testing, and calibration procedures are discussed. The specifications, capabilities and limits of the unit are then summarized.

Chapter 4 contains the setup and scope of the experimental testing program in the SWF at the NRC-OCRE laboratory, as well the results of this program. A statistical analysis of the experimental results is then used to compare the effects of various sea state parameters, and breakwater parameters. In this section, a novel image-processing tool is presented, capable of tracking the free-surface during wave conditions at the breakwater slope.

Chapter 5 presents the OpenFOAM numerical model. The computational domain, the meshing techniques, and the measurement techniques are discussed. The results of the mesh sensitivity analysis are shown, along with the effect of different wall functions and turbulence models. Finally, the calibrated model is compared both qualitatively and quantitatively to select experimental data from the NRC-OCRE experimental tests.

Chapter 6 outlines the conclusions of the current study and provides recommendations for future work.

2.0 Literature Review

The literature review presented in this section summarizes background information, and past relevant literature on the design and utilization of CAUs in rubble mound breakwaters. This portion of the literature review includes background information, different types of CAUs, a summary of armour unit classifications, placement guidelines, design considerations, and design equations.

Additionally, several past research contributions that directly inspired the current study are discussed. Lastly, this literature review introduces OpenFOAM; the software, equations, and algorithms used to develop the numerical model.

The main objectives of the literature review are to: i) provide background on the use, and design of CAUs; ii) provide background and theory on OpenFOAM, the CFD software used in the current study; iii) outline the current state of the art and research needs in field of CAU design.

2.1 Background Information

2.1.1 Rubble Mound Breakwaters with Concrete Armour Units

Traditionally, CAUs were designed to mimic quarried natural rock when the required rock was not available. Like natural rock armour, these types of units were very bulky, and resisted the energy of incoming waves through their massive weight alone. A simple example of this type of unit is a cube or prismatic concrete block.

The cost, construction issues, and stability issues associated with bulky type units spurred a field of development into a number of different shapes and types of units. In an effort to increase efficiency, many researchers tended towards more slender, porous and interlocking type units as a way to lower cost while still achieving a stable armour layer.

The performance criteria for rubble mound breakwaters are constantly evolving. There is a trend towards structures being built in increasingly deeper water and harsher environments. In these conditions, manufacturing CAUs becomes the only practical method of producing units large enough to withstand design conditions. Moreover, structures are routinely constructed in regions in which natural armour stone of the appropriate size and density cannot be sourced.

Practical difficulties can arise in the manufacturing, storage and transportation of units. This is due to the extra precaution that is required during casting. As well, problems that can arise with constructability, stacking, and transport of units because of their complex shapes and sizes. Additional precautions must be taken with respect to the concrete properties, the marine environment, and other factors unique to concrete that may not have been considered when using natural rock.

2.1.2 Types of Concrete Armour Units and Classifications

CAUs can be classified generally by shape, placement method, number of layers, and stability mechanism. Listed in Table 1 are many of the commonly used types of CAUs in breakwaters around the world, as well as information on their classifications.

Table 1: Different Types of Concrete Armour Units

Shape	Name	Year	Country	Layers	Placement	Stability
	Cube	n/a	n/a	2	Random	Weight
	Tetrapod	1950	France	2	Random	Weight + Interlocking
	Tribar	1958	USA	2	Random	Weight + Interlocking
	Dolosse	1963	South Africa	2	Random	Weight + Interlocking
	Cob	1969	UK	1	Uniform	Friction
	Antifer Cube	1973	France	2	Random	Weight
	Seabee	1978	Australia	1	Uniform	Friction
	Accropode	1980	France	1	Random	Weight + Interlocking
	Shed	1982	UK	1	Uniform	Friction
	Core-Loc	1995	USA	1	Random	Weight + Interlocking
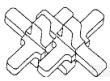	A-Jack	1996	USA	1	Random	Weight + Interlocking
	Ecopode	2000	France	1	Random	Weight + Interlocking
	X-bloc	2003	Netherlands	1	Random	Weight + Interlocking
	Accropode II	2004	France	1	Random	Weight + Interlocking

The shapes and geometry of CAUs vary widely, thus, different hydraulic and structural behaviour can be expected for each type. Although there are numerous distinct and unique shapes, the general types of shapes include bulky (e.g. cube), hollow (e.g. Cob), slender (e.g. Dolos), and with appendages (e.g Tetrapod). This can be further simplified into units with simple, or complex geometry.

The placement method refers to the method or technique in which the units are placed on the breakwater slope. The units can either be placed in a uniform pattern or grid, or placed randomly on the breakwater slope. This is discussed further in Section 2.2.1.

The stability mechanism refers to the way in which the units resist hydrodynamic forces, while maintaining layer stability as a whole. For bulky units, stability is maintained strictly through their own weight and resisting movement from hydrodynamic forces. Interlocking units typically have high porosity and slender geometry or appendages, which allow them to interlock and form a closely interconnected layer of units. This causes them to behave more as a composite unit rather than individual units. These types of units maintain stability under hydrodynamic loading through both weight and interlocking forces between adjacent units. Lastly, hollow type units are generally placed uniformly in a tight grid. These types of units resist the action of waves through friction against adjacent units. Many units use a combination of different stability mechanisms due to the complex nature of their geometry.

2.2 Design Considerations

2.2.1 Placement Guidelines and Methods

In the past, the trend was typically bulky and massive type units; these were frequently placed in randomly oriented double-layer systems. Thus, placement guidelines were not strict nor did they require much precision. The US Army Corps of Engineers, and other researchers have undertaken more recent endeavours. This is reflected in guidelines for breakwater design in The Shore Protection Manual (SPM), USACE (1984). The SPM provides detailed design guidelines for the placement of a wide range of armour units under different conditions to achieve a hydraulically stable design. Independent researchers, and armour unit manufacturers have also provided similar placement guidelines.

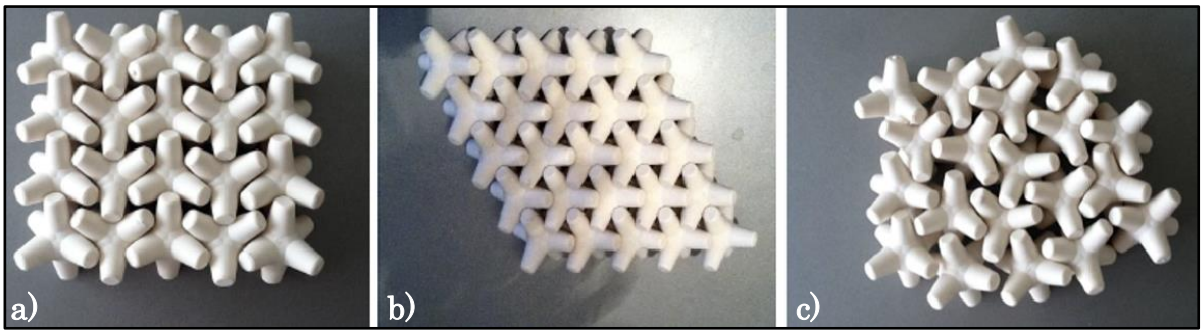

Figure 3: a) Uniform Rectangular Grid, b) Uniform Diamond Grid, c) Random Grid, all from Denechere (2009)

Examples of different placement methods commonly used in breakwater construction are shown in Figure 3.

One key consideration in the placement of concrete armour units is the individual unit orientation, or "attitude". Researchers have shown that not only is the placement of the units important to the stability of the overall structure, but the actual attitude of each individual unit may affect local stability, Latham (2013). This can pose both local and global failure issues. The units shown in Figure 4 show the possibilities of unit attitude for a Core-Loc, and a typical stereographic distribution of unit attitudes along a breakwater face following a numerical study.

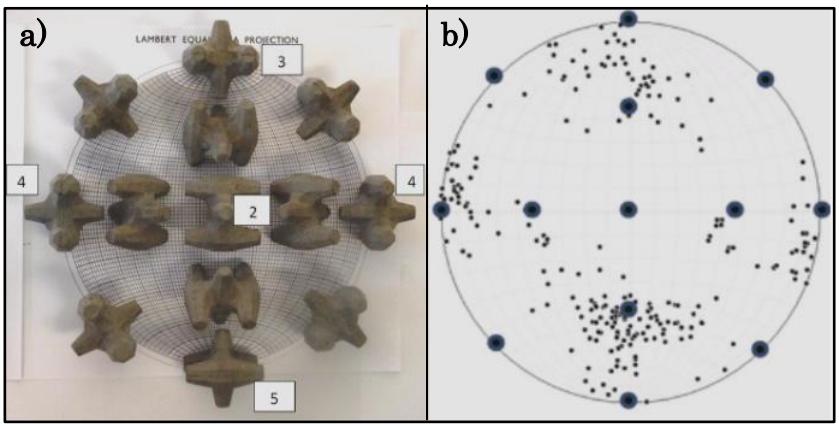

Figure 4: a) Possible Core-Loc attitudes b) Stereographic distribution of attitudes along typical breakwater, both from Latham (2013)

Rigorous placement guidelines were developed for X-Bloc armour units, which can be applied more generally to other similar bulky and interlocking type units.

Muttray et al. (2005):

- Adjacent armour units shall have different attitude
- Armour units must not be in contact with units of the same row
- Each armour unit shall be keyed into two armour units of the row below
- Armour units shall rest on three points (two neighbouring units and the slope)

Additional placement guidelines were developed for Accropode by CLI (2012):

- No unit can have more than 1/3 of the unit out of the plane, each block must be in contact with the breakwater slope
- Blocks are interlocked with one another and not free to move
- Use of lozenge-shaped grid for placement locations, local exceptions are tolerated
- Placed in a way as to prevent escape of rock fill beneath armour units form gaps between the units
- Units are placed in mostly varied attitudes

The placement grid that is referred to in the placement guidelines is shown in Figure 5, and is scalable to any sized section of breakwater. This grid prescribes uniformly spaced placement locations for the units based on the unit size and required packing density. The typical fashion in which the units are placed comprises a "family of four" placement technique, as depicted in Figure 5c. The requirement to have no touching units in a given row, but to be keyed into two units from the row below dictates that each unit is in direct contact with four other units. These four units will be the adjacent units utilized for interlocking and frictional resistance during wave action. Due to the nature of these placement guidelines, spatial differences between armour layer interaction is inherent.

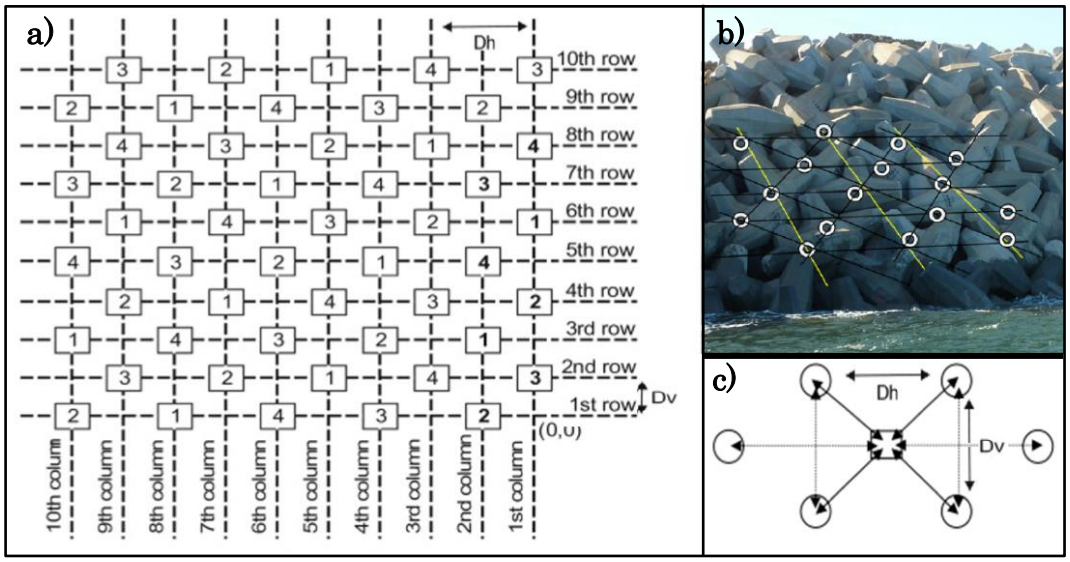

Figure 5: a) Rectangular Placement Grid Scheme, b) In-situ Placement Grid, c) "Family of Four" Placement augmented from Latham (2013)

It has also been a common construction practice, in fact recommended by manufacturers of certain CAUs, that breakwater faces with CAUs shall maintain a slope between 1H:1V to 2H:1V. CLI (2012) recommends a slope of 4H:3V for Core-Loc placement. Outside of these bounds there is minimal research or literature regarding the stability of units. Many units have placement and stability issues due to their complex geometry and their tendency to tumble, slide, or settle gradually down the breakwater slope.

A widespread method of ensuring armour unit placement in the industry today is the use of GPS equipment. During the design stage, the precise location of every armour unit can be determined. During construction, divers or workers above the water surface will check armour units manually. User-friendly software has also been developed based on the principle of GPS placement and geo-referencing; some incorporate SONAR generated bathymetry or visualizations of the bed surface and breakwater profile. An example of a modern GPS placement method is POSIBLOC™, introduced by Measuris (2016). A screen inside the crane operator's cabin, with a simple user interface, allows the operator to place the units in their desired location with astounding accuracy. A 3D bathymetric map superimposed with real-time data of ongoing construction is relayed back to the operator to aid with the visualization and placement.

2.2.2 Loads on Concrete Armour Units

Due to the hydraulic interaction of waves with the armour layer, very complex flow patterns form. It is in fact these turbulent inter-unit flow patterns that cause the dissipation of wave energy in rubble mound breakwaters. This complex interaction leads to rapidly varying hydrodynamic forces and pressures, which in turn subjects the individual units to shear, compressive, and tensile stresses. The manner in which these hydrodynamic interactions behave may give rise to secondary effects such as unit movement, impacts or appendage breakage; these processes may produce additional forces that must be considered for design. By virtue of the random nature of sea state, and interaction with the breakwater face, both spatial and temporal variations of induced forces on units have been observed, Van der Meer (1991).

CAUs may be subjected to various loading scenario throughout the service lifetime; these can be generalized into categories of static, dynamic, thermal, chemical, and abrasive loads. Examples for each type of loading scenario are presented in Table 2.

Table 2: Concrete Armour Unit Design Loads

Type of Loads	Cause of Loads
Static / Quasi - Static	Unit Weight
	Unit-Unit Contact Points
	Settlement
	Ice Shoves
Dynamic	Manufacturing and Placement
	Hydrodynamic Interaction
	Rocking, Rolling, Displacement
	Debris Impacts
	Earthquake
Thermal	Freeze-thaw Cycles
	Curing Process
	Daily Temperature Fluctuations
Chemical	Marine Chemical Attack
	Reinforcement Corrosion
Abrasive	Suspended Sediment

The primary cause of static loading in CAUs is due to gravity. Due to the complex geometry of units, especially slender units with appendages, high internal stresses can be

induced due to the unit's own weight. The unit will also be in contact with the under-layer, which will induce localized stresses depending on how the unit is resting. In addition, placement guidelines for both single and double layer systems dictate that units will be in contact with adjacent units; potentially supporting units above. Due to the combination of these gravitational effects, units will have a complex array of localized forces acting on their surfaces. These static contact loads tend to increase in number and in magnitude near the toe of the breakwater. "Force chains" can develop, where a small number of toe units will be supporting a large interconnected chain of units in contact. Special attention must be paid during the placement stage to avoid such circumstances.

CAUs will be subject to dynamic loading due to gradually and rapidly varying hydrodynamic forces from wave interaction. Incoming waves will break on, or impact the armour layer causing forces of a cyclical nature. During a typical lifespan of 50 years, an average breakwater in North America will be subject to 200 million cyclical wave loads, Burcharth (1985). While these forces may be less significant in magnitude, their cyclical nature and the required lifespan of breakwaters gives rise to the concern of concrete fatigue; this has led to breakage of armour units in the past, Maddrell (2005).

During wave impact and associated inter-unit flow, units may rock, roll, or displace from their original location. This can cause units to collide with adjacent units and produce dynamic, rapidly varying impact forces up to and exceeding the unit weight, Van der Meer (1991). Impact forces of a similar nature may also be expected from debris such as components of broken armour units, ice chunks, or any type of floating debris.

2.2.3 Breakwater Wave Interaction

2.2.3.1 Diffraction and Reflection

Breakwaters will cause incident waves to diffract around the structure. A designer must be able to quantify diffracted wave heights at different locations around the breakwater. This is typically done by relating the incident wave to the diffracted wave height using Equation 1:

$$K_D = \frac{H_D}{H_I} \tag{1}$$

Exposed, protruding sections of breakwaters will cause waves to diffract around the structure; the illustration shown in Figure 6a depicts this behaviour. Figure 6b shows a monograph, by Wiegel (1962), that can be used to determine K_D for exposed breakwaters depending on incident wave direction.

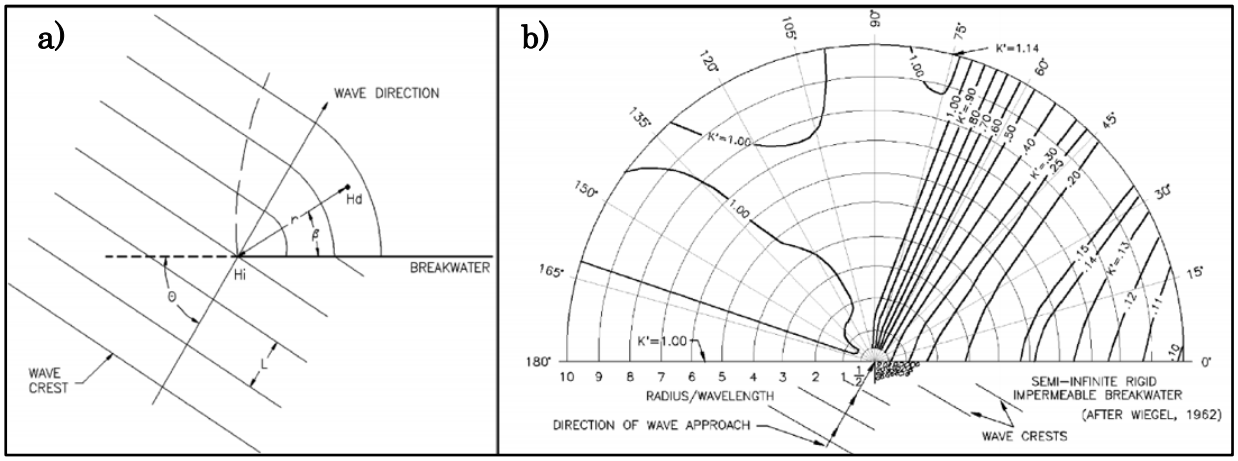

Figure 6: a) Schematic of Exposed Breakwater Diffraction, b) K_D Estimation Monograph, from Weigel (1962)

Waves will also diffract through openings in breakwaters and produce complex interference in the sheltered area. Similar to the work of Wiegel (1962), Johnson (1952) produced monographs for the determination of K_D values through different sized breakwater openings. This is shown in Figure 7.

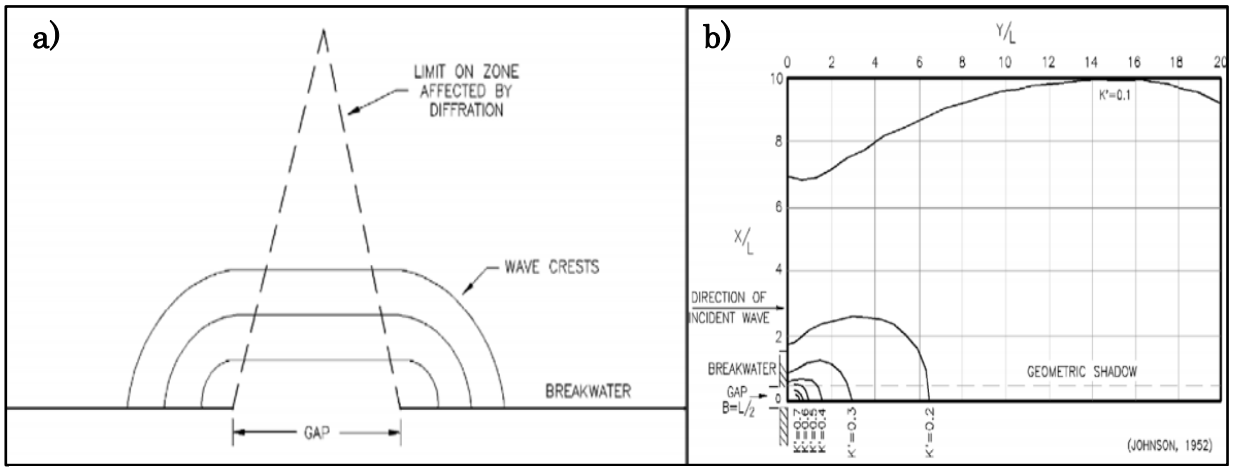

Figure 7: a) Schematic of Diffraction Through Breakwater Opening, b) K_D Estimation Monograph, from Johnson (1952)

Wave reflection is dependent on the nature of the incident wave, its' breaking characteristics, structure permeability, and many other factors. Generally, a wave that has not broken before impacting the breakwater face will contain more energy than one that has, and will also reflect a higher portion of it's incident energy. The reflection coefficient is shown in Equation 2:

$$K_R = \frac{H_R}{H_I} \quad (2)$$

This is directly related to the roughness, or smoothness of the breakwater face; a smooth face will cause less energy dissipation of the incident wave energy. Given the wide variety of possibilities for armour unit shapes, sizes, and roughness, empirical formulae have been developed to simplify the complexity of the wave-breakwater interaction. A simple method for determining reflection was proposed by Van Der Meer (2006) for irregular waves, derived from experimental testing:

$$K_R = tanh(a \cdot \xi_0^b) \quad (3)$$

Van Der Meer (2006) proved that the reflection coefficient has a relationship with the breaking characteristics of the incident waves, the armour unit geometry, and the placement method of the units. From his results with cube armour units, it is evident that the same type of unit will reflect markedly different, with only a slight change in the placement method. The following table lists the empirical constants derived from the study for various armour units:

Table 3: Empirical "a" Parameter from Van der Meer (2006)

Armour Unit Type	Value of a
Core-Loc, 1 layer	0.113
Tetrapod, 2 layer	0.102
X-bloc, 1 layer	0.112
Accropode, 1 layer	0.115
Antifer Cube, 2 layers	0.108
Cube, 2 layers (flat arrangement)	0.120
Cube, 2 layers (rough arrangement)	0.105
Cube, 1 layer	0.120

2.2.3.2 Run-up and Run-down

Wave run-up and run-down along the breakwater face occurs when incident waves impact the breakwater, and the elevation of water level oscillates below and above the still water level (SWL). The levels at which the water surface oscillates is dependent on many factors: including the waves breaking characteristics, the shape of the units, layer

roughness, and inter-unit porosity where the flow of this water will occur. As such, empirical equations vary widely from armour unit type to type.

Published in EurOtop (2007) is a comprehensive set of empirical equations for run-up and overtopping of breakwaters, with various types of armour units. Amongst these, run-up levels with 2% probability of exceedence from a given wave spectrum on a 1.5H:1V slope can be estimated using Equation 4. These values are applicable only for non-oblique waves on a standard shaped breakwater with no berm.

$$\frac{R_{u2\%}}{H_{m0}} = 1.65 \gamma_b \gamma_f \gamma_\beta \xi_{m-1,0} \tag{4}$$

With a maximum of:

$$\frac{R_{u2\%}}{H_{m0}} = 1.00 \gamma_b \gamma_{f,surging} \gamma_\beta \left(4.0 - \frac{1.5}{\sqrt{\xi_{m-1,0}}}\right) \tag{5}$$

Where: $\xi_{m-1,0} \leq 1.8$

The empirical parameters available in the EurOtop Manual, derived from experimental testing, are shown in Table 4:

Table 4: Empirical Run-up Equation Parameters from EurOtop (2007)

Type of armour	No. of layers	γ_f mean	γ_f 95% CI, low	γ_f 95% CI, high
Smooth	–	1.00		
Rock (two layers; permeable core)	2	0.40	0.37	0.43
Rock (two layers; impermeable core)	*2*	*0.55*		
Rock (one layer; permeable core)	*1*	*0.45*		
Rock (one layer; impermeable core)	*1*	*0.60*		
Cube	2	0.47	0.44	0.50
Cube (single layer)	1	0.49	0.46	0.52
Antifer	2	0.50	0.46	0.55
Haro	2	0.47	0.44	0.50
Tetrapod	2	0.38	0.35	0.42
Accropode	1	0.46	0.43	0.48
Core-Loc™	1	0.44	0.41	0.47
Xbloc™	1	0.44	0.41	0.49
Dolosse	*2*	*0.43*		
Berm breakwater	*2*	*0.40*		
Icelandic berm breakwater	*2*	*0.35*		

The extremes of the run-up and run-down elevations will dictate which locations along the breakwater slope are subjected to different types of loads. For example, units above the maximum run-up will be only subjected to static forces. Units between the run-up and run-down extremes will be subjected to these induced forces, as well as varying buoyant forces. Units below the minimum run-down will always be subjected to full buoyancy, and hydrodynamic loads from the wave action.

A simple method for estimating the run-up and run-down velocities is proposed by Abbott and Prince (1994):

$$U_{Avg} = \frac{(R_u - R_d)}{\frac{T}{2}} \tag{6}$$

This approach does however smooth extreme velocities of particular interest for design; experimental results have shown that the relative magnitude of the extreme velocities is directly related to the wave breaking characteristics.

In general, run-up is expected to counteract stabilization forces by producing drag and lift, decreasing stabilizing contact forces, lubricating frictional interfaces, and potentially causing units to be displaced from the layer. Run-down typically causes layers to be forced downwards and along the breakwater face, increasing inter-unit contact loads, and force chains towards the toe. Of course, depending on local geometry, placement, and unit attitude, this may differ and ejection during run-down can occur.

2.2.3.3 Breakwater Permeability

The permeability of the breakwater structure will govern the ability to transmit energy through the structure. In general, an armour layer resting on a permeable under-layer will be more stable. This is due to the fact that permeable breakwaters will tend to absorb more wave energy, reduce wave reflection, and lead to lower forces acting on the units. A breakwater with increased permeability will also reduce oscillations of the water surface level within the under-layer and core, and can also reduce run-up due to the volume of water that will permeate into the breakwater face. Tests have conclusively shown that units resting on an impermeable base will be less stable. CIRIA (2007) suggested a weight multiplication factor of four times between units on impermeable and permeable breakwaters.

The permeability of the breakwater structure is highly dependent on the gradation of the under-layer and core material. In order to promote permeability, while hindering the escape of under-layer and core material, the following sizing guidelines are a good general reference:

$$\frac{1}{10}W \leq W_{underlayer} \leq \frac{1}{15}W \quad and \quad \frac{1}{30}W \leq W_{core} \leq \frac{1}{50}W \tag{7}$$

2.2.4 Sea State Parameters

2.2.4.1 Wave Height and Direction

Wave height is the main parameter that must be determined in order to design CAUs. Given that wave fields and sea states are complex and highly variable, they are typically reduced to a single value of concern, known as the "Significant Wave Height". This significant wave height can then be coupled with a historical or statistical analysis, in order to determine significant wave heights for certain return periods.

In practice, researchers have used several definitions and methods to determine this parameter. The two most common, and relevant are described as follows:

1. Statistical Significant Wave Height ($H_{1/3}$):

An irregular wave field can be deconstructed into super-positions of numerous interacting individual regular wave fields. If one were to separate each individual regular wave field and consider them as separate, $H_{1/3}$ would be the value of the average of the top one third of wave heights encountered.

2. Spectral Significant Wave Height (H_{m0}):

For this method, measured wave heights and periods are fitted to an applicable wave spectrum, such as a JONSWAP spectrum. From this spectrum, the significant wave height can be computed based on integration of the spectrum. The governing equation is:

$$H_{m0} = 4.004\sqrt{m_0} \tag{8}$$

where:

$$m_n = \int_0^\infty \omega^n \cdot S(\omega) d\omega \tag{9}$$

The zeroth order moment (n=0) produces H_{m0}, a value that physically represents the variance of the water surface profile. This wave height is known as the significant wave height based on spectral analysis.

Wave direction is important for the design of CAUs because the direction of incidence can affect interaction patterns such as diffraction, refraction, run-up, and other factors that may lead to unexpected design scenarios. Wave direction is also of great important for scour and toe stability, as oblique waves can increase littoral particle velocities. This can increase littoral drift at the base of the structure that can undermine the toe.

2.2.4.2 Wave Period

The period of a wave directly affects the wavelength, celerity and steepness of the waves. Waves with higher periods will be longer, propagate faster, and be less steep. Increased wavelength, for a given wave height, will lead to a larger volume of displaced water for every wave cycle. It has been shown, through experimental study, that waves with increased period and wavelength will lead to higher stability in the armour layer. Inversely, for given wave heights, shorter periods have shown to cause more damage to amour layers. This is, of course, excluding extreme long-period waves such as tsunamis. A typical linear wave train is depicted in Figure 8.

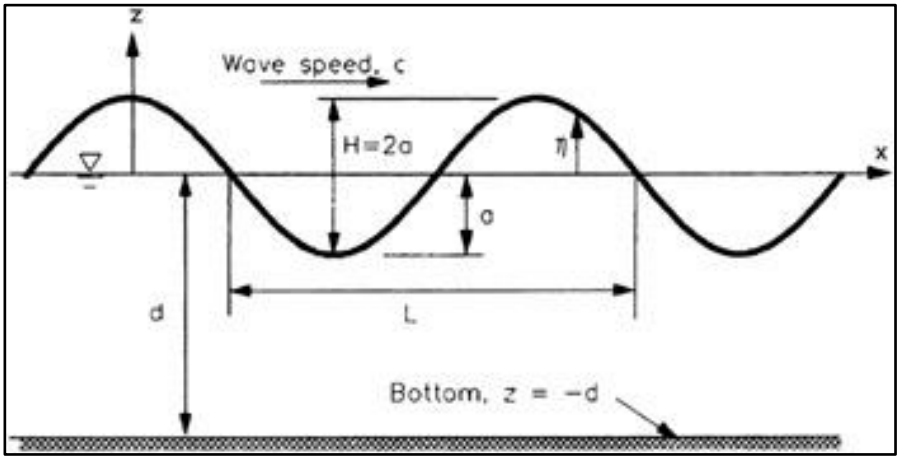

Figure 8: Wave Parameters according to Linear (Airy) Wave Theory, from Herbich (2000)

2.2.4.3 Wave Steepness

The steepness of a wave is simply the ratio of wave height to wavelength. Due to the lower volume of water contained in steep waves, run-up and run-down extremes, as well as the amount of induced inter-unit flow can be expected be to reduced, De Jong (1996). These types of high frequency waves produce a so-called slamming effect. The short period waves continually break on, and bombard the armour layer. It was due to this effect that work by Van der Meer (1988), De Jong (1996) and Sakakiyama (1990) all showed that higher wave steepness led to higher forces.

2.2.4.4 Wave Breaking Characteristics

The wave breaking characteristics refer to the shape, and level of breaking in a wave on a slope. Gentle waves on a sloped beach will tend to shoal due to depth limited effects, and will continue to increase in height and steepness until an unstable point is reached. At this point, the wave collapses on itself and breaks. Due to the high turbulence and random nature of the flow, energy is lost during the breaking process. Miche (1944) and

Battjes (1974) have shown that waves will break in deep-water at a steepness of approximately $s_0 = 0.14$, and in shallow conditions using Equation 10:

$$\left(\frac{H}{L}\right)_b = 0.14 \cdot \tanh\left(\frac{\Upsilon}{0.88} \cdot \frac{2\pi d}{L}\right)_b \tag{10}$$

Wave breaking characteristics can be broken into four different types of breaker categories as depicted in Figure 9. Wave breakers are categorized by the dimensionless surf similarity parameter, also known as the Iribarren number. For the purposes of this study, this is calculated for regular waves, and irregular waves as follows:

$$Regular: \quad \xi_0 = \frac{\tan(\alpha)}{\sqrt{\frac{H}{L_0}}} \qquad Irregular: \quad \xi_0 = \frac{\tan(\alpha)}{\sqrt{\frac{2\pi H_{m0}}{g T_{m-1,0}^2}}} \tag{11}$$

In the irregular wave equation, $T_{m-1,0} = 1.1 \cdot T_p$ for single peaked spectra; according to Zanuttigh (2006).

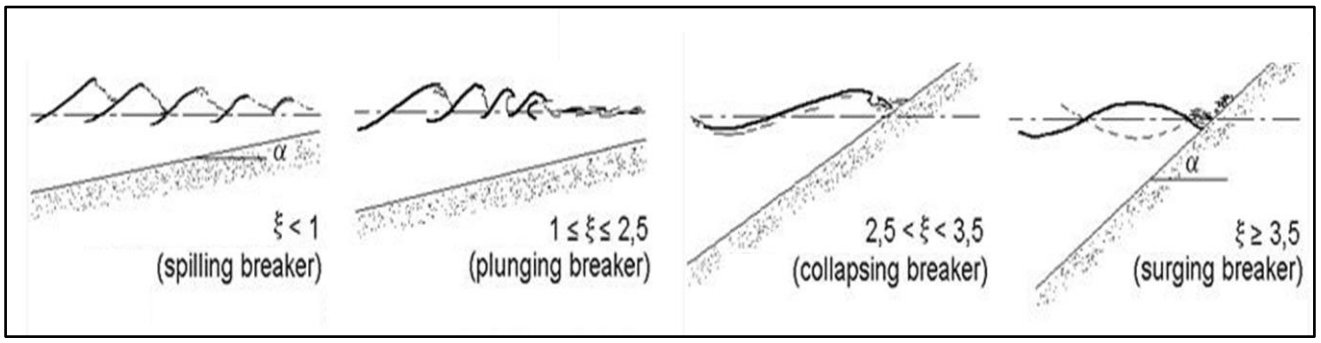

Figure 9: Types of Wave Breakers by Iribarren Number, from Douglas (2015)

The shape of the incident wave during impact with the armour layer will affect the hydrodynamic loading. Research has shown that plunging waves that break on the armour layer will generate extreme forces due to the high velocity nature of the wave impact. As well, Yoo (2013), showed that collapsing and surging type breakers on low sloped breakwaters can induce very large run-up and run-down forces, greatly increasing stresses at inter-unit contact points.

2.2.4.5 Water depth

While many empirical methods approximate values such as wavelength and wave period using deep-water assumptions; the local water depth at the toe of the structure is of great concern, Yoo (2013). Near-shore bathymetry is a key design parameter that will affect wave-breaking characteristics, and thus induced hydrodynamic forces on the armour layer.

Van der Meer (1994) showed increased toe water depth can reduce or eliminate friction with the bed surface and thus tends to reduce the amount of energy lost to bed roughness. This leads to higher wave forces on armour units. This is due to the fact that water particles in deep-water are not subjected to orbital displacement beyond a depth of L/2, according to linear wave theory. Increased water depth at the toe will require a deeper armour layer, which can increase inter-unit contact forces due to the increased amount of units and weight being supported. This effect is especially prominent for the toe of the structure, which supports the entire armour layer. Thus, Burcharth (2007) showed larger toe units are required in deep-water design

2.2.5 Armour Unit Parameters

2.2.5.1 Size, Weight and Density

For most types of CAUs, including Core-Locs, the hydraulic stability is dictated in part by the weight of the unit. Armour units ranging especially around 10-15 tonnes tend to be subjected to failure due to rocking of the armour units and subsequent inter-unit impacts. The data presented by Van Der Meer (1992) seems to have a sweet spot in terms of rocking due to relatively low weight, but enough weight to produce significant impact forces.

The three typical parameters used in CAU design are the nominal diameter, the relatively density, and the weight of the unit:

$$D_n = V_a^{\frac{1}{3}} \tag{12}$$

$$\Delta = \frac{\rho_a}{\rho_w} - 1 \tag{13}$$

$$W = \rho_a \cdot V_a \tag{14}$$

2.2.5.2 Porosity

The porosity of an armour unit refers to the ratio of volume of free space to the volume within the outline of the armour unit. The porosity of both individual units and armour layer as a whole have drastic effects on energy dissipation, hydraulic and structural performance. In general, the more complex or hollow the geometry, the higher the

porosity. This will tend to decrease as units are more closely packed together and void spaces are filled with appendages of adjacent units; thus porosity and packing density are highly interconnected.

The porosity of an entire armour layer can be expressed as follows:

$$n_v = \frac{V_{air}}{V_{total}} = 1 - \left(\frac{N_a D_n^2}{n k_\Delta}\right) \tag{15}$$

As porosity of the armour layer increases, more inter-unit pore-space for turbulent energy dissipation becomes available. Hence the increasing trend in highly porous hollow or interlocking units. This effect does have an upper limit, in that armour layer porosity reaches a point where units are not within sufficient proximity of one another. Gaps are formed where the under-layer or core is exposed and can be compromised. Increased porosity of the armour layer usually results in a rougher breakwater surface, and thus drastically decreases reflected wave energy, Van der Meer (2003).

2.2.5.3 Packing density

Packing density is a term to define the number of armour units in a given unit area. The lowest packing density that can achieve the given design criteria will require the least material and thus be considered the optimal design. Similar to having high porosity, it has been shown that certain minimum levels of packing density are required to maintain stability for different armour units, USACE (1984). Research has also shown that altering packing density drastically affects stability, hydraulic and structural performance of the armour layer and must be considered for design, Van den Bosch (2002).

The packing density of an armour layer can be calculated from the following formulae:

$$N_a = \frac{n k_\Delta (1 - n_v)}{D_n^2} = \frac{(N_x - 1)(N_y - 1)}{L_x \cdot L_y} \tag{16}$$

Packing density can vary widely across an entire breakwater, and must be considered on a global, local, or individual basis. Localized differences in packing density may lead to instability or movement and can cause progressive failure. Due to local differences in hydrodynamic forces, different areas of the breakwater may shift or settle at different rates and deviate from the desired packing density; this is illustrated in Figure 10.

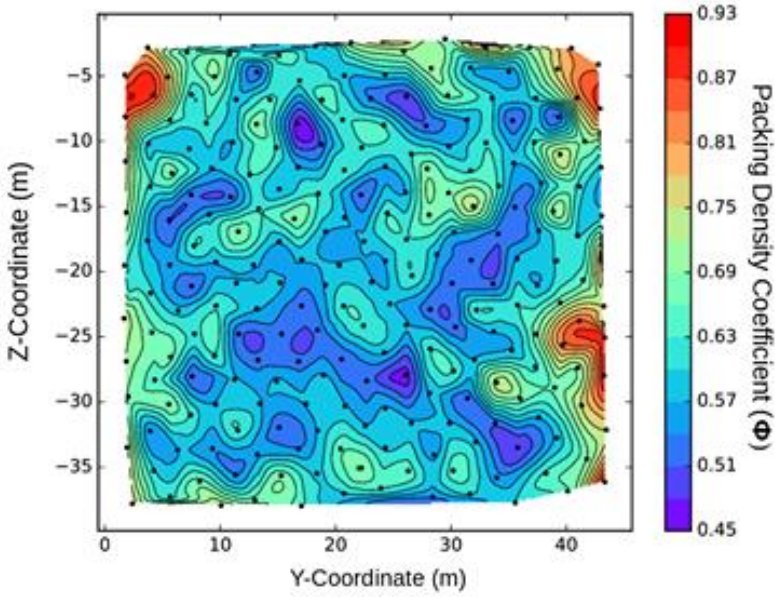

Figure 10: Locally Calculated Packing Densities along Breakwater Slope (Target 0.62)

According to the results of experimental testing by Van den Bosch (2002), increasing packing density will increase the hydraulic stability of an armour layer. This is due to the restriction of movement of the units because of their close proximity. This prevents armour units from moving or being ejected from the layer. However, in the event of rocking, due to the proximity, impacts may be more likely to occur and may increase in magnitude. This is due to units having little deceleration between wave impact and unit impact, which results in higher impact velocities. Higher packing density will lead to lower layer porosity and can generate a smoother breakwater surface; this can pose design concerns with extreme run-up and run-down conditions, as well as reflection.

2.3 Empirical Design Methods

2.3.1 Stability Number

The common trend over past decades has been to design CAUs using dimensionless wave height, or hydraulic stability number:

$$N_s = \frac{H_s}{\Delta \cdot D_n} \tag{17}$$

2.3.2 Hudson's Equation

Hudson's Equation, USACE (1984), was developed in the 1950s and was the standard design method for decades. This equation is still widely used in the industry today. The weight of a unit is calculated by considering the relationship of the unit density,

breakwater slope, and wave height. The equation is fitted with a unit-specific empirical constant, K_D, as follows:

Original form:

$$W = \frac{\gamma_a \cdot H^3}{K_D \cdot \Delta^3 \cdot \cot(\theta)} \tag{18}$$

Rewritten in 1990s:

$$\frac{H_s}{\Delta \cdot D_{n50}} = \frac{(K_D \cdot \cot(\theta))^{\frac{1}{3}}}{1.27} \tag{19}$$

The value of K_D for various armour unit types, placement types, number of layers, slopes, and wave characteristics are provided in USACE (1984). This equation is the basis of the preliminary design guidelines provided by Core-Loc manufacturer CLI. Design guidelines are provided by CLI (2012) to size Core-Loc armour units for given wave and foreshore conditions, using Hudson's Equation. These guidelines are shown in Figure 11:

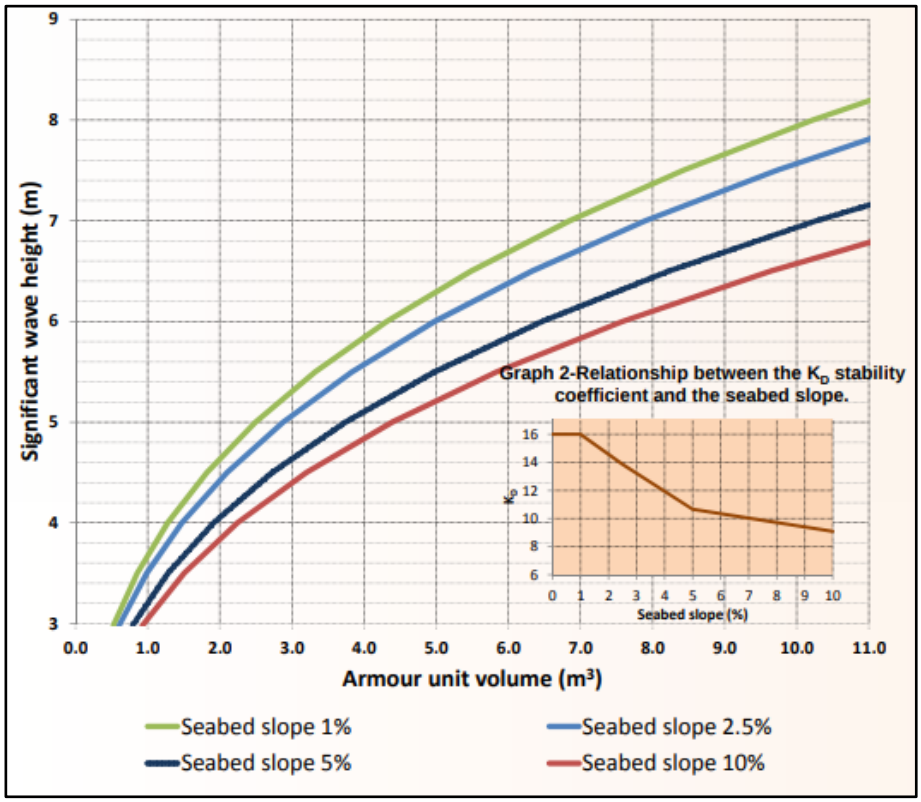

Figure 11: Core-Loc Preliminary Design Chart, from CLI (2012)

2.3.3 Van der Meer Equations

Van der Meer (1988) carried out ground-breaking experiments and incorporated data from other researchers to develop a new set of empirical design equations. They were developed under the assumption that armour layers are dynamic, and that damage is a function of the duration of wave attack. Thus, one could design an economical breakwater capable of sustaining calculable damage without failure. During this study, empirical design equations were developed for natural rock, cubes, Accropode and Tetrapod armour units:

Cubes:

$$\frac{H_s}{\Delta \cdot D_n} = \left(\frac{6.7 \cdot N_{od}^{0.4}}{N^{0.3}} + 1.0\right) \cdot s_{om}^{-0.1} \tag{20}$$

Tetrapods:

$$\frac{\mathrm{H_s}}{\Delta \cdot \mathrm{D_n}} = \left(3.75 \cdot \left(\frac{\mathrm{N_{od}}}{\sqrt{\mathrm{N}}}\right)^{0.5} + 0.85\right) \cdot \mathrm{s_{om}^{-0.2}} \tag{21}$$

Accropode:

$$\frac{H_s}{\Delta \cdot D_n} = 3.7 \qquad start\ of\ damage\ (N_{od} = 0) \tag{22}$$

$$\frac{H_s}{\Delta \cdot D_n} = 4.1 \qquad failure\ (N_{od} > 0.5) \tag{23}$$

Natural Rock:

$$\frac{H_s}{\Delta \cdot D_{n50}} = 6.2 \cdot P^{0.18} \cdot \left(\frac{S}{\sqrt{N}}\right)^{0.2} \cdot \xi_m^{-0.5} \qquad for\ plunging\ waves \tag{24}$$

$$\frac{H_s}{\Delta \cdot D_{n50}} = 1.0 \cdot P^{-0.13} \cdot \left(\frac{S}{\sqrt{N}}\right)^{0.2} \cdot \sqrt{\cot(\theta)} \cdot \xi_m^P \qquad for\ surging\ waves \tag{25}$$

Van der Meer (1991) further developed the empirical design equations mentioned previously, by considering rocking, moving, and displaced units:

Cubes:

$$\frac{H_s}{\Delta \cdot D_n} = \left(\frac{6.7 \cdot N_{omov}^{0.4}}{N^{0.3}} + 1.0\right) \cdot s_{om}^{-0.1} - 0.5 \tag{26}$$

Tetrapods:

$$\frac{H_s}{\Delta \cdot D_n} = \left(3.75 \cdot \frac{N_{omov}^{0.5}}{N^{0.25}} + 0.85\right) \cdot s_{om}^{-0.2} - 0.5 \tag{27}$$

Although a number of other formulations based on independent laboratory tests have been proposed (e.g., Hedar (1986), Medina et al. (1988), Hald (1998), Van Gent (2003), De Jong (2003), and Yoo (2013)), none have been as extensively applied as the Hudson or Van der Meer equations. It is clear there are many factors influencing the hydrodynamic response of CAUs in an armour layer; capturing this in effective design equations remains a key focus of research to the present day.

2.4 Inspiration for Current Research

Similar work by Sakakiyama (1990), with tetrapod armour units, inspired the current study. In this study, a tetrapod armour unit was mounted on a strain gauge based force transducer, within an armour layer. This study was conducted in a 51 m x 0.9 m x 1.2m deep wave flume with 15H:1V foreshore slope, with a 4H:3V breakwater slope. Four unit weights were used: 2.2 kg, 0.57 kg, 0.12 kg, and 0.06 kg. These units were then subjected to Froude-scaled wave conditions ranging from 5.7 cm to 33.3 cm in height, with periods ranging from 1.27 s to 2.32 s. For each unit weight, the period was kept constant while the height was varied. The unit location was kept constant at the SWL.

These techniques allowed the author quantify the hydrodynamic interaction of individual armour units. The results showed that individual armour units could be subjected to high slope-wise and uplift peak forces (Figure 12), with complex 3D directional patterns.

Sakakiyama (1990) showed there was a clear dependency between increasing wave steepness, and increasing hydrodynamic forces; this is depicted in Figure 13. This study also attempted to quantify the effect of scale on experimental testing in rubble mound breakwaters. As scale gets smaller, viscous forces increase in proportion to total force. This behaviour is clear in Figure 13, as the normalized hydrodynamic forces tend to increase as scale decreases.

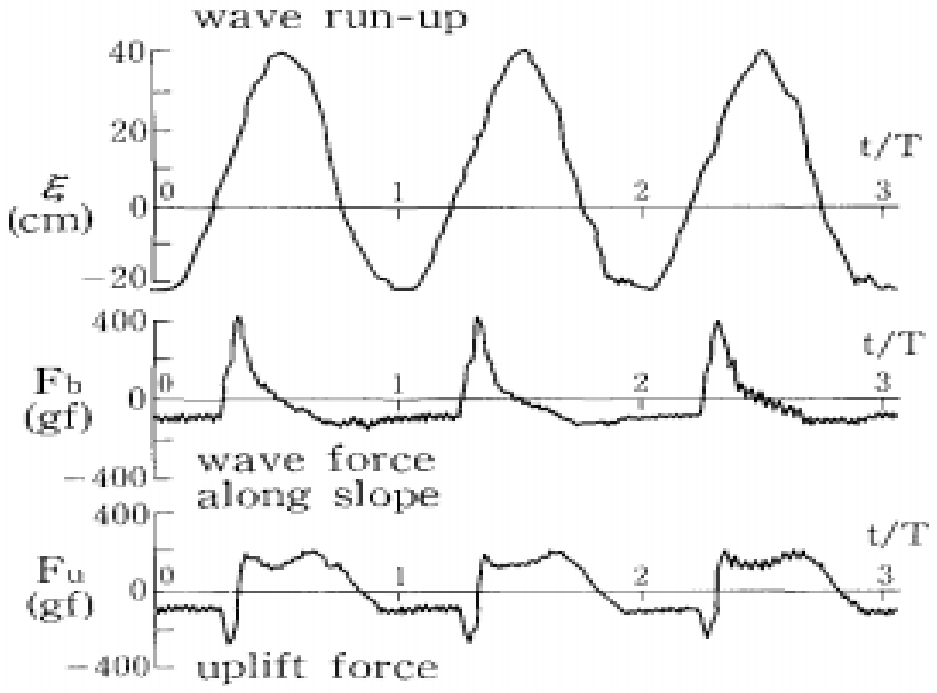

Figure 12: Time History of Wave Run-up (cm), Wave Force Along Slope (gf), and Wave Force Normal to Slope (gf), from Sakakiyama (1990)

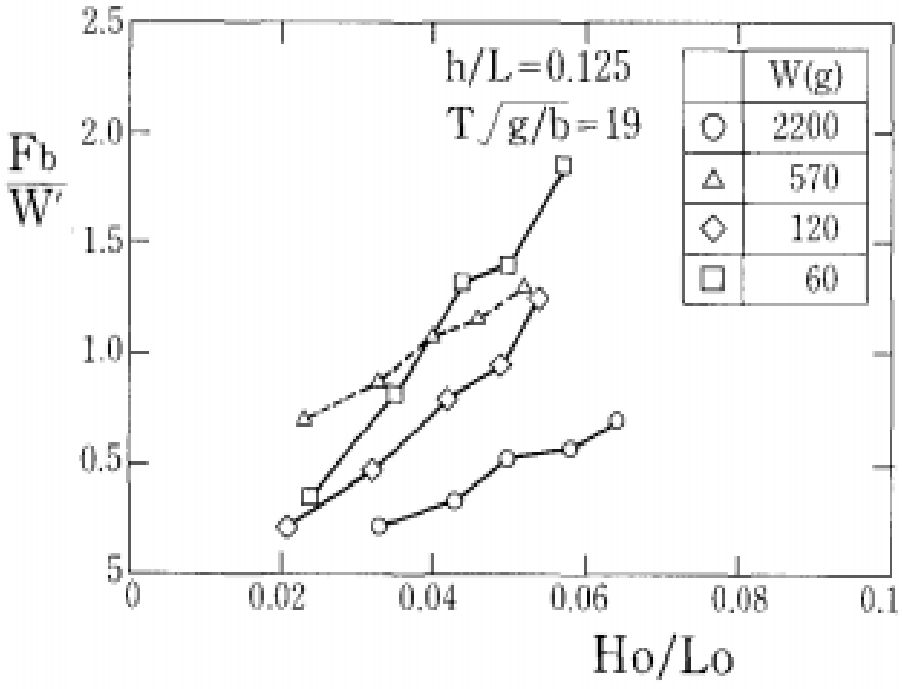

Figure 13: Wave Steepness vs. Normalized Slope-wise Wave Force, from Sakakiyama (1990)

Another key inspiration for the current study was presented by Van der Meer (1991). This study consisted of fitting cube and tetrapod armour units with accelerometers, with the goal of measuring peak impact accelerations and velocities, as well as quantifying unit rocking and unit collisions.

The results of this study showed promising insight into understanding armour unit dynamics within the armour layer, including the detection of rocking and collisions of units. The random nature of breakwater-wave interaction was proven to be highly variable, both spatially and temporally. Van der Meer concluded that wave conditions with a lower Iribarren number will tend to produce higher peak forces and accelerations. Two similar studies by Burcharth (1985) and Van der Meer (1994) instrumented armour units with strain gauges, and internal force transducers. This attempt to determine internal concrete stresses, the aforementioned studies, and other similar research were all instrumental in shifting modern design techniques for armour units away from the empirical paradigm.

The current studies' research collaborators at ICL have been developing promising coastal modeling tools. A novel and ground-breaking two-way coupling approach to modeling breakwaters with CAUs was developed by Xiang (2012). This approach couples a hydrodynamic solver with a finite-element-model discrete-element-model (FEMDEM) solver to simulate the complex free-body interactions of individual armour units, and their respective internal stresses. This software also has the capability to be coupled with a fracture analysis model by Guo (2015), which can predict breakage in the concrete armour units. An example of calculated unit velocities is shown in Figure 14a. An example of calculated stresses due to contact forces is shown in Figure 14b.

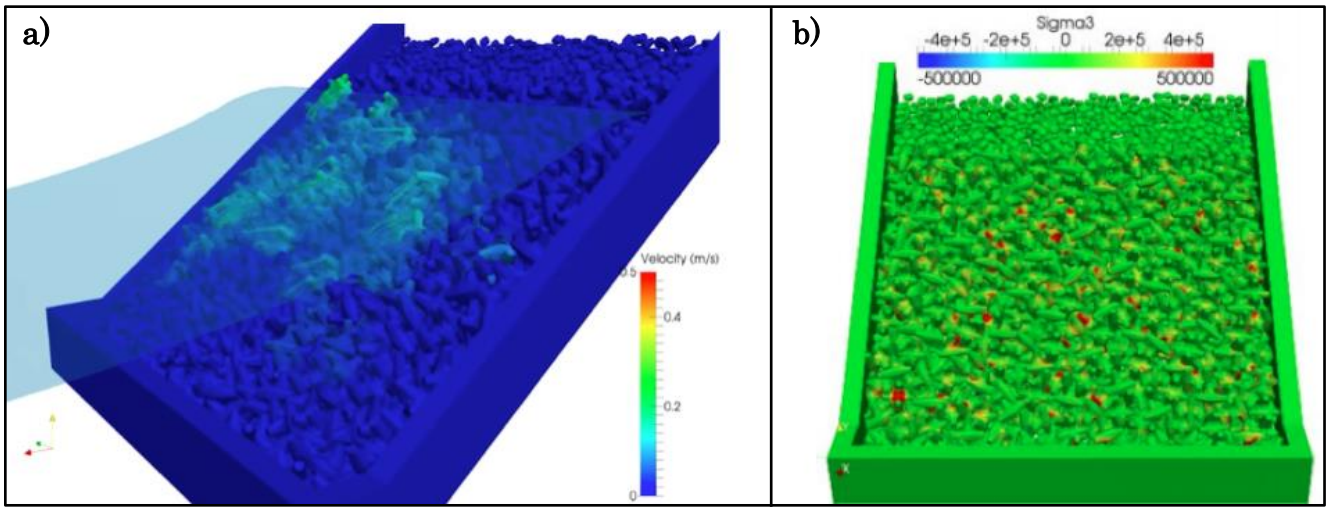

Figure 14: a) FEMDEM Results for Unit Velocities, b) FEMDEM Results for Static Contact Stresses, augmented from Latham (2013)

With increasing availability of computing power, and the possibility of validated numerical models of this type, it will be possible to simulate entire prototype breakwater

armour layers in the near future. This is something that has eluded the coastal engineering industry thus far.

More recently, the "smart-unit" trend has begun to develop. Building on work similar to Van der Meer (1994) and Burcharth (1985), researchers have begun to equip units with low-cost instrumentation commonly used in the field of robotics, or handheld electronics.

Hofland et al. (2018), at Delft University, developed wireless tetrapod and cube armour units, embedded with an accelerometer and gyroscope. The purpose of the study was to develop an instrumented unit capable of detecting the rocking motion and impacts of units during wave impact. The instrumented units developed are shown in Figure 15:

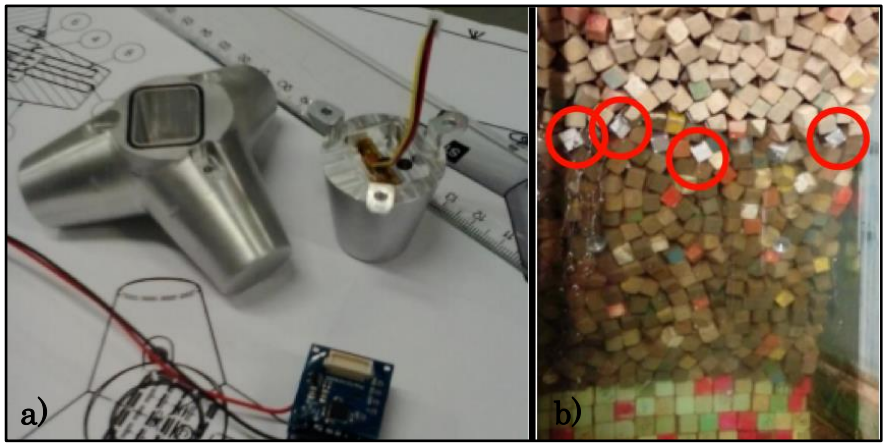

Figure 15: a) Machined Instrumented Tetrapod Unit and Instruments, b) Instrumented Cube Units In-situ during Flume Tests, augmented from Hofland et al. (2018)

The tetrapod had a characteristic height of C = 0.068 m and effective density of 2450 kg/m^3; this was tested on a 1.5H:1V breakwater slope at the SWL. Two irregular wave conditions were ran, with H_{m0} = 0.09 m and 0.11 m and T_p = 1.84 s and 1.81 s respectively. Eight cubes with a side length of 0.04 m were placed on a similar set-up, atop porous stone of D_{n50} = 0.02 m. These cubes were placed within 1-2 rows apart along the SWL, and subjected to an extensive testing program of irregular wave conditions ranging from H_{m0} = 0.08 m tov0.14 m and T_p =1.13 s to 2.12 s. Three sets of six unique signals were ran at different water depths (0.47 m, 0.56 m, 0.64 m). This effectively results in stability numbers ranging from 1.4-2.4.

The researchers showed that through careful analysis of the accelerometer and gyroscope readings, it was possible to detect individual rocking and collision events for individual armour units. Hofland et al. (2018) showed that for a randomly placed cube armour layer, the most rocking occurs approximately 2 rows of units below the SWL. As well, they showed that rocking and collision intensity is directly related to steepness, in that increased steepness will lead to more violent events. It was evident from this study that the spatial variability of rocking and induced impact velocities is rather high, even in a given constant row.

While the current study was initiated before this conference paper was published, it is of great inspiration for future iterations of "smart-units" to be developed.

With a combination of the technologies presented by Burcharth (1985), Sakakiyama (1990), Van der Meer (1994), Hofland et al (2018), other research endeavours, and the current study, the future of instrumented "smart-units" is proving to be very promising.

2.5 Openfoam

2.5.1 Description

All numerical simulations that were conducted as part of the current study were completed using OpenFOAM, an open-source CFD software developed and maintained by OpenFOAM Ltd. OpenFOAM uses the finite volume method (FVM) to solve systems of transient transport equations on structured and unstructured 3D meshes. Two mesh generation applications (blockMesh and snappyHexMesh) are provided with the basic download of the OpenFOAM software, along with additional refinement and pre-processing libraries. OpenFOAM also has the capability of loading pre-generated grids from other software.

A variety of discretization options for temporal, diffusive, convective, and source terms are available to the user, regardless of the case geometry and solver being used. Due to the open-source nature of the software, all applications and parameters can be manually edited. This allows for user-defined parameters and sub-routines, adding additional functionality to the basic OpenFOAM solvers. OpenFOAM utilizes Message Passing Interface (MPI) protocol for parallel computing cases. Simulations can be decomposed into a user-defined number of sub-domains, and individual processor performance can be optimized. All data visualization for OpenFOAM is carried out through ParaView visualization software running on the Python-VTK engine.

For the purposes of the current study, only OpenFOAM's multiphase solver "interFoam" was utilized to model the air and water phases. Additionally, a library of interFoam boundary conditions was used to simulate wave theory at inlet boundaries. This library of interFoam boundary conditions, dubbed "OlaFlow", contains boundary conditions for piston wave-makers, flap wave-makers, and user-defined water elevation time-histories according to several different wave theories. The framework for OlaFlow was developed by Dr. Pablo Higuera during his Ph.D. studies at IH Cantabria in 2015, and has been continuously updated since, Higuera (2015).

2.5.2 Governing Equations

The interFoam solver solves the 3D Navier-Stokes equations assuming two incompressible and immiscible fluids (water and air in this case). This solver employs the Volume of Fluid (VOF) method, an indicator function to represent the transport of fluid, and to calculate the water surface interface. Although both water and air are compressible (air much more than water) it is assumed for the purposes of this study that

this influence will be negligible on the final results; this assumption greatly simplifies the required computations.

The conservation of mass and momentum is captured using the continuity equation, and the momentum equation. The continuity equation is defined in terms of a given control volume, and states that the net amount of fluid flow through this control volume must be equal to zero at any instance in time.

InterFoam solves the continuity equation:

$$\nabla \cdot \mathbf{U} = 0 \tag{27}$$

As well as the momentum equation, simultaneously:

$$\frac{\partial \rho \mathbf{U}}{\partial t} + \nabla \cdot \rho \mathbf{U}\mathbf{U} = -\nabla p + \nabla \cdot (\mu \Delta \mu + \nabla^T u) + \rho g + F_s \tag{28}$$

The F_s term represents a source of momentum in the equation that is generated by the occurrence of surface tension. This term can be estimated using the following equation:

$$F_s = \sigma k(x) n \tag{29}$$

Where k and n can be calculated using:

$$k = -\nabla \cdot n = \nabla \cdot \frac{\nabla \alpha}{|\nabla \alpha|} \tag{30}$$

The VOF inside a given cell is represented by the α parameter, where $V_{fluid} = \alpha V_{cell}$. This value can range from 0 to 1 and exist at any point in between. This value is used to represent the fractional percentage of each of the two fluids in the cell. The interface between two fluids will then be represented as a mixture of the two fluids, in a thin layer between the two pure fluid phases.

$$\alpha = \begin{cases} 0 & in\ fluid\ a \\ 0 < \alpha < 1 & in\ the\ transitional\ region \\ 1 & in\ fluid\ b \end{cases}$$

This parameter is estimated using the following indicator function:

$$\frac{\partial \alpha}{\partial t} = \nabla \cdot (\alpha \mathbf{U}) = 0 \tag{31}$$

In order to maintain a sharp interface between the two fluids, but to reduce errors and sharp jumps in the phase fraction due to the inherent nature of the indicator function method, a synthetic compression term is used to estimate surface compression:

$$\frac{\partial \alpha}{\partial t} + \nabla \cdot (\mathbf{U}\alpha) + \nabla \cdot \left(\mathbf{U}_c \alpha(1-\alpha)\right) = 0 \tag{32}$$

The artificial compression term is only utilized in the transitional region surrounding the theoretical location of the interface. It is important to distinguish surface compression and fluid compressibility; surface compression refers to the process of shrinking the smeared interface caused by numerical diffusion of the phase fraction, and has nothing to do with fluid compressibility.

Another aspect of this compression term is bounding the phase fraction transport to a direction that is perpendicular to the interface, Berberovic, (2010). Thus, this term will only act as a vector on the reverse side of the interface. As a result of that, the developers of OpenFOAM came up with the following general equation to estimate U_c:

$$\mathbf{U}_c = \min[C_\alpha |\boldsymbol{U}|, max(|\boldsymbol{U}|)] \frac{\nabla \alpha}{|\nabla \alpha|} \tag{33}$$

2.5.3 Turbulence Modeling

Eddies are rotating turbulent structures that can be classified by different length and velocity scales. The largest of these scales are known as production-scale eddies; these are produced through the generation of shear through a fluid by some other object. This shear influence causes the large scale eddies that, once initiated, causes a cascade of energy to increasingly smaller scales until viscosity dominates and halts the fluid. These rotating structures are subject to stretching, warping and combining in complex ways, giving rise to apparently chaotic and random fluctuations in flow properties. It is the combination of these effects that give rise to what is known as “turbulence”. When there is turbulence present, there is increased energy dissipation, mixing, heat transfer and drag, George (2013).

Turbulence is a very complex phenomenon, and is very important in both research and practical engineering problems. In order handle turbulence in numerical modeling, several methods are available. First, Direct Numerical Simulation (DNS), utilizes the Navier-Stokes equation to explicitly resolve all scales of turbulence. This, of course, has the most stringent meshing and computational requirements of all methods. In order to resolve turbulence at small scales, very fine meshes are needed which leads to increased computational requirement. This method of handling turbulence in numerical modeling is not usually practical for most purposes.

A second method for accurately resolving turbulence in numerical models is known as the Large Eddy Simulation (LES) method. In LES simulations, a spatial filter is applied to the turbulent length scales, in order to distinguish them into two groups. The larger eddies are directly and fully resolved, thus their influence on the final solution can be directly accounted for. The influence of the smaller eddies is calculated by using a Sub-Grid Scale (SGS) model. Although methodologies such as LES have been gaining

popularity, the so-called Reynolds-Averaged Simulations (RAS) or Reynolds-Averaged Navier-Stokes (RANS) approach remains the most widely used.

In RAS models, the flow parameters in the Navier-Stokes equations are substituted by a mean value, and a turbulent oscillating component. Once plugged into the Navier-Stokes equations, these decomposed parameters are then integrated through time. This method greatly reduces the computational requirement, as the solution yields mean flow parameters. However, while this method is very useful, it also introduces an unknown stress term, known as the Reynolds Stress. Due to the additional unknowns in the system, this method gave rise to the famous "closure problem". This closure problem is the process of balancing the left and right sides of the RANS equations due to the inherent in-balance introduced by the unknown Reynolds Stress parameter.

While there have been many approaches to handling the closure problem, only a brief overview of the turbulence models used in this current study, as well as other available methods in OpenFOAM will be discussed. The RAS models included in OpenFOAM utilize the Boussinesq approximation. This method accounts for the additional Reynolds Stress term by introducing an artificial eddy viscosity parameter into the viscous stress term of the Navier-Stokes equation:

$$\mu_{eff} = \mu + \mu_t \tag{34}$$

By using the Boussinesq approximation, the problem of directly simulation energy loss due to turbulence is replaced by estimating an equivalent theoretical energy loss by virtue of an increased fluid viscosity.

The issue now becomes how to estimate this artificial eddy viscosity parameter. In OpenFOAM, this problem is handled by using either a zero-equation model, or one of several two-equation models. Zero equation models simply prescribe the value of a constant μ_t, while two equation models are discussed as follows.

$k-\varepsilon$ Turbulence model

The standard $k-\varepsilon$ model, originally proposed by Launder and Spaulding (1974), parameterizes turbulence into two variables: the turbulent kinetic energy, and the turbulent dissipation rate. Each obey a convection-diffusion equation of the form:

$$\frac{\partial \rho k}{\partial t} + \nabla \cdot \left(\rho \mathbf{U} k - \left[\mu + \frac{\mu_t}{\sigma_k} \right] \nabla k \right) = \boldsymbol{\tau} \nabla \mathbf{U} - \rho \varepsilon \tag{35}$$

$$\frac{\partial \rho \varepsilon}{\partial t} + \nabla \cdot \left(\rho \mathbf{U} \varepsilon - \left[\mu + \frac{\mu_t}{\sigma_\varepsilon} \right] \nabla \varepsilon \right) = C_{\varepsilon 1} \frac{\varepsilon}{k} \boldsymbol{\tau} \nabla \mathbf{U} + C_{\varepsilon 2} \frac{\varepsilon^2}{k} \tag{36}$$

These equations are then solved simultaneously alongside the continuity, momentum, and phase fraction transport equations. Once k and ε have been determined, the eddy viscosity is then calculated as:

$$\mu_t = \frac{C_u \rho k^2}{\varepsilon} \tag{37}$$

In addition to the standard $k - \varepsilon$ turbulence model, additional turbulence models that are available with the OpenFOAM download were explored as part of the current study. Each of these models follows a similar algorithm to the $k - \varepsilon$ turbulence model, and thus will not be explained in as great of detail.

RNG $k - \varepsilon$ Model

The Re-Normalized Group (RNG) $k - \varepsilon$ model was proposed by Yakhot et al. (1991). This modified version of the standard $k - \varepsilon$ turbulence model was developed to account for different scales of motion on the turbulent diffusion. The advantage of this model over the standard $k - \varepsilon$ model is most notable in increasing the accuracy of predicting rapidly strained and swirling flows, Choudhury, (1993).

SST $k - \omega$ Model

A popular alternative to $k - \varepsilon$ based turbulence models are what are known as $k - \omega$ turbulence models. Developed by Wilcox (1988), here, ω represents the specific rate of energy dissipation, and behaves differently than ε. This type of turbulence model is noted to have better performance in near-wall regions. Menter (1993) suggested a hybrid of $k - \varepsilon$ and $k - \omega$ models, which combined the aspects of both models into one comprehensive turbulence model, known as the Shear Stress Transport (SST) $k - \omega$ model.

In this model, the zone between the wall and extent of the boundary layer are modeled using the $k - \omega$ method, while the zone outside this region is modeled using the $k - \varepsilon$ method. This composite approach enhances performance in near-wall regions, and avoids some of the shortcomings of $k - \omega$ models in free-stream zones.

2.5.4 Finite Volume Method

The system of continuous partial differential equations (PDEs), described in the previous sections, are capable of predicting the behaviour of two fluids. However, it is impossible to achieve an analytical solution to this system; thus, steps must be taken to approximate the solution at discrete points in space and time. The interFoam solver uses a finite-volume-method (FVM) discretization technique on the modeled system, which is applied in three steps:

1. Spatial discretization
    - Discretization whereby the three-dimensional solution domain is subdivided into a number of control volumes, or computational grid cells, at which the PDEs are approximated

2. Temporal discretization
    - Discretization for which the of time from the beginning to the end of the considered frame is split into a finite number of discrete steps

3. Equation discretization
    - Transforming the continuous PDEs into a discrete form suitable for approximation at the coordinates defined in steps 1 and 2.

2.6 Discussion

Most current design techniques are based on the notion of hydraulic stability, and consider the ejection of units as the measure of being damaged. While this definitely does play a role, the complex hydrodynamic interaction and structural behaviour of the individual armour units is equally important. The units are subjected to constant loads throughout the design lifetime. Effects such as armour unit fatigue, breakage, and other secondary effects not considered in modern formulae have in fact caused numerous failures. Although they have not prompted the implementation of design standards, they have definitely set the stage and overarching direction of current research that will hopefully lead to unified design approaches and safe design regulations.

The empirical design formulae discussed in the previous sections are invaluable tools in the development of rubble mound structures. They cannot, however, be reliably used to predict structural stability for the full range of conditions to which a structure may be exposed. The design formulae are based on tests using simplified or conventional structures and therefore may not accurately reflect unconventional or unique designs. As a consequence of this, and the inherent uncertainty of existing design equations, physical model investigations remain standard practice for the optimization and detailed design of rubble mound structures.

The most common design formula, Hudson's Equation, is employed mainly because it is the method with the most literature behind it. This method has numerous inherent assumptions and limitations that affect the accuracy of the formula, and have been reflected in real world failures. The simple formulation states that in addition to the calibrated empirical parameter K_D, the unit stability is only affected by the breakwater slope, armour unit weight and size. This has shown in practice and in research to not be true. Hudson's K_D parameter assumes failure at 5% damage of the armour layer, which is not always the case. This empirical parameter also simplified scaling, and all other effects into one value; it has been a subject of debate that K_D may not be the same at drastically different length scales than those tested in the formulation. This would be congruent with the accepted notion of high error in experimental research at lower scales.

Hudson's Equation does not account for hydraulic parameters such as the wave direction, period, steepness, breaking characteristics, irregular wave trains, duration of storm, effect of adjacent units, structure permeability, or other effects that have been proven to greatly affect the design of CAUs.

The other most common design formulae, produced by Van der Meer (1988), are considerably more advanced than the Hudson approach, but are still laden with inherent assumptions and limitations due to the nature of the experimental testing the equations were derived from. The experiments were conducted using only one slope of breakwater and foreshore geometry. Several researchers have proven through that the equations can be inaccurate in shallow-water conditions. This is due to the fact that all parameters used in this formulae are dependent on deep-water wave conditions and thus do not accurately reflect local conditions at the breakwater. One can also easily see that the parameters utilized in the CAU formulae are different then the parameters utilized in the natural rock formulae. With CAUs essentially designed to behave as natural rock on rubble mound breakwaters, the fact that the equations are not dependent on the same parameters suggests further research could improve the method.

Due to the extremely complex flow of waves through a porous armour layer, direct assessment of the forces on individual units has been difficult and impractical for design purposes. This has lead to the discussed design equations, and experimental testing as the norm for design methodology. A key issue, particularly with respect to CAUs, is that empirical formulae and physical models fail to provide designers with a comprehensive physical understanding of how these armour systems respond to wave action at full scale. The empirical formulae for determining the required unit weight rely on a stability coefficient derived from model tests. These coefficients are meant to capture the inherent effects of uncertainty, interlocking, unknown scale effects and potential for fracturing without providing a physical description of how these items influence the stability, Medina et al. (2012). Due to this uncertainty, designers often resort to applying large factors of safety when sizing breakwater armour units, thereby increasing construction costs by considerable amounts.

Although a scaled physical model can assist in studying the hydraulic stability of armour units, the materials commonly used are disproportionately strong when compared to the stresses induced by the static and dynamic loading, Burcharth et al. (1991). Consequently, fracturing of the units cannot be studied simultaneously and so the interdependency of the structural and hydraulic stability is ignored. When a proper balance between the two is not achieved, it can lead to catastrophic failures of breakwaters, as was the case at The Port of Sines, Portugal in 1978 (Baird et al., (1980)) and Tripoli Harbour, Libya in 1984 (Burcharth, (1987)).

While there have been several independent research endeavours focused on understanding the actual forces and stresses subjected to CAUs, this type of force-balance approach remains in it's infancy stages. In order to perform an adequate design, one must understand all the forces acting on individual armour units in an armour layer. This is not considered in typical design methods. Methods such as those proposed by Sakakiyama (1990), Van der Meer (1990), Burcharth (1994), and Hofland et al. (2018)

have paved the way for a new paradigm of experimental testing and CAU design that will help to reduce or even eliminate the downfalls of current design methods.

In the coastal engineering field, it has never been possible to accurately produce numerical models of full prototype breakwaters, while simulating the free-body dynamics and hydrodynamic interactions. With advances in computing power, this dream will soon be a reality; work such as Xiang (2012) has shown promise to the idea of simulating full prototype breakwaters. It is research endeavours focused on quantifying the forces, stresses, and pressures acting on individual armour units that can and will be used as validation for these new numerical tools.

Based on the literature review conducted; to aid with the understanding of the interaction between waves and armour units, as well as future developments into "smart-unit" research and numerical modeling, the focus of this study is to:

- Develop and construct a 3D printed Core-Loc armour unit capable of measuring surface pressures and forces, with the ability to transmit data wirelessly
- Construct all circuitry and instrumentation from widely available, low-cost devices
- Develop interfacing tools in Python to communicate with and control the instrumented unit
- Perform comprehensive testing and calibration procedure on the instrumented unit
- Observe and analyze performance of instrumented unit in breakwater setting
- Compare the effects of different wave climates, and slope locations on the generated hydrodynamic forces and pressures on the unit
- Develop proof-of-concept for future versions of "smart-units" with more advanced capabilities
- Develop modeling rules-of-thumb for simulating breakwaters in OpenFOAM, and a calibrated numerical model capable of reproducing the experimental results

3.0 Experimental Study – Instrumented Core-Loc Unit

3.1 Description of Study

The fabrication and initial experimental testing of the instrumented Core-Loc armour unit was conducted at the UOttawa MakerSpace, and UOttawa Hydraulics Laboratory. The design of this instrumented unit took inspirations from similar previous research endeavours, incorporated them into the design, and explored additional capabilities not yet seen in literature. The objective of this portion of the study was to produce a 0.12 m instrumented Core-Loc armour unit that would be capable of being mounted on a force transducer. This unit would also be able to measure surface pressures via embedded sensors while placed in an armour layer. A total of 6 pressure sensor locations were chosen for this prototype. These pressure sensors in the instrumented unit were then subjected to a comprehensive performance testing and calibration procedure. This instrumented unit would then prove the viability of relatively low cost, widely available instrumentation for use in experimental breakwater testing; potentially paving the way for fully wireless units with additional instrumentation.

3.2 Instrumentation

The instrumented Core-Loc armour unit was powered by a Raspberry Pi 3 (Figure 16a); a low cost, Linux based computer with capabilities of interfacing with a wide variety of analog and digital instruments. This credit-card sized computer provided 5V signal to all instrumentation, stored the data, and also has the capability to transmit the data in real time via Wi-Fi or Bluetooth.

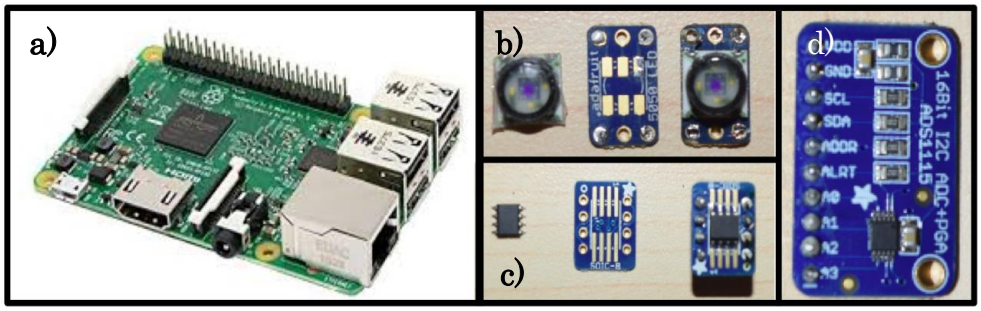

Figure 16: a) Raspberry Pi 3, b) HoneyWell TBF Pressure Sensors, c) TI INA155U Amplifiers, d) Adafruit ADS1115 Analog-Digital-Converter

Due to the small scale of breakwater testing, the size of the pressure sensors mounted on the surface of units will directly govern the lower limit of possible scales. In order to not alter unit geometry, pressure sensors must remain flush with the unit's surface; this means they must be embedded into the unit and thus have a small footprint. The pressure sensor model chosen was Honeywell TBF-LPNS001BGUCV, due to the small package size and high accuracy. A sample of this 7mm x 7mm pressure sensor is shown in Figure 16b. In order to amplify the output signal from the pressure sensors, Texas Instruments INA155U differential amplifiers were used. These types of amplifiers use

the positive and negative output signals from the pressure sensor as inputs, amplifies the voltage difference between them, and provides one single analog output than can be read by an analog-digital converter (ADC). The amplifier is shown in Figure 16c. Finally, the amplified signal from the pressure sensor must be converted into a digital signal to be read by the Raspberry Pi 3. This was achieved by using 2 Adafruit ADS1115 ADCs, shown in Figure 16d, which provided analog input for 4 channels each.

3.3 Unit Construction and Development

Core-Loc units were 3-D printed with PLA plastic at the UOttawa MakerSpace. These units were printed in such a way as to have housing for pressure sensors, housing for coupling nuts used for mounting on the force transducer, and a semi-hollow core to house the instrumentation. The combination of these design features allowed the pressure sensors to be embedded in the surface of the unit, and contained the remaining instrumentation within the unit. With the nature of the Raspberry Pi 3 i2c interface protocol, it also reduced all wiring to 5 small wires, contained in a 3mm diameter cable leaving the unit.

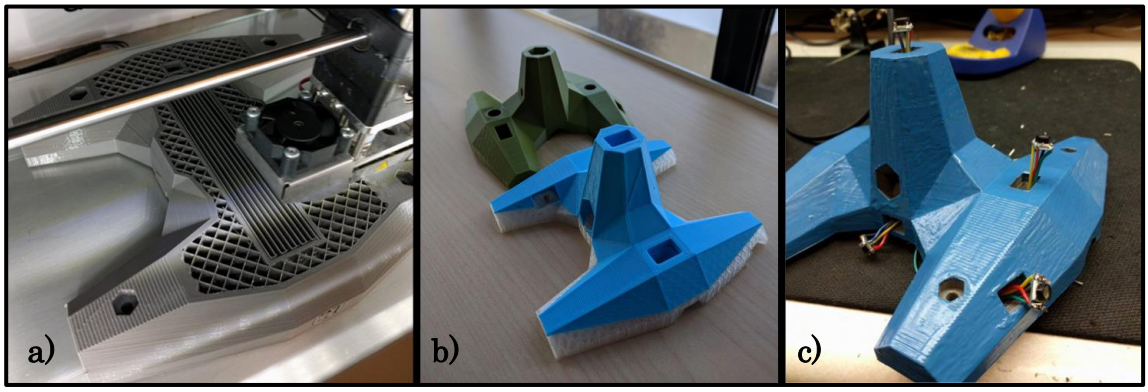

Figure 17: a) During 3D Printing, b) After 3D Printing, c) After circuit assembly

All wiring connections were soldered using the equipment and supplies at the UOttawa MakerSpace. Once completed, the pressure sensors were inserted into the housing locations and carefully sealed with marine grade silicon sealant. Extra precaution was taken to ensure no sealant came in contact with the diaphragms of the pressure sensors. Next, the unit was sealed, and the inner cavity filled with silicon to ensure zero water penetration. The shell was also coated with a thin layer of epoxy-based 3D printing sealant to seal the shell of the print. Specially printed slots were then fitted with coupling nuts, in order to allow unit mounting on a threaded rod for later testing. This is shown in Figure 17.

The resulting unit had a height of 0.12 m, and had 6 unique pressure sensor locations in key locations. These locations were chosen to best represent the full range of pressures across the surface of the entire unit, while accounting for printing and wiring logistics.

The coordinates of each pressure sensor with respect to the unit centroid are listed in Table 5.

Table 5: Instrumented Core-Loc Unit Pressure Sensor Locations

Location	X (mm)	Y (mm)	Z (mm)
Centroid	0.00	0.00	0.00
P1	-60.00	0.00	0.00
P2	-14.00	-28.00	-34.00
P3	-22.00	39.25	0.00
P4	12.00	52.00	26.00
P5	36.00	0.00	-16.25
P6	19.00	-39.25	22.00

The locations of each pressure sensor on the unit's surface are illustrated in Figure 18. A total of three sensors were embedded into each half of the unit, as the unit was 3D printed in two pieces. This simplified the assembly, and allowed an even distribution of circuitry inside the unit.

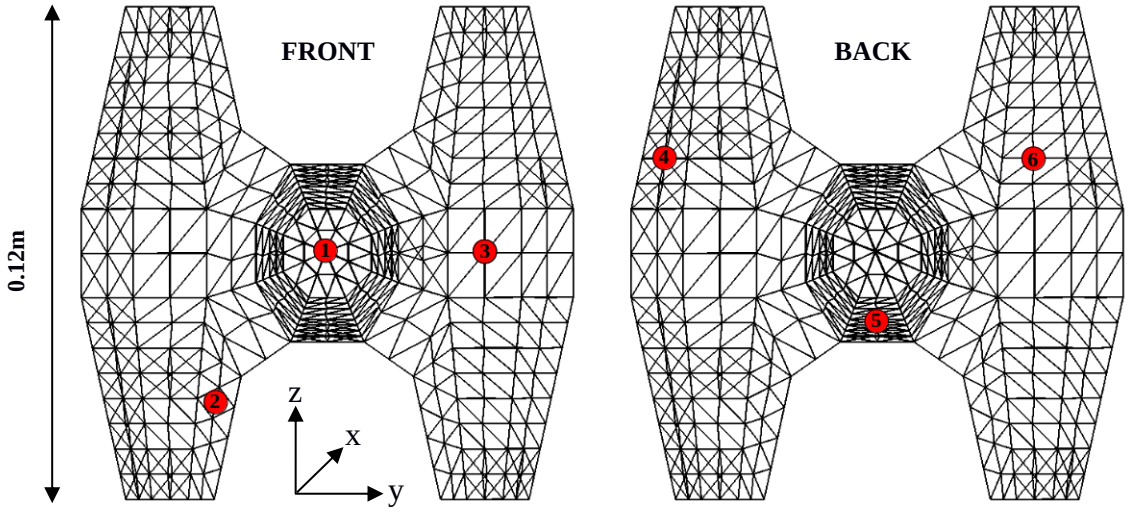

Figure 18: Distribution of Pressure Sensors on Instrumented Core-Loc unit surface

Python modules developed by Adafruit provided the basis of the interface between the Raspberry Pi 3 and the instrumentation. These modules were then tailored and modified to perform specific functions for the study purpose. The entirety of testing was done from a laptop, controlling the Raspberry Pi 3 through ssh protocol; similar to remote access.

3.4 Calibration Procedure

All initial calibration and testing was performed at the UOttawa Hydraulics Laboratory, in a 2.5m tall x 0.56m diameter vertical drop-tank. The instrumented Core-Loc unit was mounted on a threaded rod, screwed into a coupling nut intended for a future force transducer. This rod was then fixed to a frame atop the drop-tank to maintain constant and desired submergence depths. A schematic of the calibration procedure and drop-tank is shown in Figure 19.

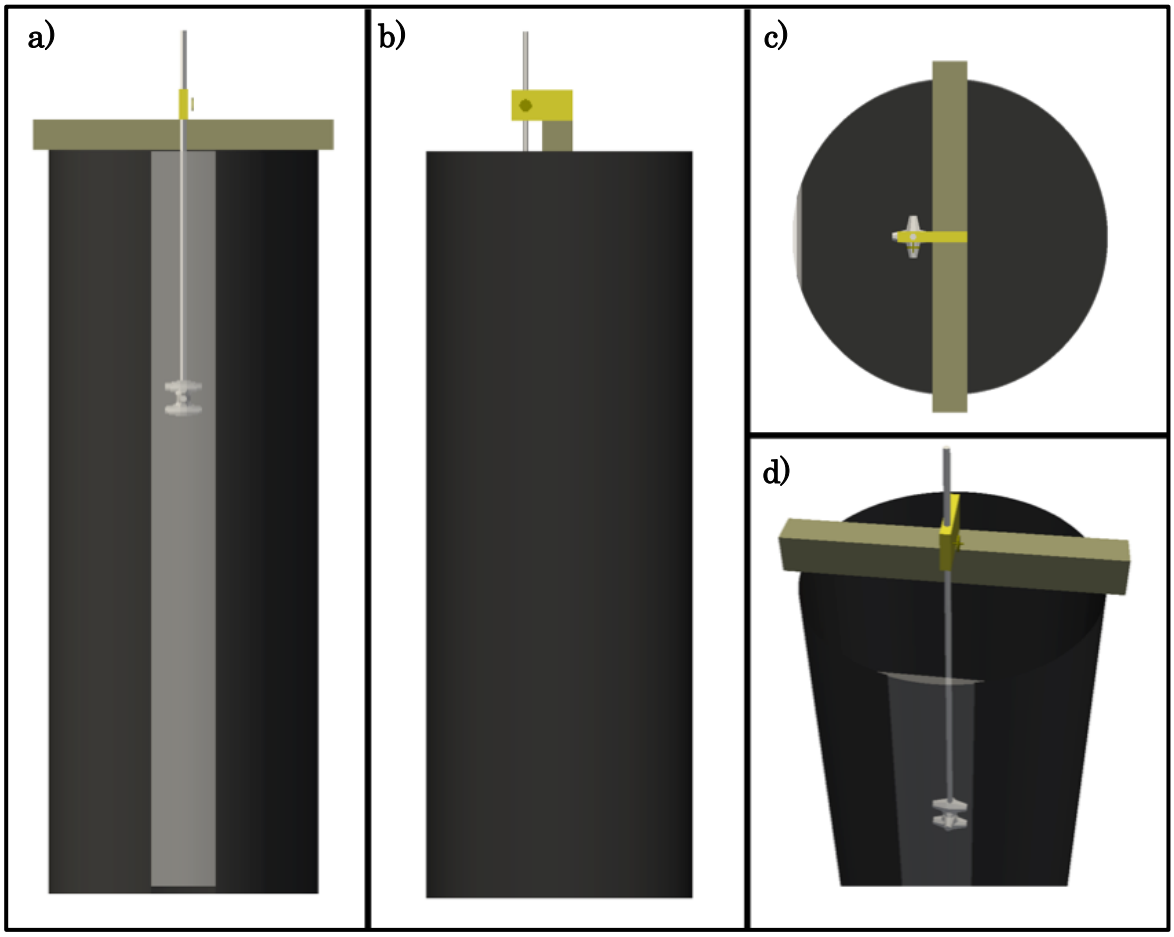

Figure 19: The Drop Tank: a) Front View, b) Side View, c) Top View, d) Isometric View

The instrumented Core-Loc unit was first subjected to a leakage test; the unit was submerged at a depth of 2 m for 48 hours to ensure its' reliability for long periods of experimental testing. The final circuit was then tested for sensor sensitivity, accuracy, repeatability, hysteresis, and other standard instrumentation properties.

In order to calibrate sensor sensitivity, a linear constant can be used to relate a change in pressure to a change in raw sensor output. This constant is known as the calibration coefficient.

Given that the chosen ADC for this study has programmable gain properties, the calibration coefficient can in turn be multiplied by a factor of 2, 4, 8, or 16. This ADC device also has 16 bit signal storage capacity, or $+/-2^{15}$ unique readings. The proper gain factor must be chosen to ensure the pressures detected do not exceed the maximum value of the ADC. As the intended purpose for this instrumented Core-Loc was for use in waters <1m, a gain factor of 8 was chosen, giving the pressure sensors a maximum operating depth of approximately 2.75m.

The calibration curves for each pressure sensor were produced by the following calibration procedure:

1. Submerge the unit to a centroidal depth of 0.20m (to ensure all sensors are fully submerged).

2. Recording the raw pressure sensor output for 30 seconds.

3. Increase the centroidal depth by 0.10m.

4. Repeat steps 2 and 3 until a centroidal depth of 2m is reached.

The entire 30-second time history recorded at each depth interval was averaged to represent a single data point for the calibration curve. This calibration curve data was then used to calculate accuracy in the form of non-linearity of the calibration curve; or the deviation from a constant calibration coefficient.

In order to assess the repeatability of measurements with the pressure sensors, each was calibrated using the aforementioned procedure 5 times on consecutive days. The deviation of the calibration coefficient from each consecutive calibration was subsequently compared.

Analyzing the 30-second time histories of each calibration point tested another aspect of accuracy. Once the sensitivity is calibrated, the pressure sensors must be able to maintain a nearly constant value at a given constant depth to ensure accurate readings. Using spectral analysis, the magnitude and frequency of the ambient noise in each sensor was calculated.

A key aspect of instrumentation is a sensor's performance during hysteresis conditions; or cyclical excitation. A pressure sensor with favourable hysteresis properties will output the same values for a given pressure reading regardless of the loading direction.

In order to assess the hysteresis performance of the instrumented Core-Loc unit's sensors, each sensor was subjected to a modified version of the aforementioned calibration procedure:

1. Submerge the unit to a centroidal depth of 0.20 m (to ensure all sensors are fully submerged).

2. Record the raw pressure sensor output for 30 seconds.

3. Increase the centroidal depth by 0.10 m.

4. Repeat steps 2 and 3 until a centroidal depth of 2 m is reached.

5. Decrease the centroidal depth by 0.10 m.

6. Record the raw pressure sensor output for 30 seconds.

7. Repeat steps 5 and 6 until initial centroidal depth of 0.20 m is reached.

8. Repeat steps 2 to 7 until a total of 5 cycles have been completed.

Lastly, the minimum threshold value of each sensor was obtained. For each sensor, this was obtained by submerging the sensor to the depth at which the first change in output signal occurs. This is then regarded to be the minimum possible depth and pressure detectable by the instrumented Core-Loc unit.

3.5 Results

As previously mentioned, the completed instrumented Core-Loc unit had a total of 6 pressure sensors in key unique locations around the unit face; the final unit height was 0.12 m. A 3m long, 3.5mm diameter cable containing the 5 wires necessary to operate the sensor circuit was used to interface with the Raspberry Pi 3. The surface of the unit was also painted white, for image processing purposes in future stages of testing. The resulting unit is shown in Figure 20.

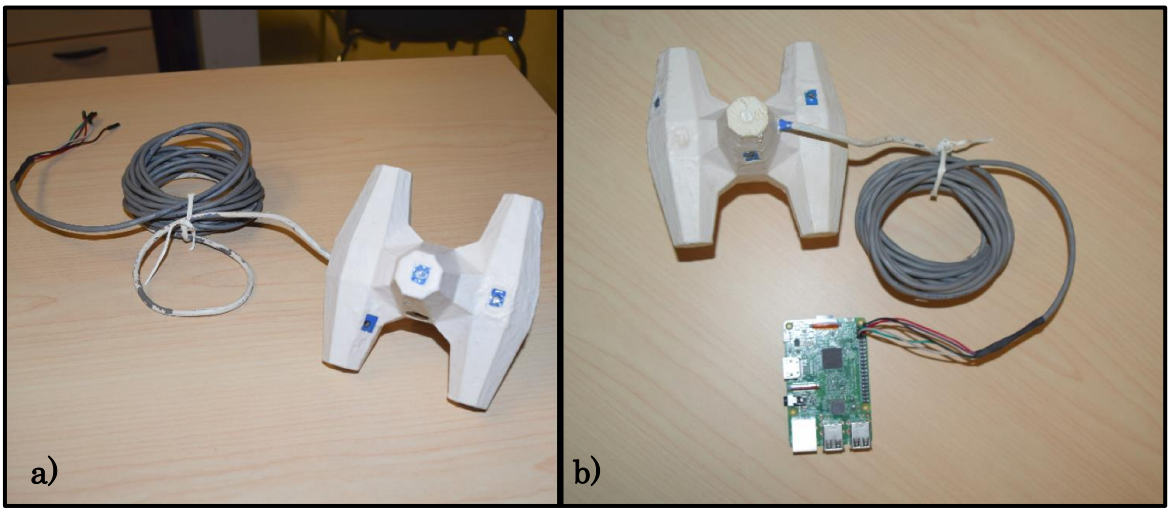

Figure 20: Instrumented Core-Loc Unit and Raspberry Pi 3 a) Front, b) Back

3.5.1 Submergence Testing

As apparent from the results of the initial submergence testing, the combination of the unit's meticulously crafted design features and precautions provided excellent performance for time periods up to 48 hours, in depths up to 2m. The intended application of the unit will not approach these conditions, thus the basic operation of the unit was deemed to be capable of performing long duration experimental testing.

During this submergence test, the opportunity was taken to assess the thermal properties of the instrumented Core-Loc unit. An initial concern of the final design was the possibility of circuit overheating. Without a proper heat sink, ventilation, and being completed encased in marine grade silicone, there is potential for temperature fluctuations to occur in the circuit and sensors themselves. This will in turn affect the resistance of the circuit and the sensitivity of the instrument. Based on an analysis of a 48-hour time history of continuous sensor operation, internal overheating of the instrumented Core-Loc unit was not present, and performance properties remained constant.

3.5.2 General Operating Ranges

In order to ensure accurate performance, and to prevent damage to the instrumented Core-Loc unit, the operational parameters and ranges must be respected. All calibration, and testing of the instrumented Core-Loc unit was performed using 5Vdc input to the sensor circuit. The instrumented unit is capable of performing at any input voltage between 1.5 - 12.0 Vdc. As all analog instruments output signals that are proportional to the input signal, altering the input voltage will affect the accuracy and sensitivity characteristics of the instrumented unit by a theoretical factor of V_2 / V_1. In order to ensure there is no damage incurred to the circuit or any instrument, the supply current must remain between 0.6 – 1.0 mA. The calibration and testing procedure was completed in temperature ranging between values of 18 – 20 °C. However, the instrumented Core-Loc unit has the theoretical capability to perform between operational temperatures of 0 – 50 °C without marked deviation from the instrument's manufacturer characteristics.

Each sensor was tested individually for minimum threshold values using the aforementioned testing procedure. For each sensor, a minimum threshold depth of < 2 mm was obtained. For each sensor, changes in the output signal were detected near-instantaneously upon contact with the water. The minimum threshold value and pressure detectable by each sensor was then assumed to be atmospheric, or 0 Pa. The instrumented Core-Loc unit achieved a maximum operating depth of $d \approx 2.75$ m before the ADC reached its' maximum value. This corresponds to an operational pressure range of approximately 0 – 27000 Pa. This can however be altered by changing the gain factor of the ADC; this will inversely affect sensitivity and resolution.

Due to the sampling limitations of the ADC, and the nature of the developed python modules, the unit is capable of 8 different sampling frequencies, depending on the number of pressure sensors being sampled. After testing, the performance of the unit showed its' capability to perform at 8 different sampling rates, listed in Table 6:

Table 6: Instrumented Core-Loc Unit Maximum Sampling Rates

Number of Pressure Sensors	Maximum Sampling Rate (Hz)
1	320
2	160
3	107
4	80
5	64
6	53
7	46
8	40

3.5.3 Pressure Sensor Sensitivity

The sensitivity of the instrumented Core-Loc unit corresponds to the ratio between increased raw output signal versus increased pressure (calculated using $P = \Upsilon h$). This calibration coefficient was calculated using Equation 38:

$$c = \frac{\Delta ADC_{Output}}{\Delta Pressure} \tag{38}$$

As expected from manufacturer tolerances, the sensitivity of each pressure sensor was nearly identical. From Equation 38, the resulting calibration coefficients for each pressure sensor are listed in Table 7. While each sensor had a slightly different zero reading, the calibration coefficient between sensors deviated by ≤ 1%. The calibration coefficient for each sensor between calibrations on consecutive days also deviated by ≤ 1.05%. This error was attributed to slight differences in ambient conditions, and potentially inadequate electromagnetic insulation of the instrumentation.

Table 7: Instrumented Core-Loc Unit Pressure Sensor Sensitivity Results

Test	P1 (mV/Pa)	P2 (mV/Pa)	P3 (mV/Pa)	P4 (mV/Pa)	P5 (mV/Pa)	P6 (mV/Pa)
Calibration #1	5.14E-04	5.17E-04	5.16E-04	5.15E-04	5.14E-04	5.14E-04
Calibration #2	5.07E-04	5.08E-04	5.13E-04	5.09E-04	5.13E-04	5.07E-04
Calibration #3	5.14E-04	5.13E-04	5.21E-04	5.18E-04	5.19E-04	5.05E-04
Calibration #4	5.14E-04	5.17E-04	5.22E-04	5.16E-04	5.15E-04	5.14E-04
Calibration #5	5.09E-04	5.08E-04	5.11E-04	5.08E-04	5.10E-04	5.05E-04
Max Error (%)	0.47	0.86	1.05	0.94	0.93	0.98

The python interface with the ADC inside the instrumented Core-Loc unit provides a digital signal with 16 bit resolution; digitizing and storing analog voltage signals represented by +/- 2^{15} unique integer values. Thus, in order to calculate the sensor output voltage, Equation 39 was employed. The reason the denominator is not 2^{16} is because voltages were only encountered in one direction (+); thus 2^{16} values are represented by $\pm 2^{15}$.

$$V_{output} = \frac{ADC_{Output}}{2^{15}} \cdot V_{max} \tag{39}$$

Where V_{max} is dictated by the ADC gain factor according to Table 8. As mentioned previously, a gain factor of 8 was chosen for the current study.

Table 8: Possible ADC Gain Factors and Input Voltage Ranges

Gain	Maximum Voltage Range
2/3	± 6.144 V
1	± 4.096 V
2	± 2.048 V
4	± 1.024 V
8	± 0.512 V
16	± 0.256 V

The resulting calibration curve for each pressure sensor, for Calibration #1 is shown in Figure 21:

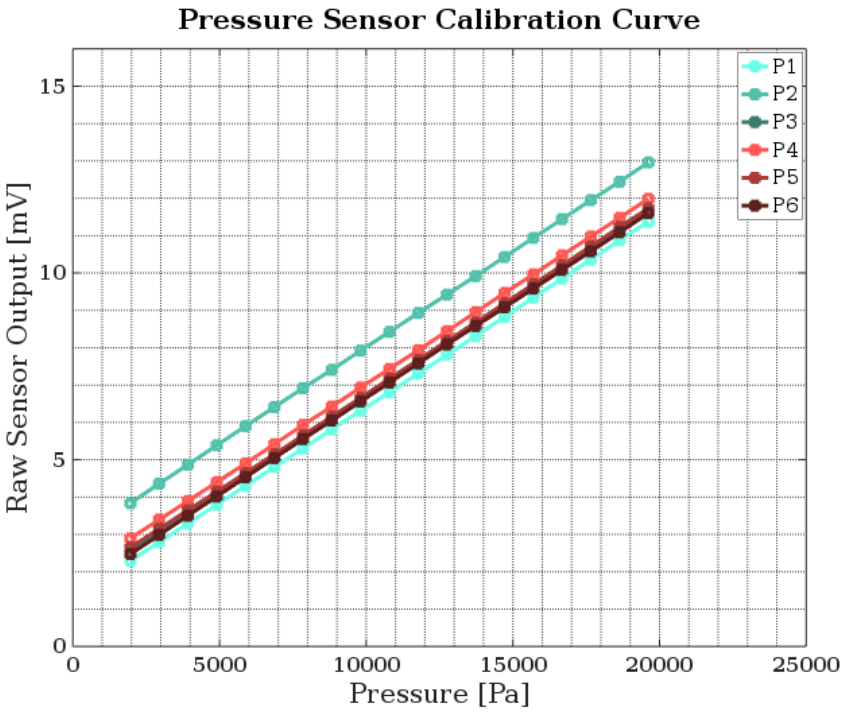

Figure 21: Pressure Sensor Calibration Curve - Calibration #1

3.5.4 Pressure Sensor Repeatability

The calibration coefficient for each subsequent calibration test was compared to the previous tests; the relative error between the tests was then calculated. The resulting calibration coefficients, and respective errors between calibrations are summarized in Table 7.

The results showed that between calibrations, the sensitivity (calibration coefficient) for each sensor changed ≤ 1.05%. One can observe the repeatability of the pressure sensor's performance in Figure 22 and Figure 23; it can be seen that the zero-value of each sensor appeared to shift slightly from day-to-day.

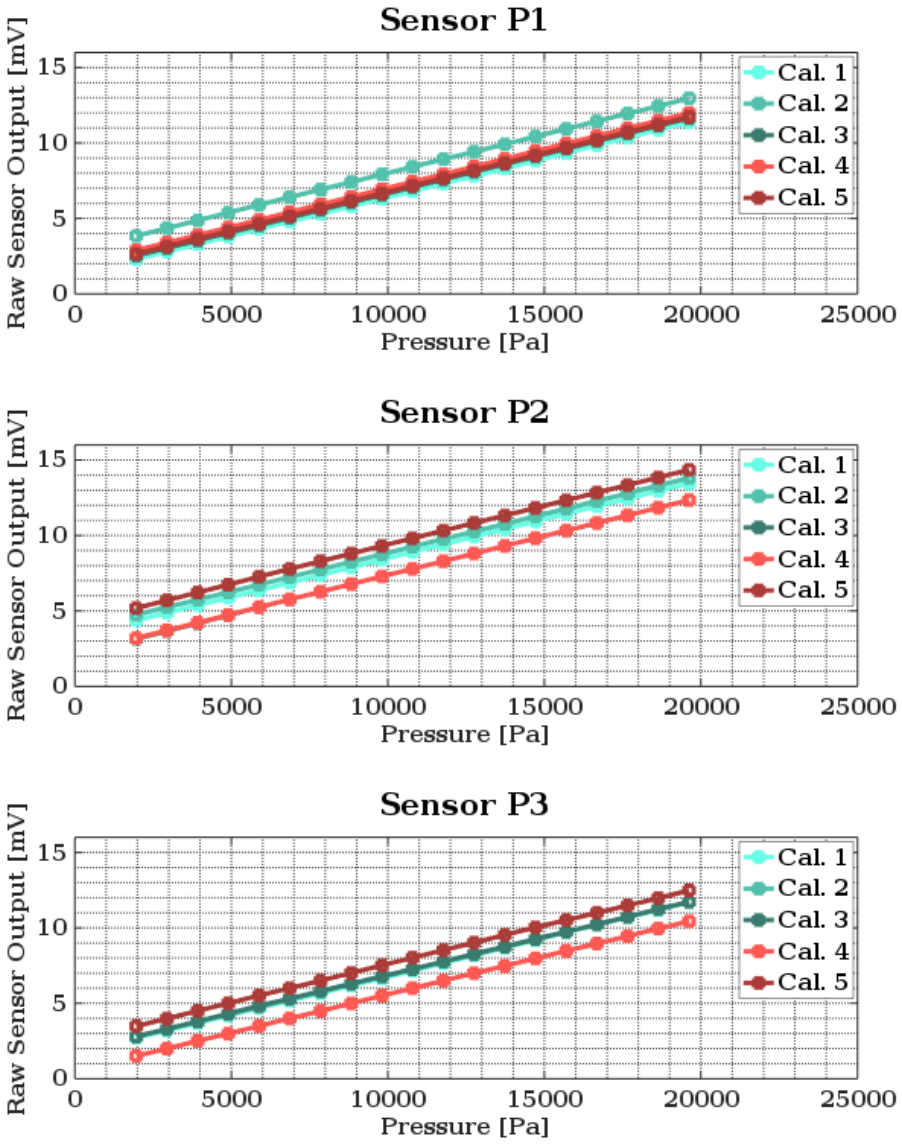

Figure 22: Pressure Sensor Repeatability Testing: Sensors P1, P2, P3 (Front of Unit)

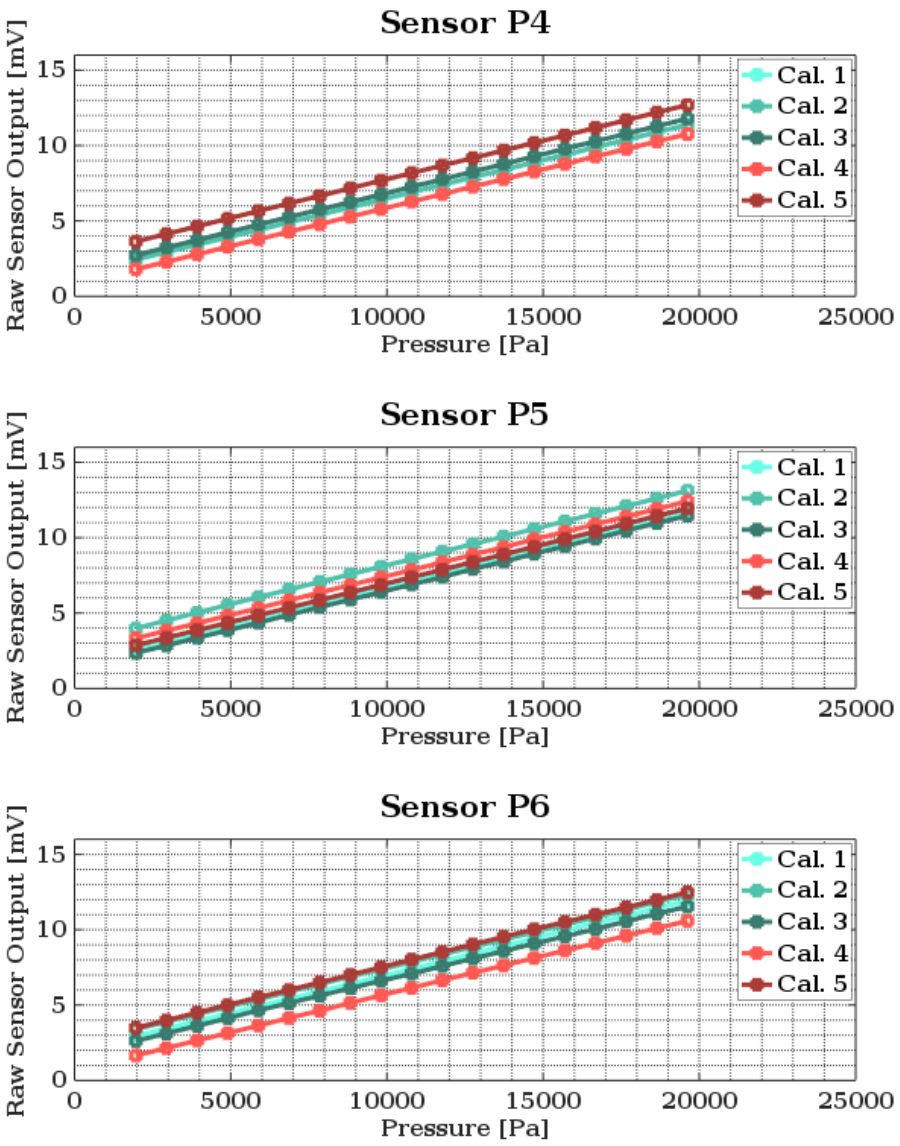

Figure 23: Pressure Sensor Repeatability Testing: Sensors P4, P5, P6 (Back of Unit)

3.5.5 Non-linearity

The results of the calibration tests showed that the instrumented Core-Loc unit had an acceptable degree of non-linearity, with an average value of 8.47E-3 % of the full-scale reading (FS). Each sensor appeared to show a slight "saggy" shape in which the end points aligned with the theoretical curve, but the data points in between were slightly lower. This effect is illustrated in Figure 24.

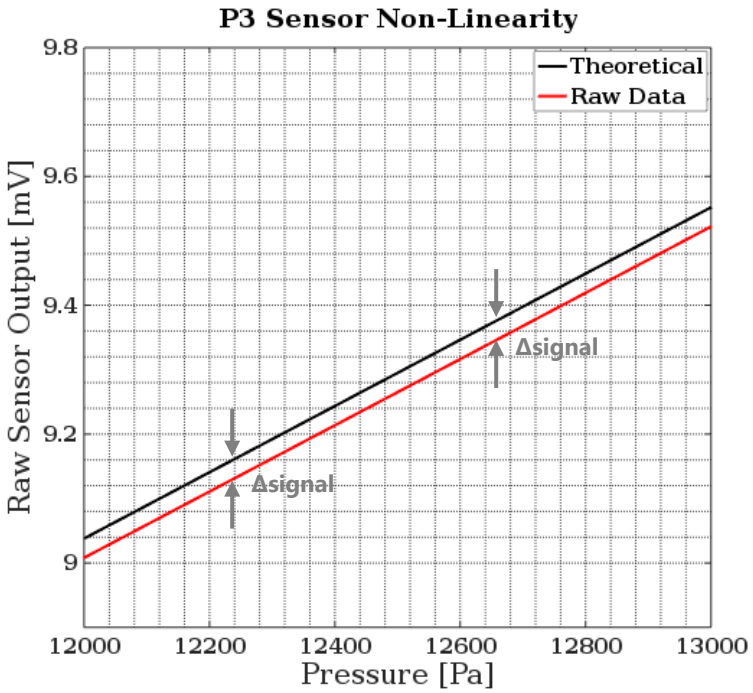

Figure 24: Pressure Sensor P3 Non-linearity Results

This effect is known as non-linearity. The non-linearity is the maximum deviation from the theoretical straight line represented by the calibration coefficient. This maximum deviation is then divided by the full-scale output of the pressure sensor and the error is represented as percentage of full-scale. The complete list of calculated non-linearity values for each sensor, and each calibration test is tabulated in Table 9.

Table 9: Instrumented Core-Loc Unit Pressure Sensor Non-Linearity

Test	P1 (% FS)	P2 (% FS)	P3 (% FS)	P4 (% FS)	P5 (% FS)	P6 (% FS)
Calibration #1	1.51E-02	5.83E-02	3.49E-03	7.30E-02	3.58E-02	2.48E-02
Calibration #2	1.45E-03	1.25E-03	7.62E-04	7.16E-04	9.27E-04	9.20E-04
Calibration #3	1.24E-03	1.39E-03	2.49E-03	1.25E-03	2.81E-03	7.36E-03
Calibration #4	1.81E-03	2.05E-03	1.09E-03	9.54E-04	1.46E-03	2.04E-03
Calibration #5	2.55E-03	1.19E-03	2.52E-03	1.56E-03	2.12E-03	1.79E-03
Mean	4.43E-03	1.28E-02	2.07E-03	1.55E-02	8.62E-03	7.39E-03

3.5.6 Noise

Due to imperfections in the circuit soldering and unit construction, as well as the influence of ambient electromagnetic noise, the pressure sensors experience a small level of signal noise that must be accounted for when considering the sensors' accuracy. An example time history of this signal noise, while kept at constant atmospheric pressure, is shown in Figure 25.

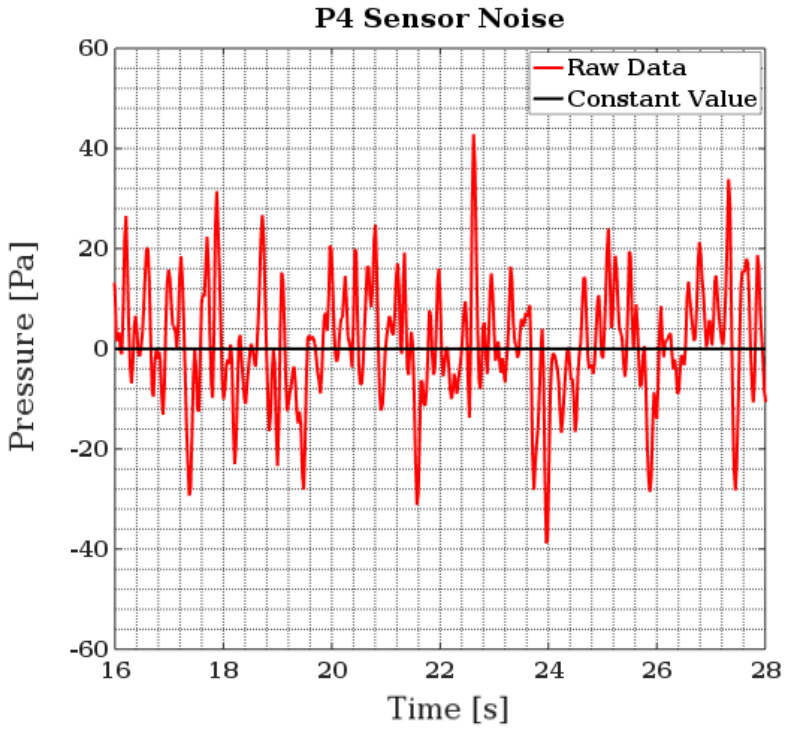

Figure 25: Pressure Sensor P4 Noise in Atmospheric Pressure Condition

In order to characterize the noise of the output signals, spectral analysis was used. A fast-fourier-transform (FFT) was applied to each output signal using the Cooley-Tukey algorithm. The FFT is a method of decomposing a signal into its' frequency components. The FFT describes the distribution of signal power and frequency components that compose the original time history. More simply, it tells one the magnitude and frequencies of waves that compose a noisy signal.

This method, then, was used in to identify the frequency and magnitude of the noise in the sensor output signal. Luckily, the noise in each of the pressure sensors was highly concentrated around a single frequency, and was easily identifiable. The average values from all rounds of calibration testing are summarized in Table 10:

Table 10: Instrumented Core-Loc Unit Error Due to Noise

Sensor	P1	P2	P3	P4	P5	P6
Frequency (Hz)	6.00E+00	6.00E+00	6.00E+00	6.00E+00	6.00E+00	6.00E+00
Amplitude (mV)	2.26E-02	1.77E-02	1.59E-02	1.53E-02	2.38E-02	2.20E-02
Error (% FS)	4.41E-03	3.46E-03	3.10E-03	2.98E-03	4.65E-03	4.29E-03

A combination of a low-pass and high-pass filters were used to ensure this specific band of frequencies was subtracted from the raw data. This filter removed frequencies in the range of 4-8 Hz to account for minor deviations. A comparison between the raw signal and filtered signal of Pressure Sensor P3 can be seen in Figure 26. It is clear that the filtering process was able to remove the static noise to an acceptable degree, while also acceptably preserving peaks in the data.

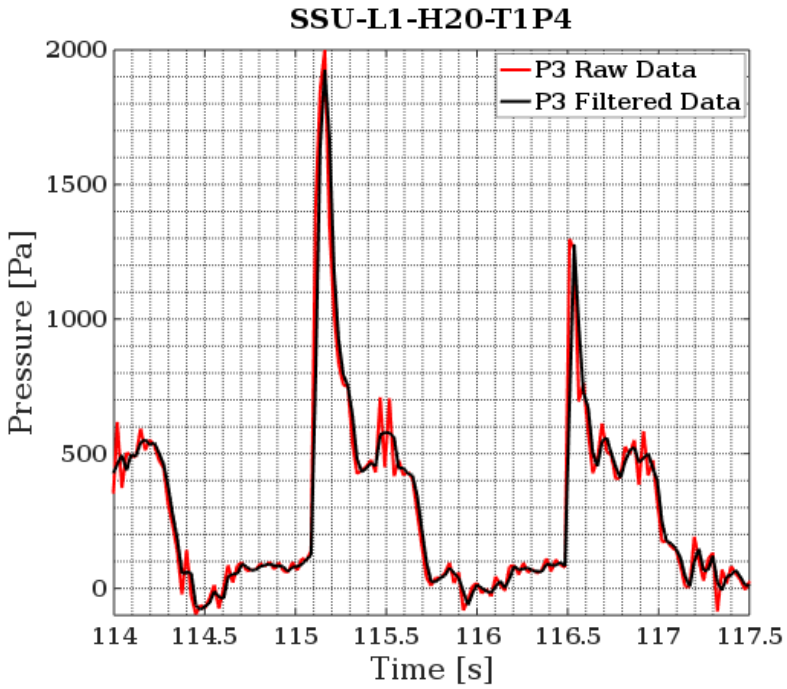

Figure 26: Comparison between Raw and Filtered P3 Pressure Data for Example Wave Signal

3.5.7 Hysteresis

The hysteresis characteristics of the pressure sensors were determined by comparing the deviation between recorded output signals at identical depths, during loading in both positive and negative directions. The maximum value of each cycle was chosen for each sensor to be representative of the maximum error due to this effect. As can be seen in

Figure 26, the instrumented Core-Loc unit performed quite well in this regard; Pressure Sensor P5 had the least desirable performance with a maximum error of 0.63% FS.

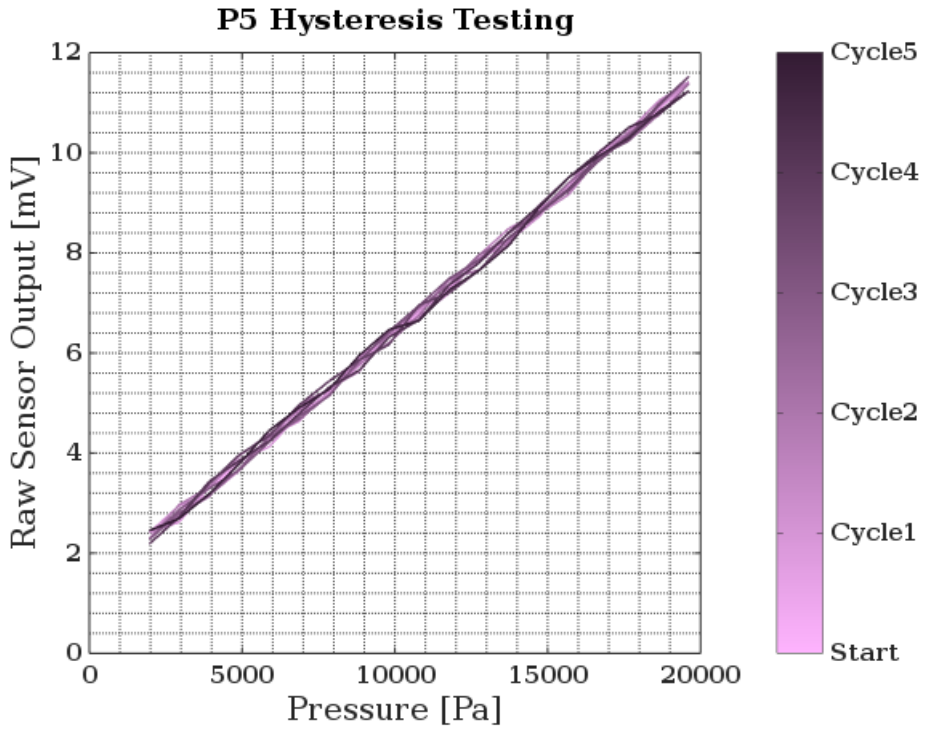

Figure 27: Instrumented Core-Loc Unit Sensor P5 Hysteresis Results

The full summary of hysteresis results for each pressure sensor is tabulated in Table 11:

Table 11: Instrumented Core-Loc Unit Pressure Sensor Hysteresis

Cycle	P1 (% FS)	P2 (% FS)	P3 (% FS)	P4 (% FS)	P5 (% FS)	P6 (% FS)
1	5.38E-01	3.90E-01	4.28E-01	2.96E-01	5.99E-01	6.04E-01
2	6.29E-01	4.49E-01	5.15E-01	2.99E-01	6.57E-01	6.26E-01
3	6.19E-01	4.73E-01	5.20E-01	3.73E-01	6.30E-01	6.21E-01
4	5.70E-01	4.61E-01	5.04E-01	3.44E-01	6.75E-01	6.08E-01
5	6.34E-01	4.77E-01	5.04E-01	3.19E-01	6.03E-01	7.03E-01
Mean	5.98E-01	4.50E-01	4.95E-01	3.26E-01	6.32E-01	6.33E-01

3.5.8 Zero Drift

From the results of the repeatability tests, it was apparent that the zero value of the pressure sensors required consideration. This is the initial raw signal value in atmospheric pressure conditions; the value of this signal appeared to change randomly from day-to-day within the range of approximately +/-1.2 mV. With the favourable results of the repeatability testing considered, the results showed that the unit could be accurately utilized with a periodic calibration, and daily zeroing of the atmospheric value.

3.5.9 Resolution

The resolution of the instrumented Core-Loc unit's pressure sensors is directly dictated by the parameters of the ADC. In practice, the resolution is a function of the maximum amount of available digital values to store the analog signal. Thus, it is also affected by the zero-drift. The resolution was simply calculated using Equation 40:

$$Resolution = \frac{Max\ Pressure}{2^{15} - ADC_{zero}} \tag{40}$$

On average, this value was between 1.1-1.3 Pa for each pressure sensor. Thus, readings with the instrumented Core-Loc unit could be taken at a very high resolution.

3.5.10 Technical Specifications Summary

Listed in Table 12 are the resulting aforementioned technical specifications from the instrumented Core-Loc unit, averaged from all calibration data.

Table 12: Instrumented Core-Loc Unit Technical Specifications

Recommended Input Voltage	1.5 – 12.0 VdC
Recommended Input Current	0.6 – 1.0 mA
Operating Temperature Range	0 – 50 °C
Operating Pressure Range	0 – 27,000 Pa
Sampling Rates	40, 46, 53, 64, 80, 107, 160, 320 Hz

Sensor	P1	P2	P3	P4	P5	P6
Sensitivity (mV/Pa)	5.12E-04	5.13E-04	5.17E-04	5.13E-04	5.14E-04	5.09E-04
Non-Linearity (% FS)	4.43E-03	1.28E-02	2.07E-03	1.55E-02	8.62E-03	7.39E-03
Noise (% FS)	4.41E-03	3.46E-03	3.10E-03	2.98E-03	4.65E-03	4.29E-03
Hysteresis (% FS)	5.98E-01	4.50E-01	4.95E-01	3.26E-01	6.32E-01	6.33E-01
Total Error (% FS)	6.07E-01	4.67E-01	5.01E-01	3.45E-01	6.46E-01	6.45E-01

3.6 Discussion

As described previously, the instrumented Core-Loc unit was 3D printed and assembled at the UOttawa MakerSpace. The assembled circuit was essentially contained within a hollow cavity in the unit that was injected with marine grade silicone, and the unit sealed with the same material.

This approach lead to a very small hollow volume within the unit, that was required to house all instrumentation and wiring. Without designed housing for the circuit, this result in a large amount of excess wire and somewhat randomly placed instrumentation inside the unit. The chaotic nature of the circuit inside the unit likely led to small noise and interference issues that were detected during the calibration process. Having proper housing and installation locations for the wiring and instrumentation would decrease these negative effects, improve the aesthetics of the circuitry, and also provide additional room that may be used for additional instrumentation.

The roughness of the surface resulting from the 3D printing process, the sealing procedure, and subsequent painting of the instrumented unit induced surface roughness on the unit that was not under stringent control. It was difficult to maintain and smooth and uniform surface across the unit due to the combination of these reasons.

The current design of the instrumented unit does not allow for access, or repair of any instrumentation or wiring. Thus, stakes are high to ensure construction is done correctly. In addition, pressure sensors are mounted flush with the surface of the unit, leaving them very susceptible to damage from handling, or even contact from other armour units. A possible recessing into the unit's surface, or some kind of protection measure may be a good idea to ensure testing with entire armour layers does not result in sensor damage.

As can be seen from the results of the calibration testing, each of the 6 sensors embedded in the instrumented Core-Loc unit performed very favourably.

The initial submergence testing and maximum operating pressure of the unit proved to be excellent for typical experimental testing purposes. With the ability to operate without noticeable error for periods up to at least 48 hours, and a maximum operating pressure of 27000 Pa, the unit proved to be adequate for the conditions expected in testing described in future sections of this thesis.

The pressure sensors are capable of operating at a range between 40-320 Hz. With each of the 6 sensors operating simultaneously, a sampling frequency of 53 Hz can be achieved. This is acceptable for typical experimental testing, and can be increased to capture peak pressure values on an individual sensor basis if necessary.

As expected from the manufacturer specifications, each of the pressure sensors operated with near identical sensitivity. The repeatability of the pressure sensors' sensitivity was assessed through 5 identical calibrations on subsequent days. The sensitivity of the pressure sensors changed $\leq 1.05\%$ between calibrations and were able to capture pressure fluctuations at a resolution of approximately 1.2 Pa, on average.

Electromagnetic and ambient noise was isolated from the raw pressure sensor signals. Spectral analysis showed that each pressure sensor displayed nearly identical noise in each respective signal, with an approximate frequency of 6 Hz and magnitude of approximately 30 Pa. Once filtered via a Butterworth filter, the resulting signal was able to maintain the overall behaviour of the raw signal, while being noticeably smoother and preserving peak values.

Ambient conditions also appeared to affect the zero-drift properties of the pressure sensors. During subsequent calibrations, it was apparent that the zero value of the pressure sensors appeared to drift randomly from day-to-day. Although this is a concern, periodically re-calibrating the unit, and re-zeroing the unit before each use can easily account for this.

The hysteresis properties of the pressure sensors were determined via a modified calibration procedure. This portion of the testing showed that the recorded raw values from each pressure sensor varied slightly for a given depth, depending on the direction of loading. Each sensor performed very well, and was able to maintain a high level of accuracy for both loading directions. On average, the error due to hysteresis experienced in each pressure sensor was in the range of 0.52 % FS.

Overall, the performance of each pressure sensor in the instrumented Core-Loc unit was favourable for use in experimental testing. Each pressure sensor is capable of reading pressures up to 27000 Pa, with an average precision of 0.54% FS.

As discussed previously, there have been numerous attempts to quantify the forces, accelerations and stresses induced on armour units during wave conditions. No approach, however, has been able to quantify the pressure distribution on the face of the unit with this degree of accuracy. The capabilities of this instrumented unit can provide insight into the complex and highly transient hydrodynamic interaction of armour units. The data that can be provided from this unit could be instrumental in the validation and development of numerical models capable of accurately simulating rubble mound breakwaters.

The results of this portion of the current study also prove the feasibility of using widely available, low cost instrumentation for measurement in a coastal engineering application. The sensors, instrumentation, and Raspberry Pi 3 used to construct this prototype totalled less than $200, this price per unit will also reduce with quantity.

The instrumentation used in the current study is typically used for cell phones, and robotics; these instruments have easy to follow documentation and interfacing capabilities. Similar instruments with accuracy and size that are favourable for experimental testing also exist. Hofland et al. (2018) showed that unit could also be instrumented with gyroscopes and accelerometers.

This study, along with other similar endeavours, will hopefully one day lead to fully instrumented wireless concrete units. These units will be concrete, easily constructed,

low-cost, fully wireless, and instrumented to collect a wide range of real-time data including: strain, pressure, acceleration, rotation, temperature, etc.

This advancement in the paradigm of breakwater testing would be able to advance the force-balance design approach necessary to adequately quantify unit stability.

3.7 Summary and Conclusions

The current study, along with previous similar research has proven the ability of relatively low-tech, low cost, widely available instrumentation to perform in a coastal engineering setting. The results of the current study, along with similar research, will hopefully lead to fully wireless and fully instrumented CAUs used to collect data in experimental testing as well as prototype monitoring.

The results of the experimental study are concluded as follows:

- The 0.12 m instrumented Core-Loc unit was 3D printed using PLA plastic at the UOttawa Makerspace in two halves.
- The unit was outfitted with 6 pressure sensors in key unique locations across the unit's surface. The wiring was housed within a hollow chamber inside the unit, and was injected and sealed with marine grade silicone.
- The small amount of room, and lack of separation of the wiring may have contributed to the ambient electromagnetic noise experienced in the sensor signals.
- Proper planning of the wiring inside the unit may have opened space to accommodate additional sensors, and reduce noise.
- The performance of the 6 sensors embedded in the instrumented Core-Loc unit showed that the sensors were able to capture pressures at a very high resolution (≈1.2 Pa) at 8 defined frequencies between 40-320 Hz.
- The sensitivity between sensors deviated by ≤1%, while the sensitivity for each individual sensor changed by ≤1.05% from each subsequent calibration.
- Each pressure sensor was determined to be capable of measuring pressures from 0-27000 Pa, with an average precision of 0.54% FS. This is subject to change based on the gain factor.
- The novel data set produced from this unit can be used to validate numerical models, provide insight into the hydrodynamic interaction of armour units, and provide the basis of a force-balance design approach.

4.0 Experimental Study - Sloped Single Unit (SSU) Tests

4.1 Description of Study

This experimental portion of the current study was performed as part of the larger research project mentioned in the preface of this thesis document. The objective of this portion of the current study was to evaluate the performance of the instrumented Core-Loc unit in a flume environment, and to assess its' measurement capabilities in wave conditions. A slope and adjustable mounting system was constructed to perform a comprehensive wave testing program. This was done to record forces and pressures acting on the instrumented Core-Loc unit during a wide range of wave conditions, at different locations along the breakwater slope.

4.2 Experimental Setup

This experimental study was performed at NRC-OCRE in Ottawa, ON. All experimental tests were performed in the Steel Wave Flume (SWF), a 60 m x 1.22 m x 1.22 m steel flume equipped with wave generators at each end, with active wave absorption capabilities. Previous foreshore bathymetry of 3% was utilized for the purpose of these experiments. At a distance of 38.7m from the wave generator, the bathymetry was removed in a rectangular shape to accommodate the installation of a slope frame. The flume and bathymetry is depicted in Figure 28.

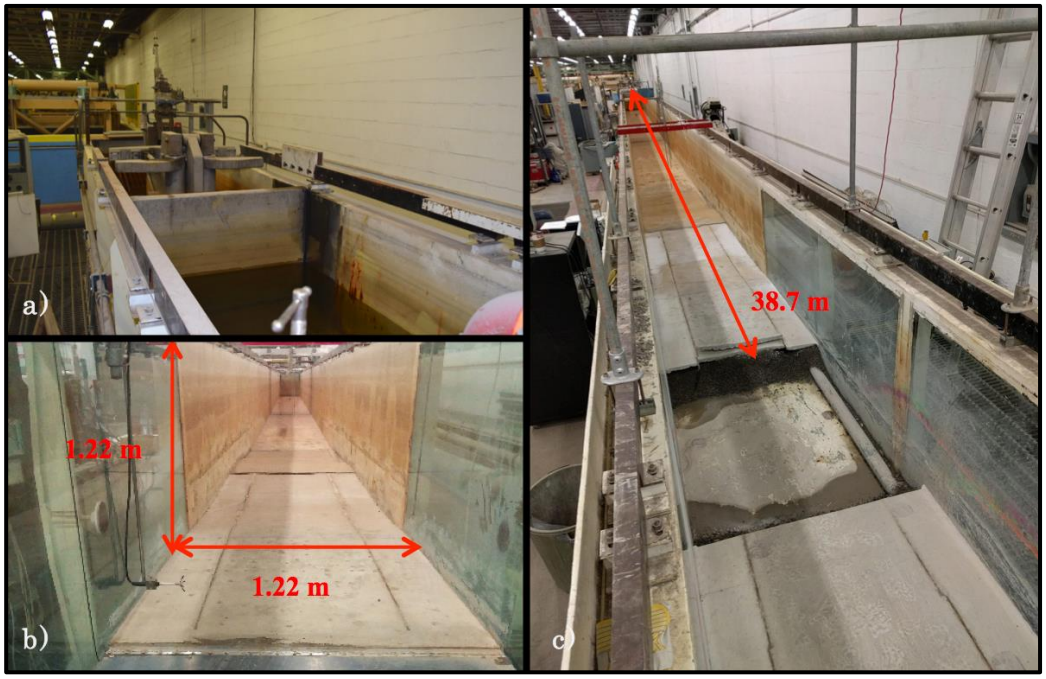

Figure 28: The NRC-OCRE Steel Wave Flume (SWF): a) Wave Maker, b) Cross-Section, c) Bathymetry and Slope Construction

A slope structure was constructed using a 15 mm thick PVC board, and 50 mm x 50 mm stainless steel hollow-square-sections as a frame. The base of the adjustable slope was designed to align with the existing toe elevation of the utilized bathymetry. This slope structure was constructed in two parts: a bottom frame, and a slope frame; these were then attached using a hinge. This gave the final design both rigidity and variability of slope. The final slope structure, in a flat position, is shown in Figure 29:

Figure 29: Constructed Adjustable Slope Frame for SSU Tests, shown in Horizontal Position

At the desired armour unit testing locations, holes were drilled through the PVC board. The frame of the slope was designed such that at these chosen testing locations, frame members were available to mount the force transducer. The force transducer was mounted to the frame on a small rectangular section of scrap PVC board as shown in Figure 30.

Atop the force transducer, a specially machined unit mount was placed; this was machined in the UOttawa Mechanical Engineering Laboratory. This mount allowed a rigid connection to the force transducer, while allowing a 1/4" threaded rod to be placed in its' centre cavity, having the capability of variable rod heights via two set screws.

The instrumented Core-Loc unit then screwed onto this rod, using the embedded coupling nuts described in Section 3. This mounting system also included a sealing precaution to ensure complete water-tightness around the drilled hole; i.e no transfer of water between sides of the slope. This arrangement is shown in Figure 30.

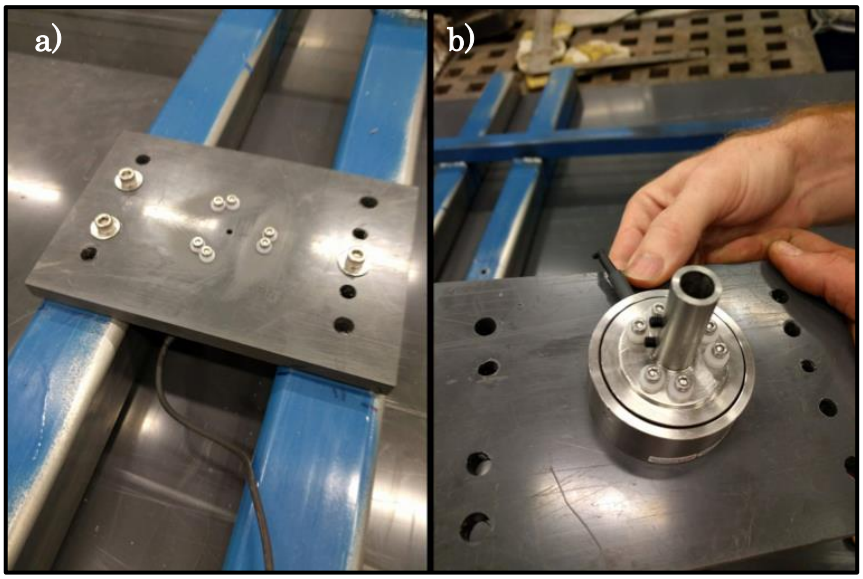

Figure 30: a) Force Transducer Mounting Arrangement under Slope Frame, b) Force Transducer and Machined Mount

Additional to this, a small, adjustable, removable frame was designed and constructed to allow for the placement of the instrumented unit at any location along the breakwater slope and across the flume, if so desired. This adjustable frame system is illustrated in Figure 31.

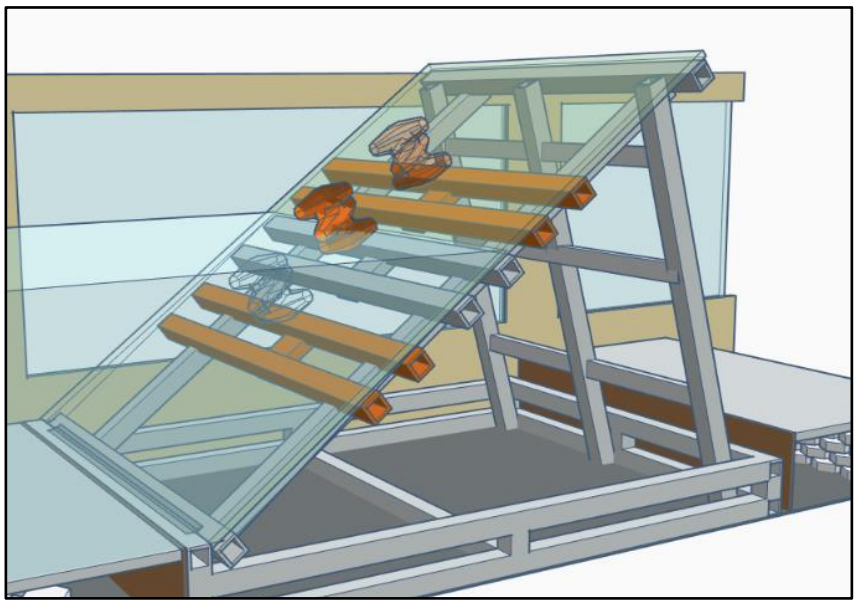

Figure 31: Rendering of Slope Frame and Adjustable Unit Mounting Frame (Orange)

This slope was then placed into the rectangular section cut from the existing bathymetry, shown in Figure 28c. The frame was supported at the desired 4H:3V slope using support frames. One support frame was placed at the mid-section of the slope, the other at the end of the slope. To ensure vibration of the slope was not induced, small wooden wedges were hammered into any potentially risky areas. Wooden struts were also directly fixed to the bottom of the PVC board, to increase the rigidity of the frame. Additionally, the slope was forced down and fixed in place via clamps and struts to ensure no uplift of the breakwater slope.

The periphery of the PVC board was sealed using off the shelf spray foam insulation, which provided a fully waterproof seal around the slope. Finally, an array of lights, and a white plastic background were installed for image processing purposes. The final slope and unit setup is shown in Figure 32:

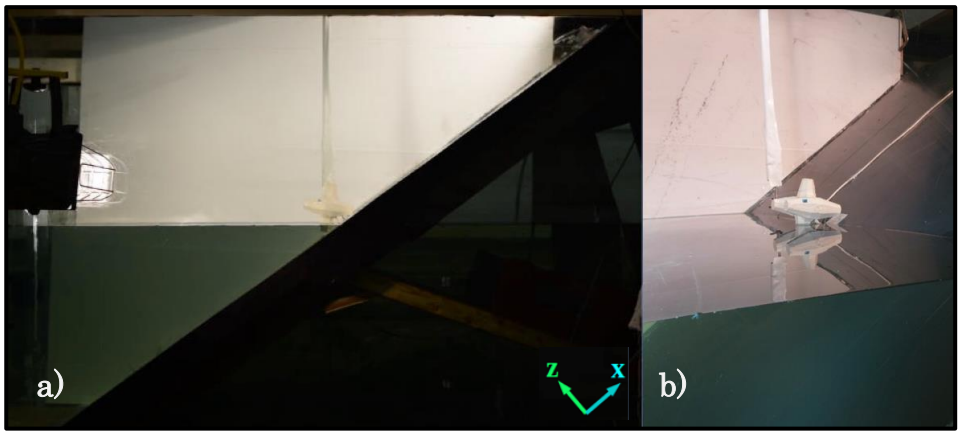

Figure 32: Final SSU Test Setup: a) Side View, b) 3D View

4.3 Instrumentation

The instrumented Core-Loc armour unit, described in Section 3, was the key piece of instrumentation in this portion of the current study. The unit was mounted on a force transducer, and controlled via the Raspberry Pi 3 to collect pressure at each of the 6 sensor locations during testing. As detailed in the unit's capabilities in Section 3.0, the unit's 6 pressure sensors collected data at a frequency of ≈ 53 Hz. This allowed for measurement of the pressure distribution across a units' surface during the complex hydrodynamic process associated with wave action.

All instrumentation, excluding the instrumented Core-Loc unit, was controlled and powered via NDAQ; a data acquisition system and interface developed and utilized at NRC-OCRE. All of the following instrumentation was sampled simultaneously at 50 Hz.

A six degree-of-freedom (6-DOF) force transducer, model ATI Mini45 IP68, was used as the force transducer. This force transducer, pictured in Figure 30, measured time histories of the hydrodynamic interaction between waves and the instrumented Core-Loc

unit. This transducer is IP68 rated, meaning it can maintain its' accuracy during the long periods of shallow water immersion encountered in this study.

Capacitance type wave gauges (WGs) were installed at 6 locations along the flume. Of these 6 locations, 5 WGs were included in a 5-probe array offshore of the existing bathymetry. This 5-probe array allowed for decomposition of superimposed incident and reflected waves to determine reflection properties of the breakwater slope. The remaining wave gauge was installed 1 m from the slope toe, to measure incident conditions at the breakwater slope. A schematic of the WG locations are shown in Figure 33, and summarized in Table 13.

A Nortek velocity sensor (ADV) was used to measure fluid velocities near the instrumented Core-Loc unit. This instrument calculates velocity by emitting acoustic frequencies that backscatter off tracer particles; the doppler shift indicates the particle velocity. This was placed in line with the centroid of the instrumented unit, one characteristic length away, C = 0.12m. This 3-axis current meter was calibrated to a maximum of 2.5 m/s (by NRC staff), has a 6mm sampling volume diameter, and samples 3-axes of velocity 5cm from the probe location. Thus, the sensor was positioned to sample the fluid velocity 0.07m from the edge of the instrumented Core-Loc unit.

4.4 Images and Videos

For the purposes of image processing, each test was recorded via a Nikon D5300 18-55 DSLR camera. This camera records videos at 30 frames per second, with a resolution of 1920x1080 pixels.

At all times during testing this camera was aligned with the centroid of the instrumented Core-Loc unit, mounted on a tripod facing perpendicular to the flume viewing window. This ensured minimal depth distortion of the water surface around the unit location.

An additional second camera, model Canon EOS T3i 18-55mm, was also mounted atop the frame supporting WG6. This provided the option of periodic aerial images or videos of the instrumented Core-Loc unit during testing.

A schematic of the entire flume layout, along with WGs, ADV, and unit locations during all rounds of testing can be seen in Figures 33 and 34. This data is also summarized in Table 13.

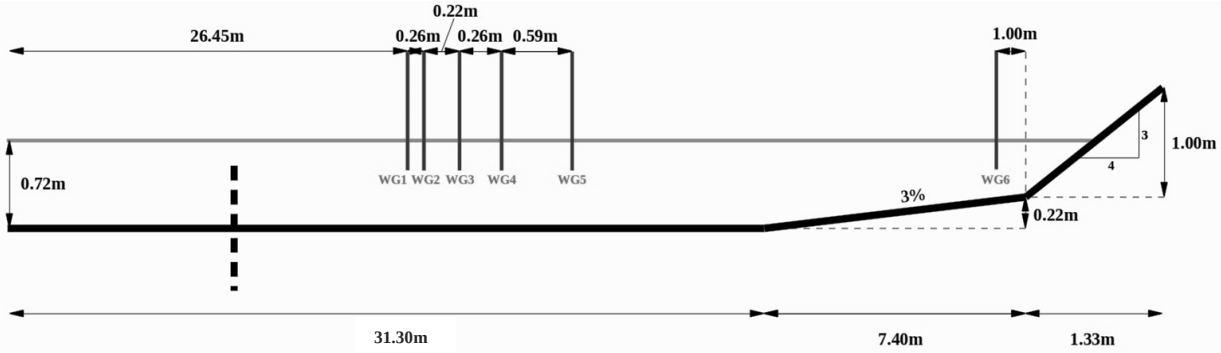

Figure 33: Schematic of SWF Setup and Wave Gauge Locations

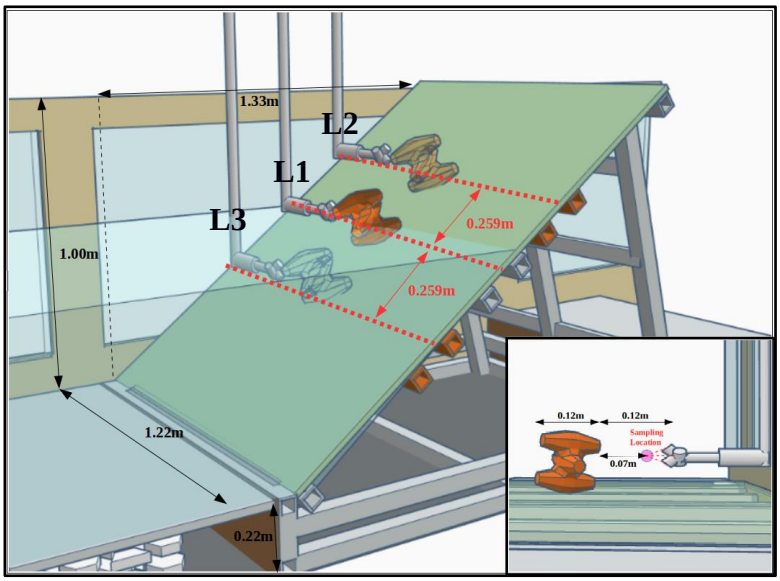

Figure 34: Schematic of SSU Test Slope, and Unit Testing Locations (L1, L2, L3)

The parameters of the experimental testing set-up is summarized in Table 13:

Table 13: Experimental Setup Parameter Summary

Offshore Length [m]	31.30					
Foreshore Length [m]	7.40					
Foreshore Slope	3%					
Deep Water Depth [m]	0.72					
Toe Water Depth [m]	0.5					
Breakwater Slope	4H : 3V					
Wave Gauge	**WG1**	**WG2**	**WG3**	**WG4**	**WG5**	**WG6**
WG Location [m]	26.45	26.71	26.93	27.19	27.78	37.70
Unit Location No.	**L1**		**L2**		**L3**	
Unit Testing Location [m] (4 rows based on $N_q = 0.62$)	SWL		SWL + 0.259		SWL – 0.259	

4.5 Testing Conditions

Each round of testing was identical and repeated for all locations (L1, L2, and L3; shown in Figure 33). The unit orientation was kept constant (Figure 32); this is not the most critical unit orientation but is very common and considered representative according to the placement guidelines. The effect of unit orientation was explored in previous phases of the research program.. The range of wave conditions chosen were based on the capabilities of the wave-maker, the reflection properties of the breakwater slope, and to achieve a wide range of wave breaker types. The complete set of testing conditions are summarized in Table 14:

From this point, the wave tests will be referred to using the following code:

Regular Waves: SSU_L1_H12_T1P4 = Location 1, H = 0.12 m, T = 1.4 s.

Irregular Waves: SSU_L2_Hs15_Tp1P4 = Location 2, H_{m0} = 0.15 m, T_p = 1.4 s.

Table 14: Summary of SSU Testing Wave Conditions

Test ID (x=1,2,3)	Wave Type	H [m]	T [s]	H_{m0} [m]	T_p [s]	ξ_0	Duration [s]
SSU_Lx_H12_T1P4	Regular	0.12	1.40	-	-	3.78	210
SSU_Lx_H12_T1P8	Regular	0.12	1.80	-	-	4.87	210
SSU_Lx_H12_T2P2	Regular	0.12	2.20	-	-	5.95	210
SSU_Lx_H12_T2P6	Regular	0.12	2.60	-	-	7.03	210
SSU_Lx_H12_T3P0	Regular	0.12	3.00	-	-	8.11	210
SSU_Lx_H15_T1P4	Regular	0.15	1.40	-	-	3.38	210
SSU_Lx_H15_T1P8	Regular	0.15	1.80	-	-	4.35	210
SSU_Lx_H15_T2P0	Regular	0.15	2.00	-	-	4.83	210
SSU_Lx_H15_T2P4	Regular	0.15	2.40	-	-	5.80	210
SSU_Lx_H15_T2P8	Regular	0.15	2.80	-	-	6.77	210
SSU_Lx_H15_T3P2	Regular	0.15	3.20	-	-	7.74	210
SSU_Lx_H15_T3P8	Regular	0.15	3.80	-	-	9.19	210
SSU_Lx_H20_T1P4	Regular	0.20	1.40	-	-	2.93	210
SSU_Lx_H20_T2P0	Regular	0.20	2.00	-	-	4.19	210
SSU_Lx_Hs15_Tp1P2	Irregular	-	-	0.15	1.20	2.90	900
SSU_Lx_Hs15_Tp1P8	Irregular	-	-	0.15	1.80	4.35	900
SSU_Lx_Hs15_Tp2P2	Irregular	-	-	0.15	2.20	5.32	900
SSU_Lx_Hs15_Tp2P6	Irregular	-	-	0.15	2.60	6.29	900

In total, 14 regular wave conditions were chosen, with an additional 4 irregular wave conditions. Regular wave tests were conducted for 210s, and irregular wave tests for 900s. The irregular wave signals were generated according to a JONSWAP spectrum, with the following parameters:

$$\alpha = 0.36$$

$$\Upsilon = 3.30$$

$$S(\omega) = \frac{\alpha g^2}{\omega^5} \exp\left[-\beta \frac{\omega_p^4}{\omega^4}\right] \gamma^a \qquad \beta = 1.25$$

$$\sigma = \begin{cases} 0.7 & \omega \leq \omega_p \\ 0.9 & \omega > \omega_p \end{cases}$$

This choice of wave conditions allowed variation of wave period, while maintaining constant wave heights of 0.12m, 0.15m and 0.20m. This also allowed for a wide range of Irribaren numbers, or wave breaking characteristics. Examples of the wide range of regular wave breaking characteristics tested are shown in Figure 35:

Figure 35: Range of Regular Wave Breaking Characteristics: a) SSU_L1_H20_T1P4 (plunging), b) SSU_L1_H15_T1P4 (collapsing), c) SSU_L1_H12_T3P0 (surging)

As would be expected, the irregular wave conditions behaved rather unpredictably. The interaction between the irregular waves with the steep slope led to a wide range of wave breaking characteristics. Examples of the wide range of conditions that were encountered in each irregular wave test are shown in Figure 36.

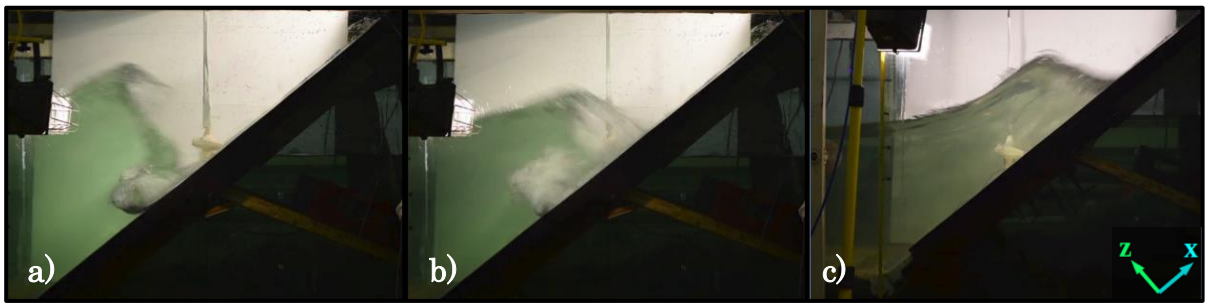

Figure 36: Example of Irregular Wave Breaking Characteristics - a) SSU_L1_Hs15_T1P2 b) SSU_L1_Hs15_T1P2, c) SSU_L3_Hs15_T1P8

4.6 Test Procedure

All instrumentation, with the exception of the ADV, was re-calibrated every morning before testing occurred. The instrumented Core-Loc unit was re-calibrated in a smaller version of the drop-tank, using the same calibration procedure outlined in Section 3.0.

The instrumented Core-Loc unit must be installed in position before testing can commence; this requires draining of the flume. This allows access to the underside of the slope frame and the setscrews on the force transducer unit mount. Once the unit is installed at any of the three locations, it remains stationary for each respective set of wave conditions. Figure 37 shows the unit being installed at the L1 location.

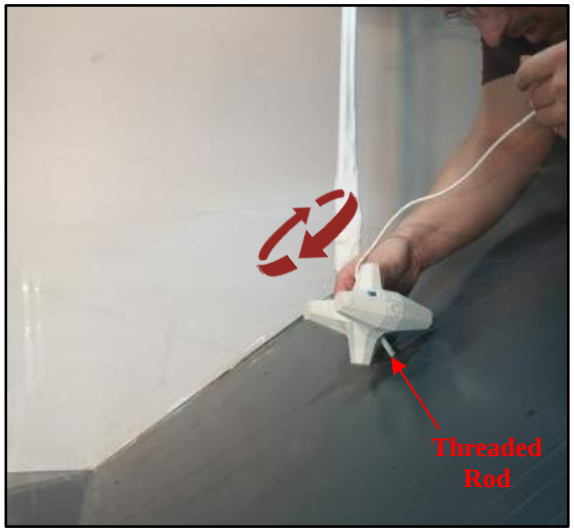

Figure 37: Installation of Unit at L1 Location via Threaded Rod

Due to the fact that the instrumented Core-Loc unit operates on its' own independent data acquisition system, a simple script was developed to activate both the Raspberry Pi 3 and the NDAQ system near-simultaneously. The intent was to reduce interpolation errors when the datasets are subsequently merged. The wave generation system was also directly controlled via the NDAQ system. Thus, the activation of all instrumentation, and wave generators, are completed in one simple step.

The generation of waves, and acquisition of data runs for a user-defined period of time; thus, the tests end automatically. As previously mentioned, regular monochromatic wave signals were generated for 210s, while the irregular signals ran for 900s.

With the unit in place, each test in the experimental program was conducted according to the following testing procedure:

1. Fill the flume to an offshore water depth of 0.72m using intake and smaller municipal tap for precision.

2. Wait approximately 120s, or until flume water surface fluctuations stop.

3. Load wave generation drive signal to NDAQ system.

4. Start wave generator, and data acquisition systems.

5. Run experiment until automatic stop at user-defined time limit.

The software developed for both the NRC-OCRE NDAQ system, and for the instrumented Core-Loc unit, utilized this procedure to output easily readable .csv files for all instrumentation results. This includes WG1-6, the ADV, 6 pressure sensors, and the 6-axis force transducer.

4.7 Image Processing

4.7.1 Description

A Nikon D5300 18-55mm DSLR camera was used to film every test. The resulting videos were then used for image processing purposes. The goal of the image processing was to develop a script capable of reading the raw video input, and delineating the water surface profile at the breakwater. Once the water surface is delineated, the submerged and un-submerged portions of the unit can be determined by slicing the unit with the delineated surface. This image processing technique allows for the determination of the buoyant force, and thus, separation of the total and hydrodynamic forces acting on the instrumented Core-Loc unit during testing. This was achieved by coupling MATLAB's Image Processing Toolbox, and Python's VTK Module into one larger script.

4.7.2 Setup

A white plastic background was installed on the flume wall opposite to the viewing window; this had the intent of blending in with the painted white unit. For each location of the experimental testing, the camera was positioned and calibrated to have the center pixel of the image at the centroid of the instrumented Core-Loc unit. This ensured minimal depth-distortion around the unit, and increased the accuracy of the water surface delineation at the unit location. Additionally, an array of lighting was installed to increase the contrast between the unit and the rest of the objects in the image (namely the water). Reflective tape was also placed beneath the unit, to decrease shadows in areas that the lighting could not reach due to poor reflectivity of the PVC slope. Lastly, a second camera was mounted alongside WG6 with its' orientation aimed at the unit and perpendicular to the slope. This was done in order to provide periodic aerial images and videos during testing, and to observe flow patterns around the unit.

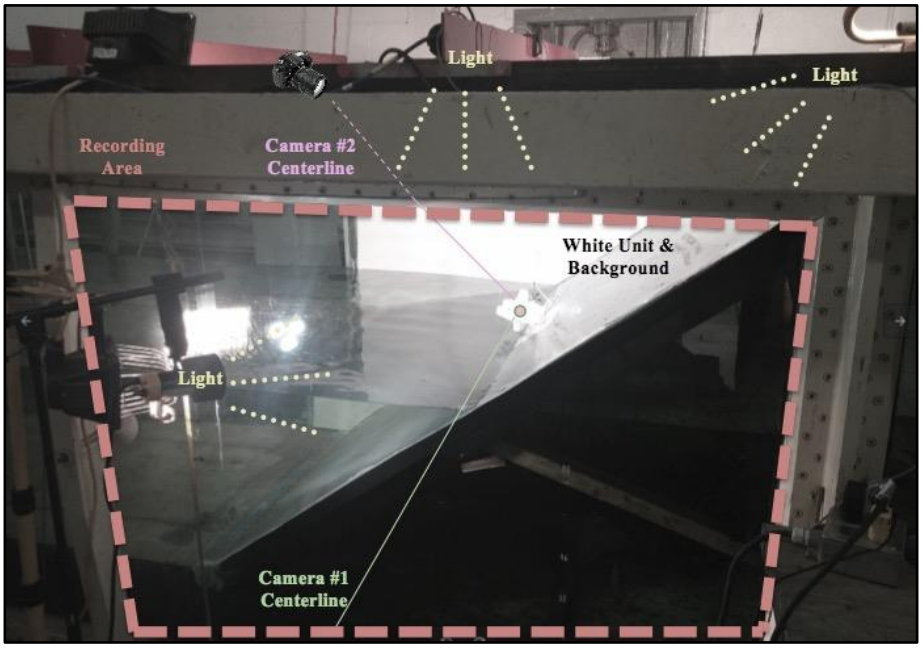

Figure 38: SSU Tests Lighting Arrangement and Camera Positioning for Image Processing

Care and precaution was taken to ensure optimal conditions for image processing. This was focused on distinguishing the instrumented Core-Loc armour unit from the moving water surface, and reducing shadows on the unit itself. This allowed for a highly simplified approach to tracking the water surface profile. This setup is shown in Figure 38.

Calibration curves to convert pixel counts to dimensions in both X and Y directions in the image arrays were developed by taking a series of calibration images. Due to the processing window method detailed below, it was only necessary to calibrate the images near the location of the unit. For each location, one calibration image was taken. Each image contained a vertical line of tape the height of the viewing window, placed on the window at the centroid of the instrumented unit. Vertical lines of tape were also placed 0.1m, 0.2m and 0.3m away from the centreline in both directions. A horizontal array of lines was also placed in a similar fashion, centred at the centroid of the instrumented unit. This 0.1m x 0.1m grid allowed the direct conversion of pixel counts into real dimensions, resulting in the following calibration relationships:

$$\Delta X_{meters} = \Delta X_{pixel} \cdot 5.638 \text{ x } 10^{-4} \qquad R^2 = 0.99 \tag{41}$$

$$\Delta Y_{meters} = \Delta Y_{pixel} \cdot 5.854 \text{ x } 10^{-4} \qquad R^2 = 0.99 \tag{42}$$

4.7.3 Water Surface Delineation Method

The MATLAB tool that delineated the water surface used raw video as input; these videos were filmed at 30 frames per second, with a resolution of 1920x1080. First, the MATLAB script split each video into individual frames. During the splitting process, the frame number, date, and time of each frame was generated for a future time series. Once split, the frames were then looped through, one by one.

A user-defined processing window was then chosen to minimize the portion of each image array that had to be analyzed. This processing window was chosen to include both upper and lower extremities of the vertical water surface fluctuations, and to include only a white background. Cropping the original images was key to ensuring a white background, and thus precluded the image processing from detecting random background objects or shadows.

Once cropped, each "true-colour" (RGB) frame from the original raw video was then converted to a binary image. This step includes two distinct parts. The RGB image is first converted to a gray-scale image; the image processing tool uses the weighted sum of the RGB-values to calculate gray-scale intensity values according to Equation 43; where R, G and B are the normalized colour codes for each pixel. For example if the pixel has an RGB value of (25,43,210), then (R,G,B) for Equation 43 is equal to (25/255, 43/255, 210/255).

$$I = 0.299 \cdot R + 0.587 \cdot G + 0.114 \cdot B \tag{43}$$

Once each pixel has been assigned its' respective I-value (0 to 1), a threshold technique is used to covert the gray-scale image to a purely binary (0 or 1) image. Numerous threshold techniques have been developed over the years that use static, dynamic, local and global approaches. The standard threshold scheme utilized by MATLAB Image Processing Toolbox functions is Otsu's method. This method assumes gray-scale images contains two classes of pixels (foreground and background) that follow a bi-model histogram versus pixel intensity. Otsu's method then assumes a threshold value, and calculates the intra-class variance (the variance within the class), which is defined as a weighted sum of variances of each class. This threshold value is then iterated until the intra-class variance in minimized.

While Otsu's method was initially explored for the purposes of this study, it was determined that through meticulous positioning of the lights and reflective tape, a much simpler single-value (t) threshold method could be used. This essentially means that once RGB images have been converted to gray-scale, a user-defined threshold value would then determine the binary outcome of the image. Once threshold is complete, the original RGB image is converted to a purely black and white binary image. This threshold method follows this expression:

$$\begin{cases} I_{pixel} \geq t & Pixel = 1 \\ I_{pixel} < t & Pixel = 0 \end{cases} \tag{44}$$

As seen in Figure 39, the combination of the ambient conditions, the lighting arrangement, the white unit, and white background resulted in very clear distinction between the unit and water. Figure 39 shows the result of the threshold technique, and conversion of RGB image to binary, capturing the wave profile.

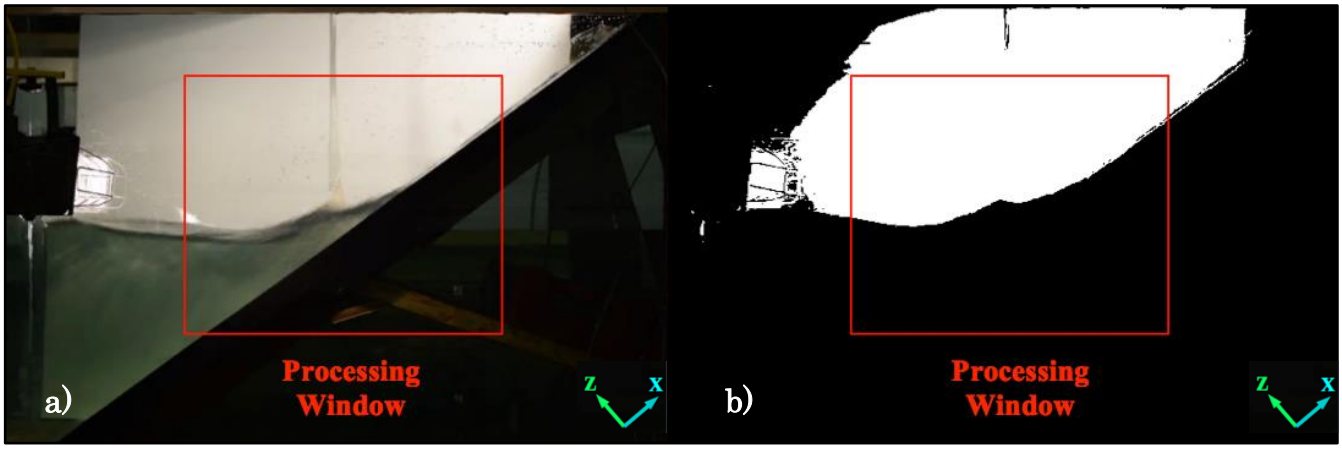

Figure 39: User-defined Image Processing Window and Image Conversion: a) Raw Image, b) Binary Image

Due to the favourable contrast in the videos, and the nature of the threshold technique, no black pixels were present above the deemed "actual" water surface profile. Thus, in order to estimate the position of the water surface at each pixel across the processing window, a simple algorithm was implemented. This algorithm looped through each pixel in the processing window; for each column of pixels, the highest black pixel was considered to represent the water surface. Ultimately, a position vs. elevation relationship for the water surface can be determined for each image, and for the time series as a whole. An example of the delineated water surface profile from this process is shown in Figure 40, superimposed on the original raw image.

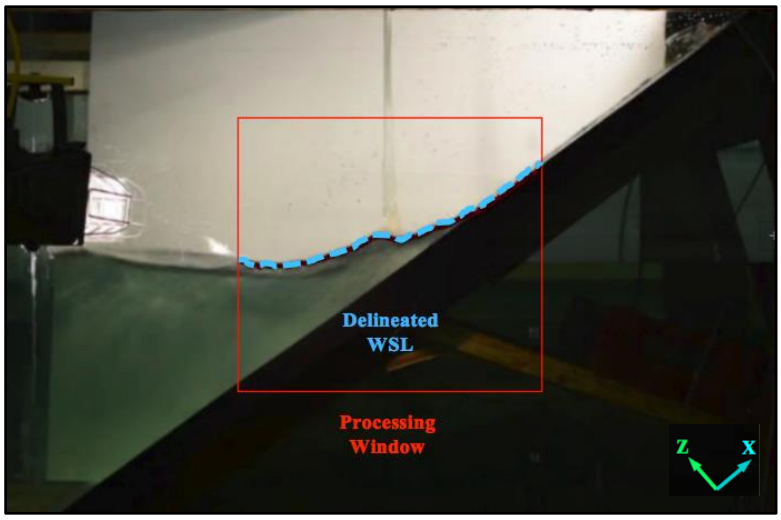

Figure 40: Example of Delineated Water Surface From Image Processing

4.7.4 Buoyancy Calculation Method

The MATLAB tool used to track the water surface profile was part of a larger script coupled with the Python Visualization Toolkit (VTK) Module. This open source, widely used, free software has an extensive repertoire of capabilities in 3D computer graphics, meshes, modeling, image processing, and visualization. VTK has an extensive information visualization framework, has a suite of 3D interaction widgets, supports parallel processing, and is used worldwide in commercial and research applications. VTK's engines are the basis for many advanced software applications such as ParaView (default OpenFOAM visualization GUI).

In order to calculate the buoyant force on the instrumented Core-Loc unit, it was necessary to calculate the submerged volume of the unit at each frame of the recorded test. Once the submerged volume is determined, buoyancy is easily calculable using Archimedes' Principle. First, the unit was scaled up to its respective pixel-size using Equations 41 and 42. Due to the copious amount of frames recorded during each test, it required less computational power to first convert only the unit to its' pixel-size, rather than convert each image to its real size; the result is the same.

Once the MATLAB tool has successfully tracked the water surface profile, for each frame, an array of points is generated. These points represent the X-pixel and Y-pixel co-ordinates of the water surface in each frame. This array of points is read by VTK, and connected end-to-end to form a polyline. This polyline is then extruded 1.22m in the cross-flume direction to form a theoretical water surface across the width of the SWF. This surface is then extruded in the negative z-direction past the bottom of the flume. A plane representing the breakwater slope then slices this 3D object; the resulting final 3D object is a theoretical mesh of the water within the processing window of the image. This mesh is then saved in STL (stereolithography) format. This process was repeated for every single frame of each recorded video. This process is illustrated in Figure 41:

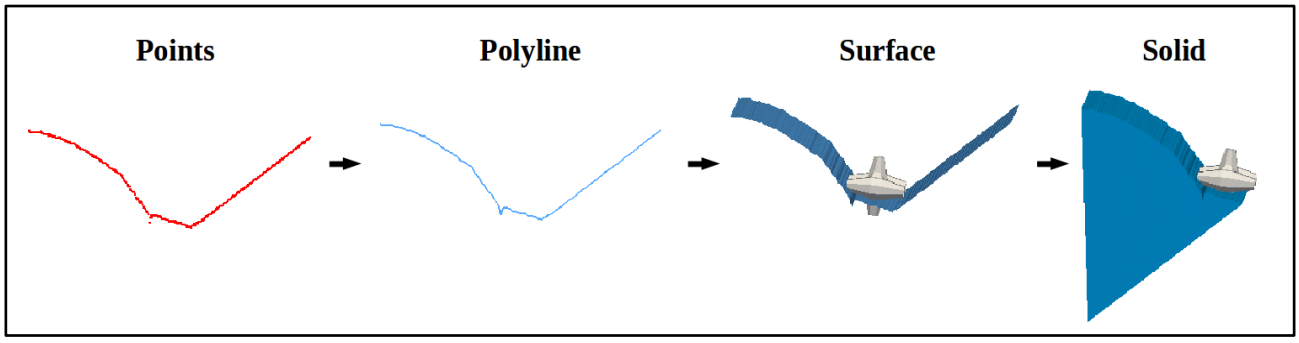

Figure 41: Process of Turning Delineated Water Surface Points into 3D Mesh of Water Profile

The result of this process, for each frame, is a 3D mesh of the water profile at each point in time. With this 3D mesh, the instrumented Core-Loc unit is positioned in its' respective location. This theoretical 3D model of the water and unit was considered to be

representative of the actual testing conditions, and was used to calculate submerged unit volumes.

The Python VTK modeling operation used to calculate the submerged portion of the instrumented Core-Loc unit was a "Boolean operation". This Boolean operation is capable of performing 1 of 3 distinct operations on a pair of 2 meshes; in this case the fluid and the unit. The possible operations are Union, Intersect, and Difference; these are illustrated in Figure 42.

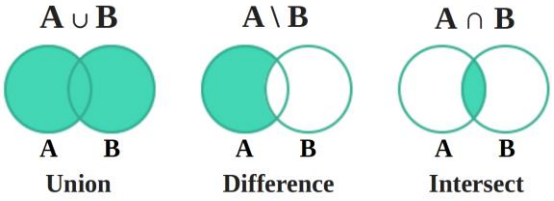

Figure 42: Types of Possible Boolean Operations on Meshes

A Boolean intersection operation was performed on the meshes of the unit and fluid, to obtain the resulting mesh representing the submerged portion of the unit. For intersection, this task is completed by assigning all cells in each of the 2 meshes the same boolean value; i.e., all cells in the mesh of the unit are equal to True, while all cells in the mesh of the fluid are also equal to True. VTK then loops through the cells of each mesh, to determine the boolean value of overlapping cells between each mesh. If the value of each overlapping cell is the same (i.e. True = True), then the cell of the unit's mesh is considered to be fully contained within the mesh of water, and thus considered to be submerged. For partially submerged cells, splitting and re-meshing the cell along the intersection of the two meshes maintains the submerged portion of the cell. In situations where the unit is either completely submerged or completely above the water level, the computational requirement was reduced by using a simple check in VTK. This check can quickly tell the user whether or not a mesh is fully contained or fully separated from another mesh. Once the third "intersected" mesh has been determined, it is also saved in STL format. The resulting intersected mesh represents the submerged portion of the unit; an example of the result of this Boolean intersection is illustrated in Figure 43.

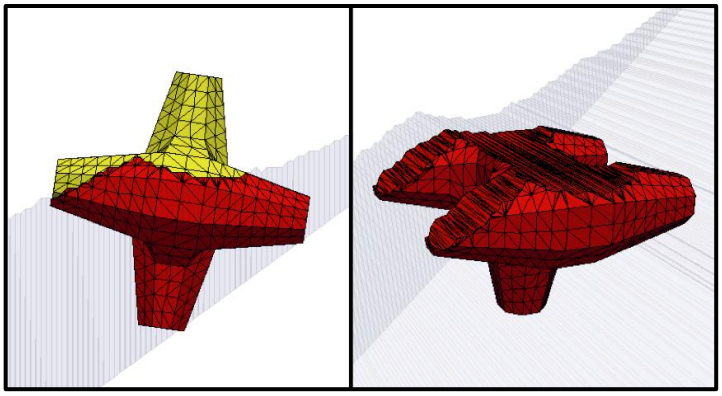

Figure 43: Example of VTK Boolean Operation and Resulting Mesh of Submerged Portion of Unit

Once the mesh of the submerged portion of the unit has been generated, the volume of the mesh is determined using VTK's mesh volume calculation tool; one of the many functions included in the VTK library. To avoid errors due to scaling and conversion back to a 0.12 m unit, the ratio of the volume of the submerged mesh to the full unit mesh is used to calculate the submerged fraction of the instrumented Core-Loc unit. Thus, the buoyant force is calculated using a combination of CLI manufacturer design equations and the Archimedes Principle:

$$F_B = \frac{V_{submerged}}{V_{unit}} \cdot V_{model} \cdot \gamma_w = \frac{V_{submerged}}{V_{unit}} \cdot 0.2211 \cdot C^3 \cdot \gamma_w \tag{45}$$

This procedure of processing images, developing 3D models and meshes, and performing mesh operations to determine buoyant forces was performed for every frame of every test video to generate a time-history of the buoyant force throughout each individual test.

Meshes for each step of this process were saved in STL format. Thus, following the generation of the buoyant force time history, VTK modeling functions can then be used to read the output files to produce a rendered 3D animation of the results. This portion of the script simply superimposed the meshes of the fluid, unit, submerged portion of the unit, the slope, and were coloured for visual purposes. The resulting animation is depicted in Figure 44, while a flowchart summarizing the entire image processing procedure is shown in Figure 45.

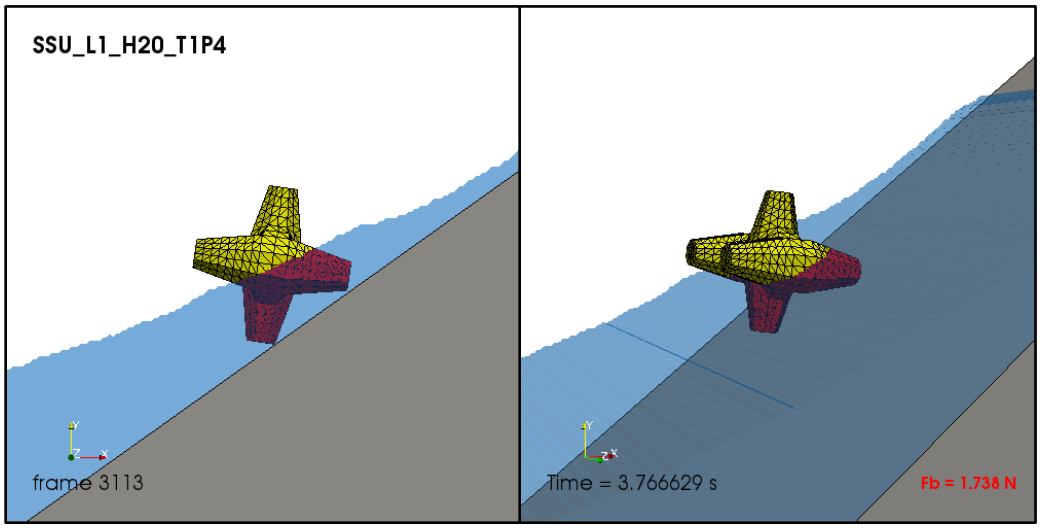

Figure 44: Example 3D Rendering of the Image Processing Results for SSU_L1_H20_T1P4 Test Condition

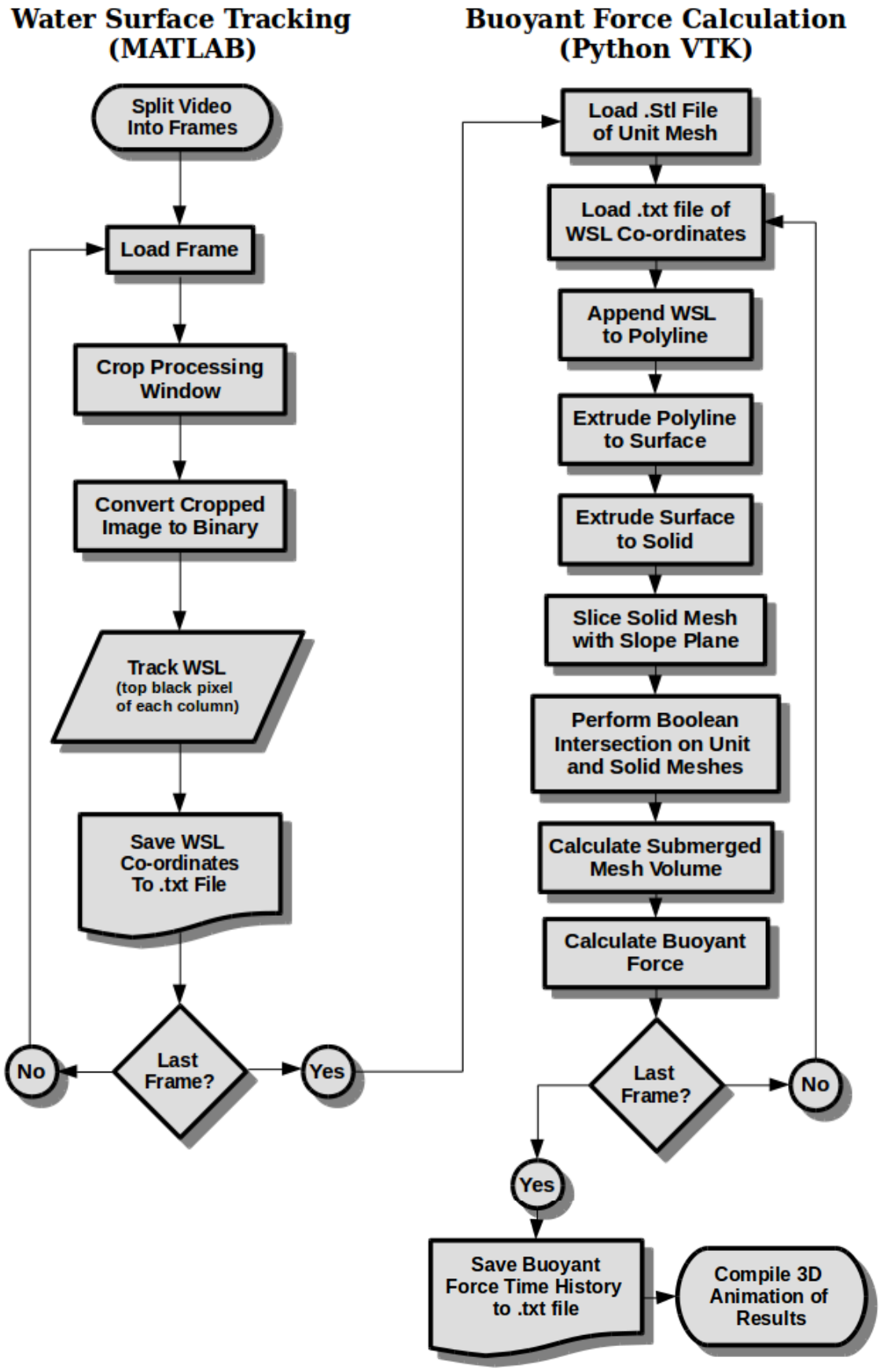

Figure 45: Flowchart of Image Processing Procedure

4.8 Results

4.8.1 Image Processing

4.8.1.1 General Performance

The positioning of the unit, the reflective tape under the unit, the white background, and lighting array included in the experimental setup provided very favourable image quality for processing purposes. As evident from the high linearity of the pixel calibration curves (Equations 41 and 42, $R^2 = 0.99$), minimal distortional error is expected to have influenced the final buoyancy calculations. Due to the inherent nature of curvilinear optical lenses, slight distortion will always occur. For the model of camera used, this distortion occurs in what is known as "barrel distortion"; the distortion is theoretically absent at the centre of the image, and very low around this location. This property, coupled with the direct position of the image center at the centroid of the unit, ensured minimal influence due to perspective distortion on the final buoyancy calculation.

Figure 46 contains an array of examples of the image processing results, for all slope locations and wave breaker types. As evident from Figure 46, the image processing tool was able to track the water surface profile with reasonable accuracy for all testing locations, and for all wave conditions (both regular and irregular).

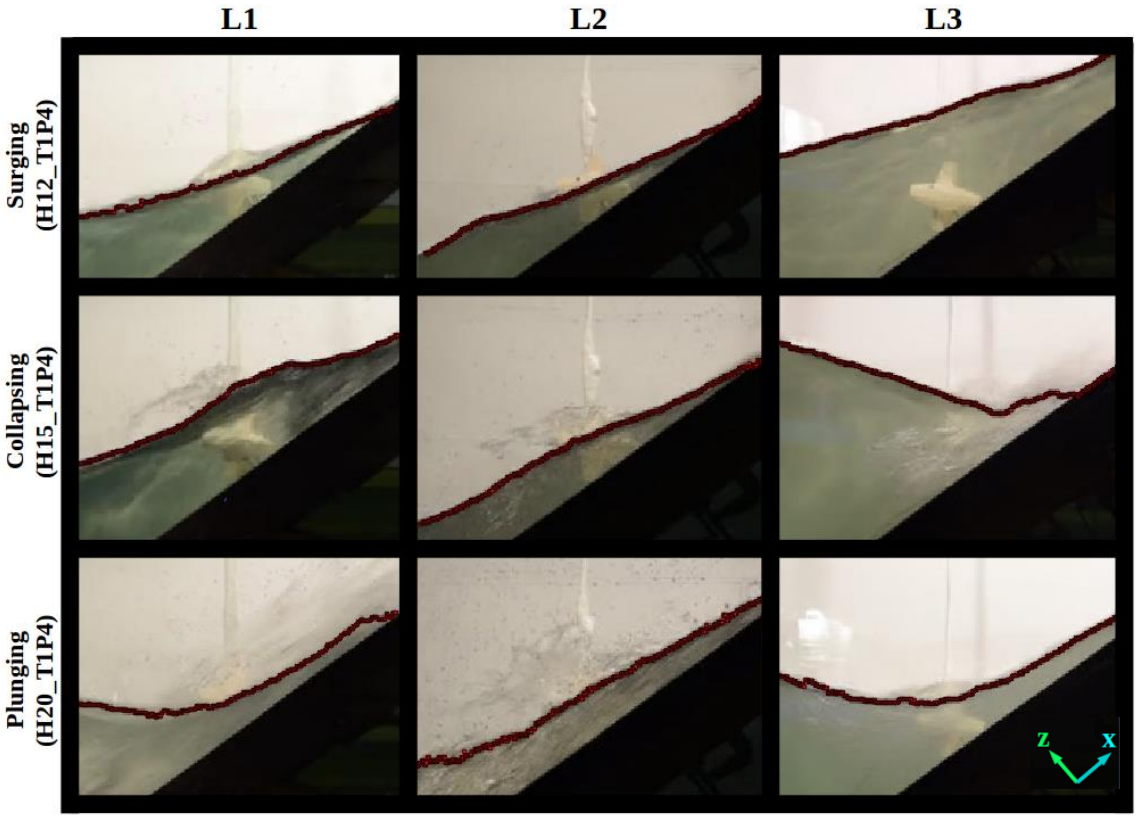

Figure 46: Examples of Image Processing Results and Water Surface Delineation for Various Test Conditions

4.8.1.2 Run-Up and Run-Down

The image processing method utilized a 3D mesh, representative of the water volume in each frame of the recorded videos. As detailed in Section 4.7, this process inherently assumed a linear extrusion of the water surface across the flume, i.e. there is no spatial variability in the cross-flume direction. As obvious from Figure 47, the spatial variability in the cross-flume direction was definitely present in the experiments. The impacting wave and resulting run-up would tend to part around the unit during testing. This was not detected by the image processing technique, as depicted in Figure 47. This induced error into the calculation of buoyant force, and the hydrodynamic force as well. This was inherently due to the fact that the water surface was being observed from the side of the flume. At the location of the unit, there are spatial differences of the water level surrounding the unit during run-up and run-down. Due to the inability to detect these spatial differences, the image processing tool tends to slightly overestimate buoyant force in run-up, and underestimate buoyant force during run-down. Consequently, this results in a slight underestimation of the hydrodynamic forces during run-up, and the opposite during run-down.

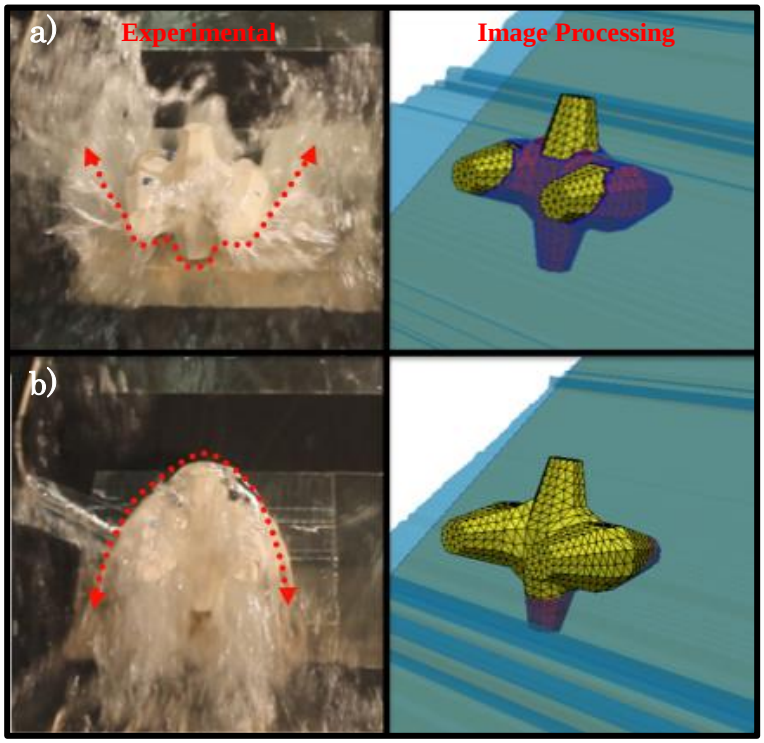

Figure 47: Spatial Variability of Flow in Cross-Flume Direction for SSU_L1_H15_T1P8 Test Condition - a) Run-up, b) Run-down

4.8.1.3 Air Entrainment

In regards to the capabilities of the image processing, an initial concern was the presence of air entrainment during impacts of waves with lower Iribarren number (collapsing, and plunging waves). However, the image processing performed particularly favourable in terms of tracking the interface between water and air, in all wave conditions. The sharp medium change, along with the lighting arrangement, exhibited a rapid change from light to dark at the fluid interface; the gray-scale conversion and threshold steps of the image processing easily picked this up. Thus, even during periods of high air entrainment, the image processing was still capable of detecting the actual fluid interface, and maintained its' integrity as a buoyancy estimation tool. This performance during high air entrainment is illustrated in Figure 48.

Figure 48: Image Processing Performance During High Air Entrainment for SSU_L2_H20_T2P0 Test Condition

4.8.1.4 Buoyant Forces

Qualitatively, the buoyant forces for the regular wave cases followed a predictable pattern. In general, the buoyant force varied from 0 N to 3.748 N (fully submerged) with a period corresponding to the given wave condition. For the irregular wave conditions, similar results were encountered but with higher variability. For these cases, the image processing was also able to detect the high frequency oscillations in the irregular wave train caused by random nature of the signals. Examples of the resulting buoyant force time histories, produced by the image processing tool, are shown in Figure 49.

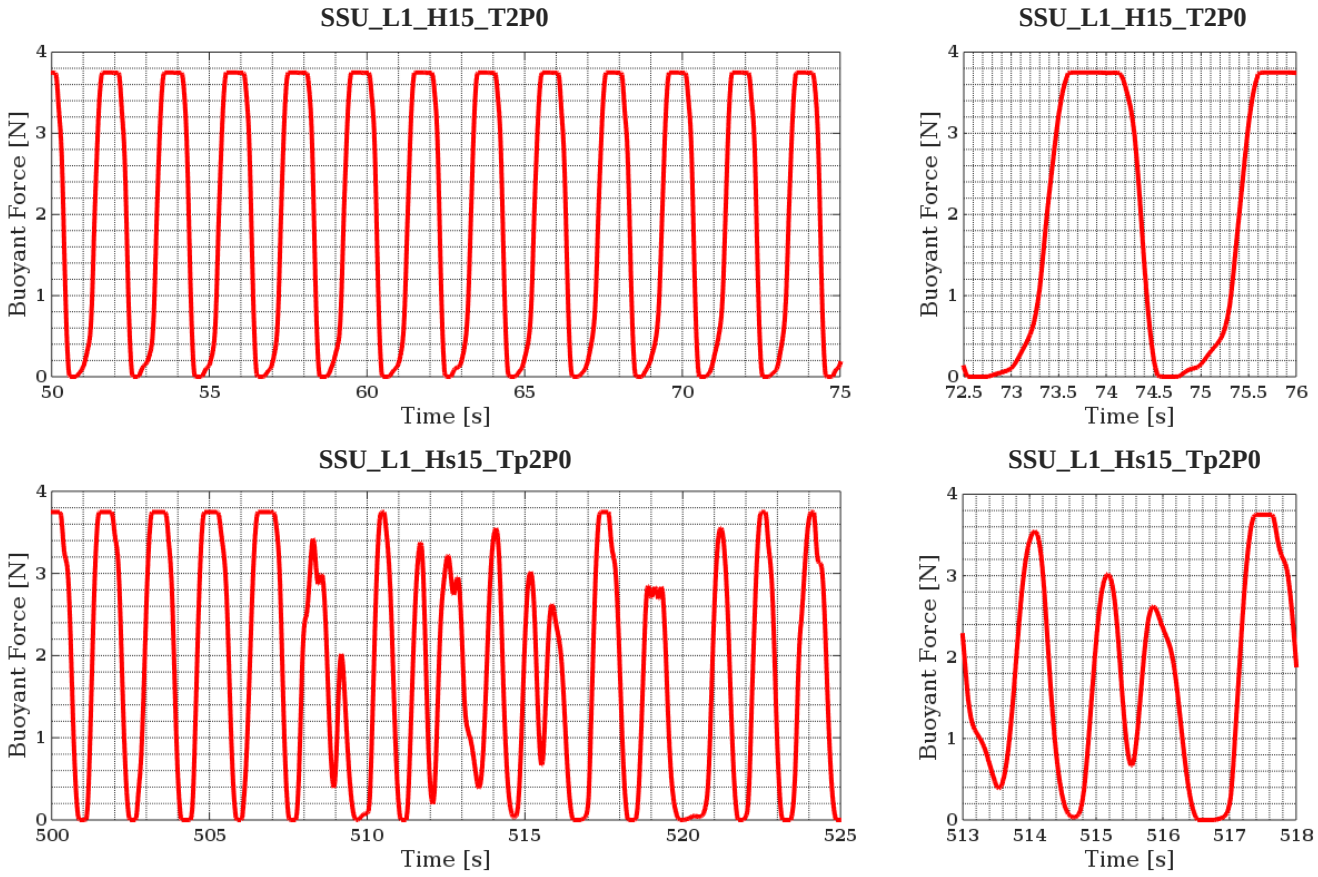

Figure 49: Resulting Buoyant Force Time Histories from Image Processing - top Regular SSU_L1_H15_T2P0, bottom Irregular SSU_L1_Hs15_Tp2P0

The buoyant force for each case was estimated at 30Hz. In order to sync this data with the corresponding NDAQ time histories from the ATI Force Transducer, the data was interpolated from 30Hz to 50Hz using a cubic spline interpolation method in MATLAB. Once aligned, the hydrodynamic force (F_H) was determined as the difference between the total force (F_T)and buoyant force (F_B), according to Equation 45. The results of this process are presented in the following section.

$$F_H = F_{Total} - F_B \tag{45}$$

This was done for both X and Z directions (slope-parallel and slope-normal); the alignment of these axes is shown in Figure 48.

4.8.2 General Hydrodynamic Behaviour

Figure 50 shows the hydrodynamic response for a regular wave condition (SSU_L1_H15_T2P0). This figure shows the time history of F_x, F_{Hx}, F_{Bx}, F_z, F_{Hz}, F_{Bz}, P3 and P5. Sensors P3 and P5 were chosen to represent the pressure on the front and back of the unit, respectively. While differing in magnitude and period, this general behaviour was encountered by all regular wave signals. This behaviour included 5 distinct events

for each wave cycle. For each wave cycle in each of the testing conditions, the following events occurred:

1. There is a pause in the signal while the wave is impacting the slope.
2. Wave run-up approaches the unit, high velocity jet impacts unit.
3. Run-up impacts and completely envelops the unit.
4. Run-up reaches maximum level, flow halts, then reverses.
5. Wave run-down and repeat.

The numbered vertical lines V1-V5 in Figure 50 represent these events, while a snapshot of each event occurring during the test is shown in for the same test condition.

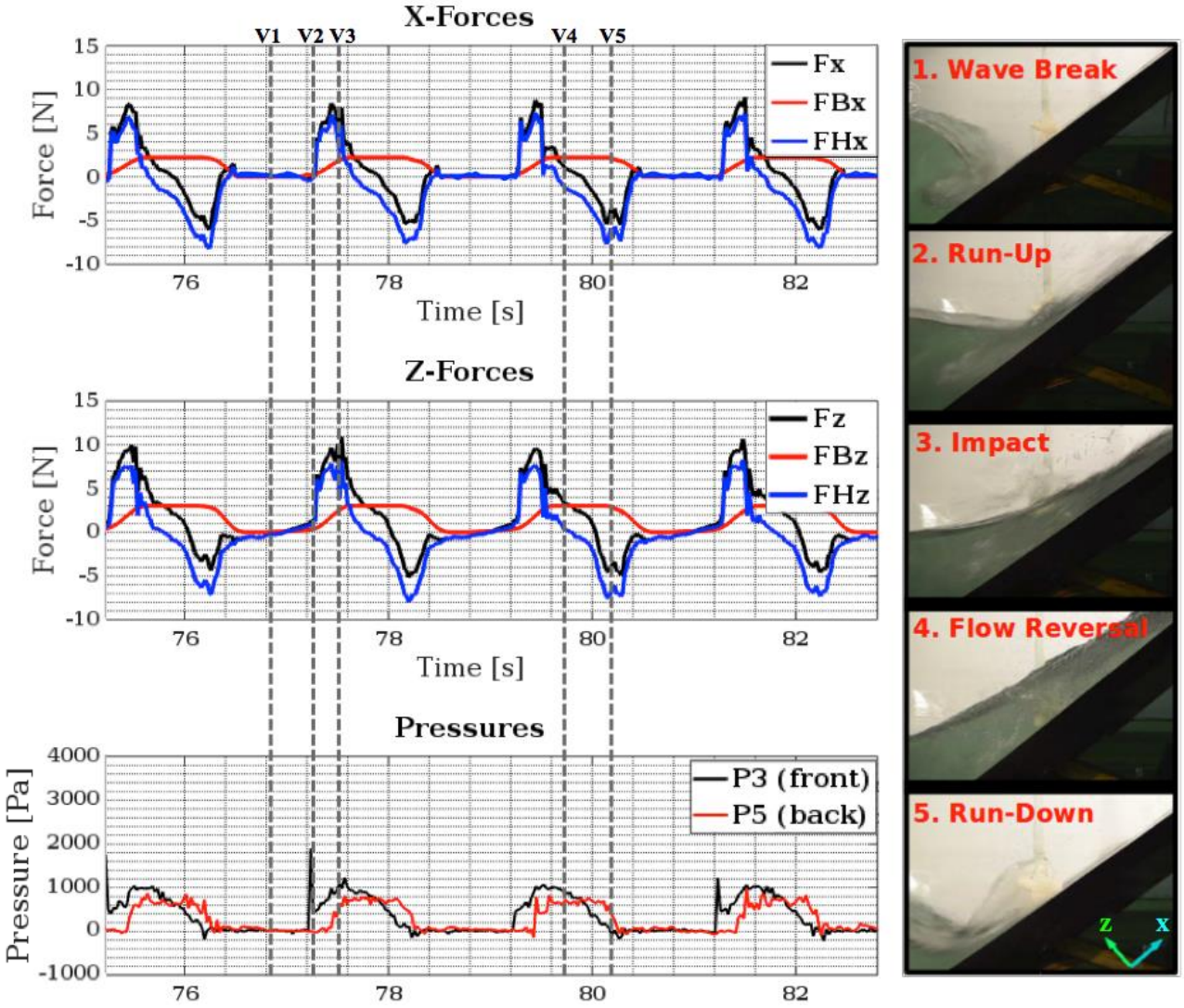

Figure 50: General Hydrodynamic Behaviour for SSU_L1_H15_T2P0 Test Condition, with Images of Each Stage of Wave Cycle

There are distinct patterns in the recorded force and pressure signals that correspond to these 5 events. During the wave breaking process (denoted by V1 in Figure 50), the unit is isolated from any hydrodynamic influence, and thus has little to zero pressure and forces. For shorter period waves than the shown test condition (approximately $\xi_0 \leq 5.0$), forces and pressures may be expected due to the last stages of run-down from the previous wave cycle. This behaviour corresponds to the slamming effect described by De Jong (2003). Due to the low period of these waves (especially for $\xi_0 \leq 3.3$), the units are repeatedly subjected to impact forces. The run-up, and run-down velocities and accelerations in these conditions are also much higher; as well, each subsequent wave reaches the slope before run-down from the previous wave is fully completed. This results in a constant back-and-forth behaviour of the hydrodynamic interaction, leading to higher instability, higher forces, and higher pressures.

During the run-up process (denoted by V2 in Figure 50), the bulk of the run-up approaches the unit. For test conditions with $\xi_0 \leq 3.3$ (plunging waves), this region of the wave cycle also included a high velocity jet due to the complex wave breaking action on the slope. This high velocity jet impacted the front of the unit before the bulk of the run-up had reached the unit's location; this high velocity jet impact produced the highest frequency and magnitude pressures spikes in the signals. The force signals in both the X and Z-directions began to rise at this point, but did not reach the maximum peak value. This effect is depicted in Figure 51, for a SSU_L1_H20_T1P4 test condition; note the high velocity, turbulent, aerated jet approaching the face of the unit.

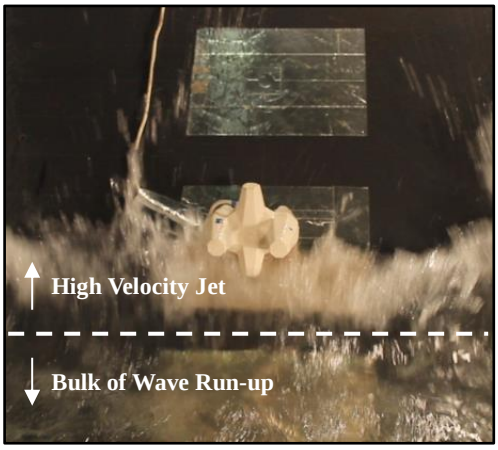

Figure 51: High Velocity Jet Impacting Front of Unit During SSU_L1_H20_T1P4 Test Condition

The run-up then reaches the unit (denoted by V3 in Figure 50); at this point there is a notable impact that is depicted in Figure 52. One can visually see the run-up impacting the unit as it creates high velocity, highly turbulent splashing behaviour while impacting and parting around the unit. It can be seen from Figure 52, as well as the force signals in Figure 50, that this impact event has two distinct parts.

First, the run-up impacts the front of the unit (Figure 52a); a fraction of a second later the unit is completely enveloped by the flow (Figure 52b). This produces an initial spike

in forces, a very brief plateau, followed shortly after by a second higher spike. The forces reach their maximum during this latter portion of the impact event.

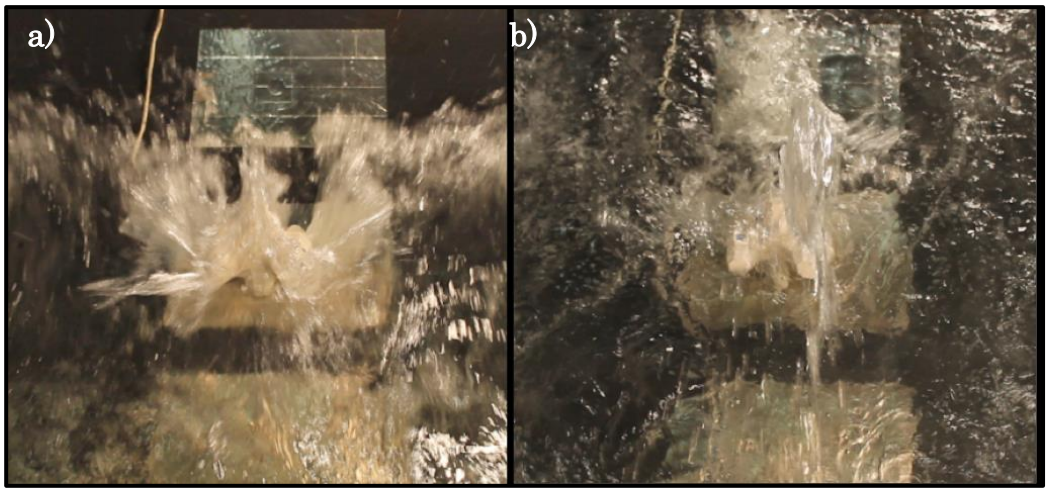

Figure 52: Wave Impact Event During SSU_L1_H20_T1P4 Test Condition - a) Run-up Impacts Unit, b) Run-up Envelops Unit

During this process, the run-up impacts and envelops the unit, and buoyancy increases to a maximum. This combination of interactions produced very high forces on the instrumented unit. During this portion of the wave cycle, high velocity and acceleration, highly turbulent flow patterns are induced by virtue of the complex unit geometry. The high velocity run-up parts around the unit; however, some flow is accelerated into the small opening between the unit and slope. This caused high pressures on the bottom of the unit and induced large uplift forces. It is believed that the X and Z forces reached similar magnitudes due to the chosen orientation of the unit. This orientation provides a large surface area and favourable impact angle on the unit's surface, which enhances the magnitude of the Z-forces. While it was expected to have notably larger drag forces than lift forces, the fact that they are similar speaks to the variability of the hydrodynamic interaction as a function of unit orientation.

Once the run-up has reached its maximum, the flow reverses (denoted by V4 in Figure 50). At this point, pressure on the front of the unit (P3) reaches a momentarily constant, near-hydrostatic value as the fluid velocity approaches zero. Directly after, pressure on the back of the unit (P5) spikes as the flow reverses direction. It can also be seen that, as the flow reverses, the hydrodynamic forces approach zero. This is exactly what is expected, as the hydrodynamic forces are dictated by the fluid velocity and acceleration; hence, when equal to zero the hydrodynamic forces go to zero. As the hydrodynamic forces approach zero, it can be seen that the total forces approach the buoyant forces in both the X and Z-direction (seen in Figure 50).

Finally, the run-down occurs (denoted by V5 in Figure 50); this manifests in decreasing buoyant forces, negative X and Z-forces, and high pressures on the back of the unit. At the beginning of the run-down process, the velocity is still low. This results in a gradual increase in negative forces. The run-down forces appear to peak in magnitude just before the unit emerges from full submergence.

For the particular wave signal shown in Figure 50, this X and Z-force peak happens to be ≈ 0.1s before the buoyant force begins to decrease. During this process, highly turbulent flow is again accelerated around and under the unit. After the run-down forces spike, this effect, along with the decreasing run-up depth at the unit, reduces the magnitude of the forces. Eventually, all readings trickle away to zero before the next wave cycle. This process is shown in Figure 53:

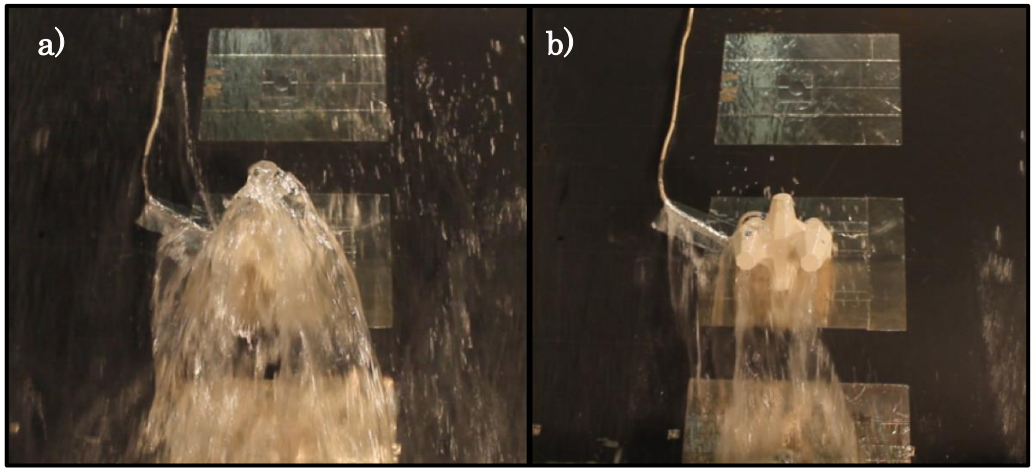

Figure 53: Run-down Interaction with Unit - a) Flow Around Unit, b) Accelerated Flow Under Unit

For L1 and L2 cases, positive forces in both X and Z-directions were generated during run-up, and negative during run-down. This represents de-stabilization forces during run-up. During run-down, forces generated in the Z-direction provide stabilization. The run-down direction, the unit orientation, and the rapidly decreasing water level at the unit appear to force the unit into the slope.

However, it should be noted there was especially unique behaviour for L3 cases during run-down, particularly with cases with $\xi_0 \leq 4.2$. Due to the closer proximity of the L3 location to the wave breaking location, the wave would tend to "fall" onto the unit. The results showed that in waves with $\xi_0 \leq 4.2$, units below the breaking level of an incoming wave experience momentary stabilization forces during initial wave impact, followed by the expected uplift force. Afterwards, the receding run-down and incoming wave causes upward flow patterns resulting in uplift forces (Figure 54b). This behaviour causes units at the L3 location to be subjected to momentary positive uplift during both run-up and run-down. This is the opposite of the behaviour encountered for L1 and L2.

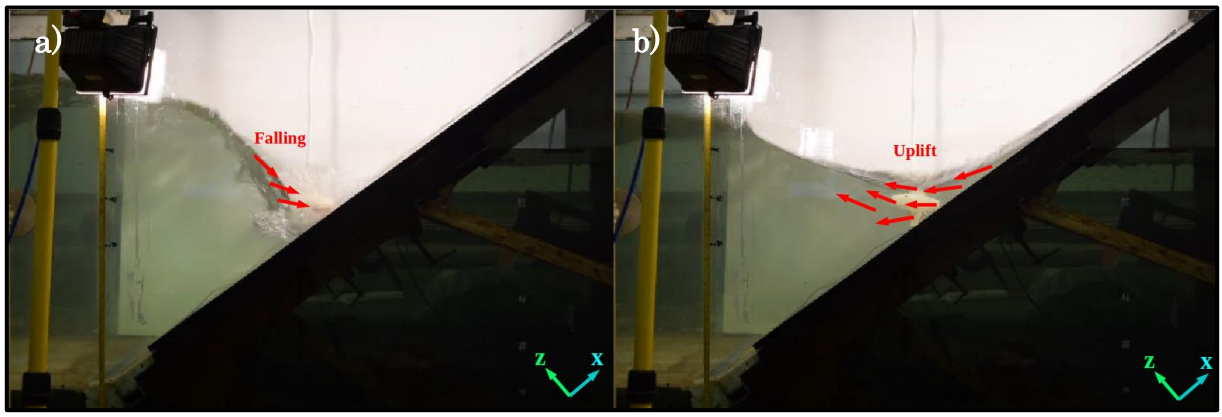

Figure 54: SSU_L3_H20_T2P0 Test Signal - a) Incoming Wave "Falling" on Unit, b) Uplift Flow Patterns During Run-Down

For all wave signals, L2 clearly experienced the lowest hydrodynamic response in terms of drag, lift and pressures. Test conditions for L1 and L3 remained comparable in magnitude, however the aforementioned behaviour was notably different. This effect of location will be explored in more detail in Section 4.8.6.

It should also be noted that throughout the entire duration of the testing program, P3 was the only pressure sensor that gave reliable data on the front of the unit. Thus of the 6 pressure sensors, only 4 sensors (P3, P4, P5, P6) will be considered as accurate results in further sections of this document.

Locations L1 and L2 also produced unique behaviour in terms of pressure readings. For these locations, P4 and P6 recorded very similar readings for every wave signal. P4 and P6 showed lower pressures than P5 in every wave test, regular and irregular. This is due to the fact that the location of these sensors is on a face of the Core-Loc that is at an angle to the mean flow direction. This causes a non-direct hydrodynamic impact, and thus lowers pressures. P5 is more aligned with the mean flow direction, and recorded higher, more variable, and distinct pressure readings for all wave cases. P3 recorded the highest magnitude pressures for all wave cases, as it receives a near direct impact from the run-up on the front of the unit. The general behaviour for each pressure sensor during a test (SSU_L1_H20_T1P4) is shown in Figure 55.

As mentioned previously, the chosen irregular wave signals were able to produce a wide range of conditions at the slope. The unique combinations of wave trains impacting the unit, on average, produced comparable or lower interaction than the regular waves. The unique superposition of the irregular waves at the toe also produced rare instances where forces and pressures greatly exceeded anything encountered in the regular waves tests. A typical time history containing P3 and P5 for an irregular test (SSU_L3_Hs15_Tp1P2) is shown in Figure 55. Note that the L3 location was the only location where pressure sensors were fully submerged at SWL conditions. Thus, the “zero value” of the pressure sensors for L3 cases are 1132 Pa, 710 Pa, 543 Pa, 700 Pa, for sensors P3, P4, P5 and P6, respectively.

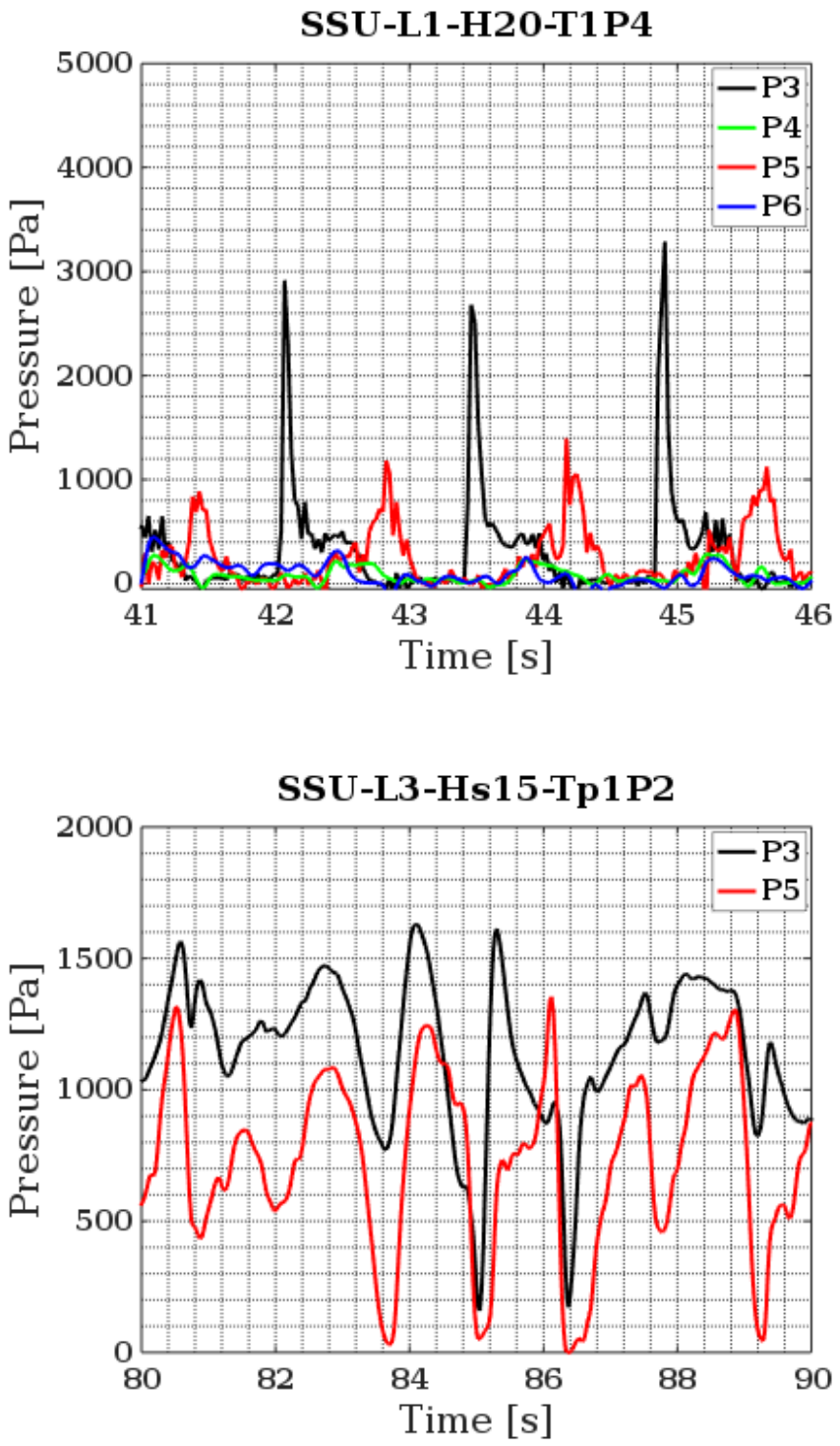

Figure 55: Top - Regular SSU_L1_H20_T1P4 Wave Signal with All Pressure Sensors, bottom - Irregular SSU_L3_Hs15_Tp1P2 Wave Signal with P3 and P5 Pressure Sensors

4.8.3 Statistical Peak Analysis

In order to represent the large amount of data collected for various wave conditions and unit locations, it was necessary to perform a statistical analysis to reduce each dataset to its' key representative values. These values could then easily be plotted, contrasted, and non-dimensionalized. This approach makes it more efficient to distinguish relationships related to force, pressure, unit location, and wave conditions on a large scale.

A total of 18 unique wave conditions (14 regular, 4 irregular), with 3 unique locations, resulted in a total of 54 unique tests. All tests were repeated at least once. During testing, due to various technical difficulties, a number of additional incomplete datasets were produced. For example, this occurred if the NDAQ system crashed and the instrumented unit continued to collect data, or vice-versa. These "incomplete" sets of data provided insight into the repeatability of the results, and the additional data was also incorporated into the following statistical analysis.

The statistical peak analysis was performed on the test data using functions from MATLAB's Signal Processing Toolbox. This was done in order to extract the key values of force and pressures, particularly for each individual wave cycle. This approach is applied to each wave in the user-defined time window, resulting in a list of values for each wave; these results could then be used for statistical analysis.

In general, for each regular wave cycle, there is both run-up and run-down. During the run-up process there is an associated maximum force in the X and Z-directions. There are also peak pressures on the front of the unit that occur during run-up action. Likewise, negative peak forces, and peak pressures on the back of the unit occur during run-down.

These peak forces and pressures are the key parameters of interest for the force balance design approach. Thus, for each wave cycle (for both run-up and run-down), the hydrodynamic interaction can be reduced to one single peak value for all of the following parameters: F_x, F_{Hx}, F_z, F_{Hz}, P3, P4, P5, and P6. These peak values that are representative of each wave cycle, are depicted in Figure 56 for a regular wave condition and an irregular wave condition.

For regular wave conditions, the peak analysis was achieved by performing a zero-crossing analysis on all force and pressure signals, to separate individual wave cycles. For regular wave conditions, this process was aided by the known parameter of wave period; thus, individual waves were easily separated. Once the wave separation is completed, the local maximum and local minimums for each wave cycle are computed.

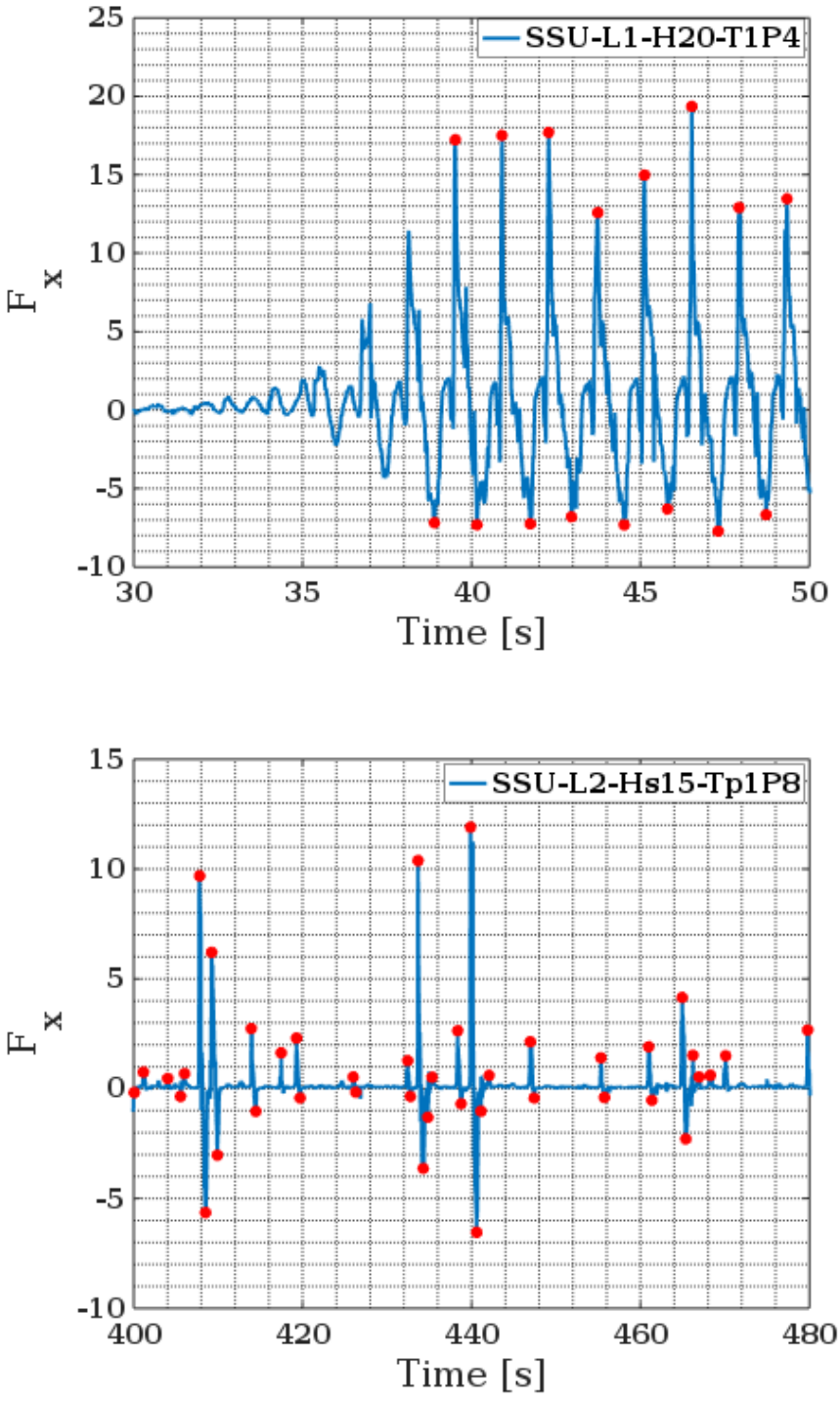

Figure 56: Example of Statistical Peak Analysis on SSU_L1_H20_T1P4 and SSU_L2_Hs15_Tp1P8 X-Force Signals, Peak Run-up and Run-down Forces

Reflection from the slope tends to build up in the flume during regular wave signals. This reflection begins to cause instability in the waves' consistency. Depending on the wave period, the time it took for waves to reach the structure ranged from ≈ 25-40 s. After this, only the first 30 seconds of wave action for the regular signals was analyzed and considered as representative of the wave conditions.

For irregular wave conditions, a similar MATLAB function was used that does not require the signal to pass through zero on the y-axis. In order to separate the irregular waves, two key parameters for the analyses were calibrated. These two parameters are the minimum peak height, and the minimum peak distance. The minimum peak height dictates the lowest possible fluctuation in the irregular wave signal that is considered as an individual wave impact. The minimum peak distance dictates the minimum distance from one peak to another. An extensive calibration of these two parameters was carried out through comparison of the force signal to the recorded test video. An example of results for the statistical peak analysis on an irregular wave signal is shown in Figure 56.

Once the key values have been extracted from the time histories, their statistical parameters are summarized, as in Table 15 for a SSU_L1_H20_T1P4 test condition:

Table 15: Statistical Peak Analysis Results for SSU_L1_H20_T1P4 Test Condition

Peak Direction	Statistical Parameter	F_x [N]	F_{Hx} [N]	F_z [N]	F_{Hz} [N]	P3 [Pa]	P4 [Pa]	P5 [Pa]	P6 [Pa]
Positive	Min.	12.52	10.95	12.56	10.98	1641.30	-	-	-
	Max.	19.10	14.78	18.39	16.35	8188.95	-	-	-
	Mean	15.95	13.68	15.07	13.29	3099.91	-	-	-
	Std. Dev.	1.21	0.82	1.30	0.98	1123.83	-	-	-
Negative	Min.	-6.12	-6.87	-6.55	-8.07	-	231.04	885.46	214.04
	Max.	-7.65	-8.77	-9.09	-11.65	-	485.14	2597.29	469.14
	Mean	-6.98	-7.90	-7.27	-8.96	-	328.66	1109.36	304.66
	Std. Dev.	0.27	0.27	0.80	0.42	-	73.71	235.40	62.71

For the tested wave condition summarized in Table 15, it is evident that the unit experienced comparable X and Z forces. The maximum total run-up forces incurred during this test were 19.10 N and 18.39 N in the X and Z-directions, respectively. In terms of purely hydrodynamic forces, the maximums incurred during run-up were 14.78 N and 16.35 N in the X and Z-directions, respectively. During run-down, maximum total forces reached -7.65 N and -9.09 N in the X and Z-directions. Given that buoyancy acts in the positive direction for both axes, the hydrodynamic run-down forces were greater in

magnitude than the recorded total forces. The hydrodynamic run-down forces peaked at maximums of -8.77 N and -11.65 N in the X and Z-directions, respectively. As mentioned previously, it is hypothesized that the X and Z-direction forces reached similar magnitudes due to the orientation of the unit. The Core-Loc shape has three main sections; two of these sections are angled at 45° to the slope. The third is also angled at 45° to the slope, but in the reverse direction (i.e 135°). Thus, the majority of the cross-sectional area is angled in such a way that, when near-horizontal run-up impacts the unit, forces in the X and Z-directions would theoretically be very similar. This is illustrated in Figure 57:

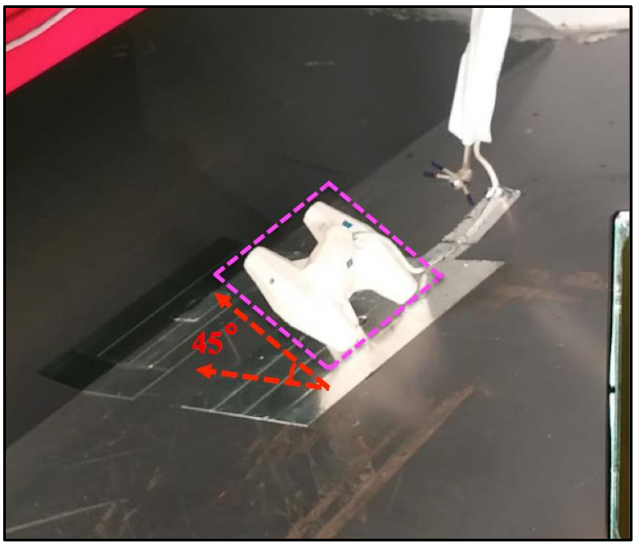

Figure 57: Main portion of Unit's Cross-Sectional Area at 45 ° to Slope

Table 15 shows the standard deviation for each force and pressure reading. It can be seen that the variability in the run-up forces is greater than the run-down forces; this is true for all wave signals, and is more prominent in wave conditions with lower Iribarren number. Given that the data presented in Table 15 is for a plunging breaker wave case (ξ_0 = 2.93), it makes sense that the run-up forces are more variable than then run-down. The breaking wave causes a highly turbulent, high velocity jet that, by its' own nature, is more variable than the run-down. Once the flow reverses on the slope, much of the turbulence from the initial wave impact has already dissipated, causing a more regular flow around the unit during run-down. This in turn, produced lower and more consistent forces during run-down.

The statistical results summarized in Table 15 also include pressure for sensors P3, P4, P5, and P6. It can be seen on the front of the unit, P3 shows the highest impact pressures; these occur during the run-up phase. On the back of the unit, both P4 and P6 produce similar results, while P5 greatly exceeds their values. Both P3 and P5 are positioned on the unit such that they are nearly perpendicular to the mean flow direction in run-up and run-down, respectively. During the high velocity jet produced in the run-up

phase, P3 peaks at a maximum value of 8188.95 Pa. With a minimum peak impact pressure of 1641.30 Pa, and a mean of 3099.91 Pa, it is clear that the pressures on the front of the unit for plunging waves are highly variable. The high standard deviation for P3 (1123.83 Pa) also speaks to the highly turbulent and variable nature of the run-up impact. During run-down, P5 peaks at a maximum pressure value of 2597.29 Pa. The standard deviation of 235.40 Pa shows there is considerably more consistency in the pressures on the back of the unit. Pressure sensors P4 and P6 are positioned such that they are not perpendicular to the mean flow directions; thus, their diaphragms are impacted at a steep angle. This produces much lower pressures readings, as can be seen by the maximum pressure values of 485.14 Pa and 469.14 Pa for P4 and P6 respectively. The similarity between the two results, and the low standard deviation, suggests that locations around the periphery of the unit have less variability in induced pressures.

As in Table 15, these statistical parameters were produced for every single testing condition. These reduced, statistical representations of the force and pressure signals form the basis of the non-dimensional analysis presented in the following sections. Please see Appendix A for the full set of statistical results for all regular and irregular wave conditions, for all locations.

4.8.4 Effect of Surf Similarity Parameter

For location L2, for three different wave signals, Figure 58 shows the total X and Z-forces as well as pressure time histories on the front and back of the unit (P3 and P5). The three wave signals shown are SSU_L2_H20_T1P4 ($\xi_0 = 2.93$), SSU_L2_H15_T2P0 ($\xi_0 = 4.83$), and SSU_L2_H15_T3P2 ($\xi_0 = 7.74$). These conditions were chosen to show the difference in the hydrodynamic interaction for plunging, collapsing, and surging wave breakers, respectively. Figure 59 also shows snapshots during wave impacts of each of these three tests. As can be seen from the snapshots of testing, the impact becomes more intense as ξ_0 decreases.

The complex hydrodynamics produced by the plunging waves produced higher, and more variable peak forces and pressures, as previously mentioned. The peak forces and pressures occurred over a shorter duration for the plunging waves. Many peak forces and pressures were only captured by one data point (i.e ≤ 0.02s in duration).

From the peak statistical analysis, the mean X-forces for the plunging, collapsing, and surging waves were 7.76 N, 3.77 N and 2.49 N respectively. The mean peak Z-forces for the plunging, collapsing, and surging waves were 7.92 N, 3.48 N, and 2.95 N respectively. The effect of surf similarity is clear from the results; a decrease in this parameter will lead to higher forces and pressures induced on the unit. A maximum peak pressure in P3 of 2454.50 Pa was recorded for the plunging wave case. The collapsing and surging cases both fluctuated between approximately 0 – 400 Pa.

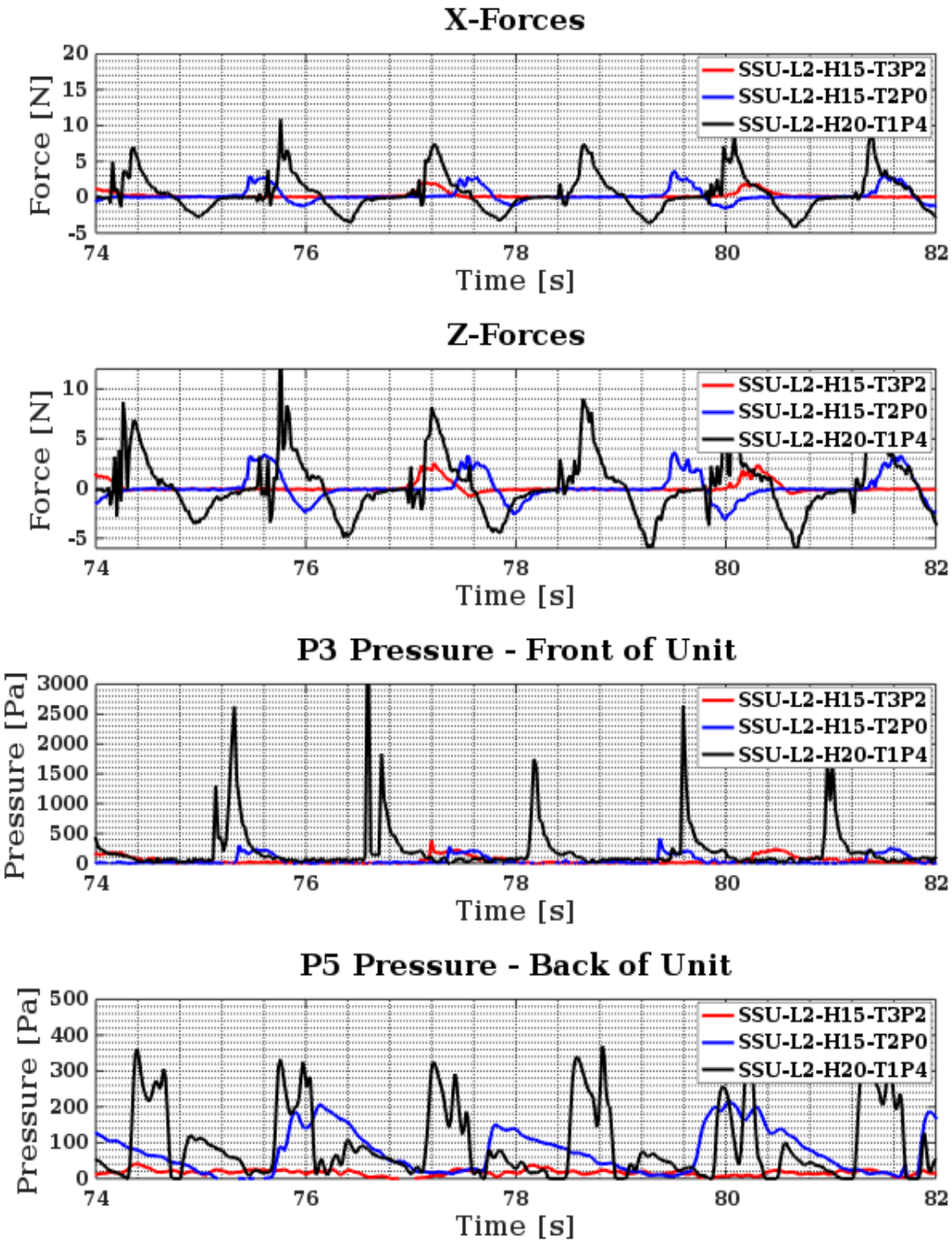

Figure 58: The Effect of Surf Similarity Parameter on Total Forces and Pressures for Constant L2 Unit Location

Figure 59: Snapshot of Wave Impacts for a) SSU_L2_H15_T3P2 (surging), b) SSU_L2_H15_T2P0 (collapsing), c) SSU_L2_H20_T1P4 (plunging) Wave Conditions

In order to visualize the effect of surf similarity on the entire SSU testing dataset, the statistical forces (F_x, F_{Hx}, F_z, F_{Hz}) were normalized via the submerged unit weight. Considering the unit was fixed in position and hollow, a theoretical density of ρ_a=2400 kg/m^3 was chosen to represent the magnitude of these forces versus a standard concrete unit. These values are then plotted against a modified non-dimensional number based on the surf similarity parameter. This modification was done to separate waves with similar Iribarren number, but different heights. For example, conditions with H = 0.12 m and T = 1.8 s corresponds to ξ_0 = 4.87. Wave conditions with H = 0.15 m and T = 2.0 s corresponds to ξ_0 = 4.84. These signals both have similar Iribarren number, but produce drastically different forces and pressures. Thus, the modification of the surf similarity parameter was necessary to visualize the entire dataset. This new parameter ($\xi_0 \cdot d \cdot L_0 \cdot H_s^{-2}$) amplifies the effect of the surf similarity parameter. Both a higher wavelength and a lower wave height increase the Iribarren number; in this new parameter these effects are greater due to the exponents of H and L_0. The irregular wave signals were combined into these plots by replacing H with H_{m0}.

Figure 60 shows the effect of this modified surf similarity parameter on the mean peak forces in the X-direction, for all wave cases. This figure includes the mean peak forces generated in both the positive and negative X-directions, as well as 3 lines representing the results of each location. Similarly, Figure 61 shows the same results, in the Z-direction.

From both Figure 60 and 61, is it clearly evident that a decrease in surf similarity will lead to higher generated forces. This effect is not as prominent in the L2 location. This same trend also held for the hydrodynamic forces, but the values were slightly smaller in magnitude.

Figure 62 shows the effect of surf similarity on the maximum peak pressures generated on both the front and back of the unit (P3 and P5 were chosen) for the L1 testing location.

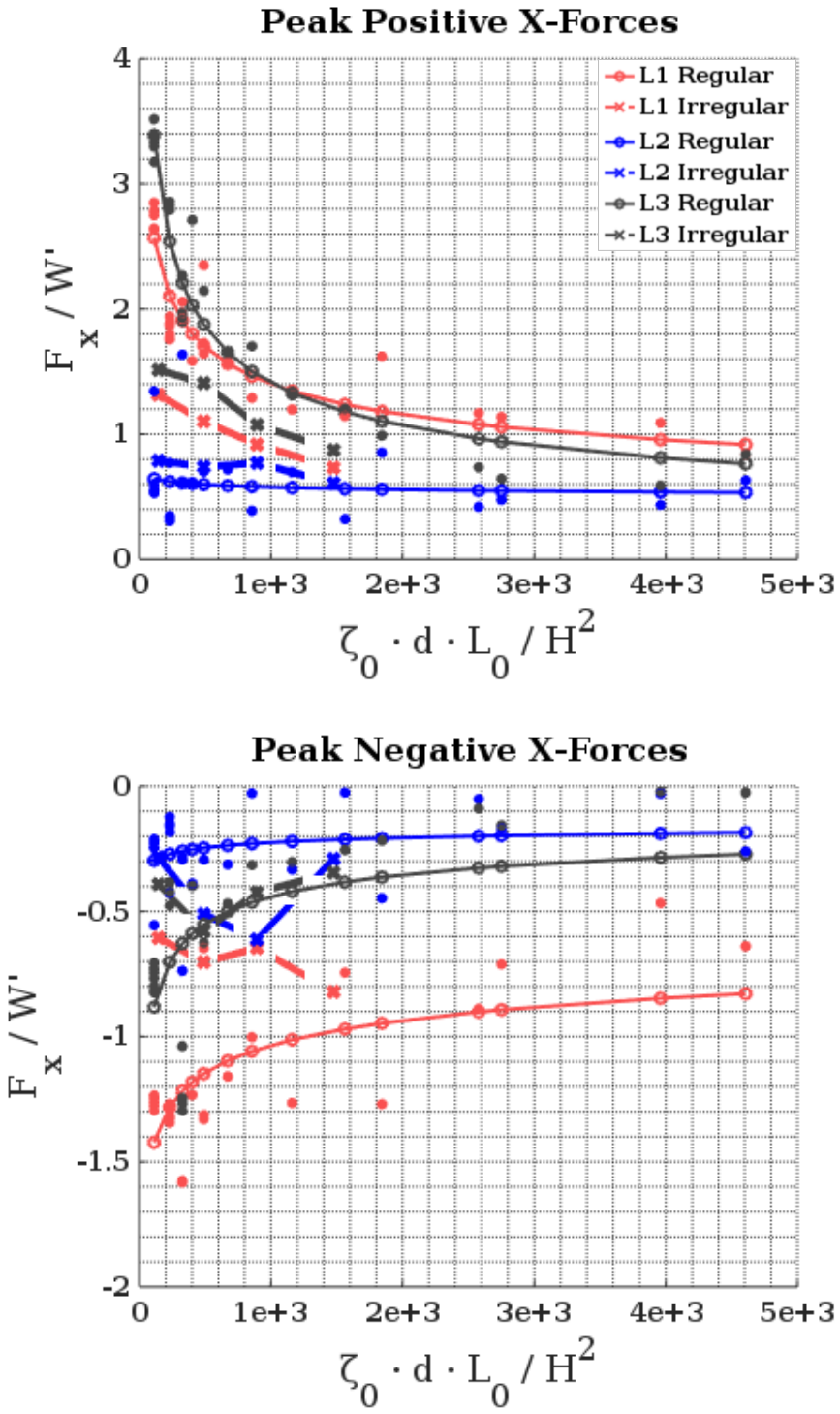

Figure 60: Normalized Mean Peak X-Forces vs. Modified Surf Similarity Parameter for all Testing Conditions

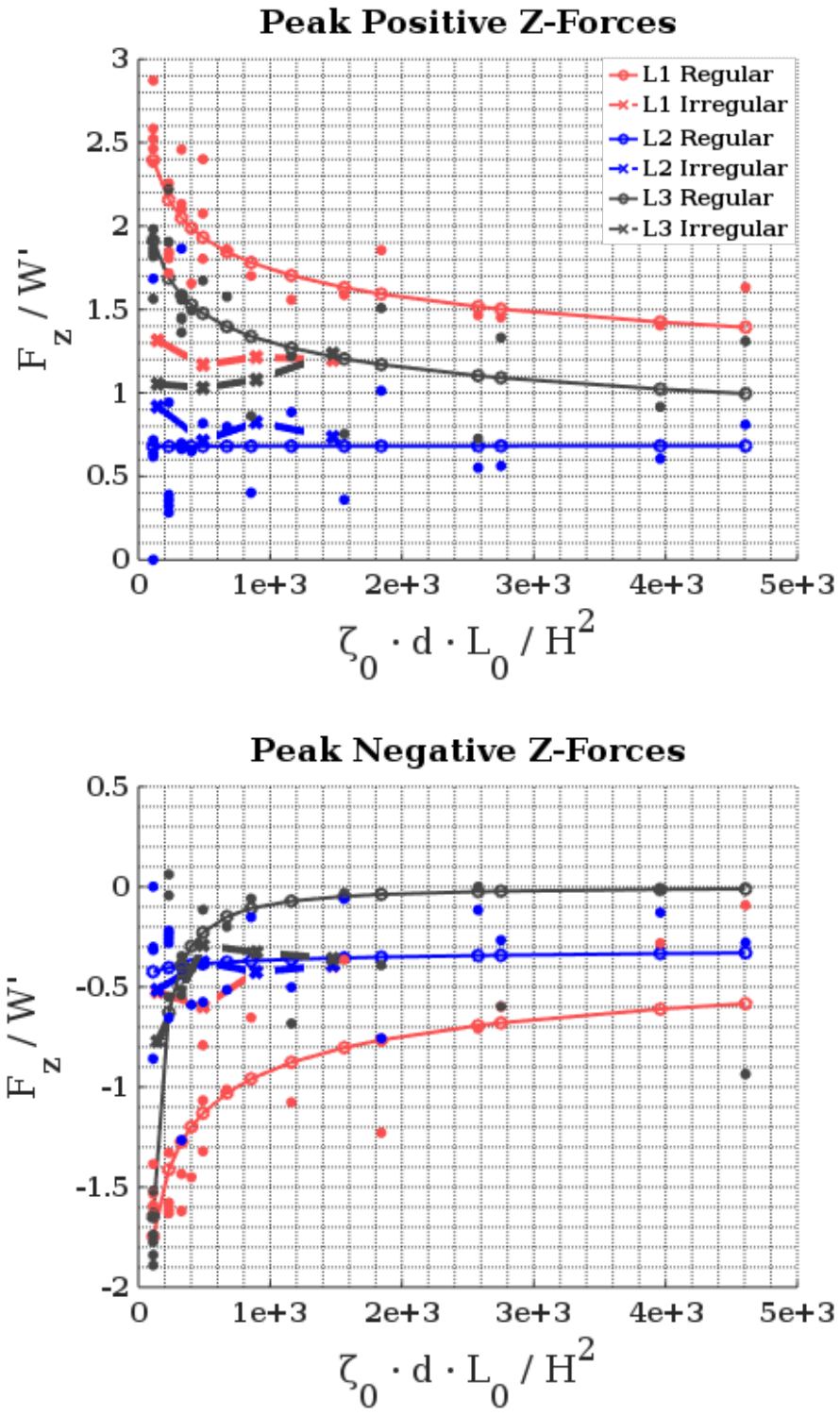

Figure 61: Normalized Mean Peak Z-Forces vs. Modified Surf Similarity Parameter for all Testing Conditions

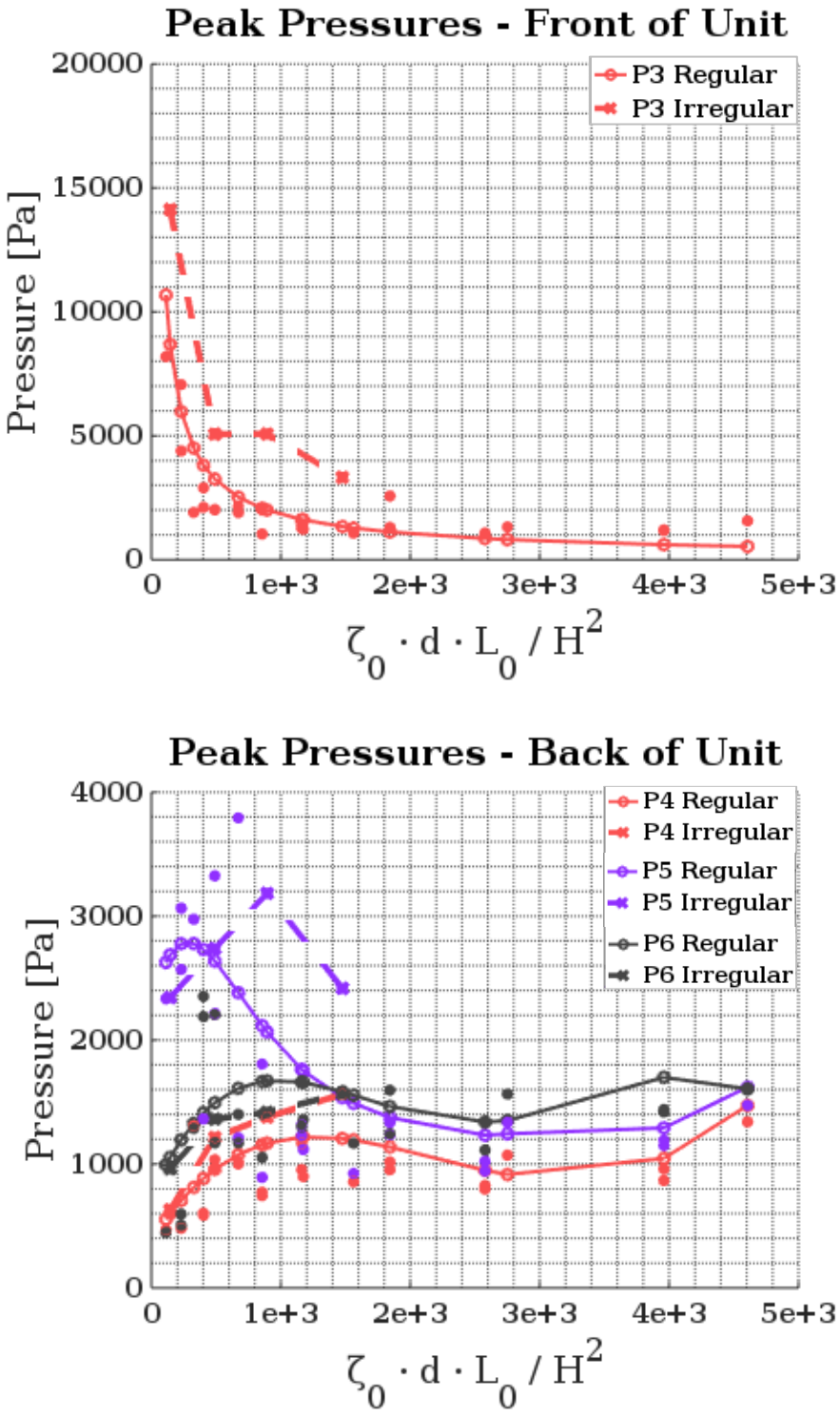

Figure 62: Max. Peak Pressures vs. Modified Surf Similarity Parameter for L1 Testing Location – top Front of Unit, bottom Back of Unit

As the pressures shown are the maximum pressures, one can see the prominent difference in both P3 and P5 for the irregular signals. As mentioned previously, the absolute maximums in the irregular signals were much higher than in the regular.

It can be seen from Figures 60, 61 and 62 that a general trend emerged. This trend included X and Z forces (total and hydrodynamic), as well as front and back pressures on the unit. With few exceptions, the results showed higher X-forces then Z-forces, i.e. higher parallel to slope than normal. This trend also showed much higher pressures on the front of the unit than the back for all wave conditions, while the disparity decreased greatly when subjected to wave conditions with a high surf similarity parameter. The pressures on the front of the unit (P3) were greatly increased by the wave conditions with low surf similarity parameter. The maximum peak pressure recorded, during regular waves, in P3 for the L1 testing location was for the H = 0.20 m, T = 1.4 s wave signal, and was 8188.95 Pa. The irregular wave condition of H_{m0} = 0.15 m, T_p = 1.2 s produced a maximum peak pressure in P3 of 14121.40 Pa.

Interesting behaviour was noticed for the L3 testing location, during wave conditions with a low surf similarity parameter. During these tests, positive X-forces, and negative Z-forces eclipsed the forces generated in the L1 location. This implies there may be a location between the toe and SWL where the forces and pressures are at maximum; this is in agreement with the results shown by Hofland et al. (2018).

It can also be noted there is a drop-off in the peak pressures recorded on the back of the unit, as the surf similarity is reduced past a certain point. It was seen both visually during testing, from the results, that the complex flows produced by the most plunging waves generated high turbulence in the flow. This dissipated the run-up energy. The run-down then resulted in lower pressures on the back of the unit.

4.8.5 Effect of Steepness

Due to the wide range of wave conditions, it was possible to analyze the effect of steepness while keeping a constant wave height. Figure 63 shows the relationship between wave steepness and the mean peak hydrodynamic X-forces (F_{Hx}) during each test with both H = 0.12 m H = 0.15 m. This set of data includes a range from $0.007 \leq s_0 \leq 0.049$.

Figure 63 shows that waves with higher steepness, will produce a larger hydrodynamic response. This was true for X-forces, Z-forces and pressures. Do to the minimal exposure to wave impacts, units in the L2 testing location appeared to have been influenced less by the wave steepness, especially for $s_0 \approx 0.02$ or less. For both L1 and L2 testing locations, the effect of steepness was highly linear on the induced hydrodynamic forces, as can be seen in Figure 63. These results are in direct agreement with the notions proposed in Van der Meer (1988), other similar studies, and empirical formulations. These results also correlate directly with the results of Sakakiyama (1990), shown in Figure 13.

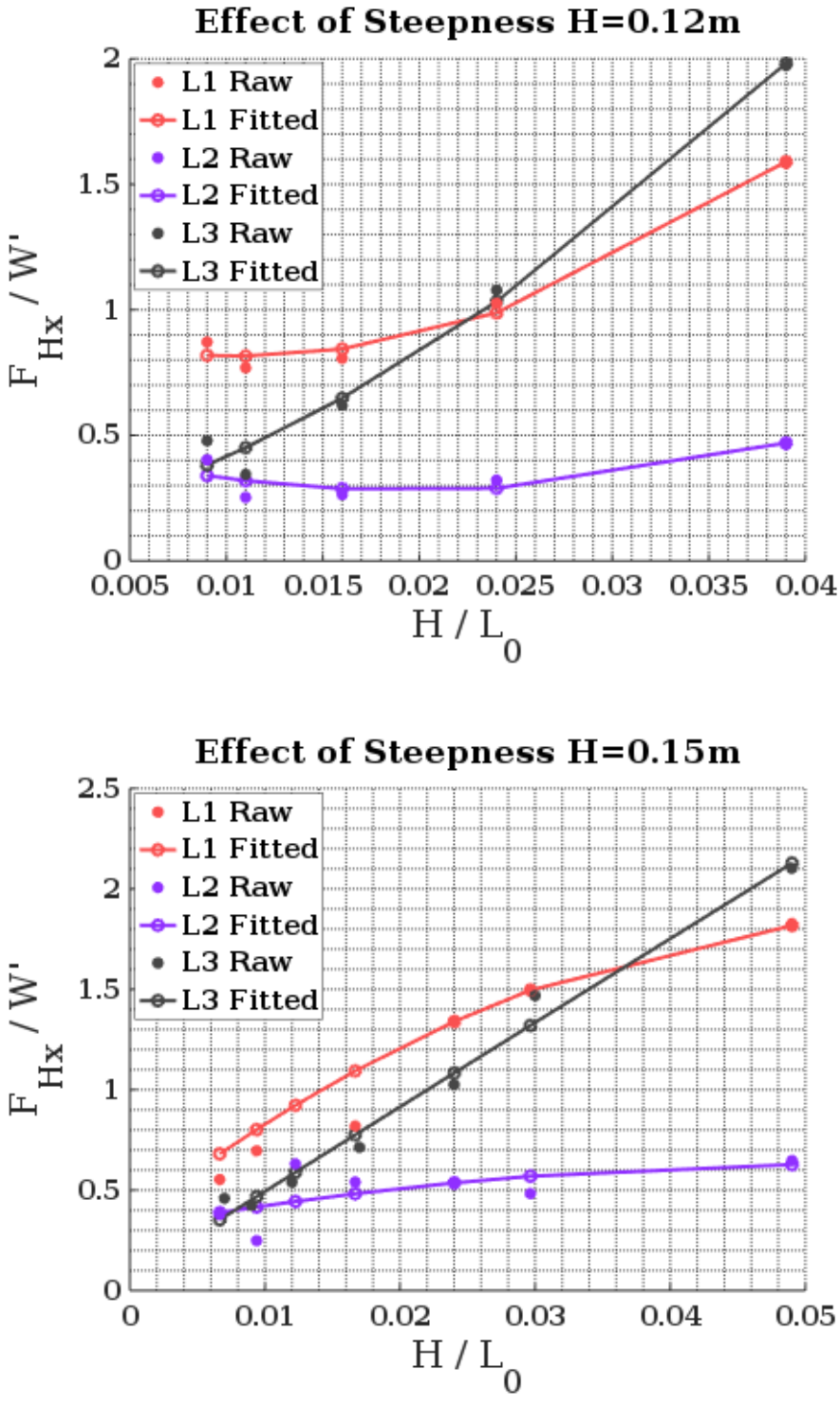

Figure 63: Normalized Hydrodynamic X-Forces vs. Wave Steepness at all Testing Locations, for Regular Waves of Heights 0.12m and 0.15m

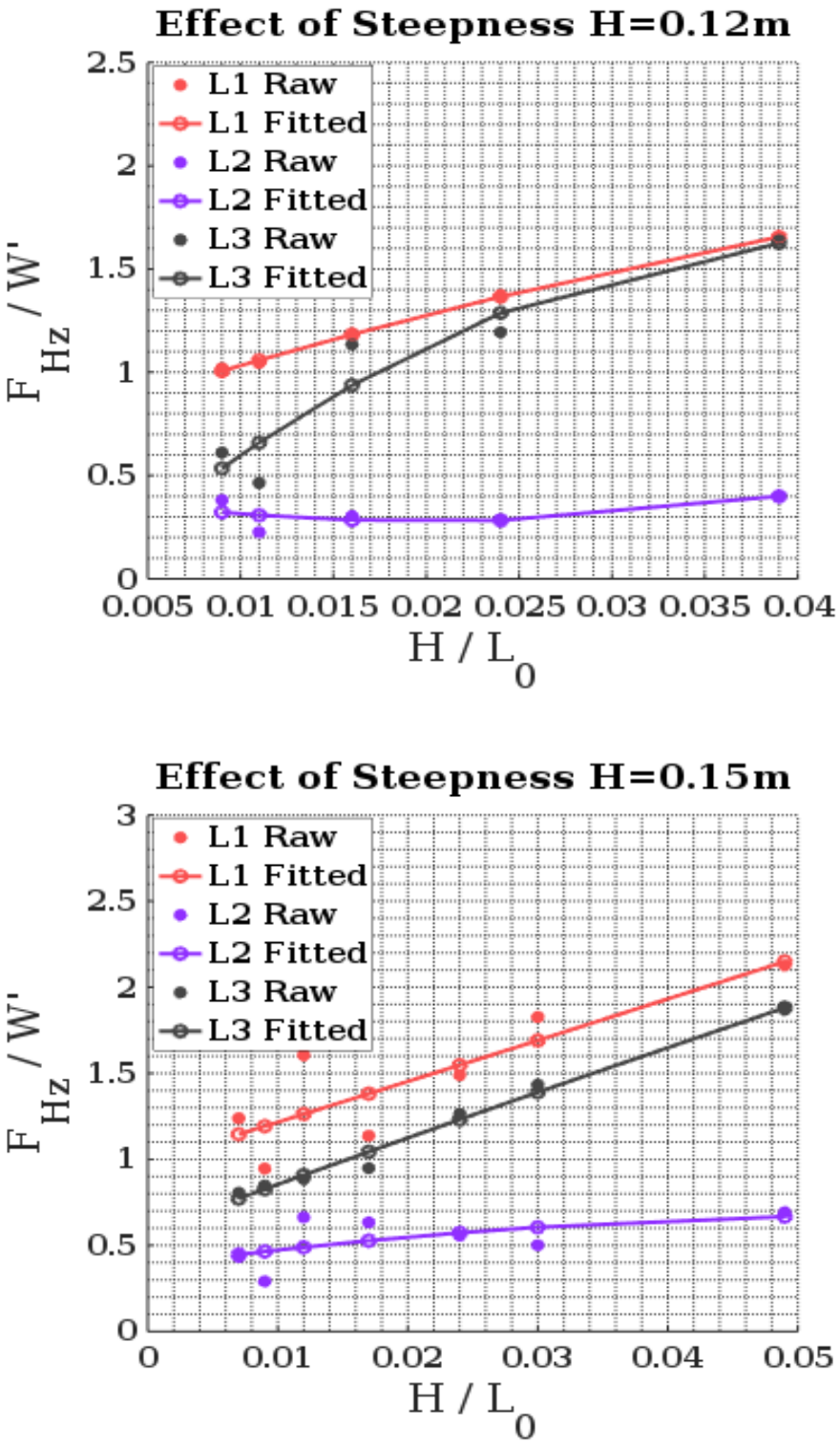

Figure 64: Normalized Hydrodynamic Z-Forces vs. Wave Steepness at all Testing Locations, for Regular Waves of Heights 0.12m and 0.15m

4.8.6 Effect of Location

The effect of unit location can be seen from Figures 60, 61, 62, 63 and 64. These plots, that are all color coded by location, show clear differences in the forces and pressures between each testing location. It is clear from the results that L1 generally experiences the most extreme hydrodynamic response to the wave conditions. L1 and L3 testing locations produced similar X-forces in the positive direction; as mentioned previously, multiple L3 wave conditions with low surf similarity surpassed generated forces at L1. Forces in the negative X-direction were greatest for L1, least for L2. In general, the L1 location produced the highest Z-forces, in both the negative and positive directions. Again, some L3 wave conditions with a low surf similarity exceeded that of L1. The L2 testing location produced the forces, and showed the least variability between different wave conditions. As mentioned previously, the fact that L3 forces exceeded L1 for several tests, it implies there is a location below the SWL that produces the highest forces, as suggested by Hofland et al. (2018).

The unique hydrodynamic behaviour, and induced flow patterns discussed in Section 4.8.2 resulted in behaviour in force signals that were unique to the L3 location; particularly for Z-forces. This unique behaviour was especially prominent in H = 0.15 m waves, with periods of $T \geq 2.8$ s. Time histories of F_{Hz} for two different wave signals are shown in Figure 65. It can be seen that the case for H = 0.15 m, T = 2.8 s the hydrodynamic interaction lasts for a longer duration, and includes a "double peak" shape. This double peak is due to the complex interaction of the run-down and incoming wave at this location, as discussed in Section 4.8.2.

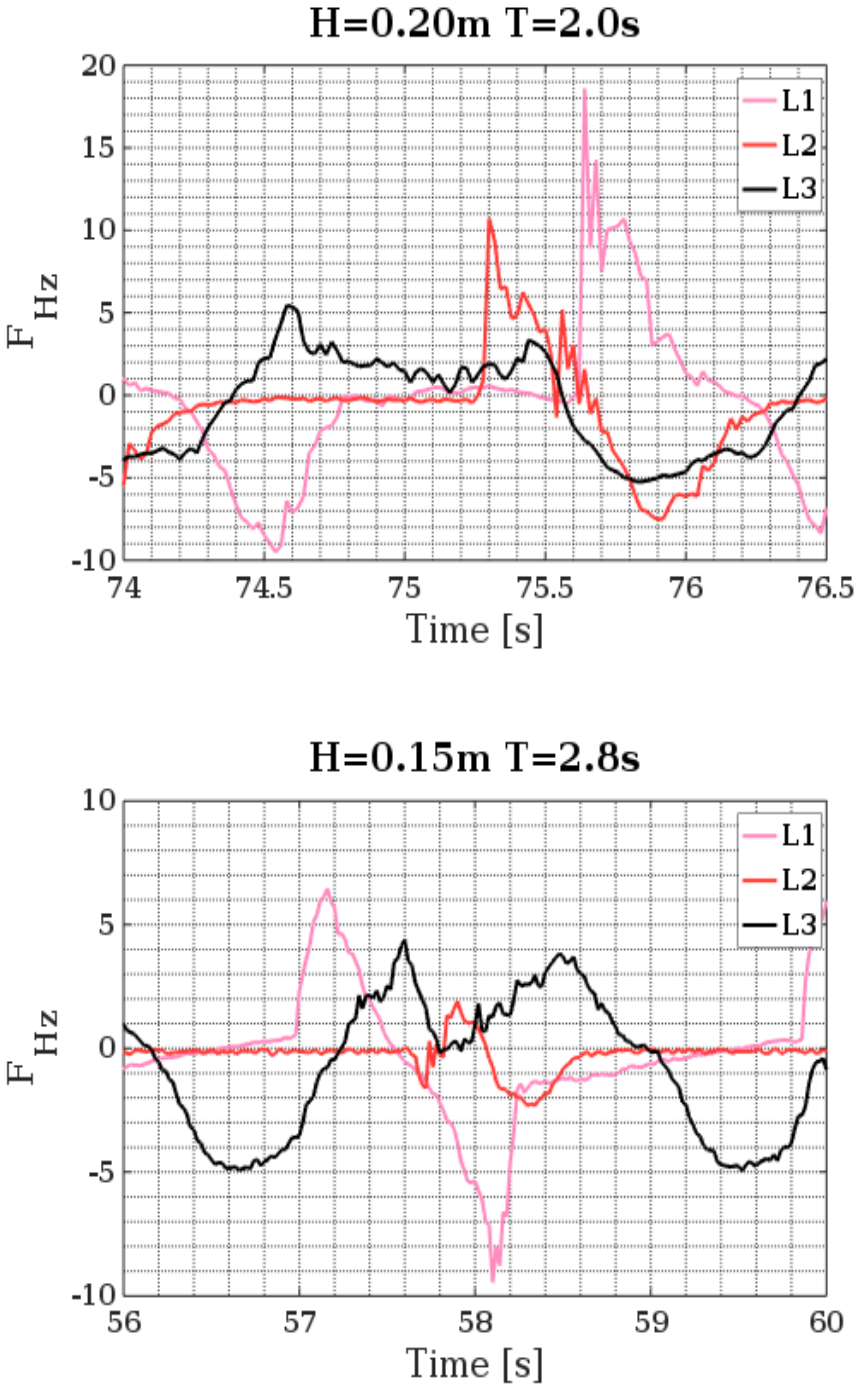

Figure 65: Comparison of Two Regular Wave Signals (H=0.20m, T=2.0s and H=0.15m, T=2.8s) at Each Testing Location

4.8.7 Hydraulic Stability

The balance of forces governs the stability of armour units. Destabilization forces are generated by hydrodynamic interaction during wave attack. In real breakwaters, these forces can also include impacts from other units, as well as other complex phenomena previously discussed. Stabilization forces are generated by the weight of the unit, and friction with the slope. In real breakwaters, these forces also include interlocking, or other stabilization mechanisms. As shown in the previous section, stabilizing Z-forces can also be generated by the hydrodynamic interaction.

For the purposes of these simplified experiments, these additional stability mechanisms are not present. Thus, the hydraulic stability of the unit is a function only of the hydrodynamic forces, friction, and unit weight. A generalized free-body-diagram of a unit during an SSU test is shown in Figure 66:

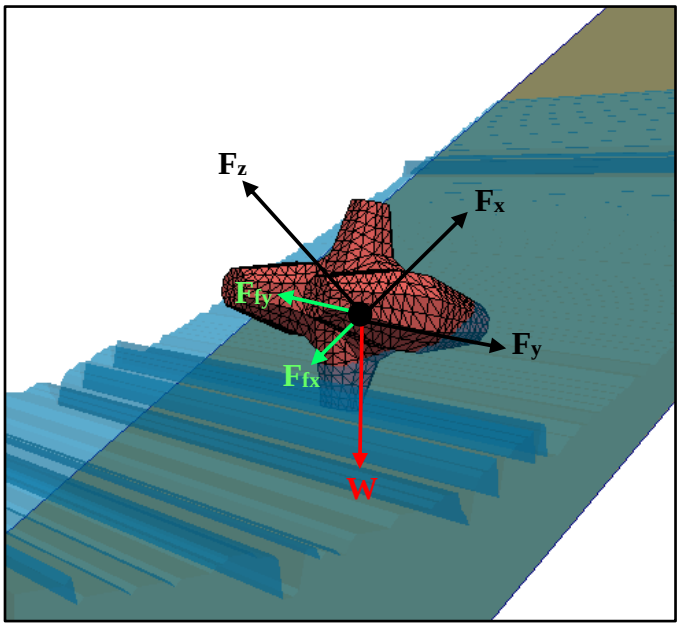

Figure 66: Idealized Free-Body-Diagram of Unit during Wave Attack in SSU Tests

For the purposes of this section, the stability of the instrumented Core-Loc unit will be determined assuming ρ_a=2400 kg/m^3. The balance of weight, induced forces, and frictional forces with the slope governs the stability in the X-direction. The frictional forces are in turn governed by the weight of the unit, and the coefficient of static friction with the slope. During positive X-forces, the weight of the unit will stabilize the unit as the weight will act in the negative direction. During negative X-forces, the unit becomes unstable due to this effect. The stability in the Y-direction was considered to be negligible, as symmetric testing conditions were present, and generated Y-forces were low in magnitude. The stability in the Z-direction is governed solely by the weight of the unit versus the induced uplift.

Thus, to estimate the weight of the unit required to remain stable (W), the following expression can be used:

$$W = \max \begin{cases} \dfrac{F_x}{\mu_s \cos(\theta) + \sin(\theta)} & for\ positive\ X - forces \\ \dfrac{F_x}{\mu_s \cos(\theta) - \sin(\theta)} & for\ negative\ X - forces \\ \dfrac{F_z}{\cos(\theta)} & for\ positive\ Z - forces \end{cases} \quad (46)$$

The coefficient of static friction, μ_s, is estimated to be 0.65. This value was prescribed by USACE (1992). This was chosen to be indicative of a friction coefficient between concrete and a gravel under-layer. Once the force balance approach has been applied, the resulting unit weights were then compared to CLI Design Guidelines. These guidelines prescribe the use of Hudson's Equation; a modified $K_D = 13$ was used to account for the foreshore bathymetry slope of 3%, as described in Section 2.3.2. Table 16 lists the calculated unit weights using both the force balance approach, and Hudson's Equation. Regular wave tests used mean peak force values, while irregular wave tests used maximum peak values for the force balance calculations.

Table 16: Summary of Calculated Design Weights vs. Hudson Equation

Wave Type	H / H_{m0} [m]	T / T_p [s]	W Force Balance [N]			W Hudson [N]
			L1	L2	L3	
Regular	0.12	1.40	10.86	4.27	12.70	0.86
	0.12	1.80	11.16	2.64	7.98	0.86
	0.12	2.20	10.41	2.36	5.63	0.86
	0.12	2.60	9.61	3.62	4.76	0.86
	0.12	3.00	9.21	3.97	6.01	0.86
	0.15	1.40	14.79	6.18	13.38	1.67
	0.15	1.80	13.61	5.36	10.97	1.67
	0.15	2.00	12.21	5.23	10.34	1.67
	0.15	2.40	10.22	5.80	7.99	1.67
	0.15	2.80	12.17	6.64	9.90	1.67
	0.15	3.20	9.53	3.68	8.73	1.67
	0.15	3.80	10.70	5.31	8.59	1.67
	0.20	1.40	18.84	11.05	16.47	3.96
	0.20	2.00	16.12	12.23	10.62	3.96
Irregular	0.15	1.20	59.80	17.03	33.14	1.67
	0.15	1.80	43.53	17.12	38.09	1.67
	0.15	2.2	32.23	11.38	24.84	1.67
	0.15	2.6	24.00	13.98	22.82	1.67

The regular wave conditions in Table 16 are also graphically depicted in Figure 67. It can be seen that the Hudson Equation grossly underestimates the required design weight for the single exposed unit, for all conditions.

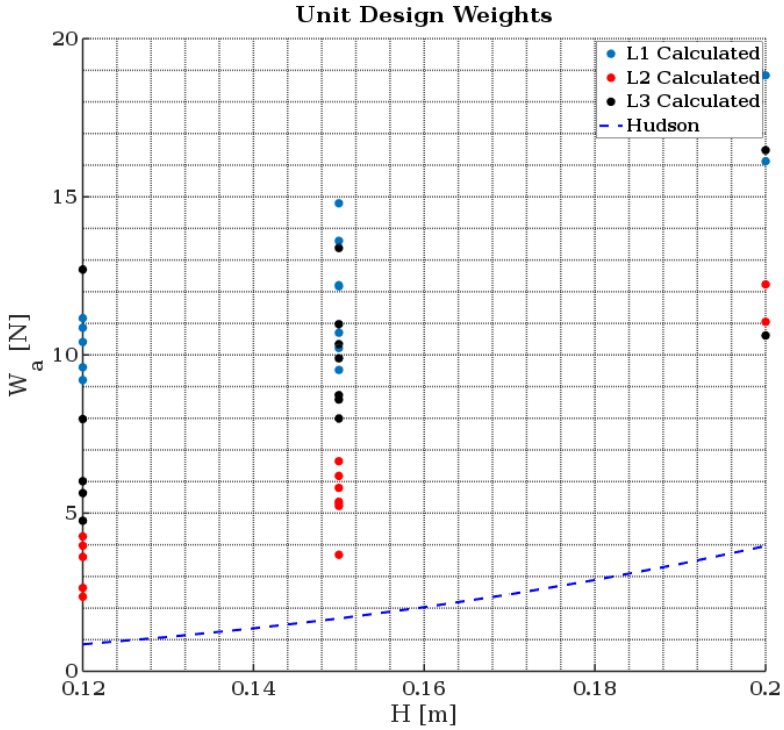

Figure 67: Armour Unit Design Weights Calculated Via Force Balance Approach vs. The Hudson Equation for Regular Waves

However, this was expected as the current study has an experimental setup that did not include surrounding units. This removes the Core-Loc's key stabilizing factor: interlocking forces. Thus, not only was the exposed unit subjected to far greater hydrodynamic forces than would be expected in a full breakwater, but the unit also did not have surrounding units for stability. This resulted in a highly unstable situation; the inadequacy of Hudson's Equation when applied to the exposed unit shows this result.

What is interesting about the testing results when compared to Hudson's Equation is not necessarily the difference in final weight; it was expected that Hudson's Equation would underestimate the weight for the SSU setup. But, there are significant differences in induced forces, and calculated design weights for constant wave heights as period is varied. This proves that Hudson's Equation is not able to capture the full design conditions in its' simplified form. Many different forces can be generated from a single wave height, while the Hudson's Equation only considered wave parameter is height. Not only this, but it is obvious from the aforementioned results, and the calculated design weights, that different locations along the slope will have different stability. This variation of forces and stability along the breakwater slope is not captured in the Hudson's Equation.

Generally speaking, L2 was the most stable. L1 was the least stable, and L3 fell between the two other locations.

These results show that there are complex hydrodynamic interactions and relationships occurring. With further testing in full breakwater settings, this force-balance approach could provide more stable designs and improved design equations.

4.8.8 Repeatability of Results

Highly complex and variable hydrodynamic behaviour was observed during testing, even for regular wave tests. In addition, the chosen sampling frequency (50Hz) poses the concern as to whether the measured results are reflective of the actual peak conditions and are repeatable. In order to assess the repeatability of the measured results, each test was repeated at least once. A number of additional "incomplete" test results were available; all data available was incorporated into the final analysis and are reflected in the results presented thus far. In order to assess the repeatability of signals, and the effect of sampling frequency, the most extreme wave tests were repeated up to 5 additional times at the highest sampling frequency possible with the instrumented unit. The plot shown in Figure 68 shows a SSU_L1_H20_T1P4 test pressure time series for 50Hz and 320Hz sampling rates. There are considerable differences between the peak pressures observed at the different sampling rates. This indicates that the peak pressures induced during wave impact influence the unit for much less than 1/50s. Additionally, there is significant variation in the peak results even when comparing the 320Hz time series. This indicates that the sampling frequency should be increased to accurately capture peak pressures, and to obtain more repeatable results. This change of sampling frequency would increase the recorded peak values of pressures and forces.

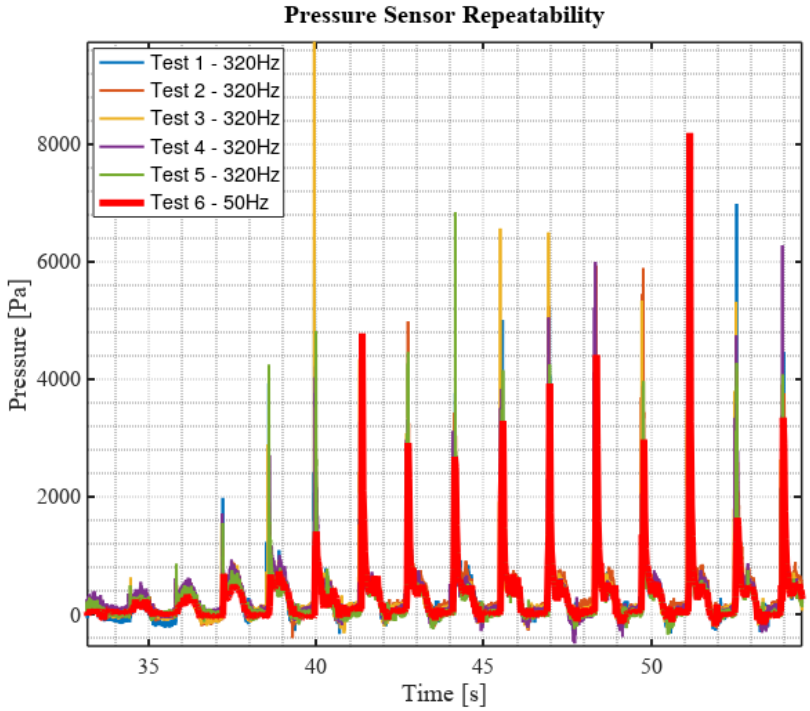

Figure 68: Repeatability of Pressure Signals for Different Sampling Rates – Example test shown SSU_L1_H20_T1P4

4.8.9 Scaling of Results

Typically, scaled breakwater testing aims to model a prototype breakwater at a specified geometric scale. Given that the focus is to accurately model the forces acting on the armour layer and individual units, Froude scaling can be used to determine the prototype-model scaling relationships. Likewise, model results can be scaled to prototype conditions using the same Froude scaling relationships. The current study took a modified approach, in the sense that geometry was limited by the size of the instrumented unit and the SWF, wave conditions were limited by the wave-maker capabilities, and there was no prototype breakwater that was being scaled down. In addition, it is important to note that the focus of the current study was to develop new measurement technologies and to assess their performance in a simplified setting before being used in more realistic scenarios. Instead, the size of the unit and maximum wave conditions that could be achieved were compared to CLI manufacturer guidelines, CLI (2012), in order to assess if testing conditions were achieving design conditions. Based on a 1:25 geometric scale, CLI (2012) dictates that (for the given foreshore slope of 3%) design wave conditions for the 0.12m instrumented Core-Loc would have a model height of 0.24m. Given the maximum wave height of 0.20m that was tested, testing conditions were very close to design conditions for a 1:25 model-prototype scale. Scaling of observed results should follow Froude scaling relationships, and non-dimensionalized quantities as presented in the current study.

4.9 Discussion

The current study was able to make use of existing bathymetry in the SWF at NRC-OCRE, providing a realistic 3% foreshore slope. This, along with calibrated wave signals, provided a wide range of wave conditions at the toe of the slope. As shown in Table 14, there were 18 unique wave signals utilized in total; 14 of these were regular wave conditions, and 4 irregular. The wave heights ranged from 0.12 m, 0.15 m, and 0.20 m, while the periods ranged from 1.4 – 3.8 s. Figures 35 and 36 show the wide range of wave breaking conditions that were encountered at the toe; the resulting Iribarren numbers ranged from $2.93 \leq \xi_0 \leq 9.92$.

The 3 locations tested (L1, L2, L3) provided insight into the spatial distribution along the breakwater slope of forces and pressures induced on armour units during wave action. From the results presented in the previous section, it is clear L1 and L3 provide valuable information. However, L2 appears to have been near the extent of the run-up for some cases, and still very high up for others. This resulted in minimal hydrodynamic interaction and less valuable data. In order to improve the investigation on the effect of location, it would be preferable to have locations spaced closer together, and closer to the SWL.

The force transducer and pressure sensors on the instrumented unit provided meaningful insight into the hydrodynamic interaction of units. The data gathered has applications in determining force-balances on units, and can be used to calculate movement or rotation stability of individual units. The pressure sensor data provided quantification of the distribution over the unit's surface, which can be used for force proxy measurements, or

for input to a finite-element-model capable of modeling the internal concrete stresses. Only 4 of the 6 pressure sensors provided useable data for the SSU testing program. The other 2 sensors appeared to have been inadvertently damaged through testing, or from dust in the testing environment. This resulted in limited information on the front of the unit, however P3 was nearly perpendicular to the mean run-up direction, and provided meaningful data. Both the force and pressure data provide a novel dataset that can be, and is, being used for numerical validation of coastal modeling tools.

The meticulous lighting arrangement at the slope location provided favourable contrast between the unit and water body; this provided images that were easily handled by the image processing tool. These images worked well with the single value threshold technique, converting gray-scale images to binary images that were used to track the water surface. The image processing technique was able to accurately track the water surface at the slope location, for the wide ranges of regular and irregular testing conditions encountered (Figure 46). This resulted in time histories ranging from 0 N to 3.748 N with a periodic pattern corresponding to the given testing condition. Irregular wave signals were much more variable and random, as depicted in Figure 49.

The image processing tool was used to calculate the buoyant force, and thus the hydrodynamic force from the total force. The hydrodynamics forces behaved similarly to the total forces, but were reduced slightly by buoyancy during wave action. This general behaviour is shown in Figure 50.

Due to the nature of the operations performed in VTK, the water surface was essentially a linear extrusion in the cross-flume direction. This means there was no spatial variability in the Y-direction for the image processing results. It is clear from Figure 47 that this variability is definitely present. In turn, the hydrodynamic forces were slightly underestimated during run-up, and slightly overestimated during run-down. This approach could have been improved by implementing a 3D image processing technique using additional cameras or more advanced techniques.

The full results from the peak statistical analysis are shown in Appendix A. This method provided peak forces and pressures that could be used for design purposes in a force balance approach.

For regular waves, the highest forces for all 3 testing locations were generated during an H = 0.20 m, T = 1.4 s testing condition. The mean X-forces in the positive direction were determined to be 15.95 N, 8.58 N, and 16.45 N for L1, L2, and L3 respectively. Similarly, Z-forces in the positive direction were determined to be 15.07 N, 7.92 N, and 13.12 N for L1, L2, and L3 respectively.

The highest pressures were also generated for the same H = 0.20 m, T = 1.4 s testing condition, for all locations. The maximum pressure recorded on the front of the unit (P3) was 8188.95 Pa, 2454.50 Pa and 1554.59 Pa for L1, L2, and L3 respectively. The maximum pressures on the back of the unit were recorded with Sensor P5, with a value of 2597.29 Pa, 364.67 Pa and 1439.76 Pa, for L1, L2 and L3 respectively.

While on average lower, the irregular wave conditions produced maximum peak forces and pressures that greatly exceeded anything encountered in the regular wave tests. The highest forces and pressures were generated for all locations with H_{m0} = 0.15 m, with either T_p = 1.2s or 1.8 s. Maximum peak X-forces in the positive direction reached 41.50 N, 30.68 N, and 42.66 N for L1, L2 and L3 respectively. Maximum peak Z-forces in the positive direction reached 47.84 N, 17.62 N, and 25.56 N for L1, L2, and L3 respectively.

The effect of surf similarity is shown in Figures 60, 61 and 62 through the modified non-dimensional parameter discussed in Section 4.8.4. From Figures 60 and 61, is it clear than a decrease in this parameter will result in an increase in forces for both X and Z-directions. As well, from Figure 62, pressures can be expected to increase. The result from the current study proves quantitatively that plunging breakers will induce larger hydrodynamic impact than waves with calmer breaking characteristics.

The effect of steepness is also closely tied to surf similarity, and is shown in Figure 63 and 64 for both 0.12 m and 0.15 m wave conditions. It is clear that there is a close relationship between wave steepness and the induced hydrodynamic forces. The results show that increased steepness leads to higher forces; this is in line with the work presented by Van der Meer (1988) in that higher steepness leads to instability.

L1 and L3 showed comparable hydrodynamic interaction, as seen in Figures 60 and 61. It appears from the results that the L3 location recorded higher positive X-forces, and negative Z-forces during the test conditions with plunging breakers. This leads to the thought that there may be a location between the SWL and the toe of the structure that receives the highest forces. This is proposed to be 2 rows below SWL by Hofland et al. (2018); it is apparent from the current study that this effect is still noticeable 4 rows below SWL. L2 only received appreciable hydrodynamic influence during plunging wave conditions. Unique conditions were encountered at the L3 location due to the influence of reflected waves at the toe. This lead to complex flow patterns and resulting force signals; these signals had a double-peak behaviour as shown in Figure 65.

As expected, CLI recommendations (Hudson's Equation) were not able to safely design the armour unit for the given exposed conditions. This was expected due to the fact that the unit was completely unprotected and did not have interlocking forces to aid its' stability. Figure 67 shows that the unit weights were grossly underestimated for all conditions. Notably, there is a spread of stable design weights for constant wave heights, using the force balance design approach. This is due to the fact that different wave steepness, and surf similarity will lead to different forces and pressures. This is not something that is taken into account in current design methods.

4.10 Summary and Conclusions

Based on the analysis of the results from the extensive SSU testing program at NRC-OCRE, it can be concluded that:

- A wide range of wave conditions were tested, with Iribarren numbers ranging from $2.93 \leq \xi_0 \leq 9.92$
- The chosen unit locations provided valuable insight into the effect of slope location on hydrodynamic interaction; the spacing could be tighter and closer to the SWL
- The image processing tool was capable of accurately tracking the water surface profile at the testing location, for all regular and irregular wave conditions
- The image processing tool was able to calculate the buoyant force and isolate the hydrodynamic force from the total force, for all test signals
- A peak statistical analysis was performed on the force and pressure signals, in order to extract key information and reduce the dataset for non-dimensional plots
- A reduction in surf similarity appeared to result in a drastic increase in generated forces in both the X and Z-directions; pressures increased in all sensors as well
- Steepness appeared to have a very close relationship with the generated hydrodynamic forces on the unit, increasing wave steepness lead to increased hydrodynamic forces
- While L2 provided meaningful data only during plunging wave conditions, the L1 and L3 locations showed similar results in terms of magnitude, but L3 had complex flow patterns due to reflection at the toe
- The tests showed that there may be a location below the SWL that is subjected to the highest impacts
- Standard design methods were not capable of designing the unit's weight for this exposed testing condition
- The variability of stable unit weight for a given wave height, as calculated by the force balance approach, showed standard design methods are highly idealized

5.0 Numerical Study – OpenFOAM Model

5.1 Computational Domain

The purpose of the numerical model was to replicate the results of the SSU Tests. Thus, the computational domain chosen for the numerical model was a full-scale replica of the SWF, from the location of WG5 to the end of the breakwater slope, Figure 68.

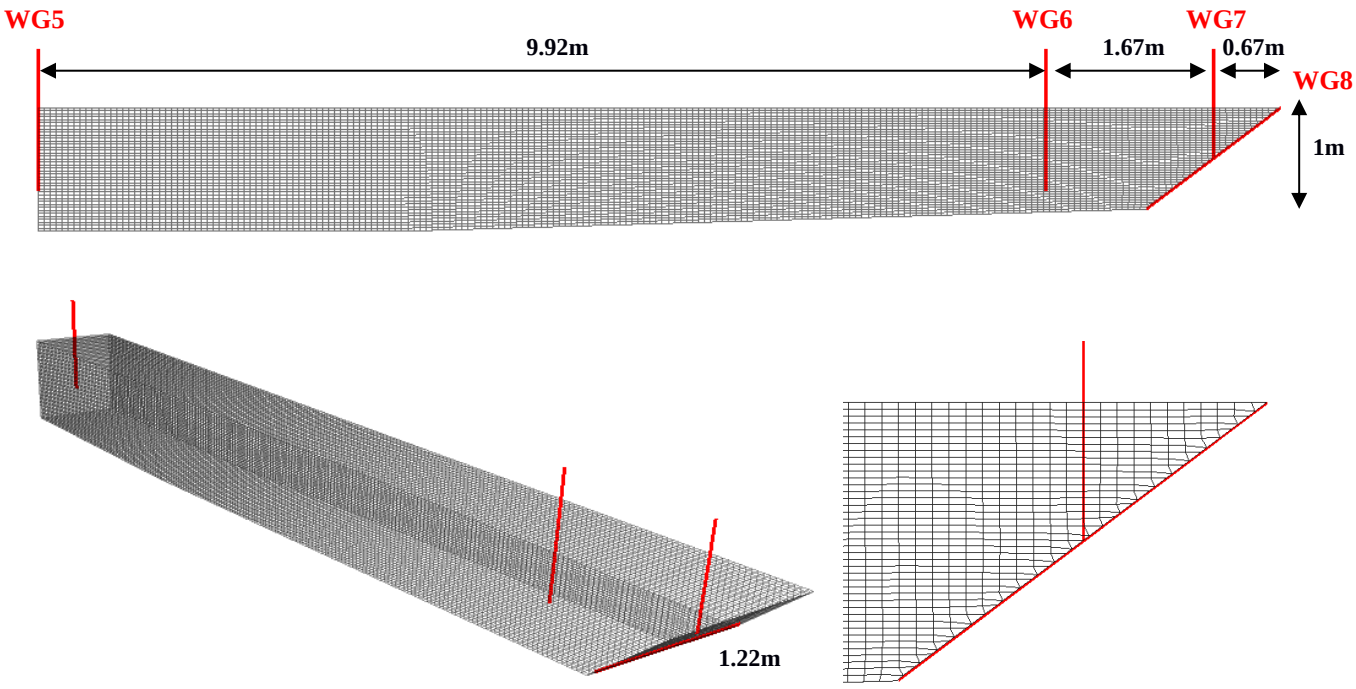

Figure 69: Computational Domain For Numerical Study (mesh size exaggerated for visual purposes)

The location of WP5 was chosen to truncate the extent of the domain. It was deemed acceptable to neglect the rest of the domain, as WP5 could be used as inlet conditions for the numerical model. This resulted in a 12.26 m long x 1.22 m wide x 1.22 m domain that included an offshore section, the 3% slope bathymetry, and the breakwater. This domain was meshed using OpenFOAM's blockMesh utility. The slope section is sliced and re-meshed along a numerical slope, using OpenFOAM's snappyHexMesh utility. This slope is meant to represent the breakwater slope. A general schematic of the computational domain is shown in Figure 68.

For all aspects of the numerical study, the mesh was kept structured and static. Key parameters were sampled at each time step while the solver was running. Numerical WGs were inserted into the numerical domain at WG5 and WG6 locations. These WGs

were placed to record time-histories of the phrase fraction (α). Two additional WGs (WG7 and WG8) were inserted into the numerical domain; one vertical at the unit centroid, and one along the breakwater slope, Figure 68. These phrase fraction recordings are then integrated along the WG direction, to provide the water depth at that location, for each time step.

A force sampling function provided within OpenFOAM was used to calculate the forces induced on the unit. This function integrates the total pressure on each cell face of the unit, and includes tangential viscous stresses across the units' surface to calculate the total force. Finally, numerical probes were used to sample the total pressure at locations around the units' surface that corresponded to P1-P6 locations.

The OpenFOAM results required for visualization purposes were recorded at 25 Hz, half of the sampling frequency used during the SSU Tests.

5.2 Initial Conditions

The solution to the transient Navier-Stokes equations requires boundary conditions for the fields of transport. Once the mesh is generated, initial values for the velocity, pressure, phase fraction, and turbulent quantities are set, using OpenFOAM's setFields utility. Since this case is considered static at initial conditions, only the phrase fraction need be defined. A constant phase fraction of α=1 was prescribed at t=0 for all cells contained within $Z \leq 0.72$ m (the offshore water depth in the SSU Tests). The total pressure and velocity fields will be calculated in the first time step according to the prescribed distribution of the phrase fraction and boundary conditions. This distribution is shown in Figure 69.

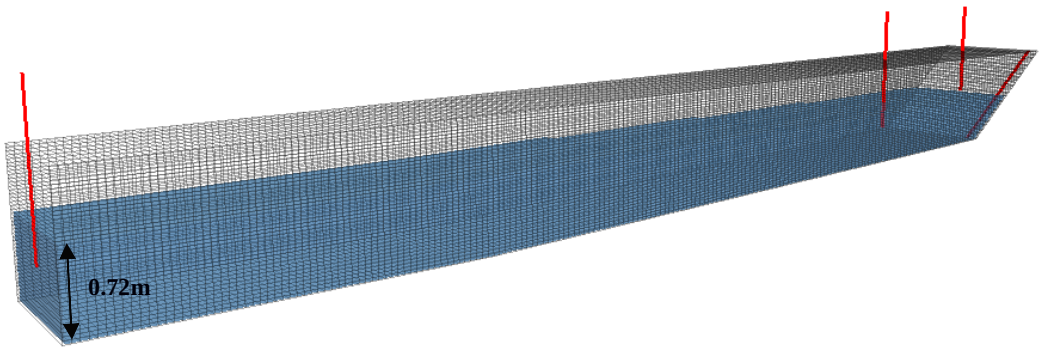

Figure 70: Initial Conditions for Phase Fraction (α)

5.3 Boundary Conditions

In addition to initial field values, boundary conditions must be provided at all cells forming the outer limits of the computational domain. The inlet, the flume walls, the flume bottom, the breakwater slope, the unit face, and the atmospheric opening represent these boundaries. Due to the nature of the set-up, the inlet also acts as the outlet.

For the inlet, OlaFlow boundary conditions were utilized. OlaFlow is a compilation of wave generation and absorption libraries that are compatible with the OpenFOAM interFoam (and interDymFoam) solver. OlaFlow provides wave generation boundary conditions for wave-makers, paddles, and various wave theories. OlaFlow's wave absorption boundary condition mimics the behaviour of real active wave absorption. Waves approaching the inlet from a negative direction are absorbed and consequently leave the domain, not affecting the flume conditions.

On the flume walls, the flume bottom, the breakwater slope, and the unit face, a fixedFluxPressure boundary condition was utilized to calculate pressure. This boundary condition adjusts the gradient of the pressure field perpendicular to the wall or face, to ensure the flux through that boundary is equal to zero.

Similar to the pressure field, a zeroGradient boundary condition is applied to the phrase fraction to ensure zero flux of the phrase fraction field through any of the listed walls or faces. Turbulence parameters are then calculated at these solid boundaries using applicable turbulence models.

The atmospheric opening of the flume is modeled using a totalPressure boundary condition; essentially applying a fixed value of zero for total pressure on any cells in this patch. A pressureInletOutletVelocity boundary condition is also applied to handle transport of the phase fraction through this boundary. When flow is directed outwards, the numerical solver utilizes the total pressure of zero condition as a cell face boundary, and elements of the phase fraction field leave the domain. When flow is directed inward, the total pressure of zero cell faces act as inlet condition. Thus, flow can leave the flume, but not re-enter the flume. In these cases, the "returning" flow is replaced by air in the computational domain. Luckily in all aspects of SSU Testing, this was not a concern.

5.4 Calibration of Numerical Parameters

In order to calibrate the numerical model, several key parameters were investigated. A comprehensive mesh sensitivity analysis was performed in order to observe the effect of different mesh size, to achieve mesh independent results, and to optimize the simulation time. Several different turbulence models were also utilized in this numerical study, and their performance investigated. Lastly, the wall function and wall roughness was varied on the unit.

5.4.1 Mesh Resolution

A structured grid was used in the calibration of the mesh resolution. It has been shown, through past numerical studies as part of the joint collaborative project, waves can be better preserved with cell aspect ratios of approximately 2 in the Z-direction. This "shorter" cell configuration reduces numerical diffusion of the waves, and reduces rapid "steps" in both the inlet conditions and propagating waves.

The calibration of the mesh resolution was completed with respect to inlet conditions, wave propagation to the slope, run-up behaviour, and the hydrodynamic interaction with the unit. This calibration procedure explored meshes with size 6x6x3 cm, 4x4x2 cm, 2x2x1 cm, 1x1x0.5 cm, and refinements of various degrees around the unit location.

The effect of mesh resolution on inlet conditions is shown in Figure 70 (top), for plunging (H=0.20cm, T=1.4s) wave conditions. This corresponds to WG5 location.

It can be seen that while period is maintained, there are large "steps" in the water surface. The 6x6x3 cm mesh does not accurately preserve the height of the wave, and corresponding water surface. The 4x4x2 cm mesh performs better, however the results are still not desirable. It can be seen that the 2x2x1 cm mesh performs adequately when compared to the experimental wave signal. The 1x1x0.5 cm mesh resolution performs best, however the additional computing time was not justified when compared to the 2x2x1 cm mesh and was subsequently dropped from the calibration.

The numerical results of wave propagation are shown in Figure 70 (bottom), at the WG6 location. Similar to the inlet location, the 2x2x1 cm mesh was deemed acceptable for further testing and is shown against the experimental signal.

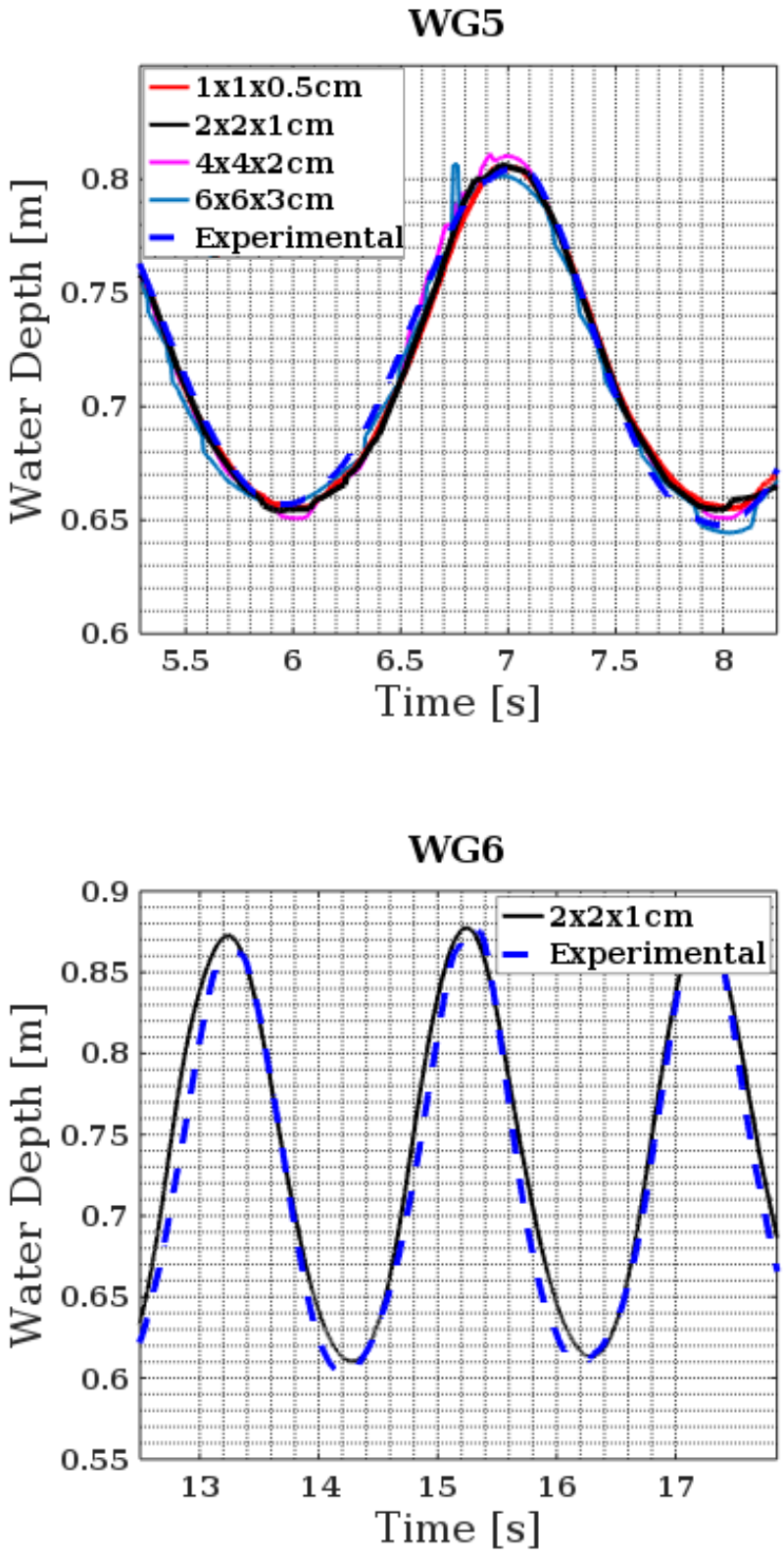

Figure 71: Results of Mesh Resolution Calibration for SSU_L1_H15_2P0 at Inlet (top) and at the toe location (bottom)

Run-up depth at the unit location was also investigated with respect to mesh size. In order replicate SSU results, the numerical model must accurately represent the hydrodynamic impacts of the wave run-up. The effect of mesh resolution on run-up depth at the unit location is shown in Figure 71, this is compared to experimental data augmented from the image processing results.

During the image processing phase, the water surface was tracked along the entire processing window, therefore it was possible to simply plot a time history of the water surface at the centroid of the unit, or the numerical WG7 location.

It can be seen from Figure 71 that the 2x2x1 cm mesh performed favourably against the experiment data. Both of the larger mesh sizes were incapable of accurately modeling the run-up depths at the unit. Once the waves begin to stabilize (≈13 s), the 2x2x1 cm mesh is able to replicate the experimental results with an average error of 1.78% between peak values.

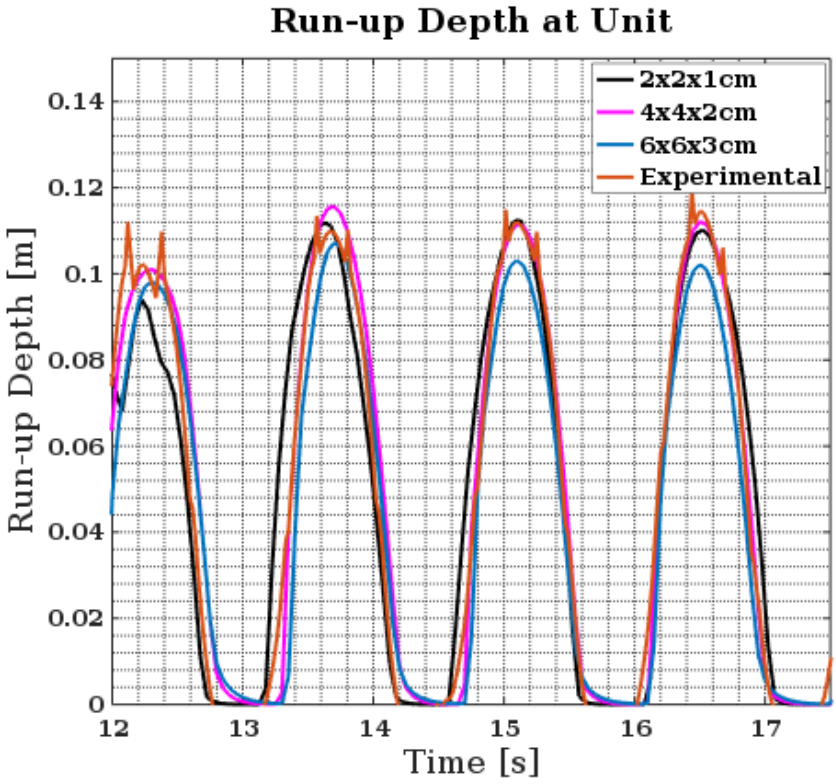

Figure 72: Mesh Resolution Calibration for Run-up Depth at Unit (WG7) during SSU_L1_H15_T1P4 Test Condition

A cubic region surrounding the unit was further refined. This refinement region would then be able to capture the high velocity, highly turbulent flow patterns expected in the simulations. A prismatic refinement region was defined, encompassing the unit and the domain within a 0.24m box centered at the unit location. Once the region had been refined, the mesh of the unit was then incorporated using OpenFOAM's snappyHexMesh utility. This process was similar to the process outlined in Section 5.1. Figure 72 depicts this refinement region, and the results of the snappyHexMesh utility.

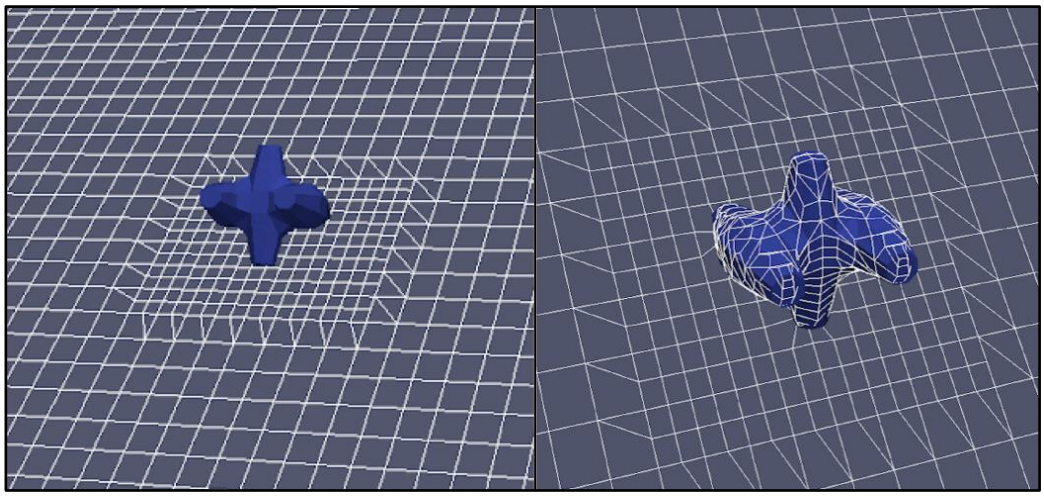

Figure 73: Refinement Region around Unit in and Results of snappyHexMesh Utility

The results captured by the refinement region are subjected to the level of refinement that is prescribed during the meshing process. The higher the level of refinement, the higher the accuracy will be. This will also be coupled with drastically increased computation time, and larger courant numbers.

The level of refinement around the unit was chosen by analyzing the effect of mesh resolution on the force acting on the unit. In order to choose the mesh resolution, a qualitative analysis was done with respect to mesh independence.

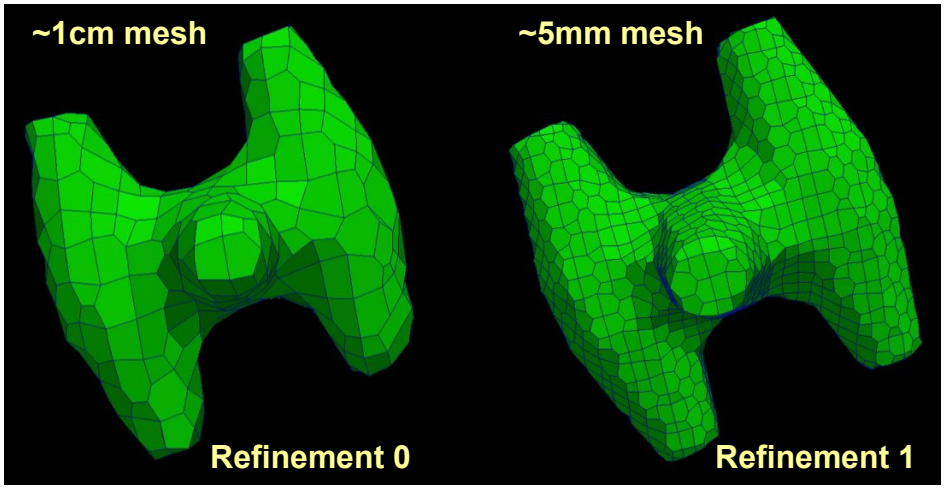

Figure 74: Mesh Refinement Around Unit with Factor of 2 (1x1x1 cm) and 4 (0.5x0.5x0.5 cm)

Figure 73 shows two different levels of refinement around the unit, by factors of 2 and 4. Given that the chosen base mesh is 2x2x1 cm is size, the resulting meshes for the levels of refinement shown in Figure 73 are 1x1x1 cm and 0.5x0.5x0.5 cm in size.

The results of this investigation showed that the overall shape of the unit could be maintained to an acceptable degree of accuracy with cubic cells ≈ 1cm in height. This level of refinement is capable of providing the snappyHexMesh utility with enough nearby domain node points to "snap" to the mesh node points, resulting in a preserved unit shape. The preservation of the unit shape is shown in Figures 72 and 73.

These two levels of refinement around the unit were then tested with a SSU_L1_H15_T2P0 wave condition. Figure 74 shows the resulting X-Force acting on the unit.

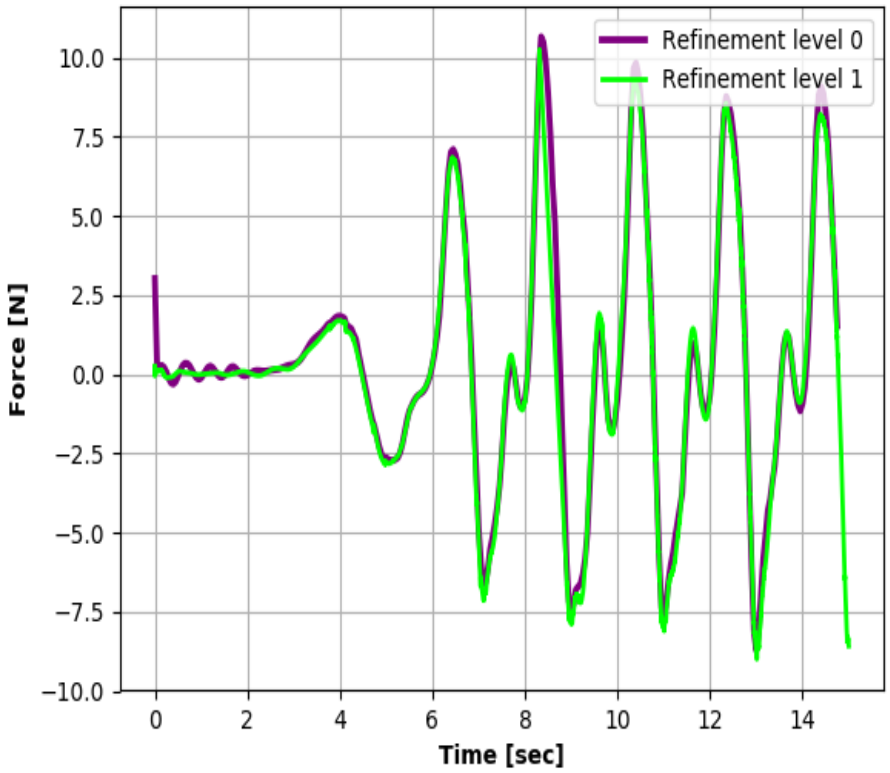

Figure 75: Calibration of Mesh Resolution for Refinement Region Around Unit, X-Force during SSU_L1_H15_T1P4 Test Condition

Figure 74 shows that mesh independence can be reached for the force signals by using a refinement region around the unit with cubic cells ≈ 1cm in height. There appeared to be no appreciable difference between the results when comparing the force signal for both levels of refinement.

Based on the analysis of the results presented thus far, the mesh resolution to be further calibrated against the experimental data was chosen to be 2x2x1 cm for the flume, with 1x1x1 cm cells around the unit.

For further calibration, a single test condition of SSU_L1_H12_T3P0 was chosen. This signal was chosen due to the high period; resulting in less extreme conditions and thus manageable computation times. This signal still produced relatively high forces and pressures during the experimental testing, and was considered an ideal dataset for validation due to the smooth nature of the signal.

5.4.2 Turbulence Model

The typical approach to modeling turbulence numerically is the eddy viscosity approach. During the calibration of the turbulence model, three different models were tested. Each of these turbulence models are two-equation models, whose solutions are used in determine the viscous stress tensor in the momentum equation (Equation 28). The three models selected for this study (previously discussed in Section 2.5.3) are: the standard $k-\varepsilon$, $RNG\ k-\varepsilon$, and $SST\ k-\omega$ models. The resulting time histories for pressure on Sensor P3 during a SSU_L1_H12_T3P0 test condition is plotted versus the experimental data in Figure 75.

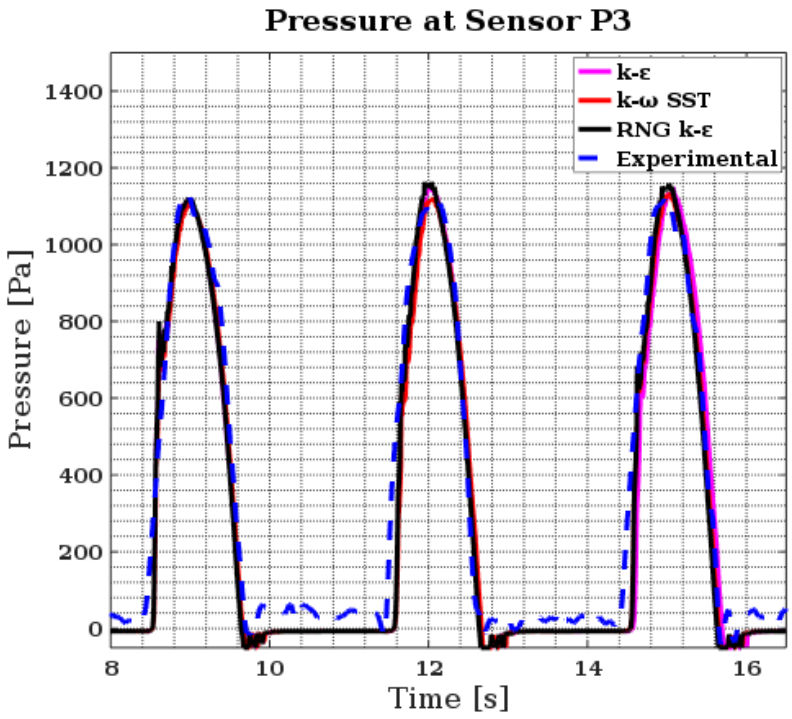

Figure 76: Comparison of Turbulence Models for Pressure on Sensor P3 During SSU_L1_H12_T3P0 Test Condition

The results of the turbulence model comparison showed no significant differences between the models for this test condition. It can be seen that small negative pressures ≈ -50 Pa or greater are generated during wave impact in the numerical models. This behaviour does show up in the experimental data as well, however the numerical model appears to slightly overestimate this effect. In the experimental signal, negative pressures were ≥ -10 Pa and considered to be noise or hysteresis error.

Both the $RNG\ k-\varepsilon$, and $SST\ k-\omega$ turbulence models appear to slightly overestimate the peak pressures during wave impact. At approximately t = 12 s, the standard $k-\varepsilon$ model appears to match nearly perfectly with the experimental results. Meanwhile, both of the other models overestimate the pressure by approximately 40 Pa, a 3.57% error.

While no major discrepancies were encountered from any of the tested turbulence models, the best agreement was seen with the standard $k-\varepsilon$ model; this model was the one chosen for further testing.

5.4.3 Wall Function

The effect of wall roughness on the simulated forces and pressures was explored as part of this numerical study.

The state of a concrete armour unit will degrade constantly over time. If there is significant wave action, or unit-unit interaction, the outer surface of the units may become rough. Theoretically, rougher surfaces will lead to higher generated shear forces on the unit, and thus higher total forces.

The effect of wall roughness in the numerical model is shown in Figure 76 for smooth, 1 mm, and 2 mm wall roughness heights. This data is shown against the experimental results for X-forces during a SSU_L1_H12_T3P0 wave condition.

It can be seen that, in general, there is very good agreement between the generated forces. There are some minor undulations that occur in the experimental signal that do not occur in the numerical, but they are not of any relevance for analysis.

As expected, higher wall roughness led to higher generated total forces. The general behaviour was identical for the three cases, but increased slightly in magnitude as wall roughness increased. The 2mm case resulted in a peak X-Force approximately 0.1 N (1.97%) greater than the smooth case, on average.

The behaviour of the numerical signal was also similar to the experimental data. Figure 76 shows a similar 3-plateau type shape between the numerical and experimental signals at each peak. The second plateau in the numerical results appears to last twice as long (≈ 0.1 s in total), while the first and third plateaus last less than half as long (≈ 0.03 s in total) than the experimental signal.

There were no major differences between the results for the three tested roughness heights. During unit printing, construction and sealing, the surface lost some of its original smoothness. Upon inspection of the unit during and after testing, it appeared a fair value to assume as roughness height was 1mm. This is the wall function chosen for further testing.

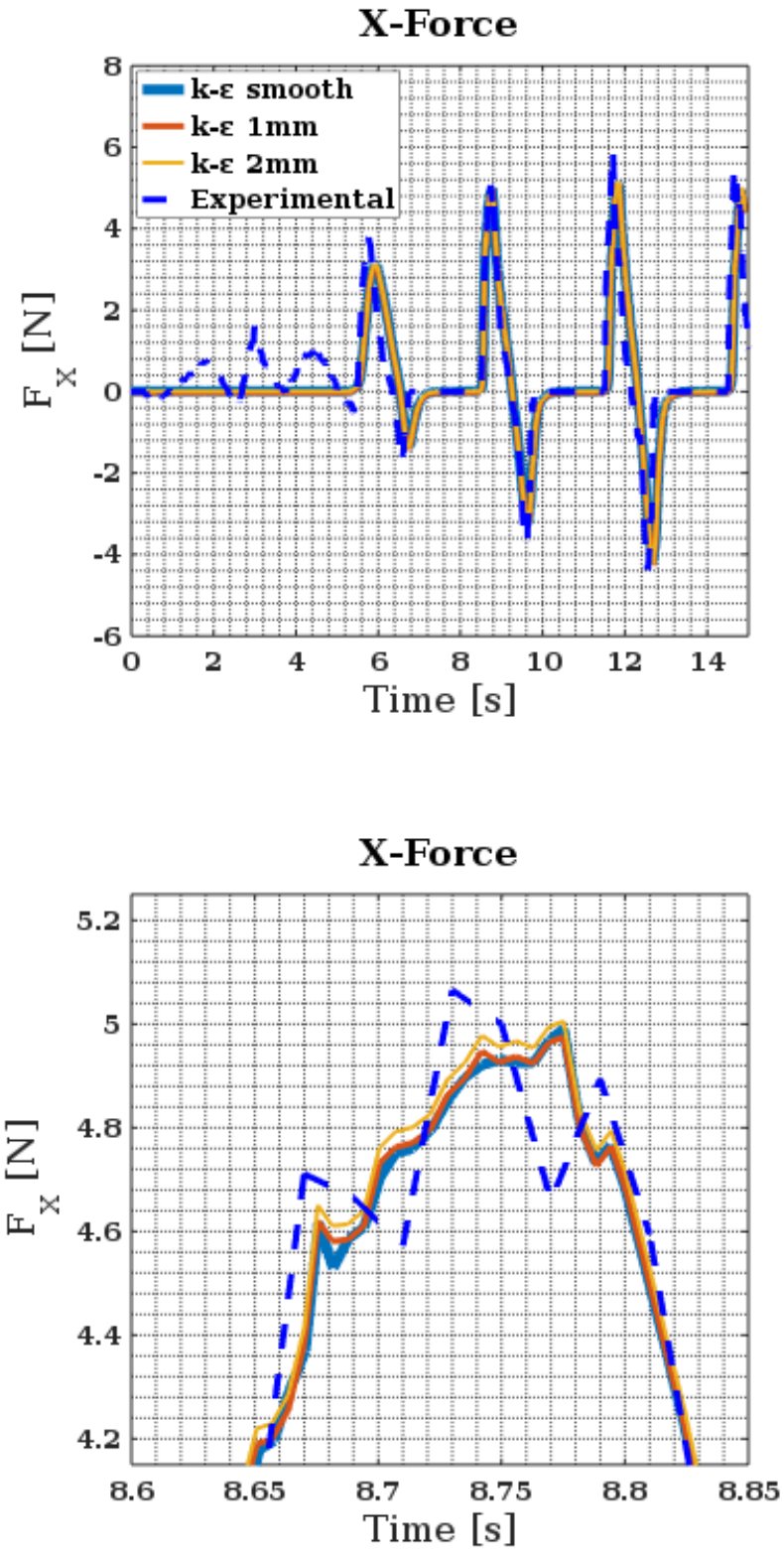

Figure 77: Comparison of Wall Roughness Height on X-Force for SSU_L1_H12_T3P0 Test Condition

5.5 Comparison of Calibrated Model

The calibrated model was constructed using the lessons learned from the mesh sensitivity and refinement analysis, the turbulence model analysis, as well as the wall function analysis. The calibrated model utilized a 2x2x1cm mesh resolution. The mesh was further refined at the unit location, in a box centred and surrounding the unit with a side length of 0.24 m. This box was refined to a cubic resolution of 1x1x1 cm, as described in Section 5.4.1. A standard $k - \varepsilon$ model was utilized as a turbulence model, and a roughness height of 1mm was used in the description of the wall function.

Through the mesh sensitivity analysis, it was clear that the numerical model was capable of reproducing the wave conditions to a reasonable degree of accuracy. It was also proven that the numerical model is capable of preserving wave conditions to the slope, and reproducing run-up levels at the unit with reasonable accuracy.

Thus, the validation between the numerical and experimental results is focused mainly on the general hydrodynamic behaviour, the forces and the pressures.

Figure 77 shows a comparison between a rendering of the numerical results, and an image during the experimental testing for an SSU-H12-T3P0 test condition.

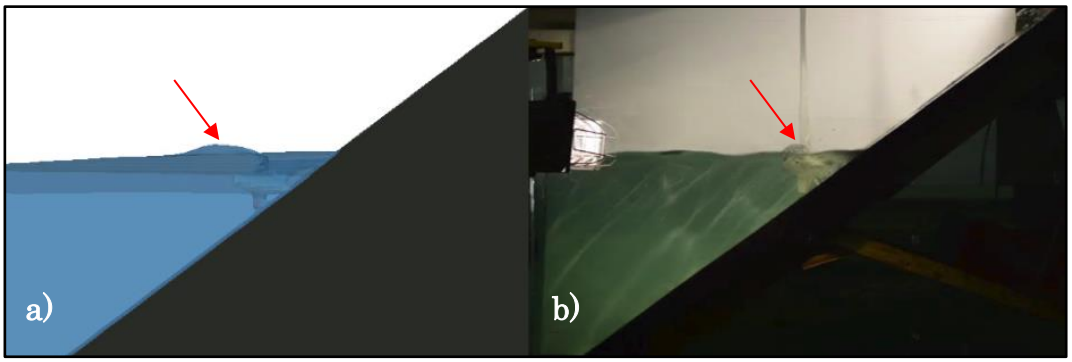

Figure 78: Comparison Between Calibrated a) Numerical Model and b) Experimental Results for SSU_L1_H12_T3P0 Test Condition

One can observe a small bulge in front of the unit (red arrow) in both the numerical and experimental images. This is due to the impact of the wave on the front of the unit. It can be seen from Figure 77 that this bulge was captured by the numerical model, but is slightly overestimated in spatial extent.

Figure 78 shows a comparison for the same SSU_L1_H12_T3P0 test condition, facing the front of the unit. Impressively, the numerical model was able to capture the highly complex and turbulent flow patterns around the unit. The general shape of the run-down is captured, while the flow under the unit and over the unit is also captured. This shows that, upon first analysis, the chosen level of mesh resolution and refinement around the unit was adequate for reproducing the experimental conditions.

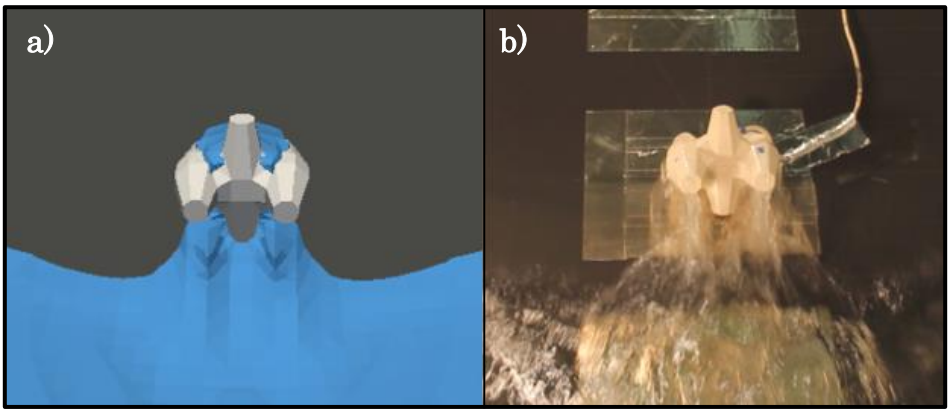

Figure 79: Comparison of Flow Around Unit between a) Calibration Numerical Model and b) Experimental Result for SSU_L1_H15_T3P0 Test Condition

Figure 79 shows a rendering of the numerical results generated using ParaView, showing the general hydrodynamic behaviour of the wave signal, and the pressure distribution on the unit during wave impact. The signal shown is the same SSU_L1_H12_T3P0 signal that was used for validating the numerical model.

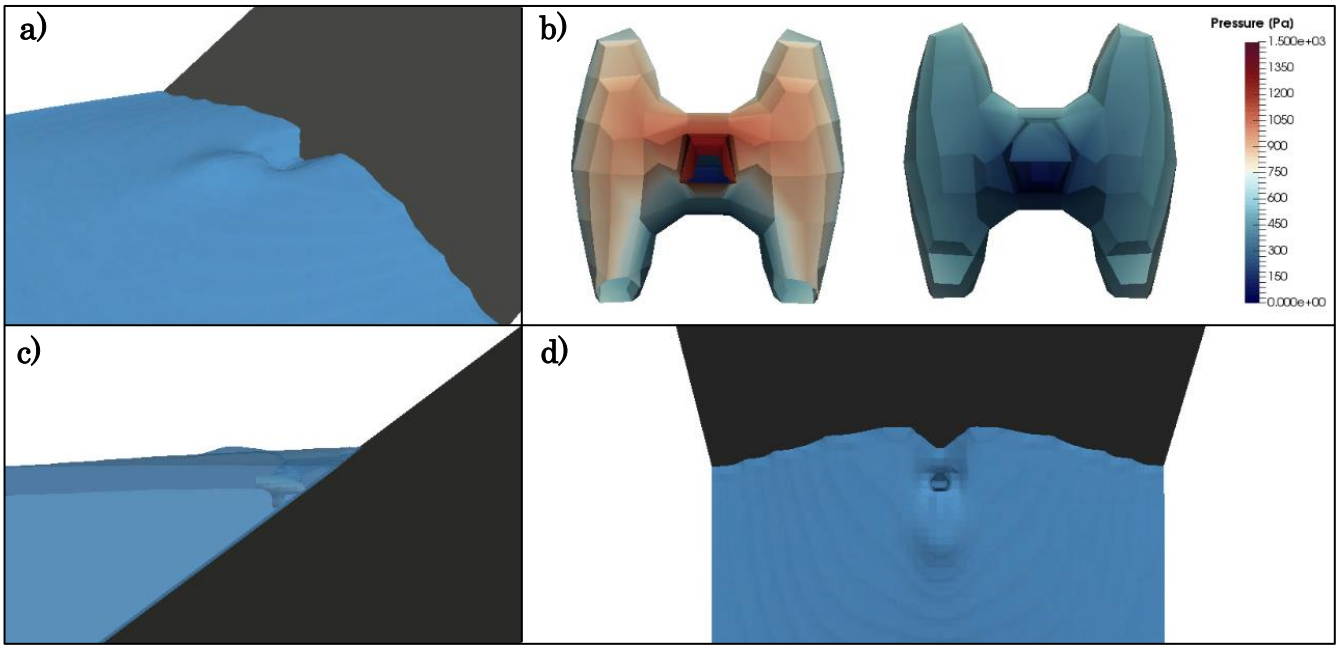

Figure 80: General Hydrodynamic Behaviour and Induced Pressures on Unit During Wave Impact, for SSU_L1_H12_T3P0 Test Condition

Figure 80 shows a comparison between the X and Z-forces for the same SSU_L1_H12_T3P0 test condition, for both the numerical model and experimental results.

First, it is obvious that the small undulations generated at the unit are not present in the numerical model. It can be seen that the X-forces appear to be underestimated for the first wave impact, but are matching nearly identically with the experimental signal as the waves reach steady periodic conditions. At this point, the numerical model remains stable in its signal for the remainder of the test. The experimental signal varies slightly above and below this value due to reflection interference in the flume. This result is in good agreement with the experimental values. The positive peak Z-forces however, appear to be underestimated by ≈ 1 N or more, after the first wave impact. After this point, the numerical model remains constant. Negative peak Z-forces are also over-estimated.

While the general hydrodynamic behaviour appears to be favourable, this result shows that the level of resolution chosen for the numerical model may not have been fine as necessary. The peak magnitudes, due to wave impacts, in the experimental results are not captured in the numerical results, nor is the receding run-down. The numerical model appears to underestimate the positive peaks in both X and Z-directions, and overestimate the negative peaks in the Z-direction.

Figure 81 shows the comparison of the same experimental signal for the pressure results at Sensors P3 and P5. It is clearly evident from the results of both sensors that the numerical model was not capable of capturing the complex pressure fluctuations associated with the highly complex turbulent flows around the unit. The pressure sensor reading drops sharply after the peak, while in the experimental results there was a clear gradual receding nature to the signal. Similar to the force results, the pressure results are clearly smoother in the numerical model as they appear to have not captured the true highly turbulent nature of the flow induced by wave impact.

In pressure sensor P3, negative pressures in the range of 0 to -50 Pa were experienced in the numerical model that appeared much greater than any negative pressure in the experimental signal. The results appear to be in good alignment with the experimental data for the P3 pressure sensor, in terms of capturing only the peak pressure magnitude once the waves level off.

It can be seen however, that the peak pressures are highly underestimated in the numerical model, for pressure sensor P5. In the experimental testing, the reversal of flow, and associated run-down pressures exceeded the numerical results by 300 Pa or more. In order to get a sense of the pressure distribution on the back of the unit, Figure 82 shows the same comparison for pressure sensor P6. It is clear that pressures were underestimated at all locations on the back of the unit during run-down. Again, at this location (P6), the numerical model underestimates the signal by approximately 200 Pa or more.

It does however appear that the discrepancy between the numerical and the experimental results for pressure on the back of the unit remains rather constant once the experimental wave signal levels off. This may be a constant that can be used in future calibrations and can be incorporated into the numerical results.

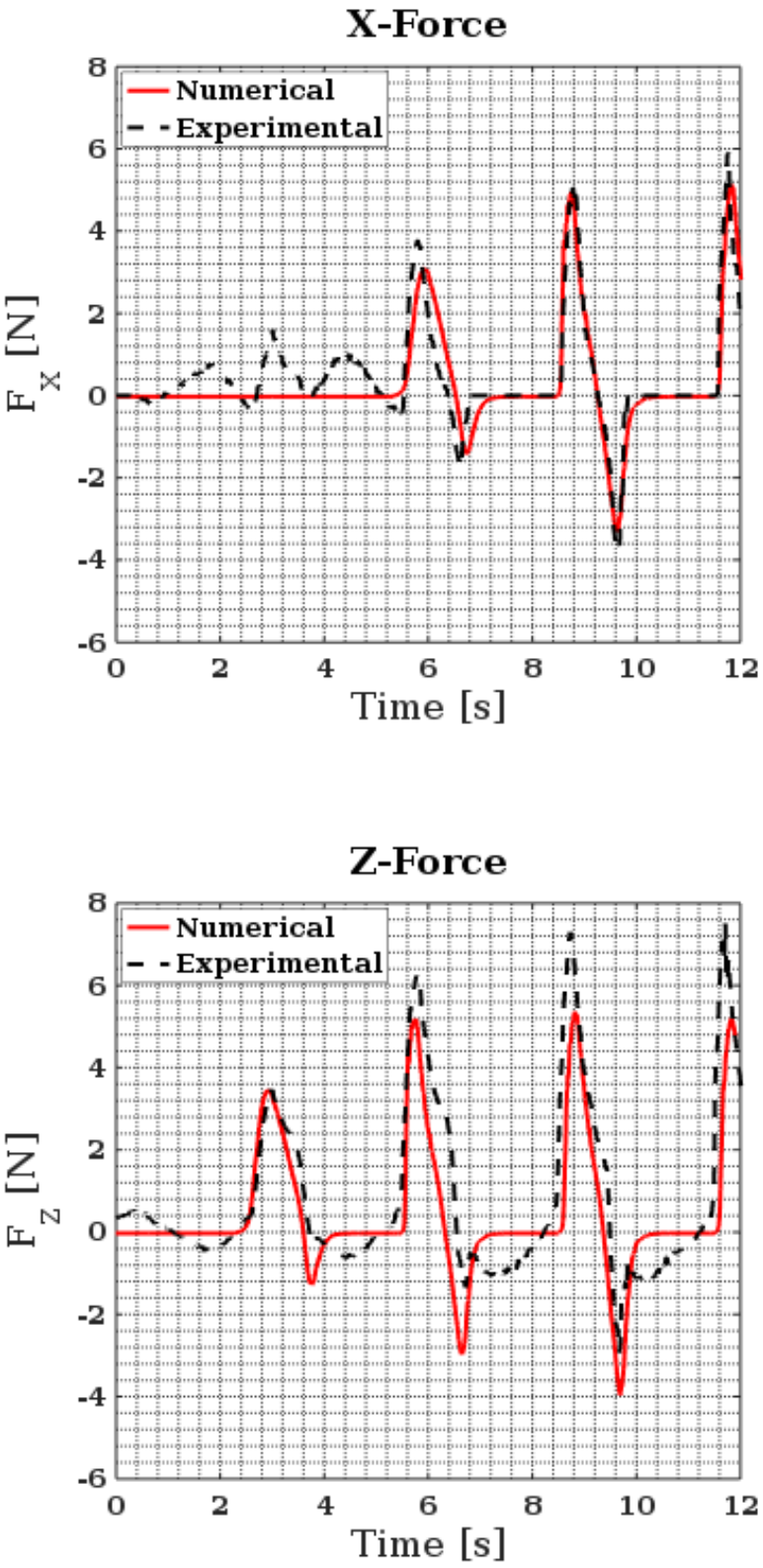

Figure 81: Comparison of Calibrated Numerical Model vs. Experimental Results for SSU_L1_H12_T3P0 Test Condition - top X-Force, bottom Z-Force

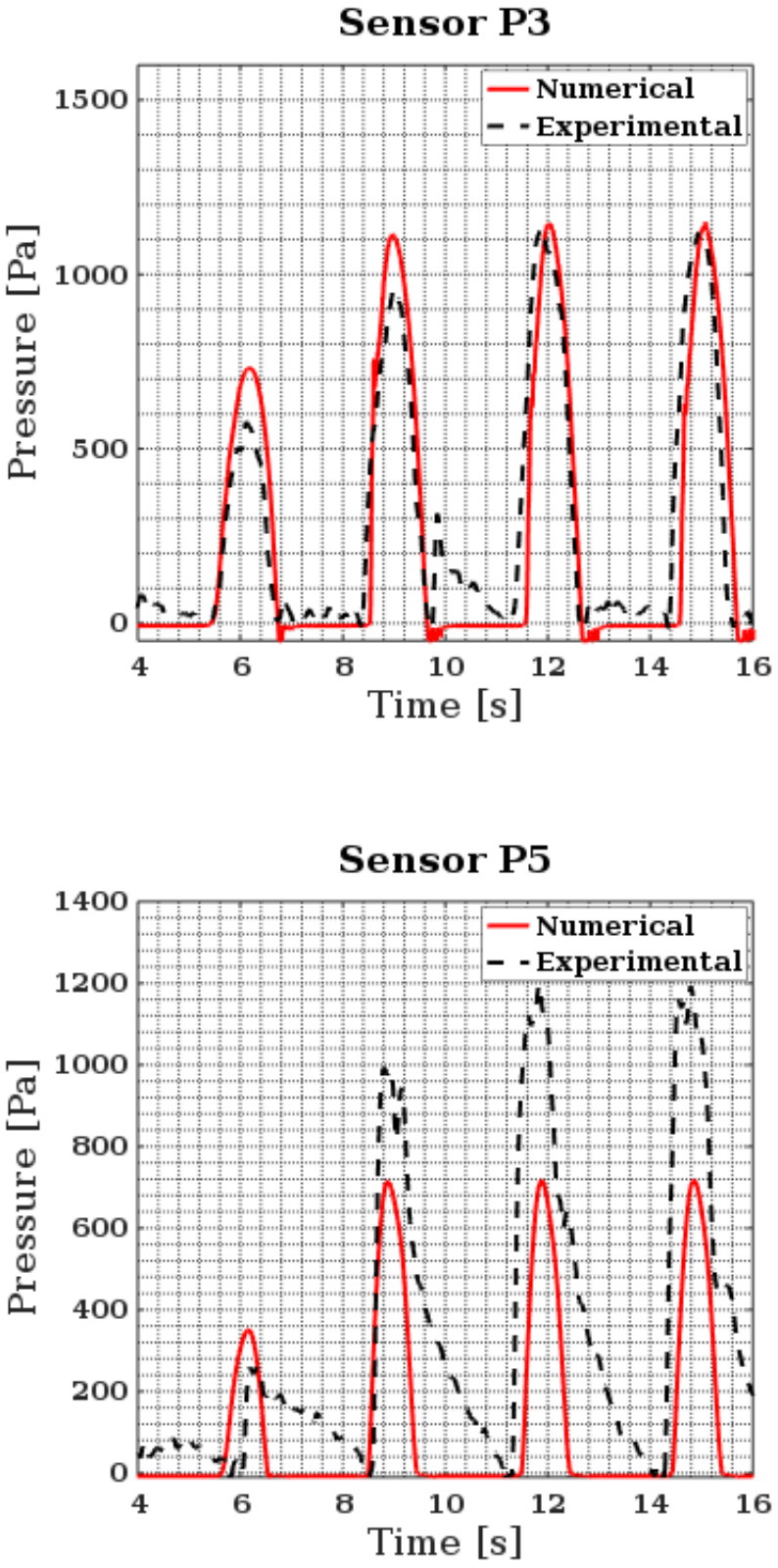

Figure 82: Comparison of Calibrated Numerical Model vs. Experimental Results for SSU_L1_H12_T3P0 Test Condition – top Sensor P3, bottom Sensor P5

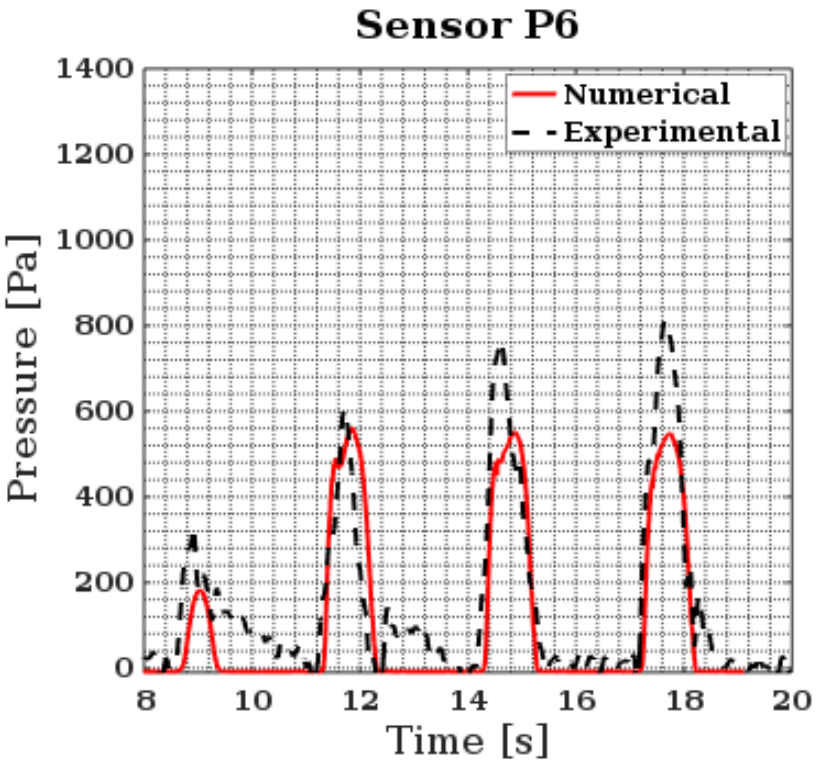

Figure 83: Comparison of Calibrated Numerical Model vs. Experimental Results for SSU_L1_H12_T3P0 Test Condition – Sensor P6

5.6 Discussion

The truncated extent of the full domain that was chosen for the numerical model appeared to be able to capture the full shoaling characteristics and replicate the wave conditions in the SSU experiments.

As part of the mesh calibration process, general rules of thumb were determined that may be useful for future modeling of concrete armour units in breakwaters. First, using grid cells with aspect ratios of 2 or greater near the free surface appeared to better preserve wave conditions in a numerical environment. Second, in order to preserve the shape of a Core-Loc armour unit to a reasonable degree for numerical purposes, the unit should be meshed with no more than 10 cells across the width of the main face of the unit, as well as the height. This general rule appeared to capture the unit to a fair degree of accuracy for modeling purposes, and integration into structured meshes. Figure 73 shows this level of refinement.

The mesh calibration procedure showed that the OlaFlow inlet condition libraries were capable of replicating the SSU test conditions to a reasonable degree. Figure 70 shows that for mesh resolution of 2x2x1 cm or finer, the inlet conditions and propagation characteristics to the toe of the structure can be accurately reproduced. Figure 71 shows that the run-up depth at the location of the unit can also be accurately reproduced. From

these results, it was concluded that the 2x2x1 cm mesh resolution was capable of reproducing the SSU testing conditions. As shown from Figure 74, it appeared that mesh independence could also be reached with a level of refinement around the unit locations resulting in grid cells of size 1x1x1 cm. This was in agreement with the general rule of thumb stated above, resulting in roughly 12 grid cells across the face of the unit.

Three turbulence models were investigated as part of calibrating the numerical model. The standard $k-\varepsilon$, $RNG\ k-\varepsilon$, and $SST\ k-\omega$ turbulence models were compared. From the results shown in Figure 75, there were no notable differences between the three models. The standard $k-\varepsilon$ model showed the highest accuracy compared to the experimental results, and was thus deemed the best choice for modeling the SSU tests.

The investigation into the effect of changing wall roughness showed that increasing the wall roughness resulting in increased forces on the unit (Figure 76). From the numerical results, it appeared that a 2 mm wall roughness height showed the closest match to the experimental data. However, upon inspection of the unit, it was deemed acceptable that an assumed value of 1 mm for wall roughness height of the unit would be used.

The calibrated model was compared to a SSU_L1_H12_T3P0 test condition. As shown in Figures 77, 78 and 79, the general hydrodynamic behaviour was captured well by the numerical model. As shown in Figure 80, both the X and Z-forces were in agreement with the experimental result until reflection begins to oscillate. It can be seen from Figure 81 that the peak magnitudes of pressure on Sensor P3 were captured to a high degree of accuracy in the numerical model. However, for all sensors on the back of the unit (P4, P5, P6), the peak pressures were underestimated. For all force and pressure signals, the turbulent run-down portion of the signal was not captured in the results.

5.7 Summary and Conclusions

The current numerical study in OpenFOAM was carried out to produce general rules of thumb for modeling concrete armour units in rubble mound breakwaters. In addition, this numerical model was developed in an attempt replicate the conditions and results of the SSU testing program. From the results of the numerical study, it can be concluded that:

- OpenFOAM coupled with OlaFlow wave boundary conditions provides a robust, open-source, high performance CFD tool capable of modeling breakwater-wave interaction

- Core-Loc unit's shape can be preserved with approximately 10 cells or greater spanning the height and width of the unit, refinement around the unit should follow this general rule

- Wave conditions, and propagation characteristics can be better preserved by using grid cells with aspect ratios of 2 or greater near the free surface; a dynamic mesh

around the interface may also improve the accuracy at the cost of increased computation time

- Inlet conditions, propagation to the toe, and run-up depth at the unit was accurately reproduced using a structure grid with 2x2x1 cm size

- Refinement around the unit resulting in a grid of size 1x1x1 cm appeared to show mesh independence in terms of forces on the unit

- The three turbulence models investigated showed no appreciable difference between them

- The highest wall roughness of 2 mm appeared to match the experimental data closest, although 1 mm was deemed more acceptable based on analysis of the unit surface

- The calibrated model was capable of reproducing X and Z-forces to within 0-2 N of error during peak forces; Z-forces appeared to be more underestimated than the X-forces in the numerical model

- The peak magnitudes modeled in Sensor P3 were highly accurate when compared to the experimental data. Pressures measured on the back of the unit were consistently underestimated

- Run-down behaviour was not captured in any of the force or pressure signals in the numerical results

6.0 Conclusion

In the current study, three separate endeavours were undertaken in order to further advance the modeling techniques of rubble mound breakwaters.

First, was the development of the instrumented Core-Loc unit. A unit capable of measuring pressures and forces induced during wave action. This included a comprehensives performance testing and calibration phase. Second, another comprehensive testing program was undertaken to test the unit in a breakwater environment. This testing program was targeted at isolating the effect of different breakwater slope location, and the effect of different wave breaking characteristics. Third, a numerical model was developed in OpenFOAM with the goals of developing general rules of thumb, and replicating the experimental test results.

The results of the current study show that, in general, the paradigm of using instrumented “Smart-Units” for experimental testing can provide valuable insight into the hydrodynamic interaction between waves and armour units; this is not typically captured in standard experimental testing techniques. This study proved readily available, low-cost, relatively low-tech instrumentation is capable of advancing armour

unit design towards the force balance approach. In addition, the current study shows that these types of instrumented unit can be used to produce novel datasets that can be used to calibrate numerical models. These numerical models would then be able to fully replicate real breakwater interaction, and provide insight that has thus far eluded the coastal engineering community.

The major results and conclusions are summarized below for each of the three distinct aspects of the current study.

Experimental Study – Instrumented Core-Loc Unit:

- The unit was outfitted with 6 pressure sensors in key unique locations across the unit's surface. The wiring was housed within a hollow chamber inside the unit. The unit included embedded coupling nuts for mounting on force transducers

- The performance of the 6 sensors embedded in the instrumented Core-Loc unit showed that the sensors were able to capture pressures at a very high resolution (≈ 1.2 Pa) at 8 defined frequencies between 40-320 Hz

- Proper planning of the wiring inside the unit may have opened space to accommodate additional sensors, and reduce ambient noise

- The sensitivity between sensors deviated by ≤ 1 %, while the sensitivity for each individual sensor changed by ≤ 1.05 % from each subsequent calibration.

- Each pressure sensor was determined to be capable of measuring pressures from 0-27000 Pa, with an average precision of 0.54 % FS. This was subject to change based on the gain factor

Experimental Study – Sloped Single Unit (SSU) Tests:

- A wide range of wave conditions were tested, with Iribarren numbers ranging from $2.9 \leq \xi_0 \leq 9.915$

- The developed image processing tool was capable of accurately tracking the water surface profile at the testing location for all regular and irregular wave conditions, and provided reasonably accurate estimates of the buoyant force

- A peak statistical analysis was performed on the force and pressure signals, in order to extract key information and reduce the dataset to representative values for non-dimensional plots

- A reduction in surf similarity resulted in a drastic increase in generated forces in both the X and Z-directions. This included both total and hydrodynamic forces. Pressures increased in all sensors as well

- Steepness appeared to have a very close relationship with the generated hydrodynamic forces on the unit, increasing wave steepness lead to increased hydrodynamic forces and pressures, this is in agreement with the findings of Sakakiyama (1990), Van der Meer (1988) and other similar formulations

- The tests showed that there may be a location below the SWL that is subjected to the highest impacts, as proposed by Hofland et al. (2018)

- Standard design methods were not capable of designing the unit's weight for this exposed testing condition

- The variability of stable unit weight for a given wave height, as calculated by the force balance approach, showed standard design methods are highly idealized and do not account for the wide range of possible wave loading scenarios

Numerical Study – OpenFOAM Model:

- A Core-Loc unit's shape can be preserved with approximately 10 cells or greater spanning the height and width of the unit, refinement around the unit should follow this general rule

- Inlet conditions, propagation to the toe, and run-up depth at the unit was accurately reproduced using a structure grid with 2x2x1 cm size

- Refinement around the unit resulting in a grid of size 1x1x1 cm showed mesh independence in terms of forces on the unit

- The calibrated model was capable of reproducing X and Z-forces to within 0-2 N of error during peak forces. Z-forces appeared to be more underestimated than the X-forces in the numerical model.

- The peak magnitudes modeled in Sensor P3 were highly accurate when compared to the experimental data. Pressures measured on the back of the unit were consistently underestimated.

- Run-down behaviour was not captured in any of the force or pressure signals in the numerical results

7.0 Recommendations for future work

Throughout this study, several aspects of the methodology were revealed that might benefit from further investigation. As well, pitfalls in certain aspects of the methodology prompted recommendations that may benefit future similar research.

Below are lists of general observations or recommendations that may aid in future research of a similar nature. These are subdivided into three sections as follows:

Experimental Study – Instrumented Core-Loc Unit:

- In order to maintain long-term integrity of the pressure sensors, ensure the sensors are slightly recessed into the unit, or somehow protected if they are flush

- The coupling nuts used to mount the unit on force transducers can be replaced with a low-cost accelerometer and gyroscope, like instruments typically used in cell phones; this would allow the unit to be fully free and able to move

- While this methodology and technology can easily be translated to concrete armour units, as opposed to 3D printed, special precaution must be taken during the casting phase, and to ensure protection of the circuit from moisture during operation

Experimental Study – Sloped Single Unit (SSU) Tests:

- In order to explore the effect of toe water depth, this parameter could be varied in future testing

- This same technology could be applied to any size unit above the size used in the current study, and may even be possible to go slightly smaller; this would allow quantitative investigation into the effect of scale

- For future testing into the investigation of unit location on the slope, it is recommended that adjacent rows be chosen closer together. In addition it is recommended that these rows not extend as far up the slope, and have more data points below the SWL to capture the unique behaviour mentioned in Section 6.0.

- In order to more accurately capture the buoyant force in future testing, a 3D image processing technique could be employed, or a dense array of WGs around the unit.

Numerical Study – OpenFOAM Model:

- In order to accurately model the highly turbulent flow patterns, investigate a model that is capable of modeling air entrainment and compressibility

- Investigate the effect of using a dynamic mesh around the free surface, and around the armour unit during to capture turbulent run-up and run-down events

- Perform an LES simulation on the numerical model to better capture the turbulent behaviour around the unit

8.0 References

1. Baart (2010). “Toe Rock Stability for Rubble Mound Breakwaters”. Proc. International Conference On Coastal Engineering (ICCE 2010), P. 13.

2. Bakker (2003). “Development of Concrete Breakwater Armour Units.”1st Coastal, Estuary and Offshore Engineering Specialty Conference of the Canadian Society for Civil Engineering.

3. Battjes (1974). “Surf similarity”, Proceedings of 14th Coastal Engineering Conference, Copenhagen, Denmark, American Society of Civil Engineers, New York, pp.466-480.

4. Bradbury (1988). “Rock Armour for Rubble Mound Breakwaters, Sea Walls, And Revetments: Recent Progress”. Report SR 150, Hydraulics Research, Wallingford.

5. Bradbury (1991). “Rock Armour Stability Formulae-Influence of Stone Shape and Layer Thickness.” Coastal Engineering 1990: Pp. 1446-1459.

6. Bruce (2009). “Overtopping Performance of Different Armour Units for Rubble Mound Breakwaters.” Coastal Engineering, Vol. 56, Pp. 166-179.

7. Burcharth (1985). “Fatigue in Breakwater Concrete Armour Units”. In B. L. Edge (Ed.), Proceedings of the 19th International Conference on Coastal Engineering: ICCE '84: Houston, Texas, September 3-7 1984. (pp. 2592-2607). Chapter 174.American Society of Civil Engineers.

8. Burcharth (1995). “Rubble Mound Breakwater Failure Modes. Proc. Final Workshop: RubbleMound Failure Modes”, Sorrento, Italy, November 1995.

9. Burcharth (1998). “Influence of Core Permeability On Accropode Armour Layer Stability.” In Allsop, N. W. H. (Ed.), Coastlines, Structures and Breakwaters: Proceedings of The International Conference. Thomas Telford Ltd.

10. Burcharth (1999). “Scaling of core material in rubble mound breakwater model tests”, Proc. Copedec-V, Capetown, South Africa.

11. Burcharth (2007). “Aspects related to design and construction of breakwaters in deep water”. Project and Construction of Deep Port Water: Maritime Works Symposium, Delft University 2007.

12. Burcharth, (1987). “The Lessons From Recent Breakwater Failures: developments in breakwater design”, Paper presented at Technical Congress On Inshore Engineering, Vancouver, Canada.

13. Calabrese (2008). “Wave Reflection at Rubble Mound Breakwaters Ranging from Submerged to Exposed.” Conference: International Conference On Coastal Engineering, At Hamburg, Germany, Volume: Poster Proceedings ICCE 2008.

14. CEH (2012), “Cube Concrete Armour Units”, Image, http://theconstructor.org/concrete/compressive-strength-of-concrete- cubes/1561/.

15. CIRIA. (2007). “The Rock Manual: The Use of Rock in Hydraulics Engineering”, 2nd Ed. CIRIA C683.

16. CLI (2012). “Guidelines for Design – Core-Loc Design Guide Table”, Preliminary Design Guidelines, Concrete Layer Innovations, table extracted from http://www.concretelayer.com/sites/default/files/CORE-LOC%E2%84%A2_Design_Table_2012_0.pdf

17. CLI (2018). “Core-Loc Breakwater”, image extracted from http://www.concretelayer.com/

18. De Gerloni (1991). “The Safety of Breakwaters Against Wave Overtopping”, Proceedings of ICE Conference: Breakwaters and Structures, Thomas Telford UK, pp. 246-259.

19. De Jong (1996). “Wave Transmission at Low-Crested Structures”, Master’s Thesis, Delft University, The Netherlands, http://repository.tudelft.nl/islandora/object/uuid:e091d54b-bffa-44ba-8d5d-850cdc03731a/datastream/OBJ/download.

20. De Jong (2003). “Experimental Research On the Stability of Armour and Secondary Layer in A Single Layered Tetrapod Breakwater.” M.Sc. Thesis.

21. Denechere (2009). “Advanced System for Visualising Placement of Armour Units Underwater.” Coastal Structures, Vol. 4.

22. Dentale (2014). “Numerical Wave Interaction with Tetrapod Breakwater.” International Journal of Naval Architecture and Ocean Engineering, Col. 6, Issue 4, Pp. 800-812.

23. Dentale (2014). “Rubble Mound Breakwater: Run-up, Reflection, and Overtopping by Numerical 3-D Simulation”, Proceedings of a conference on Coasts, Marine Structures and Breakwaters 2013, London (2013), pp. 1–10.

24. Domingo (2012). “Evaluation of concrete armour units used to repair damaged dolos breakwaters”, Master’s Thesis, Delft University, The Netherlands, http://repository.tudelft.nl/islandora/object/uuid:18e5b375-11aa-4529-844f-7a40017d4de1?collection=education.

25. Douglas (2015). “Breaker Types”, Redrawn after U.S. Department of Transportation – Federal Highway Administration (FHWA), image extracted from https://en.wikipedia.org/wiki/Iribarren_number#/media/File:Breaking_wave_types.svg

26. Esteban (2012). “Stability of Rubble Mound Breakwaters Against Solitary Waves”, Proceedings from Conference Coastal Engineering 2012 .

27. EurOtop. (2007). “Manual On Wave Overtopping of Sea Defences and Related Structures”. An Overtopping Manual Largely Based On European Research, But for Worldwide Application. Van Der Meer, J.W., Allsop, N.W.H., Bruce, T., De Rouck, J., Kortenhaus, A., Pullen, T., Schüttrumpf, H., Troch, P. And Zanuttigh, B., Www.Overtopping-Manual.Com.

28. FEMA (2005). “Wave Run-Up and Overtopping”, Coastal Flood Hazard Analysis and Mapping Guidelines- Focused Study Report.

29. Gerding (1993). “Toe Structure Stability of Rubble Mound Breakwaters”. M.Sc. Thesis Delft and Delft Hydraulics Report H1874. Delft University of Technology, Delft.

30. Guo (2015). "Numerical simulation of breakages of concrete armour units using a three-dimensional fracture model in the context of the combined finite-discrete element method" Computers & Structures, 146:117-142.

31. Hasselmann (1973). “A Parametric Wave Prediction Model”, Journal of Physical Oceanography, Vol. 6: pp. 200-228.

32. Herbich (2000). “Linear Wave Theory”, Handbook of Coastal Engineering, McGraw-Hill Companies, Inc. Image extracted from https://www.globalspec.com/reference/63553/203279/linear-wave-theory

33. Higuera, P.C. (2015). “Aplicación de la Dinámica deFluidos Computacional a la Acciónde l Oleaje Sobre Estructuras”. PHd. Thesis. Universidad De Cantabria Departamento de Ciencias y Técnicasdel Agua y del Medio Ambiente

34. Hofland (2016a). “Wave Generation and Wave Measurements in the New Delta Flume”, Proceedings of the 6th International Conference on the Application of Physical Modelling in Coastal and Port Engineering and Science (Coastlab16 – Ottawa, ON), Delft University.

35. Hofland (2016b). “AUTOMATIC SETTLEMENTANALYSIS OF SINGLE-LAYER ARMOUR LAYERS”, Proceedings of the 6thInternational Conference on the Application of Physical Modelling in Coastal and Port Engineering and Science (Coastlab16), Ottawa, Canada, May 10-13, 2016.

36. Hofland et al. (2018). "Smart Rocking Armour Units", Proceedings of the 7th International Conference on the Application of Physical Modeling in Coastal and Port Engineering and Science, CoastLab18, Santander, Spain, May 22-26, 2018.

37. Holzhausen (1992). “New Stability Formula for Dolosse”, Proc. 23rd ICCE, Pp. 1231-1244.

38. Houmb (1976). “Parameterization of wave spectra and long term joint distribution of wave height and period”. Proc. Conf on Behaviour of Offshore Structures, Trondheim 1976.

39. Hughes (1993). “Physical Models and Laboratory Techniques in Coastal Engineering”. World Scientific. ISBN 978-981-02-1541-5.

40. Inman (2001). “History of Early Breakwaters”. Association of Coastal Engineers Newsletter, Alexandria, VA.

41. Ismail (1999). “MEASUREMENT OF REINFORCEMENT CORROSION IN MARINE STRUCTURES”, MALAYSIAN SCIENCE & TECHNOLOGY CONGRESS '99, Symposium A; Agriculture, Biology, Marine, Medicine, Social Science, Basic Sciences. 25-27 October, 1999. Kuala Lumpur.

42. Karsten (2007). “Statistical Description of Wave Parameters”. Available from Http://Www.Coastalwiki.Org/Wiki/Statistical_Description_Of_Wave_Parameters.

43. Latham (2013). “New Modelling and Analysis Methods for Concrete Armour Units Systems Using FEMDEM.” Journal of Coastal Engineering, Vol. 77, Pp. 151- 166.

44. Latham (2014). “Numerical Modelling of Forces, Stresses, and Breakages of Concrete Armour Units”, ICCE Coastal Engineering 2014, Imperial College London.

45. Liu (2013). “Modeling of Earth Surface Dynamics and Related Problems Using OpenFOAM.” CSDMS 2013 Meeting. Department of Civil and Environmental Engineering University of Texas at San Antonio, Texas.

46. Losada (2001). “Formulas for The Calculation of Breakwaters.” Chapter in Book: Ramon Iribarren, Chapter: Formulas for The Calculation of Breakwaters, Publisher: CEDEX.

47. Maddrell (2005). “Lessons Re-Learnt from the Failure of Marine Structures, ICE Conference Coastlines, Structures, and Breakwaters 2005. Conference Proceedings.

48. Majestic (2016). “Rubble Mound Breakwater Trunk and Head”, Image, http://www.majesticjetties.ae/marine_civil_works/.

49. Melby (1994). “The Core-Loc: Optimized Concrete Armour”Coastal Engineering Proceedings, Vol. 24.

50. Mesuris (2016). “POSIBLOC VISIBLOC CORE LOC”, Video, https://www.youtube.com/watch?v=PqetpYZyhp8.

51. Miche (1944). “Mouvement ondulatoires de la mer en profondeur constante ou decroissante”, Annales des Ponts et Chaussees.

52. MIT (2011). “2.019 Design of Ocean Systems”, Course Lecture 9, Mechanical Engineering Department, Course 2.019, https://ocw.mit.edu/courses/mechanical-engineering/2-019-design-of-ocean- systems-spring-2011/lecture-notes/MIT2_019S11_OWE.pdf.

53. Molland (2008). “The Maritime Engineering Reference Book: A Guide to Ship Design”, Construction and Operation, ELSEVIER Butterworth-Heinermann, ISBN 0750689870.

54. Muttray (2005), “Placement and structural strength of Xbloc® and other single layer armour units”, Coastlines, Structuresand Breakwaters, Thomas Telford 556–567.

55. Muttray (2008). “Design of Concrete Armour Layers, Xbloc Design Guidelines”, Delta Marine Consultants, H.J. Nederhorststraat 1, 2800 AG Gouda. The Netherlands, http://www.xbloc.com/downloads/conference-papers-publications/2008-design-of-concrete-armour-layers/item1241

56. Nistor (2016), “Concrete Armour Units”, Course Lecture (CVG5160), University of Ottawa Faculty of Engineering.

57. Oever et al (2006) “Theoretical and experimental study on the placement of Xbloc® armour units”, Proceedings of the International Conference on Coastal Engineering, ASCE, San Diego (2006).

58. Palmer (1998). “Design and Construction of Rubble Mound Breakwaters”, IPENZ Transactions, Vol. 25, No. 1.

59. Putnam (1948). “Diffraction of Water Waves by Breakwaters”, American Geophysical Union, University of California: Fluid Mechanics Laboratory, No. HE-116-280, Scripps Institution of Oceanography).

60. Reedijk (2003). “Development of The Xbloc Breakwater Armour Unit”. 2nd International Conference On Port & Maritime R&D and Technology.

61. Reedijk (2008). “Effect of Core Permeability On Armour Layer Stability.” ASCE, Proceedings of 31st International Conference On Coastal Engineering, Hamburg, Germany.

62. Sakakiyama (1990). "Scale Effect of Wave Force on Armor Units". Coastal Engineering, Volume 22 Chapter 128, 1990, pp. 1716-1729.

63. Salauddin (2015). "Physical Model Tests On New Armour Block Crablock for Breakwaters to Come to Preliminary Design Guidance."M.Sc. Thesis. UNESCO-IHE Institute for Water Education, Delft, The Netherlands.
64. Sayao (2016). "Stability and Damage of Tetrapod-Armoured Breakwaters." Proceedings of The 6th International Conference On the Application of Physical Modelling in Coastal and Port Engineering and Science (Coastlab16).

65. Scaminee (1998). "Tripoli breakwater reconstruction - evaluation and modification 1982 NEDECO design", Student's Master's Thesis, Delft University

66. Schuttrumph (2010). "Wave Run-Up and Wave Overtopping at Armoured Rubble Slopes and Mounds." Chapter 15, EurOtop Overtopping Manual.

67. Sciortino (2010). "Fishing Harbour Planning, Construction and Management- Ch.7: Breakwaters." FAO Fisheries and Aquaculture Technical Paper. No. 539. Rome, FAO. 337p.
68. Shetty (2005). "Concrete Technology (Theory & Practice)", S. Chand Publishing London, UK, 2005.

69. Swinford (2012). "Hurricane ANDREW", Image, http://enb110-ajs-2012.blogspot.ca/2012_10_01_archive.html.

70. TAW (2002). "Technical Report Wave Run-up and Wave Overtopping at Dikes". TAW, Technical Advisory Committee on Flood Defenses. Author: J.W. van der Meer.

71. Thompson (1975). "Riprap Design for Wind Wave Attack." A Laboratory Study in Random Wave, Wallingford, EX707.

72. USACE (1984). "The Shore Protection Manual", US Army Corps of Engineers: Waterways Experiment Station, Vol. 1-2.

73. USACE (1992). "Revision of Thrust Block Criteria", Engineer Technical Letter 1110-3-446, Department of The Army, U.S. Army Corps of Engineers, Washington, D.C. 20314-1000, 20 August 1992.

74. USACE (2002). "US Army Corps of Engineers Coastal Engineering Manual", US Army Corps of Engineers, Vol. 1-6.

75. Van Damme (1988). "Quality and Durability of Concrete Armour Units", Proceedings of ICE Coastal Engineering 1988, Chapter 156: Concrete Armour Units, pp. 2101-2115

76. Van den Bosch (2002). “INFLUENCE OF THE DENSITY OF PLACEMENT ON THE STABILITY OF ARMOUR LAYERS ON BREAKWATERS”, ICCE Conference Proceedings 2002.

77. Van Der Meer (1987). “Stability of Breakwater Armour Layers-Design Formulae.” Coastal Engineering, Vol. 11, Pp. 219-239.

78. Van Der Meer (1988). “Stability of Cubes, Tetrapods and Accropode.” Design of Breakwaters, Thomas Telford, London, 71-80.

79. Van der Meer (1990). “Stability of low-crested and reef breakwaters”. Proc. 22th. ICCE, Delft.

80. Van der Meer (1991). “Rocking armor units: Number, location and impact velocity”. Elsevier, J. of Coastal Engineering, Vol. 15. No's 1, 2.

81. Van der Meer (1994). "Stresses in Tetrapod Armour Units Induced by Wave Action", Coastal Engineering, Volume 24 Chapter 123, 1994, pp. 1713-1726
82. Van der Meer (1995). “Conceptual design of rubble mound breakwaters”. World Scientific. In: Advances in Coastal and Ocean Engineering, Volume 1. Ed. P.L.F. Liu, pp. 221-315.

83. Van Der Meer (1998a). “Geometrical Design of Coastal Structures.” Chapter 9 In Seawalls, Dikes and Revetments Edited by K. W. Pilarczyk, Balkema, Rotterdam.

84. Van Der Meer (1998b). “Wave Run-Up and Overtopping.” Chapter 8 In Seawalls, Dikes and Revetments Edited by K. W. Pilarczyk, Balkema, Rotterdam.

85. Van Der Meer (1999). “Design of Concrete Armour Layers.” Proc. Coastal Structures, A.A. Balkema, Rotterdam, Pp. 213–221 ISBN 90 5809 092 2.

86. Van der Meer (2006). “Wave reflection from coastal structures”, Proc. ICCE 2006, vol. 5, 4337-4349.

87. Van Der Meer (2011). “Design Aspects of Breakwaters and Sea Defences.”5th International Short Conference On Applied Coastal Research.
88.
89. Van Gent (1999). “Single-Layer Rubble Mound Breakwaters.” Conference: Coastal Structures, At Santander.

90. Van Gent (2001). “Rubble Mound Breakwaters: Single Armour Layers and High-Density Concrete Units.” Conference: Coastlines, Structures and Breakwaters, ICE, London.

91. Van Gent (2003). “Stability of Rock Slopes with Shallow Foreshores.” Conference: Coastal Structures, At Portland.

92. Van Gent (2014). “Rock Toe Stability of Rubble Mound Breakwaters.” Coastal Engineering, Volume 83, Pp. 166-176.

93. Van Rijn (2016). “Stability Design of Coastal Structures.” Independent Consultant, Available At : Http://Www.Leovanrijn-Sediment.Com/.

94. Verdegaal (2013). “The Influence of Core Permeability On the Stability of Interlocking Single Layer Armour Units.” M.Sc. Thesis. Delft University of Technology Faculty of Civil Engineering and Geosciences Section Hydraulic Engineering.

95. Wang (2015). “Nonlinear Passive Control of a Wave Energy Converter Subject to Constraints in Irregular Waves”. Journal Energies, Vol. 8, ISSN 1996-1073.

96. Weigel (1962). “Diffraction of waves by semi-infinite breakwaters”. Journal of Hydraulic Div. Proceeding: ASCE 88(HY1): 27-44.

97. Wiebe (2016). “UAV Technology Applications in Coastal Engineering”, Proceedings of the 6th International Conference on the Application of Physical Modelling in Coastal and Port Engineering and Science (Coastlab16), Ottawa, Canada, May 10-13, 2016.

98. Xiang (2012). “Modelling of fluid-solid interactions using an adaptive mesh fluid model coupled with a combined finite-discrete element model”. Ocean Dynamics, 62:1487-1501.

99. Yoo (2013). “Local parameter for armor weight estimation”. Journal of Coastal Research: Special Issue 65 - International Coastal Symposium Volume 1: pp. 422 – 427.

Appendix A: Statistical Peak Analysis Results

Total X-Forces (F_x)								
Test ID	Positive Peaks				Negative Peaks			
	Min.	Max.	Mean	Std. Dev.	Min.	Max.	Mean	Std. Dev.
SSU_L1_H12_T1P4	7.23	9.65	8.32	0.67	-5.10	-7.32	-6.47	0.44
SSU_L1_H12_T1P8	5.93	7.84	6.76	0.40	-4.62	-6.84	-5.26	0.50
SSU_L1_H12_T2P2	5.27	6.84	6.00	0.35	-3.01	-4.92	-3.91	0.32
SSU_L1_H12_T2P6	5.25	7.21	6.12	0.45	-1.97	-2.94	-2.37	0.21
SSU_L1_H12_T3P0	5.06	6.81	5.22	0.42	-2.73	-4.89	-3.45	0.46
SSU_L1_H15_T1P4	9.01	11.80	10.17	0.55	-5.70	-7.78	-6.95	0.40
SSU_L1_H15_T1P8	8.02	10.21	9.06	0.49	-5.39	-8.07	-6.89	0.48
SSU_L1_H15_T2P0	6.70	9.88	8.25	0.46	-4.83	-7.61	-6.08	0.49
SSU_L1_H15_T2P4	5.87	7.60	6.28	0.52	-5.50	-6.77	-5.94	0.26
SSU_L1_H15_T2P8	8.02	8.85	8.50	0.23	-6.17	-7.33	-6.47	0.53
SSU_L1_H15_T3P2	5.43	6.35	5.98	0.21	-3.39	-4.29	-3.73	0.18
SSU_L1_H15_T3P8	4.00	5.50	4.40	0.32	-2.77	-3.89	-3.36	0.19
SSU_L1_H20_T1P4	12.52	19.10	15.95	1.21	-6.12	-7.65	-6.98	0.27
SSU_L1_H20_T2P0	10.18	13.49	10.80	0.97	-6.69	-9.04	-8.29	0.51
SSU_L1_Hs15_Tp1P2	0.02	37.35	6.90	5.23	-0.10	-23.76	-3.18	2.14
SSU_L1_Hs15_Tp1P8	0.02	41.50	5.78	3.75	-0.01	-15.96	-3.69	2.80
SSU_L1_Hs15_Tp2P2	1.95	19.61	4.81	2.86	-0.17	-14.05	-3.39	2.76
SSU_L1_Hs15_Tp2P6	1.00	14.63	3.83	2.77	-1.03	-15.87	-3.41	2.90
SSU_L2_H12_T1P4	2.68	4.11	3.21	0.32	-1.69	-2.45	-2.04	0.13
SSU_L2_H12_T1P8	1.94	2.63	2.04	0.27	-0.13	-0.19	-0.15	0.01
SSU_L2_H12_T2P2	1.35	2.11	1.68	0.15	-0.12	-0.14	-0.13	0.01
SSU_L2_H12_T2P6	1.93	2.53	2.20	0.16	-0.24	-0.30	-0.27	0.01
SSU_L2_H12_T3P0	2.17	2.74	2.28	0.16	-0.12	-0.17	-0.16	0.01
SSU_L2_H15_T1P4	3.61	4.43	4.04	0.18	-1.81	-2.58	-2.24	0.14
SSU_L2_H15_T1P8	3.38	4.45	3.68	0.27	-1.19	-1.79	-1.54	0.11
SSU_L2_H15_T2P0	3.59	4.07	3.77	0.15	-1.52	-1.89	-1.34	0.18
SSU_L2_H15_T2P4	3.42	4.42	3.65	0.26	-1.56	-1.91	-1.75	0.06
SSU_L2_H15_T2P8	3.70	4.83	4.47	0.38	-1.92	-2.86	-2.35	0.16
SSU_L2_H15_T3P2	2.15	2.67	2.49	0.25	-0.76	-1.13	-0.89	0.08
SSU_L2_H15_T3P8	2.80	4.30	3.31	0.42	-1.07	-1.76	-1.37	0.12
SSU_L2_H20_T1P4	7.09	9.44	7.76	0.63	-2.31	-3.79	-2.91	0.28
SSU_L2_H20_T2P0	5.45	7.88	7.05	0.58	-3.17	-4.68	-3.87	0.26
SSU_L2_Hs15_Tp1P2	0.53	23.01	4.13	4.08	-0.23	-5.76	-1.49	1.04
SSU_L2_Hs15_Tp1P8	0.52	30.68	3.87	3.95	-0.24	-8.56	-2.68	1.83
SSU_L2_Hs15_Tp2P2	0.51	19.80	4.04	3.47	-0.41	-8.80	-3.21	1.88
SSU_L2_Hs15_Tp2P6	0.94	13.07	3.19	2.36	-0.34	-6.32	-1.53	0.73
SSU_L3_H12_T1P4	11.66	14.94	14.23	0.74	-1.70	-2.47	-2.09	0.12
SSU_L3_H12_T1P8	7.98	11.26	8.93	0.57	-1.29	-2.02	-1.65	0.12
SSU_L3_H12_T2P2	5.74	8.08	6.31	0.58	-1.21	-1.58	-1.34	0.08
SSU_L3_H12_T2P6	3.44	4.47	3.85	0.35	-0.39	-0.52	-0.47	0.03
SSU_L3_H12_T3P0	2.62	3.31	3.09	0.22	-0.10	-0.13	-0.11	0.01
SSU_L3_H15_T1P4	10.09	13.69	12.99	0.87	-2.07	-3.10	-2.50	0.19
SSU_L3_H15_T1P8	9.14	12.30	11.26	0.82	-2.93	-3.77	-3.28	0.16
SSU_L3_H15_T2P0	7.05	10.58	8.67	0.72	-2.12	-3.08	-2.46	0.20
SSU_L3_H15_T2P4	6.24	7.28	6.87	0.32	-1.27	-1.89	-1.59	0.10
SSU_L3_H15_T2P8	4.09	5.66	5.19	0.52	-0.99	-1.33	-1.14	0.06
SSU_L3_H15_T3P2	2.69	3.93	3.38	0.32	-0.77	-0.99	-0.82	0.05
SSU_L3_H15_T3P8	3.77	5.56	4.41	0.47	-0.12	-0.17	-0.13	0.01
SSU_L3_H20_T1P4	14.47	19.93	16.45	0.71	-3.46	-4.80	-4.32	0.27
SSU_L3_H20_T2P0	10.52	14.75	11.89	0.86	-4.54	-5.99	-5.45	0.29
SSU_L3_Hs15_Tp1P2	0.01	25.92	7.94	5.16	0.00	-9.74	-2.06	2.10
SSU_L3_Hs15_Tp1P8	0.00	42.66	7.38	4.47	0.00	-14.96	-3.04	3.31
SSU_L3_Hs15_Tp2P2	0.00	16.63	5.64	3.13	0.00	-13.78	-2.23	2.88
SSU_L3_Hs15_Tp2P6	0.01	14.36	4.58	2.97	0.00	-16.92	-1.81	2.38

Hydrodynamic X-Forces (F_{Hx})								
Test ID	Positive Peaks				Negative Peaks			
	Min.	Max.	Mean	Std. Dev.	Min.	Max.	Mean	Std. Dev.
SSU_L1_H12_T1P4	6.07	9.40	7.71	0.61	-6.86	-9.23	-7.27	0.66
SSU_L1_H12_T1P8	5.63	7.12	5.97	0.36	-5.76	-8.78	-6.97	0.49
SSU_L1_H12_T2P2	3.33	4.91	3.93	0.28	-2.95	-4.95	-4.16	0.38
SSU_L1_H12_T2P6	3.25	7.21	5.74	0.30	-4.02	-5.13	-4.67	0.19
SSU_L1_H12_T3P0	3.86	4.80	4.25	0.27	-3.21	-5.09	-3.97	0.32
SSU_L1_H15_T1P4	8.01	9.35	8.90	0.26	-8.18	-9.88	-8.59	0.41
SSU_L1_H15_T1P8	6.78	10.21	7.26	0.94	-4.81	-7.08	-6.21	0.45
SSU_L1_H15_T2P0	5.61	9.78	6.51	0.79	-4.23	-7.46	-6.29	0.65
SSU_L1_H15_T2P4	3.30	4.55	3.99	0.24	-4.67	-6.57	-5.99	0.39
SSU_L1_H15_T2P8	6.64	8.85	6.97	0.62	-5.19	-6.62	-5.61	0.30
SSU_L1_H15_T3P2	2.97	6.35	3.39	0.79	-1.96	-3.98	-2.54	0.37
SSU_L1_H15_T3P8	2.36	2.88	2.69	0.10	-2.31	-3.58	-2.38	0.37
SSU_L1_H20_T1P4	10.95	14.78	13.68	0.82	-6.87	-8.77	-7.90	0.27
SSU_L1_H20_T2P0	7.07	9.22	8.62	0.56	-6.03	-9.49	-7.41	0.58
SSU_L1_Hs15_Tp1P2	1.07	37.05	5.31	5.06	-1.03	-23.77	-3.98	2.21
SSU_L1_Hs15_Tp1P8	1.34	39.26	4.02	3.11	-0.93	-16.53	-3.92	2.67
SSU_L1_Hs15_Tp2P2	1.14	19.31	3.95	2.71	-1.00	-16.14	-3.94	2.58
SSU_L1_Hs15_Tp2P6	0.18	14.35	2.44	2.43	-1.96	-18.12	-1.13	2.98
SSU_L2_H12_T1P4	1.94	2.68	2.25	0.14	-1.89	-2.68	-2.08	0.15
SSU_L2_H12_T1P8	1.33	1.93	1.57	0.12	-0.47	-0.71	-0.60	0.04
SSU_L2_H12_T2P2	1.05	1.63	1.29	0.10	-0.66	-0.93	-0.79	0.04
SSU_L2_H12_T2P6	1.17	1.56	1.23	0.11	-0.37	-0.46	-0.41	0.01
SSU_L2_H12_T3P0	1.77	2.10	1.96	0.05	-0.82	-1.16	-1.00	0.05
SSU_L2_H15_T1P4	2.44	3.59	3.15	0.21	-2.07	-3.23	-2.60	0.18
SSU_L2_H15_T1P8	2.03	2.89	2.35	0.16	-1.78	-2.34	-1.90	0.14
SSU_L2_H15_T2P0	2.06	2.73	2.60	0.17	-1.64	-2.80	-1.84	0.32
SSU_L2_H15_T2P4	2.25	3.35	2.63	0.24	-1.99	-2.94	-2.49	0.13
SSU_L2_H15_T2P8	2.65	3.90	3.07	0.30	-2.16	-3.23	-2.50	0.22
SSU_L2_H15_T3P2	1.05	1.38	1.21	0.06	-0.89	-1.27	-1.10	0.07
SSU_L2_H15_T3P8	1.43	2.38	1.84	0.16	-1.22	-1.71	-1.33	0.11
SSU_L2_H20_T1P4	4.46	5.76	5.49	0.29	-2.84	-3.89	-3.12	0.20
SSU_L2_H20_T2P0	6.08	8.74	6.94	0.49	-4.34	-5.53	-4.69	0.24
SSU_L2_Hs15_Tp1P2	0.25	22.08	3.85	4.06	-0.49	-8.16	-1.72	0.98
SSU_L2_Hs15_Tp1P8	0.31	29.06	3.33	4.04	-0.51	-9.88	-2.45	1.77
SSU_L2_Hs15_Tp2P2	0.37	17.55	3.60	3.22	-0.47	-9.19	-2.65	1.97
SSU_L2_Hs15_Tp2P6	1.04	12.92	3.17	2.42	-0.37	-6.43	-1.43	0.76
SSU_L3_H12_T1P4	7.94	11.62	9.61	0.65	-2.92	-4.19	-3.74	0.27
SSU_L3_H12_T1P8	4.45	6.25	5.25	0.28	-2.34	-3.28	-3.04	0.19
SSU_L3_H12_T2P2	2.34	3.20	3.02	0.24	-2.47	-3.53	-3.01	0.18
SSU_L3_H12_T2P6	1.47	2.15	1.68	0.16	-1.31	-1.82	-1.61	0.08
SSU_L3_H12_T3P0	1.99	2.87	2.33	0.19	-1.24	-1.74	-1.49	0.07
SSU_L3_H15_T1P4	8.68	12.80	10.24	0.75	-3.65	-4.86	-3.83	0.31
SSU_L3_H15_T1P8	5.50	8.22	7.15	0.50	-4.13	-5.74	-4.42	0.38
SSU_L3_H15_T2P0	4.31	5.34	4.99	0.20	-3.61	-5.36	-4.22	0.38
SSU_L3_H15_T2P4	3.19	4.17	3.47	0.21	-2.64	-3.68	-3.01	0.20
SSU_L3_H15_T2P8	2.26	2.86	2.62	0.10	-2.24	-2.78	-2.46	0.10
SSU_L3_H15_T3P2	1.97	2.60	2.07	0.16	-1.25	-1.76	-1.45	0.08
SSU_L3_H15_T3P8	2.07	2.86	2.24	0.21	-1.43	-2.23	-1.76	0.14
SSU_L3_H20_T1P4	11.62	14.96	13.13	0.50	-3.77	-5.69	-4.82	0.30
SSU_L3_H20_T2P0	5.94	8.74	7.66	0.57	-4.81	-7.09	-6.06	0.39
SSU_L3_Hs15_Tp1P2	2.08	19.35	6.39	3.05	-1.61	-10.36	-3.24	1.65
SSU_L3_Hs15_Tp1P8	1.54	38.30	5.26	2.87	-1.56	-12.46	-3.80	2.34
SSU_L3_Hs15_Tp2P2	1.17	12.91	3.64	1.97	-1.56	-13.74	-3.44	2.22
SSU_L3_Hs15_Tp2P6	0.97	11.76	3.10	1.61	-1.12	-14.63	-2.62	1.63

Total Z-Forces (F_z)								
Test ID	Positive Peaks				Negative Peaks			
	Min.	Max.	Mean	Std. Dev.	Min.	Max.	Mean	Std. Dev.
SSU_L1_H12_T1P4	6.90	10.17	8.69	0.79	-6.92	-9.67	-7.61	0.68
SSU_L1_H12_T1P8	7.32	9.73	8.93	0.63	-2.86	-4.36	-3.43	0.40
SSU_L1_H12_T2P2	7.31	10.41	8.33	0.75	-1.53	-2.35	-1.91	0.21
SSU_L1_H12_T2P6	5.25	8.21	7.69	0.83	-3.51	-4.58	-3.72	0.31
SSU_L1_H12_T3P0	5.94	7.97	7.17	0.49	-1.33	-2.92	-1.48	0.56
SSU_L1_H15_T1P4	9.01	14.91	11.84	1.09	-5.62	-7.67	-6.97	0.71
SSU_L1_H15_T1P8	9.15	11.21	10.89	0.74	-4.83	-7.28	-5.60	0.62
SSU_L1_H15_T2P0	8.07	10.05	9.76	0.67	-4.47	-6.54	-5.32	0.51
SSU_L1_H15_T2P4	7.43	8.75	8.18	0.30	-5.14	-7.29	-5.65	0.60
SSU_L1_H15_T2P8	7.85	8.85	7.74	0.41	-5.12	-8.06	-6.45	0.57
SSU_L1_H15_T3P2	6.35	7.35	6.62	0.25	-2.58	-4.03	-3.15	0.30
SSU_L1_H15_T3P8	3.26	5.10	4.56	0.21	-0.40	-0.54	-0.48	0.18
SSU_L1_H20_T1P4	12.56	18.39	15.07	1.30	-6.55	-9.09	-7.27	0.80
SSU_L1_H20_T2P0	10.49	15.93	12.90	1.19	-6.43	-8.28	-7.53	0.54
SSU_L1_Hs15_Tp1P2	0.00	47.84	6.90	5.79	-0.01	-16.30	-2.76	1.88
SSU_L1_Hs15_Tp1P8	0.00	34.83	6.13	4.76	-0.01	-18.76	-3.14	3.03
SSU_L1_Hs15_Tp2P2	0.00	25.78	6.37	3.86	0.00	-14.83	-2.23	2.70
SSU_L1_Hs15_Tp2P6	0.01	19.20	6.29	3.30	0.00	-15.04	-2.07	2.56
SSU_L2_H12_T1P4	3.25	4.23	3.41	0.36	-2.92	-3.71	-3.09	0.29
SSU_L2_H12_T1P8	1.71	2.59	2.11	0.20	-0.66	-0.97	-0.80	0.10
SSU_L2_H12_T2P2	1.56	2.28	1.89	0.31	-0.26	-0.35	-0.32	0.20
SSU_L2_H12_T2P6	2.73	3.59	2.89	0.28	-0.49	-0.68	-0.61	0.18
SSU_L2_H12_T3P0	2.63	4.10	3.18	0.28	-0.59	-0.81	-0.68	0.12
SSU_L2_H15_T1P4	3.95	6.08	4.94	0.50	-2.91	-4.40	-3.44	0.44
SSU_L2_H15_T1P8	3.40	4.50	4.29	0.42	-2.50	-3.93	-3.02	0.33
SSU_L2_H15_T2P0	2.52	3.84	3.48	0.39	-2.35	-3.11	-2.70	0.20
SSU_L2_H15_T2P4	4.00	4.92	4.64	0.33	-2.37	-3.24	-2.63	0.32
SSU_L2_H15_T2P8	4.32	6.43	5.32	0.52	-3.23	-4.89	-3.97	0.45
SSU_L2_H15_T3P2	2.21	3.33	2.95	0.45	-1.14	-1.67	-1.40	0.25
SSU_L2_H15_T3P8	3.49	4.59	4.25	0.41	-1.26	-1.83	-1.46	0.32
SSU_L2_H20_T1P4	7.26	9.43	7.92	0.80	-3.58	-4.37	-3.94	0.34
SSU_L2_H20_T2P0	7.76	8.84	7.78	0.54	-6.32	-8.43	-7.64	0.50
SSU_L2_Hs15_Tp1P2	0.56	17.62	4.82	5.59	-0.16	-9.64	-2.70	3.03
SSU_L2_Hs15_Tp1P8	0.00	15.70	3.74	4.94	0.00	-5.54	-1.98	2.83
SSU_L2_Hs15_Tp2P2	0.73	15.10	4.33	4.31	-0.02	-6.18	-2.23	2.92
SSU_L2_Hs15_Tp2P6	0.88	9.31	3.86	3.01	-0.49	-3.54	-2.06	1.13
SSU_L3_H12_T1P4	6.02	9.71	7.83	0.77	-1.65	-2.79	-2.15	0.35
SSU_L3_H12_T1P8	4.04	5.33	4.52	0.40	-0.27	-0.38	-0.31	0.15
SSU_L3_H12_T2P2	3.47	5.27	3.95	0.39	-0.14	-0.20	-0.17	0.04
SSU_L3_H12_T2P6	2.95	4.72	3.81	0.33	0.00	0.00	0.00	0.02
SSU_L3_H12_T3P0	3.70	6.06	4.81	0.48	-0.04	-0.07	-0.05	0.07
SSU_L3_H15_T1P4	7.81	12.99	10.00	0.99	-2.52	-3.39	-2.89	0.29
SSU_L3_H15_T1P8	7.57	9.74	8.78	0.55	-0.57	-0.68	-0.60	0.17
SSU_L3_H15_T2P0	6.41	10.76	8.27	0.94	-0.86	-1.14	-1.05	0.17
SSU_L3_H15_T2P4	6.09	8.25	6.39	0.78	-3.23	-4.48	-3.59	0.46
SSU_L3_H15_T2P8	6.49	8.95	7.92	0.61	-1.60	-2.37	-2.06	0.29
SSU_L3_H15_T3P2	6.41	8.73	6.99	0.70	-2.85	-3.88	-3.13	0.37
SSU_L3_H15_T3P8	5.59	8.32	6.87	0.49	-3.96	-5.80	-4.91	0.32
SSU_L3_H20_T1P4	10.80	17.44	13.12	1.12	-7.91	-11.29	-9.65	0.78
SSU_L3_H20_T2P0	9.04	14.82	11.82	0.98	-2.44	-3.35	-2.68	0.34
SSU_L3_Hs15_Tp1P2	0.01	25.56	5.53	3.43	-0.01	-27.76	-4.06	4.53
SSU_L3_Hs15_Tp1P8	0.01	22.21	5.41	2.15	-0.01	-13.50	-1.54	1.39
SSU_L3_Hs15_Tp2P2	0.01	21.82	5.66	2.42	-0.02	-10.01	-1.72	1.15
SSU_L3_Hs15_Tp2P6	0.01	15.46	6.48	2.73	-0.01	-12.83	-1.88	1.38

Hydrodynamic Z-Forces (F_{Hz})								
Test ID	Positive Peaks				Negative Peaks			
	Min.	Max.	Mean	Std. Dev.	Min.	Max.	Mean	Std. Dev.
SSU_L1_H12_T1P4	7.26	9.27	8.06	0.33	-5.43	-8.54	-6.62	0.59
SSU_L1_H12_T1P8	6.09	8.43	6.69	0.24	-4.80	-7.24	-5.57	0.38
SSU_L1_H12_T2P2	5.31	6.37	5.74	0.18	-2.73	-3.33	-3.00	0.13
SSU_L1_H12_T2P6	4.25	7.21	5.09	0.36	-4.27	-5.95	-5.04	0.36
SSU_L1_H12_T3P0	3.98	6.16	4.97	0.42	-2.67	-3.65	-3.05	0.18
SSU_L1_H15_T1P4	9.01	12.85	10.36	0.56	-7.24	-11.21	-8.76	0.72
SSU_L1_H15_T1P8	7.88	10.21	8.90	0.40	-5.74	-8.13	-7.46	0.32
SSU_L1_H15_T2P0	5.95	8.88	7.25	0.55	-5.39	-7.40	-6.79	0.30
SSU_L1_H15_T2P4	5.17	7.14	5.54	0.16	-3.42	-4.47	-3.66	0.12
SSU_L1_H15_T2P8	5.35	7.85	6.81	0.60	-6.26	-8.34	-6.95	0.34
SSU_L1_H15_T3P2	4.12	6.35	4.61	0.19	-3.33	-4.58	-4.09	0.23
SSU_L1_H15_T3P8	4.64	5.85	5.03	0.55	-1.48	-1.84	-1.67	0.08
SSU_L1_H20_T1P4	10.98	16.35	13.29	0.98	-8.07	-11.65	-8.96	0.42
SSU_L1_H20_T2P0	7.89	14.53	10.03	0.87	-7.95	-9.47	-8.69	0.36
SSU_L1_Hs15_Tp1P2	0.02	37.35	6.89	5.23	-0.10	-23.76	-3.48	2.14
SSU_L1_Hs15_Tp1P8	0.02	41.50	5.87	3.75	-0.01	-15.96	-3.82	2.80
SSU_L1_Hs15_Tp2P2	1.95	19.61	6.16	2.86	-0.17	-14.05	-3.81	2.76
SSU_L1_Hs15_Tp2P6	1.00	14.63	5.29	2.77	-1.03	-15.87	-4.30	2.90
SSU_L2_H12_T1P4	1.64	2.34	1.94	0.12	-0.87	-1.23	-1.13	0.05
SSU_L2_H12_T1P8	1.18	1.55	1.41	0.10	-1.21	-1.44	-1.30	0.04
SSU_L2_H12_T2P2	1.30	1.84	1.48	0.07	-1.13	-1.39	-1.26	0.06
SSU_L2_H12_T2P6	0.96	1.18	1.10	0.05	-0.99	-1.36	-1.07	0.04
SSU_L2_H12_T3P0	1.61	2.12	1.86	0.10	-1.10	-1.79	-1.43	0.16
SSU_L2_H15_T1P4	2.99	4.39	3.38	0.16	-2.63	-3.47	-2.97	0.15
SSU_L2_H15_T1P8	2.33	2.86	2.44	0.04	-1.80	-2.51	-1.96	0.07
SSU_L2_H15_T2P0	2.48	3.01	2.71	0.10	-2.35	-3.37	-2.65	0.15
SSU_L2_H15_T2P4	2.45	3.74	3.09	0.27	-2.81	-3.34	-2.98	0.08
SSU_L2_H15_T2P8	2.19	3.17	2.73	0.22	-2.15	-3.52	-2.75	0.29
SSU_L2_H15_T3P2	1.10	1.63	1.42	0.13	-1.16	-1.50	-1.39	0.05
SSU_L2_H15_T3P8	1.62	2.66	2.11	0.20	-1.71	-2.35	-1.88	0.08
SSU_L2_H20_T1P4	5.42	8.67	7.05	0.71	-3.93	-5.05	-4.80	0.11
SSU_L2_H20_T2P0	6.58	8.03	7.57	0.39	-6.32	-7.58	-7.40	0.08
SSU_L2_Hs15_Tp1P2	0.53	13.01	2.87	4.08	-0.23	-5.76	-2.87	1.04
SSU_L2_Hs15_Tp1P8	0.52	18.68	2.69	3.95	-0.24	-8.56	-2.21	1.83
SSU_L2_Hs15_Tp2P2	0.51	11.80	2.73	3.47	-0.41	-8.80	-2.10	1.88
SSU_L2_Hs15_Tp2P6	0.52	8.82	2.36	3.58	-0.29	-6.06	-0.73	0.14
SSU_L3_H12_T1P4	6.44	8.46	7.99	0.62	-3.04	-4.09	-3.25	0.10
SSU_L3_H12_T1P8	4.58	6.98	5.82	0.54	-2.60	-3.44	-2.94	0.16
SSU_L3_H12_T2P2	3.12	4.91	3.53	0.18	-2.06	-3.32	-2.59	0.24
SSU_L3_H12_T2P6	1.76	2.54	2.27	0.22	-1.76	-2.51	-1.99	0.11
SSU_L3_H12_T3P0	2.42	3.48	2.98	0.24	-2.44	-3.13	-2.63	0.09
SSU_L3_H15_T1P4	8.51	11.65	9.10	0.25	-4.51	-5.75	-5.32	0.19
SSU_L3_H15_T1P8	6.18	7.40	6.98	0.32	-2.80	-4.48	-3.53	0.35
SSU_L3_H15_T2P0	5.60	6.53	6.16	0.23	-3.45	-4.60	-3.93	0.24
SSU_L3_H15_T2P4	4.28	4.99	4.62	0.15	-2.74	-4.35	-3.46	0.34
SSU_L3_H15_T2P8	3.59	5.21	4.31	0.31	-3.33	-4.85	-3.76	0.21
SSU_L3_H15_T3P2	3.56	4.54	4.13	0.24	-2.38	-3.22	-2.95	0.13
SSU_L3_H15_T3P8	3.63	4.71	3.92	0.12	-1.76	-2.57	-2.09	0.16
SSU_L3_H20_T1P4	7.16	9.19	8.59	0.58	-6.14	-7.95	-7.35	0.21
SSU_L3_H20_T2P0	4.34	5.54	4.82	0.20	-3.60	-5.19	-4.29	0.32
SSU_L3_Hs15_Tp1P2	0.01	25.92	4.41	5.16	0.00	-19.74	-4.16	2.10
SSU_L3_Hs15_Tp1P8	0.00	37.66	3.46	4.47	0.00	-14.96	-3.08	3.31
SSU_L3_Hs15_Tp2P2	0.00	16.63	3.37	3.13	0.00	-13.78	-2.99	2.88
SSU_L3_Hs15_Tp2P6	0.01	14.36	4.20	2.97	0.00	-15.92	-3.83	2.38

Test ID	Pressures															
	P3				P4				P5				P6			
	Min.	Max.	Mean	Std. Dev.	Min.	Max.	Mean	Std. Dev.	Min.	Max.	Mean	Std. Dev.	Min.	Max.	Mean	Std. Dev.
SSU_L1_H12_T1P4	774.22	2110.80	1187.96	372.55	200.79	607.99	422.49	111.82	757.00	1363.93	1100.85	131.71	185.79	602.99	383.49	99.31
SSU_L1_H12_T1P8	844.73	1035.25	966.83	42.62	543.79	808.62	727.53	73.78	610.49	892.09	731.72	60.65	526.79	771.62	678.53	58.56
SSU_L1_H12_T2P2	764.52	1069.99	1016.48	47.84	439.96	888.58	755.16	74.67	457.09	923.51	775.24	76.96	424.96	856.58	738.16	71.62
SSU_L1_H12_T2P6	822.88	1035.33	941.05	60.87	508.59	870.25	687.29	87.69	736.30	942.86	817.81	53.55	482.59	827.25	679.29	77.23
SSU_L1_H12_T3P0	970.64	1199.84	1106.26	45.69	743.69	901.70	737.63	62.76	756.30	1192.68	1084.81	106.88	698.69	859.70	736.63	57.49
SSU_L1_H15_T1P4	1136.88	4385.25	2118.43	664.06	241.45	489.30	346.45	62.17	570.86	2570.01	1016.31	291.67	236.45	481.30	336.45	52.11
SSU_L1_H15_T1P8	841.04	2011.86	1256.12	183.65	739.96	1065.91	952.44	73.41	598.66	1213.89	915.74	193.97	714.96	1033.91	910.44	65.43
SSU_L1_H15_T2P0	874.94	1900.81	1185.07	159.15	628.36	1017.79	838.49	94.91	643.10	1092.19	914.25	309.13	593.36	1015.79	814.49	87.53
SSU_L1_H15_T2P4	640.16	1430.76	1229.02	148.75	772.90	1211.22	993.09	103.84	682.07	1228.61	1009.69	95.69	753.90	1166.22	975.09	98.78
SSU_L1_H15_T2P8	924.89	1304.10	1138.89	62.95	640.25	965.33	897.93	69.98	714.71	1235.77	992.59	82.61	640.25	953.33	863.93	59.18
SSU_L1_H15_T3P2	1113.05	1320.11	1211.12	59.01	839.20	1082.31	967.17	86.79	850.67	1336.19	1034.18	126.27	790.20	1071.31	953.17	71.28
SSU_L1_H15_T3P8	1255.54	1565.97	1437.04	79.64	1017.30	1345.05	1197.25	79.57	1099.28	1473.74	1266.20	72.45	1001.30	1340.05	1193.25	76.54
SSU_L1_H20_T1P4	1641.30	8188.95	3099.91	1123.82	231.04	485.14	328.66	73.71	885.46	2597.29	1109.36	235.40	214.04	469.14	304.66	62.71
SSU_L1_H20_T2P0	1215.73	1906.21	1421.14	101.98	1071.56	1313.08	1198.33	61.14	804.83	1974.41	923.30	233.79	1060.56	1308.08	1172.33	57.53
SSU_L1_Hs15_Tp1P2	62.68	14121.40	998.40	1142.72	101.46	650.92	266.52	113.43	57.50	2343.09	345.29	294.09	62.46	629.92	223.52	111.18
SSU_L1_Hs15_Tp1P8	112.65	5062.39	913.36	609.70	114.27	1246.64	435.56	266.28	83.67	2738.27	508.47	404.85	95.27	1213.64	431.56	254.27
SSU_L1_Hs15_Tp2P2	101.84	5070.07	820.18	513.01	144.40	1407.66	518.01	282.45	106.89	3183.55	478.88	387.11	102.40	1378.66	474.01	281.47
SSU_L1_Hs15_Tp2P6	111.41	3317.77	728.66	451.78	142.26	1569.02	550.10	312.82	100.71	2416.95	639.48	371.91	96.26	1562.02	517.10	303.29
SSU_L2_H12_T1P4	166.99	1477.22	750.03	518.64	94.33	223.24	151.47	41.99	52.72	708.25	282.12	165.35	46.33	220.24	122.47	37.90
SSU_L2_H12_T1P8	64.41	879.99	251.68	170.37	48.72	573.30	441.81	150.33	12.56	228.14	30.74	22.97	33.72	568.30	398.81	143.31
SSU_L2_H12_T2P2	242.28	568.73	225.98	149.45	54.58	304.64	69.93	37.96	12.04	43.49	25.69	7.40	13.58	264.64	27.93	32.91
SSU_L2_H12_T2P6	72.10	561.20	205.64	129.22	47.15	386.19	49.32	72.08	12.61	336.26	58.78	55.91	13.15	362.19	46.32	61.34
SSU_L2_H12_T3P0	27.15	537.64	157.34	138.31	50.70	175.70	67.80	45.02	13.24	480.73	46.22	70.86	44.70	151.70	63.80	31.05
SSU_L2_H15_T1P4	491.97	1888.80	1189.40	402.43	94.22	264.94	194.69	57.31	68.70	532.20	189.82	91.45	47.22	258.94	160.69	48.32
SSU_L2_H15_T1P8	202.52	868.70	409.80	154.76	59.62	336.82	150.71	66.16	45.54	431.84	163.01	74.74	35.62	293.82	145.71	53.55
SSU_L2_H15_T2P0	212.25	472.90	387.67	79.47	89.73	266.71	172.10	48.86	35.50	293.71	172.30	78.47	41.73	227.71	133.10	45.37

SSU_L2_H15_T2P4	164.71	424.23	353.74	65.59	98.35	285.89	215.09	41.87	61.68	347.71	175.06	65.31	71.35	242.89	167.09	35.45
SSU_L2_H15_T2P8	314.33	510.20	445.05	441.08	103.80	334.91	211.23	44.79	69.90	447.32	231.45	94.11	75.80	293.91	176.23	43.28
SSU_L2_H15_T3P2	178.31	313.44	255.77	49.08	22.35	71.51	55.24	22.96	21.72	177.13	51.03	8.54	10.35	51.51	39.24	18.74
SSU_L2_H15_T3P8	279.31	497.42	376.56	61.61	23.96	255.42	97.56	65.09	11.95	536.73	146.71	144.78	13.96	220.42	56.56	58.09
SSU_L2_H20_T1P4	771.78	2454.50	1742.40	663.99	163.81	419.53	269.32	65.13	66.00	364.67	156.71	63.23	141.81	372.53	268.32	63.73
SSU_L2_H20_T2P0	472.11	1339.00	1079.10	139.26	191.21	559.81	343.29	85.00	168.37	721.46	372.87	90.24	159.21	514.81	294.29	71.09
SSU_L2_Hs15_Tp1P2	637.75	8129.00	1619.80	1057.70	34.72	400.15	144.66	56.68	31.10	495.18	104.37	72.20	32.72	376.15	99.66	55.88
SSU_L2_Hs15_Tp1P8	480.90	7207.20	1211.50	902.64	59.36	699.97	172.69	120.63	37.10	2502.50	179.49	236.69	36.36	649.97	142.69	107.34
SSU_L2_Hs15_Tp2P2	541.03	5545.60	1258.20	886.30	43.36	721.42	182.89	149.85	33.43	1074.60	144.65	170.38	34.36	678.42	170.89	137.16
SSU_L2_Hs15_Tp2P6	432.20	5929.38	1597.10	1234.30	59.39	527.44	387.69	283.43	33.09	1400.50	224.43	292.14	51.39	503.44	368.69	278.57
***SSU_L3_H12_T1P4**	265.62	809.51	413.88	112.12	320.47	496.73	387.78	30.97	273.58	1581.07	793.08	175.62	282.47	457.73	337.78	30.37
***SSU_L3_H12_T1P8**	653.33	749.15	709.21	23.60	699.94	816.30	774.19	37.75	625.88	749.71	689.99	28.54	663.94	778.30	725.19	24.65
***SSU_L3_H12_T2P2**	844.32	986.50	915.74	20.67	816.33	941.37	853.89	29.08	830.65	933.36	875.04	26.07	811.33	925.37	848.89	20.13
***SSU_L3_H12_T2P6**	684.18	876.33	802.60	45.19	687.48	894.74	816.97	36.59	756.37	890.20	827.53	31.24	666.48	845.74	774.97	36.17
SSU_L3_H12_T3P0	804.36	987.40	919.78	40.25	807.08	971.21	938.59	33.12	847.80	1080.58	1002.54	47.30	787.08	949.21	890.59	31.45
***SSU_L3_H15_T1P4**	244.06	751.46	439.32	115.27	276.94	602.25	375.69	80.82	640.59	1435.91	933.94	116.64	242.94	569.25	343.69	67.81
***SSU_L3_H15_T1P8**	685.42	810.04	763.07	26.44	712.21	910.22	846.76	37.54	646.34	876.51	755.42	40.73	693.21	873.22	800.76	34.22
***SSU_L3_H15_T2P0**	765.28	923.42	849.41	41.76	716.92	925.00	861.35	70.66	708.44	859.11	778.73	37.08	716.92	923.00	822.35	57.94
***SSU_L3_H15_T2P4**	1033.61	1354.82	1209.07	61.00	975.67	1254.38	1088.24	63.54	944.70	1317.20	1096.54	76.04	931.67	1228.38	1074.24	62.15
***SSU_L3_H15_T2P8**	741.06	1009.81	905.35	58.87	794.10	953.97	877.45	41.55	779.06	1053.83	921.90	64.48	759.10	916.97	844.45	39.21
***SSU_L3_H15_T3P2**	1011.05	1164.64	1113.18	35.78	935.72	1140.70	1031.86	50.03	947.07	1228.77	1107.73	70.94	923.72	1093.70	1007.86	41.72
***SSU_L3_H15_T3P8**	1198.14	1397.04	1324.37	52.34	1192.70	1357.83	1253.43	56.10	1381.96	1520.41	1459.28	34.17	1151.70	1321.83	1242.43	44.37
***SSU_L3_H20_T1P4**	658.86	1554.59	951.74	159.94	304.15	833.59	555.10	108.70	690.16	1439.76	965.62	152.02	283.15	804.59	523.10	100.23
***SSU_L3_H20_T2P0**	830.65	1182.76	949.22	75.91	877.17	1109.64	1007.74	54.56	644.63	979.99	844.40	63.33	844.17	1064.64	975.74	40.84
***SSU_L3_Hs15_Tp1P2**	30.93	2507.23	385.98	216.31	81.44	1739.10	378.14	218.81	50.93	2059.94	435.68	223.03	39.44	1727.10	360.14	208.21
***SSU_L3_Hs15_Tp1P8**	49.56	3919.21	539.35	278.37	88.31	1178.41	527.34	229.36	43.80	2244.51	582.32	283.32	49.31	1155.41	487.34	217.54
***SSU_L3_Hs15_Tp2P2**	52.79	1310.29	590.88	261.73	68.61	1293.15	583.69	258.03	51.43	1599.11	665.11	310.67	39.61	1252.15	572.69	256.07
***SSU_L3_Hs15_Tp2P6**	39.30	1689.74	643.28	324.38	92.96	1639.82	611.34	320.28	45.03	1910.69	718.29	359.17	50.96	1628.82	604.34	310.21

L3 pressures are zeroed with the following initial values: 1132 Pa (P3), 710 Pa (P4), 543 Pa (P5), 700 Pa (P6)